PENTLANDITE EXSOLUTION IN THE Fe-Ni-S SYSTEM:

A MECHANISTIC APPROACH TO PENTLANDITE/PYRRHOTITE ORE TEXTURES

(VOLUME II)

(2 VOLUMES)

by

DAVID PATRICK KELLY

Submitted to the
University of Aston in Birmingham
for the degree of
Doctor of Philosophy

Department of Geological Sciences

May 1985

TABLE OF CONTENTS

VOLUME II

Page

Page

Page

APPENDICES

List of Abbreviations commonly used in Captions for Tables, Line Diagrams and Photomicrographs.

Photomicrographs.

PPL	plane, linearly, polarised light
XP	crossed polars
unXP	slightly uncrossed polars
Oil	oil immersion
f.o.v.	field of view

Minerals or Phases

MSS	monosulphide solid solution	Str	Strathcona
Po	pyrrhotite	CC	Copper Cliff
Mcl Po	monoclinic pyrrhotite	dissem.	disseminated ore
Hex Po	hexagonal pyrrhotite	interm.	'intermediate' ore
Tr	troilite	mass.	massive ore
Mck	mackinawite	xtal	crystal
Pn	pentlandite	grn	grain
vl	violarite	bound	boundary
Py	pyrite		
Cp	chalcopyrite		
Cub	cubanite		
Sph	sphalerite		
Mt	magnetite		
Ilm	ilmenite		

$-\Delta G_{vol}$	volume free energy difference between MSS and Pn. Driving force for pentlandite nucleation.
$+\Delta G_{strain}$	strain free energy term associated with nucleation of Pn in MSS. Volume dependent.
$+\Delta G_{surf}$	surface free energy term across the MSS/Pn interface. Area dependent.
SSpn	supersaturation of Pn in MSS
Y_D	effective interdiffusion distance of Fe, Ni and S in MSS
T or Temp	temperature
T_c	the 'critical' temperature, at which Pn exsolution is initiated
ΔT	the degree of undercooling below the MSS/Pn solvus
T-T-T-X	time-temperature-transformation-composition diagram

TABLE 2.1 Minerals and Phases in the Fe-Ni-S System*

Mineral Name abbreviation	Composition	Thermal max	Stability °C min	Structure Types (cell edges, A°)	Remarks
Monosulphide-solid sol^n, MSS	$(FeNi)_{1-2}S$	1192-992 (1)(2)	∿200°C(3)(4)	Hexagonal, $P6_3/mmC$(5) a∿3.45, c∿5.88 to 5.34(6)	Solid solution from $Fe_{1-x}S$ to $Ni_{1-x}S$, complete from 992°C to ∿200°C. M/S solid solution decreases with falling temp. (see table 2.2) C parameter varies with comp. (6) superstructuring present in limited comp. ranges (5) (section 2.3.1)
Pyrrhotite solid sol^n. Po	$Fe_{1-x}S$	m.p=1190(1)	308-108°C(3)(8)	Hexagonal 1C, $P6_3/mmC$(7) a∿3.45, c∿5.88	Low temperature breakdown results in variety of pyrrhotite types of particular composition with superstructures based on repeats of high temperature subcell (see table 2.6)
	$N_{1-x}S$	999(9)	282(10)	Hexagonal $P6_3/mmc$(5) a∿3.43 c∿5.34	Lower stability dependant on Ni/S ratio, involves eutectic breakdown to $NiS+Ni_3S_4$ (10)
Millerite ml	NiS	379(10)	---	Hexagonal, R3m(11)(12) a=9.61, c=3.14	Inverts above 379°C to become part of $N_{1-x}S$ end member of MSS.
Pentlandite Pn	$(FeNi)_9S_8$	610°C(13)	---	Cubic Fm3m (14) a=10.18 to 10.09	Considerable Fe/Ni solid solution (see table 2.4), a parameter decreases with increasing Ni(6) Forms by subsolidus reactions (2,15)

TABLE 2.1 cont'd

Vaesite vs	NiS_2	m.p.=1022(9)	---	Cubic Pa3 $\bar{a}$=5.67	Melts syntectically to two liquids (9) Mutual solid solubilities of FeS_2 and NiS_2 decrease with decreasing temperature. (17)
Pyrite py	FeS_2	743 (16)	---	Cubic Pa3 a =5.417	Breakdown to 1CPo +$S_{(liq)}$
Bravoite bv	$(Fe,Ni)S_2$	137(18)	---	Cubic Pa3 a =5.51	(19) suggests bv is always metastable
Violarite vl	$FeNi_2S_4$	461(20)	---	Cubic Fd3m a =9.46	Solid solution with Ni_3S_4 complete at 356°C(20)
Polydymite pm	Ni_3S_4	356(20)	---	Cubic Fd3m a =9.48	
Heazlewoodite solid sol^n Hzs	$(FeNi)_{3\pm x}S_2$	862(2)	---	?Cubic $F\bar{4}3m$ a ∿5.22	Presence of Fe raises max stability of $Ni_{3\pm x}S_2$ analog (2); amount of Fe in solid sol^n decreases as temp decreases(2,21) Temperature of inversion to hz structure comp. dependant(9).
Heazlewoodite Hz	Ni_3S_2	556-524(10)	---	Hexagonal R32(22) a =5.74 c =7.14	May contain minor Fe in solid sol^n.
Godlevskite solid sol^n. gss	$(Ni,Fe)_7S_6$	650-573(2)(21)	---		Presence of Fe raises max. stability of Ni_7S_6 analog(2); amount of Fe in solid sol^n decreases as temp. decreases. Temperature of inversion to αgd struct. comp. dependant(9)

TABLE 2.1 cont'd

Godlevskite	$Ni_7S_6(\alpha)$	400-397(10)	-	Orthorhombic Bmmb(23) $\underline{a}$= 3.27, b= 16.16, c= 11.36	May contain minor Fe in solid sol^n.
Kamacite km	α(Fe,Ni)			Cubic Im3m $\underline{a}$ = 2.8864 (24)	High temperature γ phase transforms to $\alpha+\gamma$ at temperatures between ~900°C and ~390°C as Ni content increases from 0 wt% to 50 wt%.(25)
Taenite tn	γ(Fe,Ni)			Cubic Fm3m $\underline{a}$ = 3.5238→3.5956 (100wt%Ni (39wt%Ni)	$\underline{a}$ increases as Ni content decreases (26)
Awaruite aw	Ni_3Fe			Cubic	

* References in brackets

(1) Jensen (1942) (2) Kullerud (1963a) (3) Craig (1973) (4) Barker (person. commun. 1980) (5) Francis 1974 (6) Misra and Fleet (1973b) (7) Nakazawa and Morimoto (1971) (8) Kissin and Scott (1982) (9) Arnold and Malik (1975) (10) Kullerud and Yund (1962) (11) Grice and Ferguson (1974) (12) Rajamani and Prewitt (1974) (13) Kullerud (1963b) (14) Rajamani and Prewitt (1973) (15) Naldrett et al (1967) (16) Kullerud and Yoder (1959) (17) Clark and Kullerud (1963)

(19) Shimazaki (1971) (20) Craig (1971) (21) Misra and Fleet (1973a) (22) Westgren (1938) (23) Fleet (1972)

(24) Swanson et al. (1955) (25) Owen and Liu (1949) (26) Bradley et al. (1937)

TABLE 2.2 Compositional variation of the MSS sulphur-poor boundary with temperature (the MSS-pentlandite solvus) (data from Naldrett et al, 1967, figs. 7,8)

600°C at%			500°C at%		
S	Fe	Ni	S	Fe	Ni
50.0	50.0	-	50.0	50.0	-
50.0	48.5	1.5	50.0	48.5	1.5
49.8	46.4	3.8	50.2	46.1	3.7
50.3	42.2	7.5	50.6	41.9	7.5
50.2	34.7	15.1	50.8	34.1	15.1
50.3	25.4	24.2	50.5	25.4	24.1
50.5	16.0	33.5	50.6	16.0	33.4
50.0	9.7	40.3	50.2	9.7	40.1
49.9	4.9	45.3	50.1	4.9	45.0
50.0	-	50.0	50.0	-	50.0

400°C at%			300°C at%		
S	Fe	Ni	S	Fe	Ni
50.0	50.0	-	50.0	50.0	-
50.1	48.4	1.5	50.8	47.7	1.5
50.9	45.4	3.7	51.5	44.8	3.7
51.1	41.4	7.5	51.6	40.9	7.5
51.3	33.7	15.0	51.8	33.2	15.0
50.6	25.3	24.1	50.9	25.2	24.0
50.8	16.0	33.2	50.9	16.0	33.1
50.4	9.7	39.9	50.6	9.7	39.7
50.4	4.8	44.7	50.8	4.8	44.4
50.4	-	50.0	51.0	-	49.0

TABLE 2.3 Equilibrium Compositions of coexisting MSS and Pentlandite

2.3a Electron Microprobe data* from this study

Sample No.		Initial MSS Composition (as weighed out) S	Fe	Ni	600°C Equilibrium Compositions (t 25 dys) MSS S	Fe	Ni	Tot.	( )
PNX2	wt%	37.36	57.70	4.94	-	-	-		
	at%	51.05	45.26	3.69	homogeneous				
PNX5	wt%	36.82	58.20	4.98	37.05	59.33	4.87	101.3	(10)
	at%	50.47	45.80	3.73	50.22	46.17	3.61		
PNX6	wt%	36.61	58.38	5.00	-	-	-	-	-
	at%	50.25	46.00	3.75	homogeneous				
PNX7	wt%	36.38	58.60	5.02	36.35	58.80	4.70	99.9	(11)
	at%	50.00	46.23	3.77	50.00	46.43	3.77		
PNX8	wt%	36.21	58.76	5.02	36.61	59.76	4.15	100.5	(9)
	at%	49.82	46.40	3.77	50.02	46.87	3.10		
	(inhomogenous minor Pn + tn)				tn	31.11	68.72	99.8	(5)
						32.24	67.76		
PNX15	wt%	37.20	51.90	10.90	-	-	-		
	at%	50.99	40.85	8.16	homogeneous				
PNX16	wt%	36.90	52.14	10.96	-	-	-		
	at%	50.67	41.11	8.22	homogeneous				
PNX17	wt%	36.70	52.30	11.00	-	-	-		
	at%	50.46	41.28	8.26	homogeneous				
PNX20	wt%	36.80	46.80	16.40	-	-	-		
	at%	50.67	37.00	12.33	homogeneous				
PNX21	wt%	36.60	47.00	16.40	-	-	-		
	at%	50.45	37.22	12.35	homogeneous				

* Details of operating conditions, standards used and accuracy of electron microprobe analyses given in Appendix I.
( ) Indicates number of individual spot analyses on each phase.

TABLE 2.3 cont'd

2.3a Electron Microprobe data* from this study

		400°C Equilibrium Compositions (t 78 dys) MSS					Pentlandite				
Sample No.		S	Fe	Ni	Tot.	( )	S	Fe	Ni	Tot.	( )
PNX2	wt%	37.42	57.86	4.89	99.8	(13)		no Pn.			
	at%	51.15	45.20	3.65							
PNX5	wt%	36.76	58.56	3.89	99.2	(8)		minor Pn.			
	at%	50.70	46.37	2.93							
PNX6	wt%	36.81	59.40	3.44	99.7	(8)					
	at%	50.57	46.85	2.58					Pn		
PNX7	wt%	36.83	60.40	2.80	100.0	(12)	32.96	39.75	26.49	99.2	(5)
	at%	50.43	47.48	2.09			46.92	32.49	20.59		
PNX8	wt%	36.62	60.78	2.32	99.7	(7)	32.98	40.46	25.78	99.2	(5)
	at%	50.32	47.94	1.74			46.92	33.05	20.03		
								no tn			
PNX15	wt%	37.03	52.44	10.57	100.0	(11)	33.06	33.18	33.18		(3)
	at%	50.79	41.29	7.92			47.07	27.12	25.80		
PNX16	wt%	37.39	53.17	10.00	100.6	(14)	32.93	32.64	34.14	99.7	(8)
	at%	50.96	41.60	7.44			46.83	26.65	26.52		
PNX17	wt%	37.43	53.75	9.29	100.5	(16)	32.98	33.11	33.81	99.9	(10)
	at%	51.02	42.06	6.92			46.81	26.98	26.21		
PNX20	wt%	37.45	46.37	16.36	100.2	(13)	32.93	31.38	35.27	99.6	(4)
	at%	51.30	36.46	12.24			46.90	25.66	27.24		
PNX21	wt%	37.13	48.25	14.83	100.2	(13)	32.77	31.46	35.88	100.1	(13)
	at%	50.91	37.98	11.11			46.65	25.45	27.90		

* Details of operating conditions, standards used and accuracy of electron microprobe analyses given in Appendix I.
( ) Indicates number of individual spot analyses on each phase.

TABLE 2.3b Electron microprobe data from Misra and Fleet (1973a)

	MSS			Pentlandite			MSS			Pentlandite		
at%	S	Fe	Ni	S	Fe	Ni	S	Fe	Ni	S	Fe	Ni
				600°C						500°C		
	50.23	46.00	3.77	46.40	33.29	20.31	49.84	48.01	2.15	46.68	35.44	17.88
	50.59	39.56	9.85	46.48	28.04	25.48	50.48	45.52	4.00	47.18	32.38	20.54
	50.70	34.94	14.36	46.29	25.48	28.23	50.84	40.05	9.11	47.38	28.50	24.12
	50.90	21.56	27.54	46.43	19.91	33.66	51.06	29.55	19.39	46.77	22.20	31.03
	50.45	17.00	32.65	46.43	13.57	40.00	50.82	19.19	29.19	46.73	20.46	32.81
	50.20	14.46	35.34	46.06	11.36	42.58	49.67	13.63	36.70	46.40	17.82	35.78
							50.11	4.65	42.24	46.83	15.06	38.01
				400°C						300°C		
	49.30	49.08	1.62	45.97	36.84	17.19	49.50	49.03	1.47	45.60	39.78	14.62
	49.75	48.01	2.24	46.45	36.38	17.17	49.60	46.84	3.56	46.48	34.85	18.67
	50.27	43.94	5.79	46.50	31.44	22.06	51.36	32.48	16.16	46.65	23.05	30.30
	51.14	30.95	17.91	46.57	23.45	29.98	51.92	23.25	24.83	46.71	20.06	33.23
	51.36	21.82	26.82	46.86	21.17	31.97	50.97	16.81	32.60			
	49.37	37.42	12.85	47.28	18.45	34.25	51.08	14.76	34.16	46.47	18.45	35.08
	50.50	6.15	43.35	46.66	14.03	39.31						

Accuracy estimated at ± 0.4 at% for S, Fe and Ni (Misra and Fleet 1973a)

TABLE 2.4 Solid Solution Limits of Pentlandite (from 1. - Misra and Fleet (1973a) 2. - Shewman and Clark (1970)

Annealing temp. °C	Fe-Ni Solid Solution Limits in at% Ni		S solubility limits at Fe:Ni = 1:1		
	1.	2.	1.	at%S	2.
600°C	20.3-42.6	23.7-31.2	46.4		48.1-47.2
500°C	17.9-38.0	19.3-37.4	47.3-46.8		47.8-46.8
400°C	17.2-39.3	17.9-32.0	46.5-46.0		47.6-46.9
300°C	14.6-33.8	-	46.6-46.2		-
230°C	15.1-34.1	-	46.5-46.9		-

TABLE 2.5 Interatomic distances (A°) and important bond angles in Pentlandites (from Rajamani and Prewitt, 1973) (standard deviations in brackets)

Atoms	Interatomic distances	
	Frood Pentlandite	Outokumpu Pentlandite
M(o)-S2(x6)	2.377(2)	2.373(1)
M(t)-S1	2.154(1)	2.140(1)
M(t)-S2(x3)	2.258(1)	2.238(1)
M(t)-M(t)(x3)	2.531(1)	2.518(1)
M(t)-M(t)(x3)	3.518(1)	3.494(1)
S1-M(t)(x4)	2.154(1)	2.140(1)
S2-M(o)	2.377(2)	2.373(1)
S2-M(t)(x4)	2.258(1)	2.239(1)
S2-S2(x4)	3.362(2)	3.355(2)
	Important bond angles	
S2-M(o)-S2	90.0	90.0
S1-M(t)-S2	107.18(4)	107.42(3)
S2-M(t)-S(2)	111.66(4)	111.45(2)
M(t)-M(t)-M(t)	90.0	90.0
M(t)-S1-M(t)	109.47	109.47
M(t)-S2-M(t)	68.19(4)	68.44(3)
M(t)-S2-M(o)	127.55(4)	127.32(3)

TABLE 2.6 Synthetic and Natural Pyrrhotite-Types*

Pyrrhotite type	Composition	Thermal Max.	Stability, °C Min	Structure Type (Cell edges, A°)	Remarks
Pyrrhotite solid-sol^n.	$Fe_{1-x}S$ 42.8-50.0 at%Fe	m.p.=1190(1)	308-100 (2)(3)	Hexagonal 1C, $P6_3/mmc$(2) $\underline{a} \sim 3.45$, $\underline{c} \sim 5.75$	Solid sol^n limits 47.5-50at%Fe at ~308°C; low temp. transformations dependant on comp. (2)(3).
Troilite	FeS	140(4)		Hexagonal 2C, $P\bar{6}2c$ (5) $\underline{a}$=3A=5.962, $\underline{c}$=2C=11.750	
4C-type monoclinic pyrrhotite	Fe_7S_8 (2)(6)	254(3)		Monoclinic, C2/c or Cc(7) $\underline{a}=2\sqrt{3}A=11.90$, $\underline{b}$=2A=6.87 $\underline{c}$=4C=22.88, $\beta=90\ 30'$	Stacking faults may result in minor deviation from stoichiometric Fe_7S_8 (8)(9)
3C-type pyrrhotite	Fe_7S_8 (14)	?	?	Hexagonal $P3_12_1/P3_221$ (14) $\underline{a}$= 2A=6.866, $\underline{c}$= 3C=17.088	Synthesised by vapour transport at high temp, no known natural occurrence (14)
'Hexagonal or Intermediate Pyrrhotite Types					
mC-type pyrrhotite	$Fe_{1-x}S$, 47.4-47.8at% Fe (3)	308(3)	262(3)	Hexagonal? (2) $\underline{a}$=2A, $\underline{c}$=mC, 3.0<m<4.0	No known natural occurences.
nA-type pyrrhotite	$Fe_{1-x}S$, 47.2-47.9 at% Fe (3)	∿ 266(3)	209(3)	Hexagonal? (2) $\underline{a}$=nA, 40<n<90, $\underline{c}$=3C	Only known natural occurence: Broadlands geothermal field, New Zealand (3)
nC-type pyrrhotite	$Fe_{1-x}S$, 47.2-48.1 at%Fe (3)	∿213(3)	∿ 100(3)	Orthorhombic (2)(6) $\underline{a}$=2A, $\underline{c}$=nC, 3.0<n<6.0	Antiphase domain models suggested for nA-type superstructures by (10) (11), and for nC-type superstructures by (12). Implies these non-integral superstructure types metastable in Fe-S system, contrary to (3).

TABLE 2.6 Continued....

5C-type pyrrhotite	Fe_9S_{10}	(2)	~100(2)	Hexagonal (2) (6) a=2A=6.88, c=5C=28.70	
11C-type pyrrhotite	$Fe_{10}S_{11}$	(2)	~100(2)	Orthorhombic, Cmca or C2ca (2)(6) a=2A=6.892, b=2√3A=11.952 c=11C=63.184	(2)(6) suggest 5c, 11c and 6c special cases of nC type superstructures in which vacancies well ordered
6C-type pyrrhotite	$Fe_{11}S_{12}$	(2)	~100(2)	Orthorhombic? (2) (13) a=2A=6.895, b=2√3A=11.953 (13) c=6C=34.518	

* numbers in brackets are references:

(1) Jensen (1942) (2) Nakazawa and Morimoto (1971) (3) Kissin and Scott (1982)

(4) Yund and Hall 1968 (5) Evans (1970) (6) Morimoto et al 1974a

(7) Tokonami et al (1972) (8) Nakazawa et al (1975a) (9) Putnis and McConnell (1980)

(10) Morimoto et al (1975b) (11) Nakazawa et al (1975b) (12) Pierce (1979)

(13) Koto et al 1976 (14) Keller-Besrest et al.(1982)

TABLE 2.7 Definition of terms applied to pyrrhotite group minerals in this study

Pyrrhotite solid solution: the high temperature (>308°C) $Fe_{1-x}S$ solid solution possessing the NiAs type, 1C, structure.

Pyrrhotite group: all iron monosulphides of general formula $Fe_{1-x}S$ ($0<x<0.125$) that possess the NiAs substructure. The term includes both troilite and pyrrhotite as defined below.

Troilite: stoichiometric FeS of space group $P\bar{6}2c$ and stable below ∿140°C (Evans 1970).

Pyrrhotite: all members of the pyrrhotite group excluding troilite.

Hexagonal Pyrrhotite: all pyrrhotites in the composition range $\sim Fe_9S_{10}$ - $Fe_{11}S_{12}$ that exhibit a hexagonal symmetry by means of diffractometry excluding consideration of weak, low angle superstructure reflections. This usage is equivalent to the intermediate pyrrhotite defined by Morimoto et al (1975a).

Monoclinic Pyrrhotite: pyrrhotite of composition $\sim Fe_7S_8$ possessing the 4C-superstructure and exhibiting monoclinic symmetry by means of diffractometry.

Fig. 2.1 Phase relations in the condensed Fe-Ni-S system at 1100°C (after Kullerud 1963a)

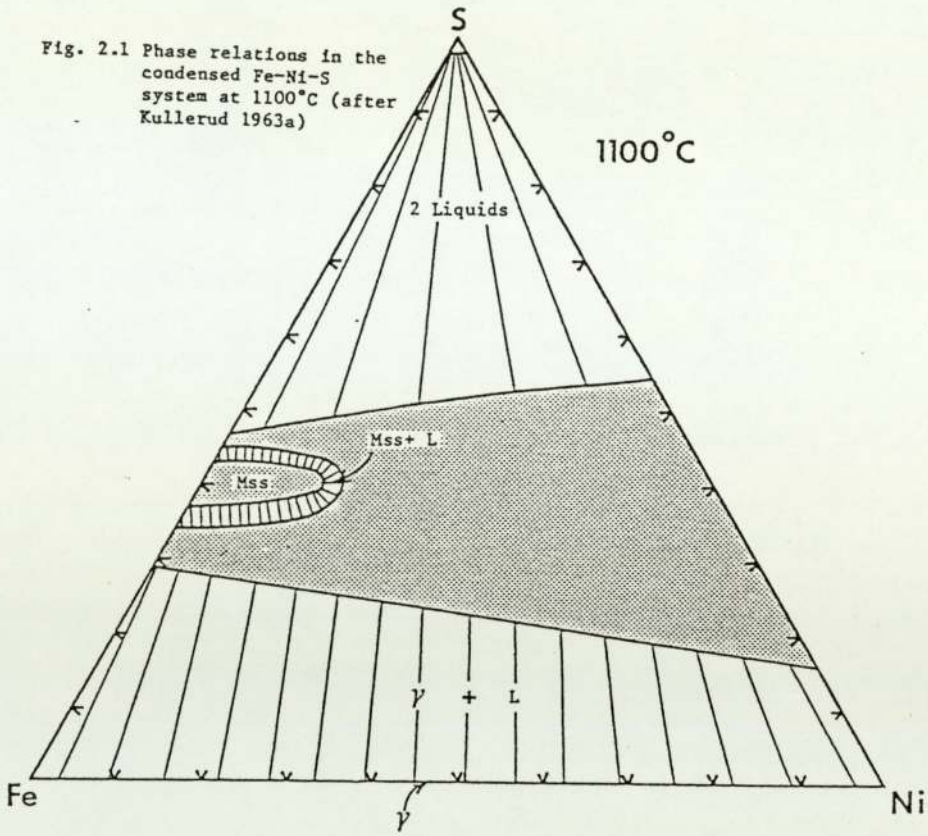

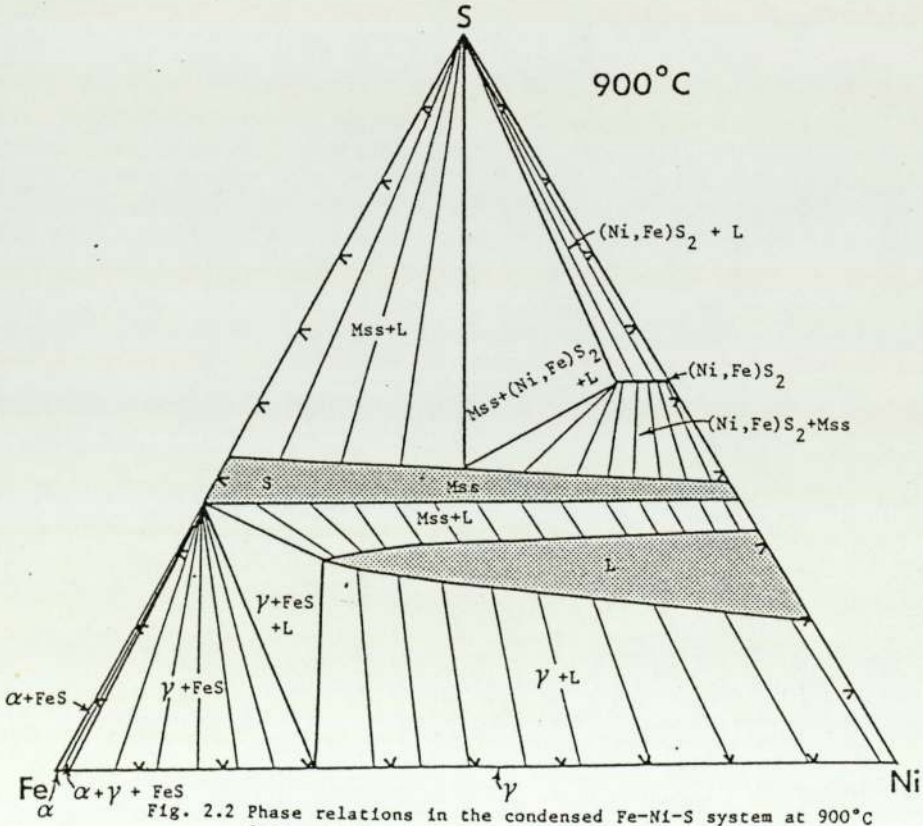

Fig. 2.2 Phase relations in the condensed Fe-Ni-S system at 900°C (after Kullerud 1963a)

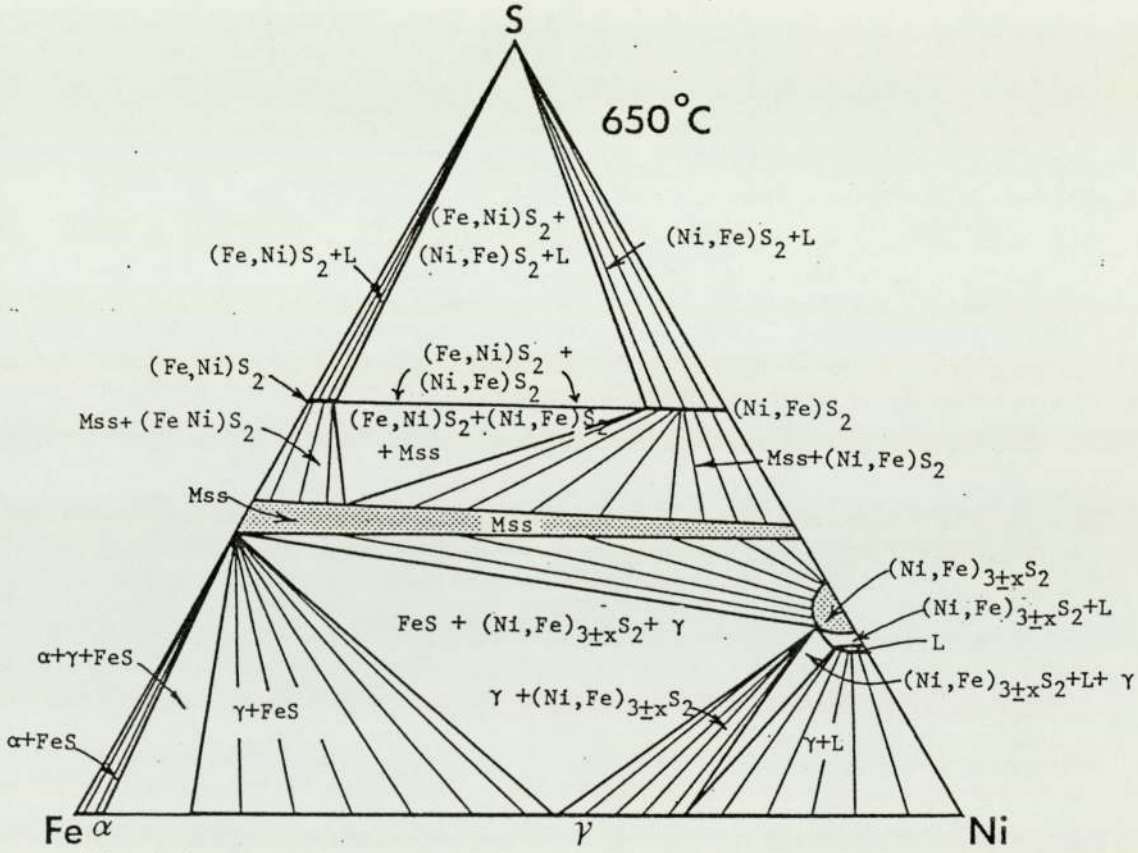

Fig. 2.3 Phase relations in the condensed Fe-Ni-S system at 650°C (after Kullerud 1963a)

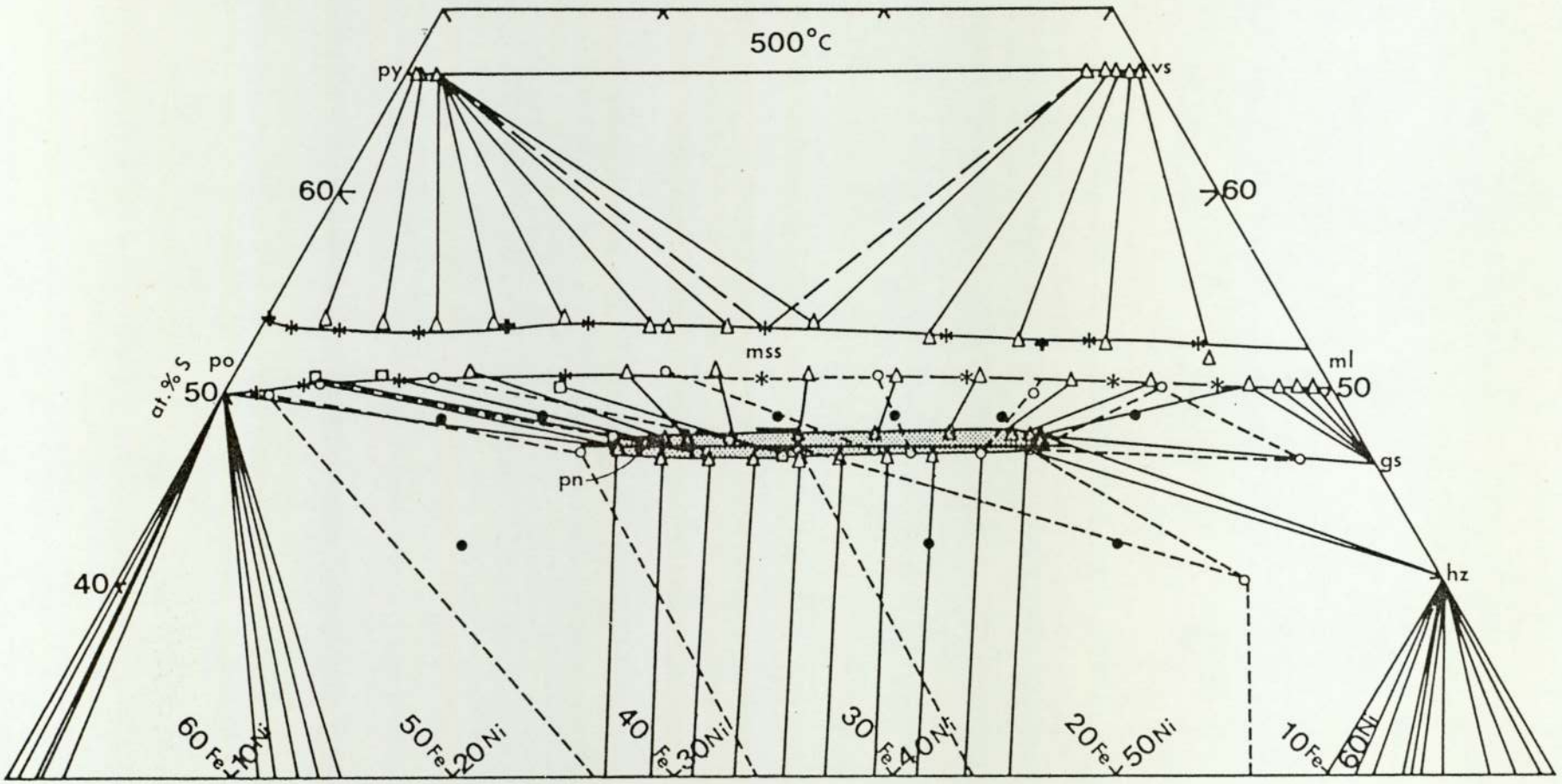

□ Malik & Arnold (1972)
∗ Naldrett et al (1967)
+ Naldrett et al (1967)
Δ Shewman & Clark (1970)
● Misra & Fleet (1973a) - bulk
○ Misra & Fleet (1973a) - single phase

Fig. 2.4a PHASE RELATIONS IN THE CENTRAL PORTION OF THE Fe-Ni-S SYSTEM AT 500°C (COMPILED BY BARKER - (PERSON. COMMUN. 1980) FROM PUBLISHED DATA

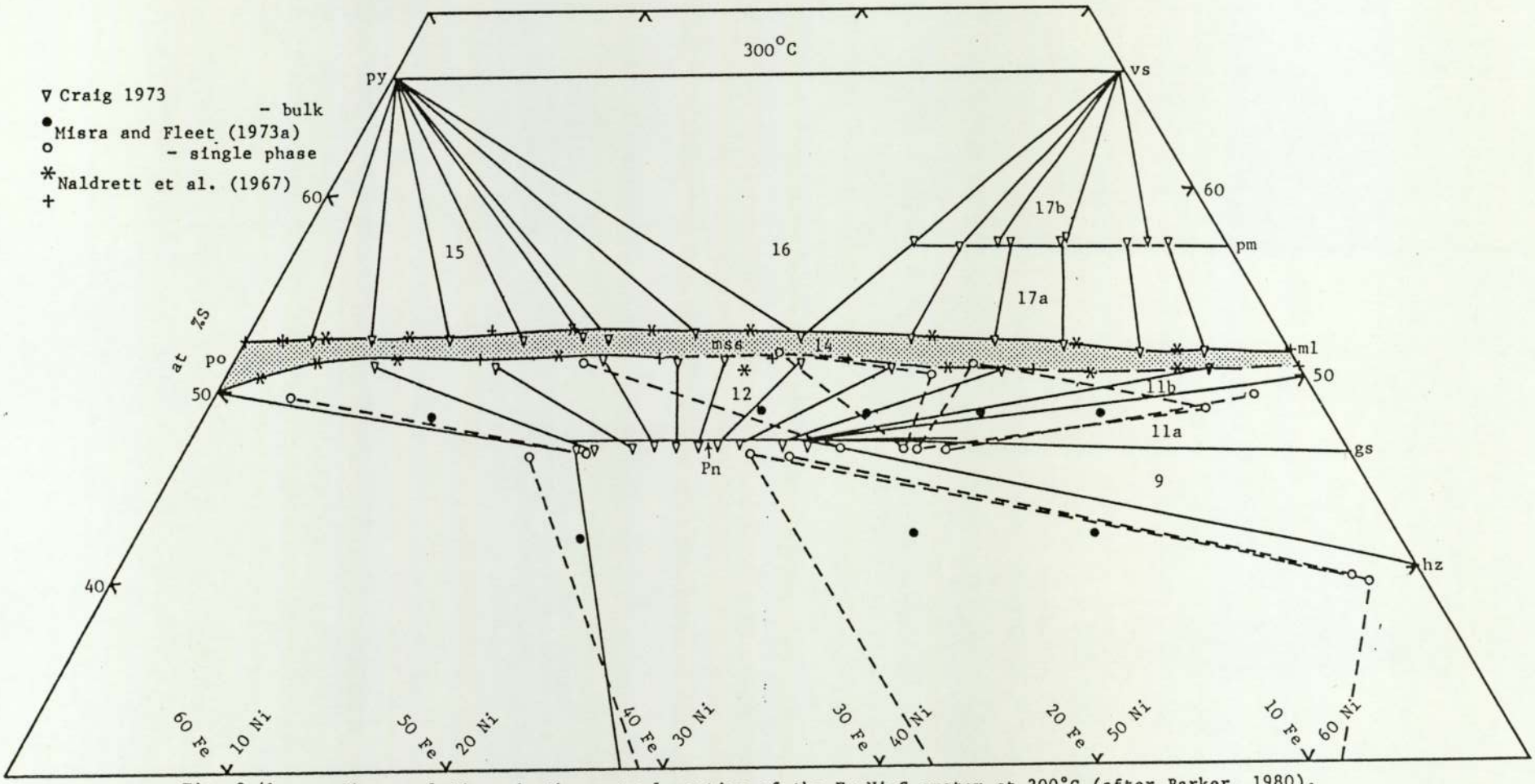

Fig. 2.4b Phase relations in the central portion of the Fe-Ni-S system at 300°C (after Barker, 1980).

Fig. 2.5

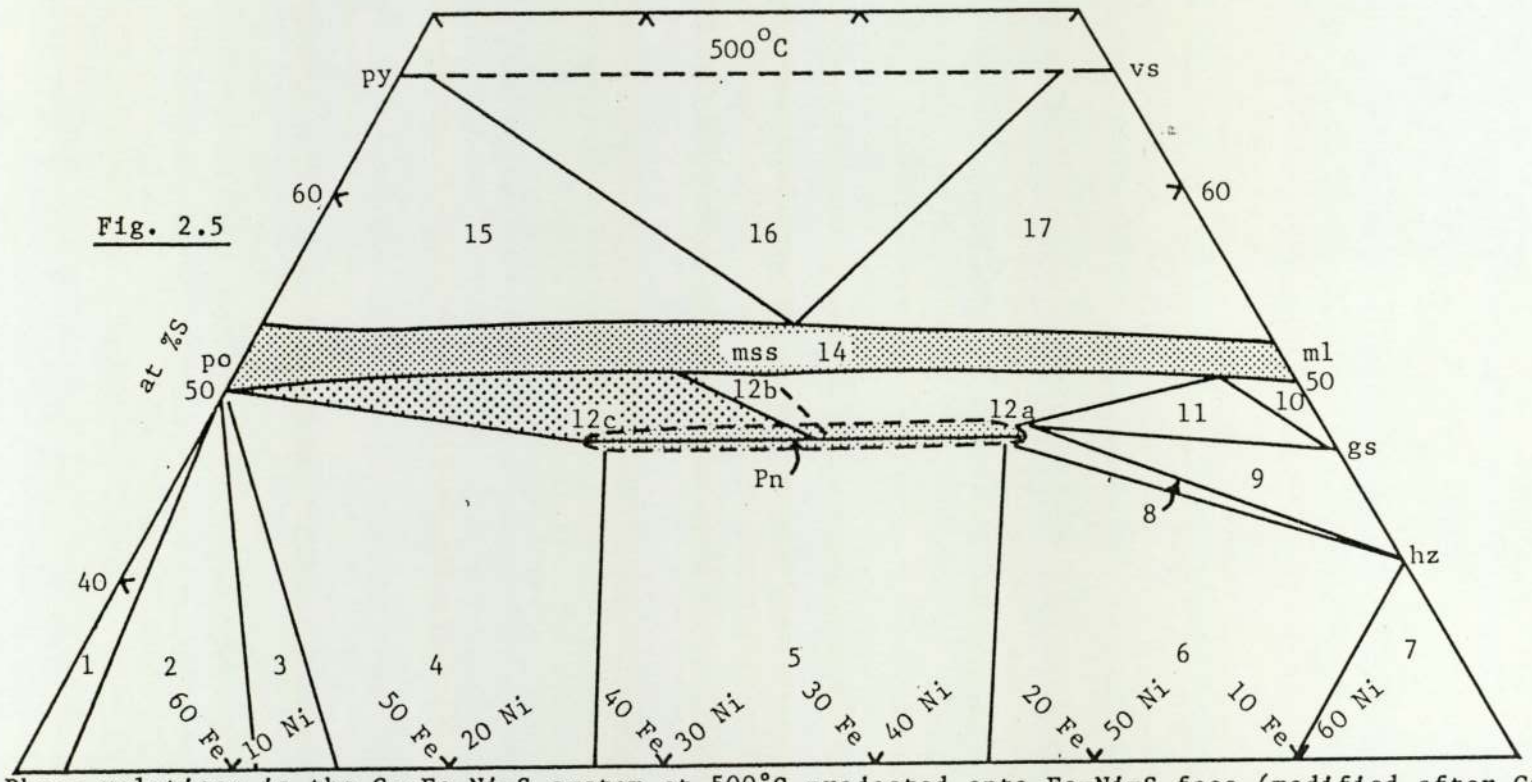

Phase relations in the Cu-Fe-Ni-S system at 500°C projected onto Fe-Ni-S face (modified after Gill, 1976)

Key: phases present in equilibrium with vapour: 1. FeS+ αFeNi+bnss 2. FeS+ α(fe-Ni)+γ(FeNi)(tn)+bnss 3. FeS+tn+bn 4. FeS+Pn+tn+bnss 5. Pn+tn+bnss 6. Pn+hz+tn+bnss 7. h_3+aw+bnss 8. Pn+hz+bn 9. Pn+gs+hz+bnss 10. MSS+gs+bnss 11. MSS+Pn+gs+bnss 12a. MSS+Pn+bnss 12b. MSS+Pn+ISS+bnss 12c. MSS+Pm+ISS 14. MSS 15. MSS+Py+?ISS 16. MSS+py+vs+?ISS 17. MSS+vs+?ISS or ?bnss.

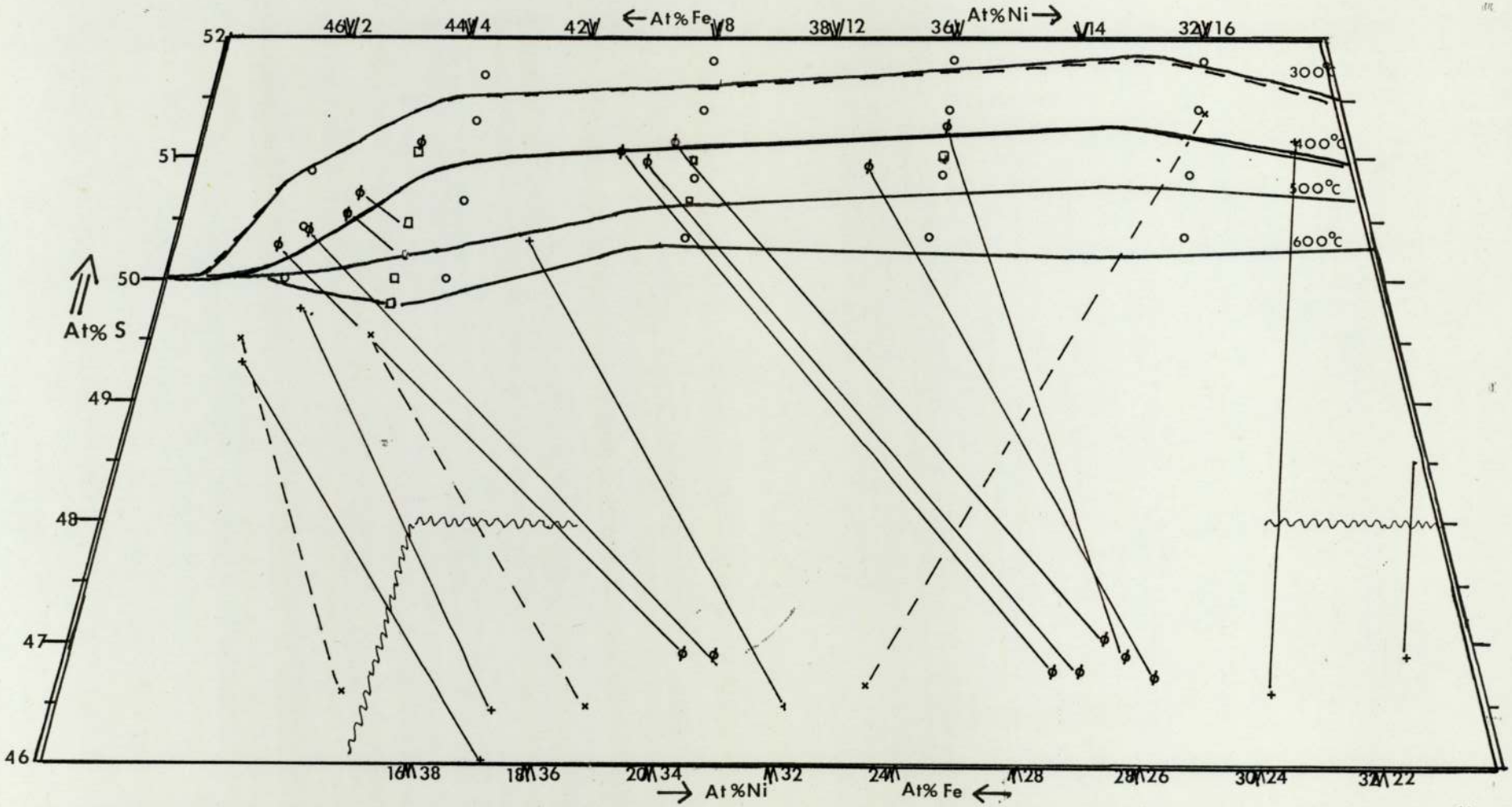

○ MSS compositions synthesised in this study for use in isothermal runs

□ Compositions only run at 400°C

Coexisting equilibrium MSS and Pn compositions

— MSS/Pn solvus (data from Naldrett et al, 1967)

ϕ 400°C (this study)

+ 400°C

× 300°C (Misra and Fleet, 1973a)

Fig. 2.6 MSS compositions synthesised in this study and equilibrium MSS + Pentlandite compositions plotted in the Fe-rich MSS and pentlandite fields.

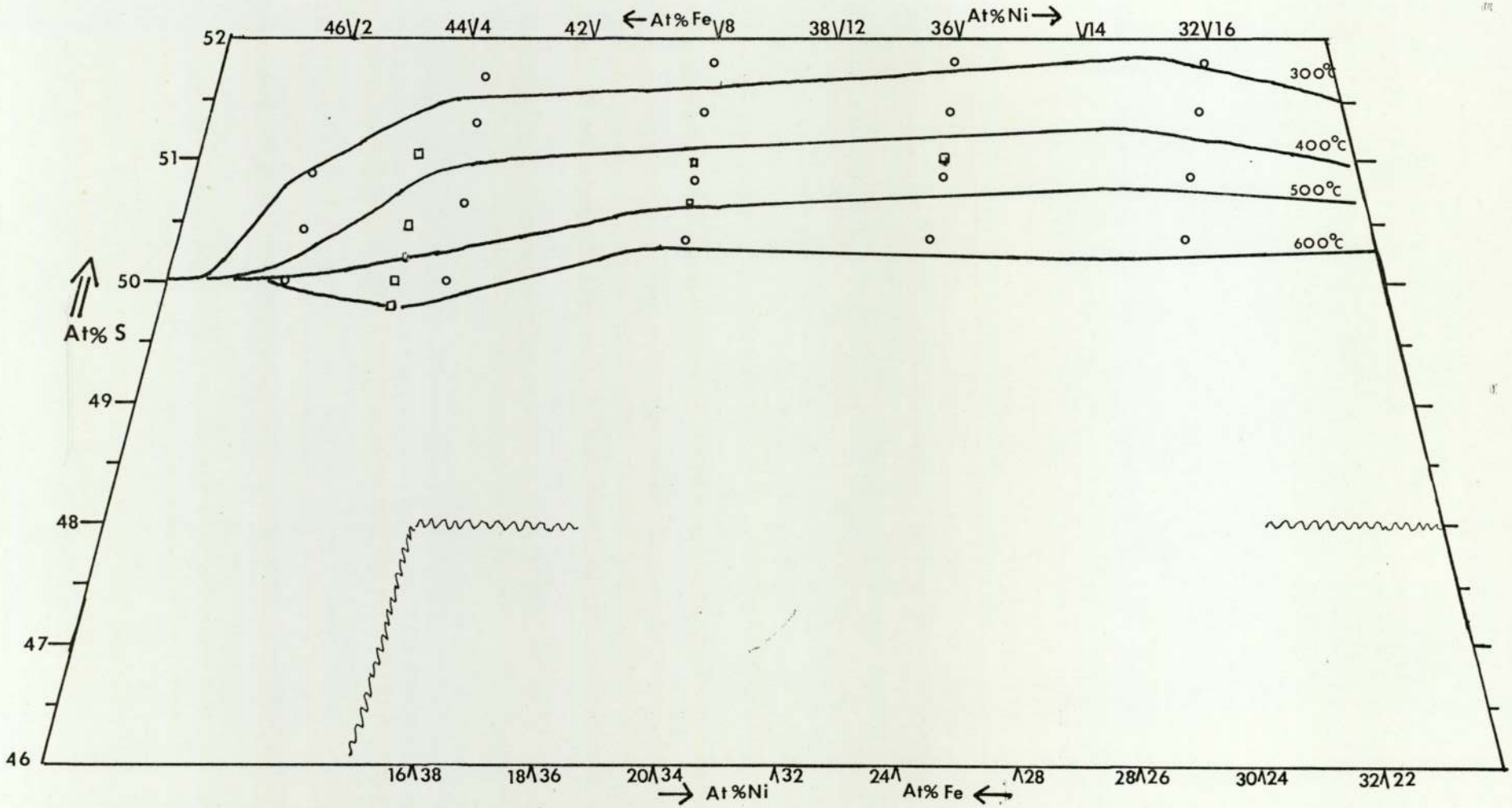

○ MSS compositions synthesised in this study for use in isothermal runs

□ Compositions only run at 400°C

—— MSS/Pn solvus (data from Naldrett et al, 1967)

Fig. 2.6 MSS compositions synthesised in this study and equilibrium MSS + Pentlandite compositions plotted in the Fe-rich MSS and pentlandite fields.

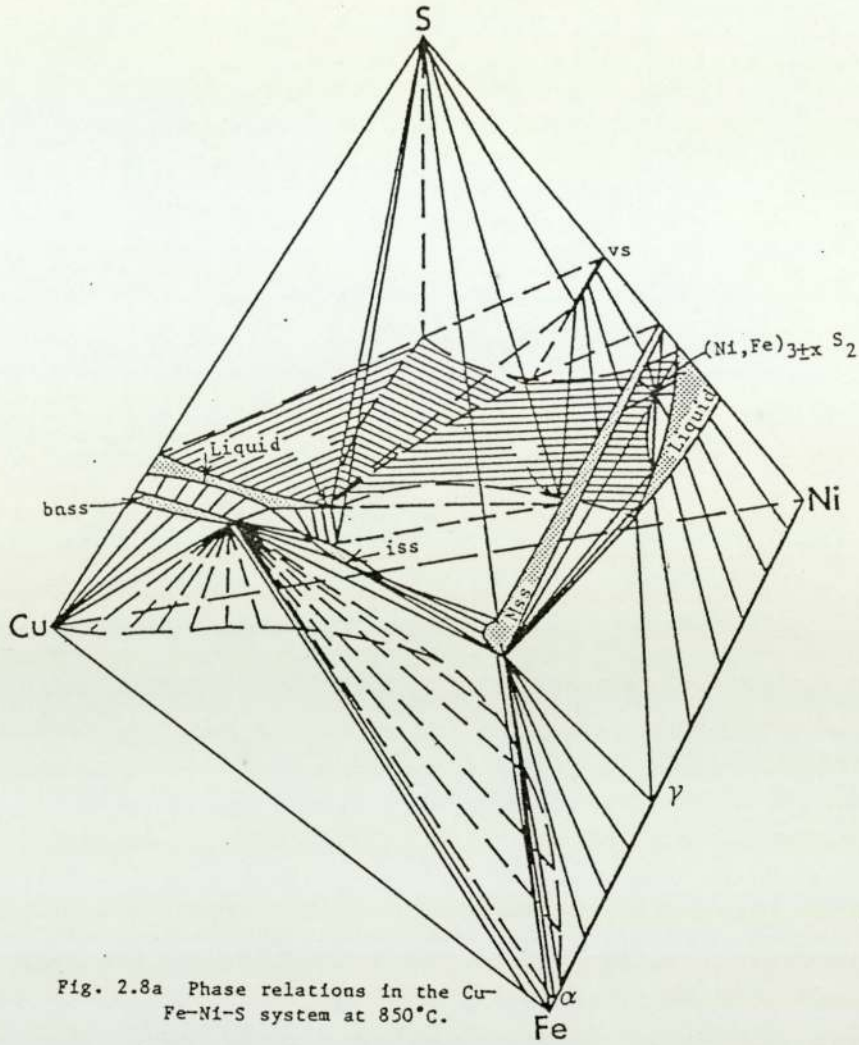

Fig. 2.8a Phase relations in the Cu-Fe-Ni-S system at 850°C.

Fig. 2.8b Phase relations in the Cu-Fe-Ni-S system at 1000°C (after Craig and Kullerud 1969)

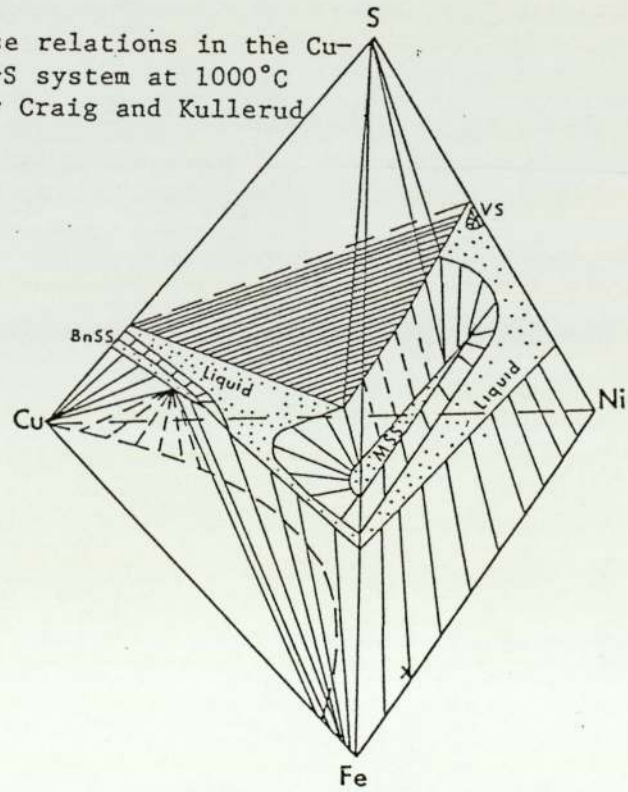

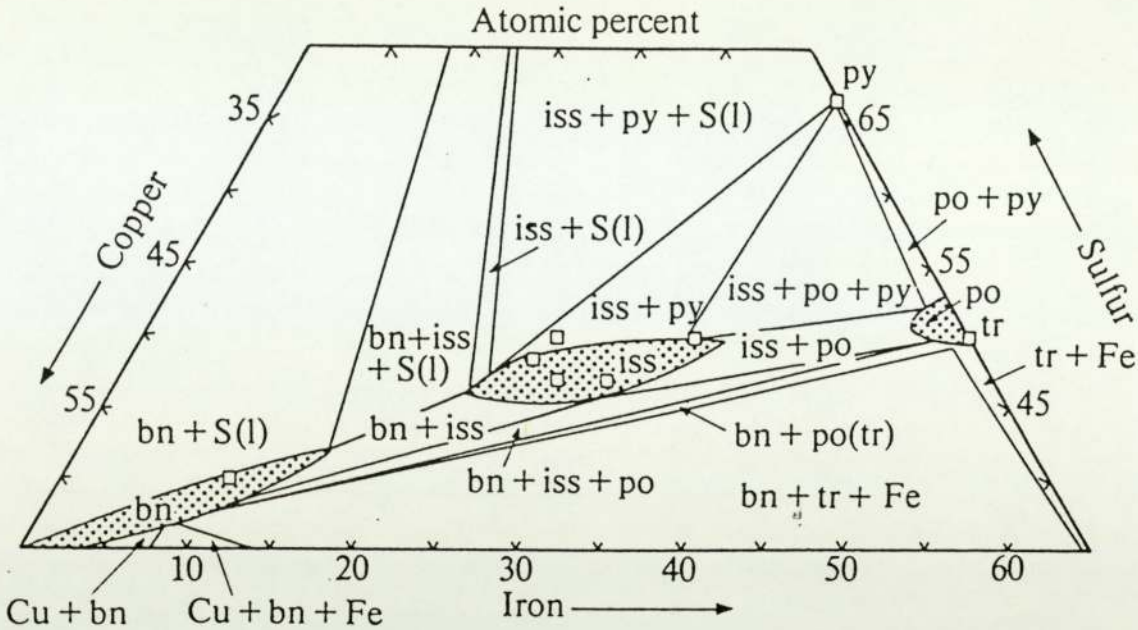

Fig. 2.7 Phase relations in the central portion of the Cu-Fe-S system at 600°C (after Cabri, 1973).

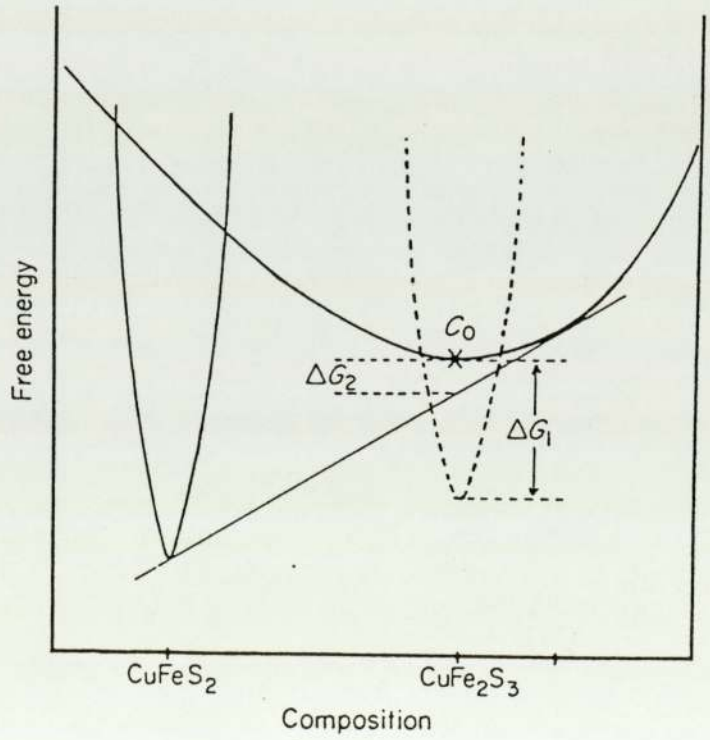

Fig. 2.9 Schematic free energy-composition diagram for ordered chalcopyrite, ordered low cubanite and disordered ISS at low temperature (<210°C). (After Putnis and McConnell, 1981).

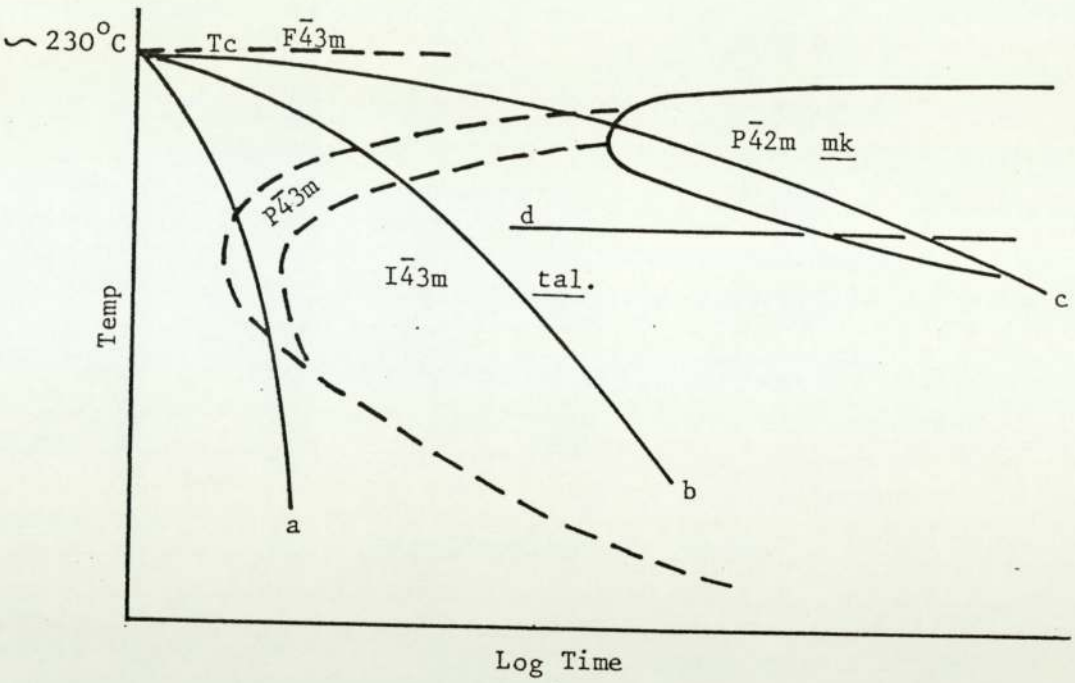

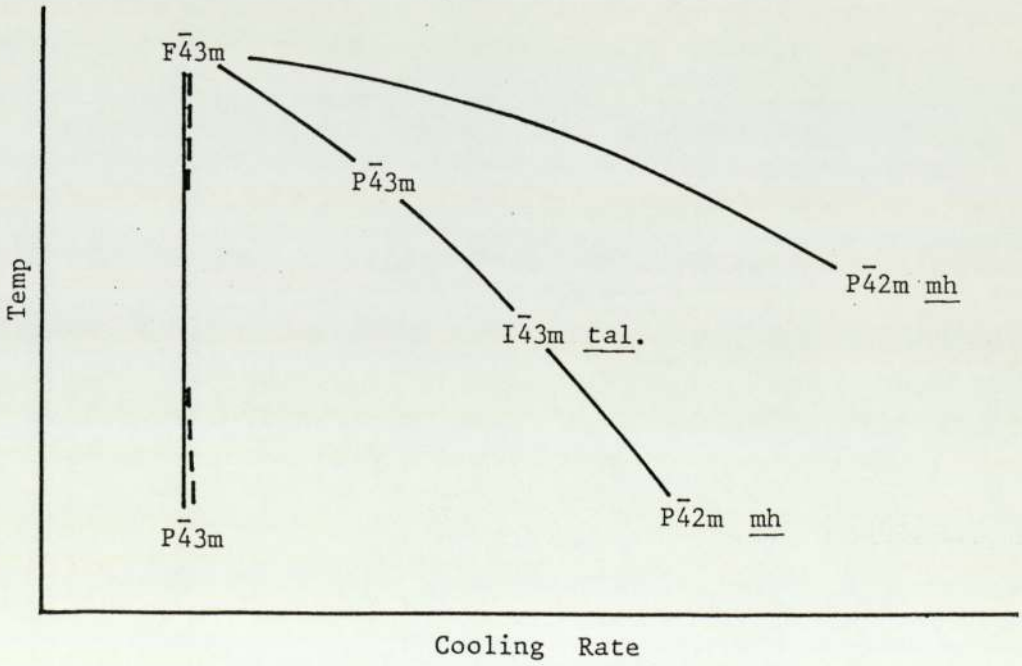

Fig. 2.10 a & b. Time-temperature-transformation diagrams for cation-ordering transformations in ISS of composition~$Cu_9Fe_9S_{16}$ (modified after Putnis, 1978).

Fig. 2.11a

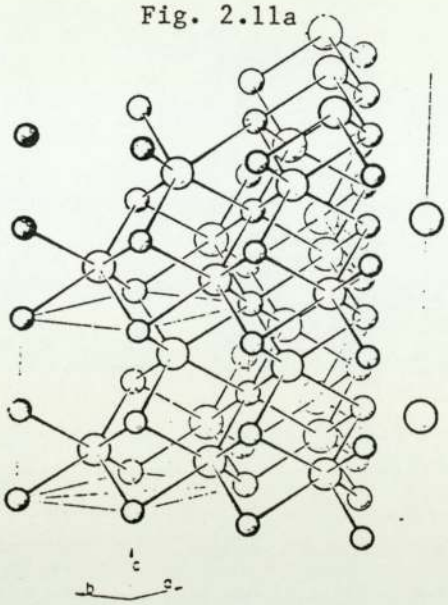

Fig. 2.11b

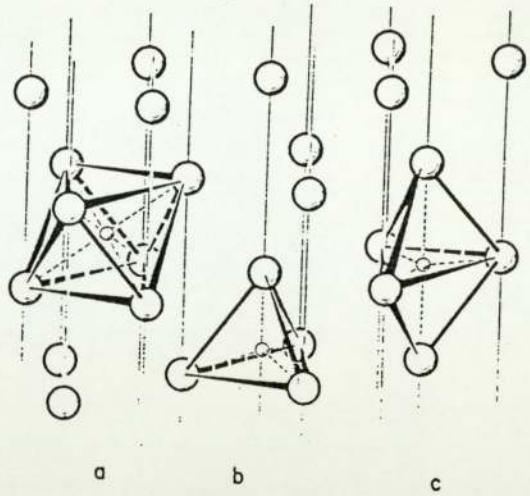

Fig. 2.11a The Ni-As-type structure of MSS smaller circles represent metal atoms, larger circles the sulphur atoms

Fig. 2.11b The arrangement of (a) octahedral (b) tetrahedral and (c) trigonal bipyramidal holes (sites) in a close packed hexagonal sulphur sublattice. (both after Kjeshus and Pearson, 1965).

Fig. 2.12

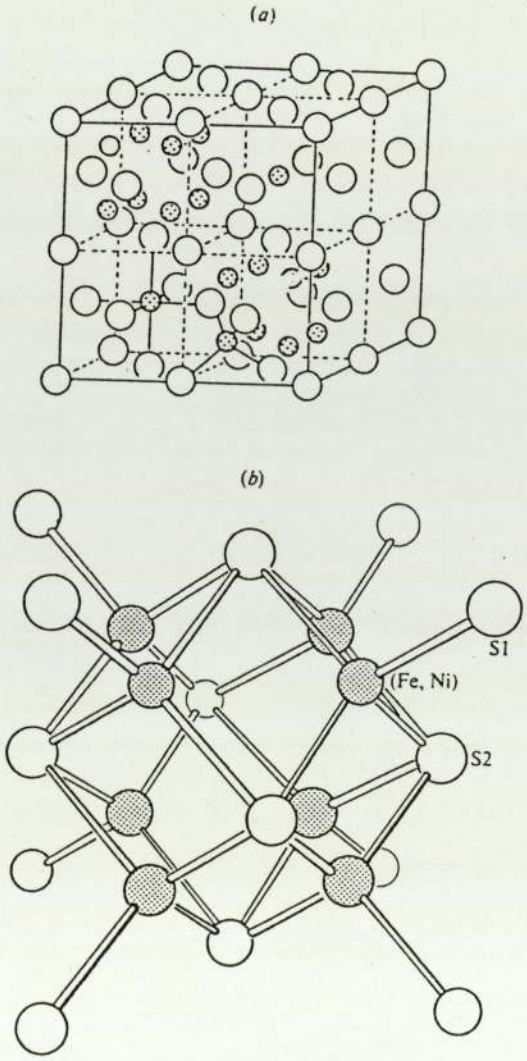

Fig. 2.12 The crystal structure of pentlandite (a) the face centred cubic (Fm3m) unit cell of pentlandite; (b) the cube cluster of tetrahedrally coordinated cations occurring in pentlandite (after Rajamani and Prewitt, 1973).

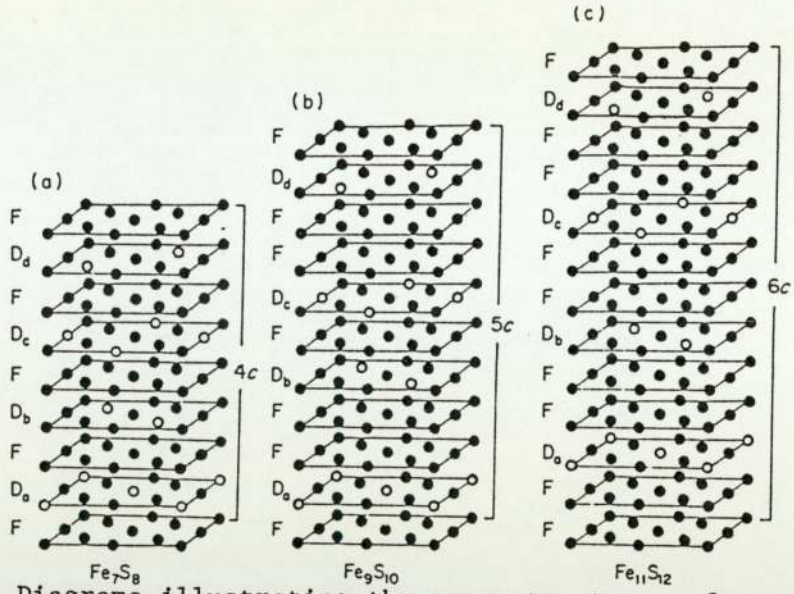

Fig. 2.13 Diagrams illustrating the superstructures of an ordered distribution of vacancies in (a) the 4C monoclinic pyrrhotite structure ($\sim Fe_7S_8$) (b) the 5C 'hexagonal' pyrrhotite structure ($\sim Fe_9S_{10}$) (c) the 6C hexagonal pyrrhotite structure ($\sim Fe_{11}S_{12}$). Only the cation layers are shown; filled circles are Fe atoms, open circles represent vacant sites.(after Putnis and McConnell, 1981).

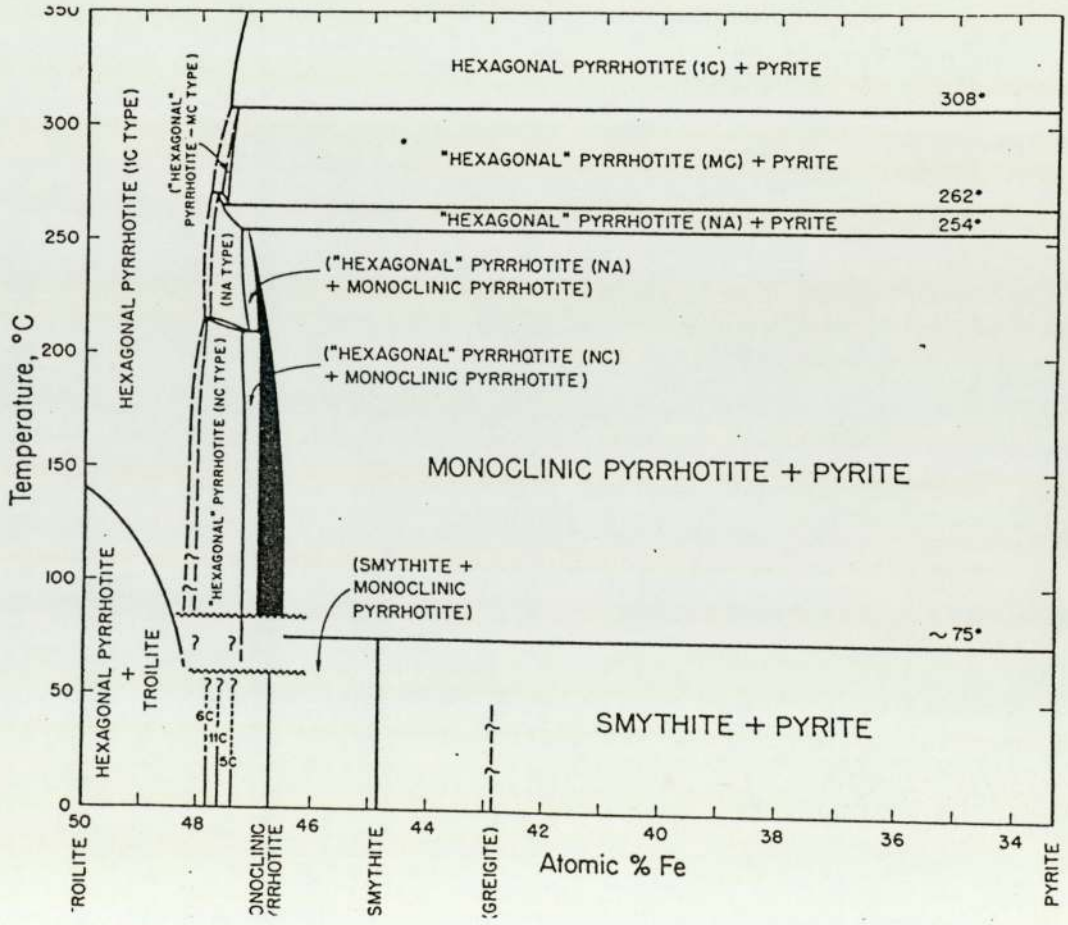

Fig. 2.14 Low temperature phase relations in the Fe-S system (after Kissin and Scott, 1982).

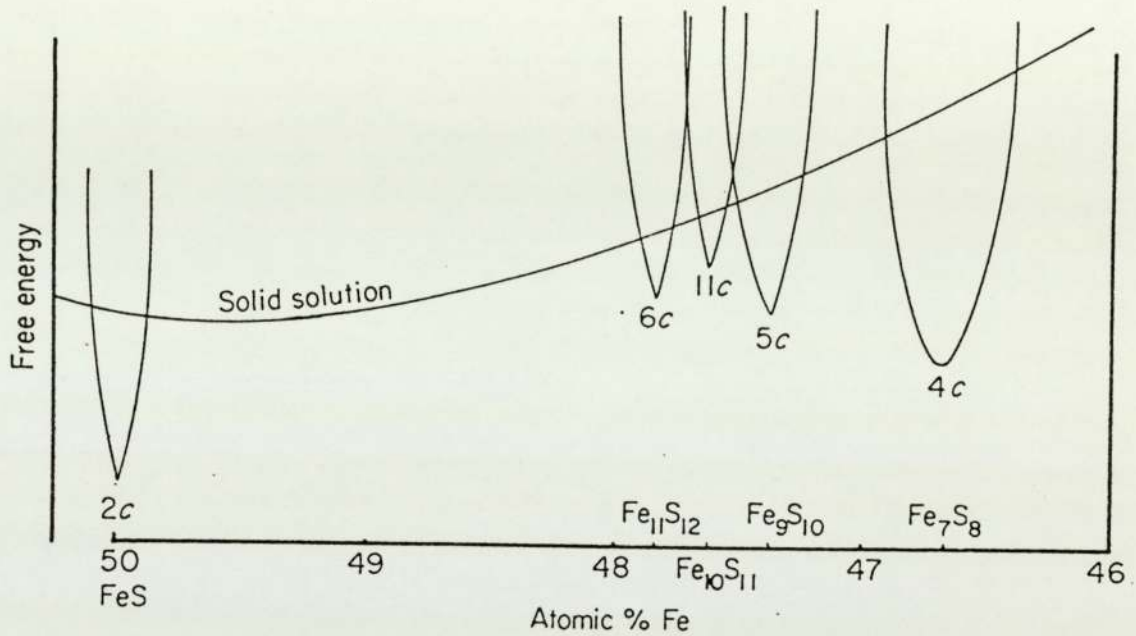

Fig. 2.15 Schematic free energy vs. composition diagram for some of the ordered structures at low temperature (<100°C). The assemblage 2C+4C ($FeS+Fe_7S_8$) is assumed to be more stable than the ordered 'hexagonal' pyrrhotite structures. (after Putnis and McConnell, 1981).

Figs. 3.1 to 3.19 Photomicrographs and schematic diagrams illustrating variations in the form and development of different MSS/pentlandite textures from the synthesis and isothermal annealing experiments

The initial composition of the MSS sample is indicated by its Fe/Ni and M/S ratios. Annealing times and temperatures are also indicated.

Fig. 3.1a Homogeneous MSS sample, Fe/Ni 5, M/S 0.961. Typical small grain aggregate of interlocking polygonal MSS grains in various orientations, with ~120° T-junctions (x490, f.o.v. 210 μm, unXP, Oil)

Fig. 3.1b Homogeneous MSS sample, Fe/Ni 10, M/S 0.934. Part of an extended grain aggregate of interlocking MSS grains. Smaller 'sub-grains' occur interstitial to and on the grain boundaries of the larger grains. Some of these have 'plucked' leaving rounded to angular 'holes' (x300, f.o.v. 350 μm, PPL, Oil)

Fig. 3.1c Inhomogeneous MSS sample PNX51 [~Fe/Ni 10 ~ M/S 1.000] . Quenched from 850°C. Grains of heazlewoodite (light grey) with fine rims of taenite (white) intergranular to MSS grains (darker grey). Note the crenulate indented nature of the heazlewoodite/MSS boundaries. (x1000, f.o.v. 105 μm, PPL, Oil)

Fig. 3.1d PNX51 after reannealing at 300°C for 100 hrs. Complete conversion of heazlewoodite + taenite to coarse granular interstitial pentlandite (white, left hand margin). Exsolved wiry, pervasive pentlandite lamellae within the MSS grains (cf Fig. 3.12a) (x500, f.o.v. 200 μm, PPL, Oil)

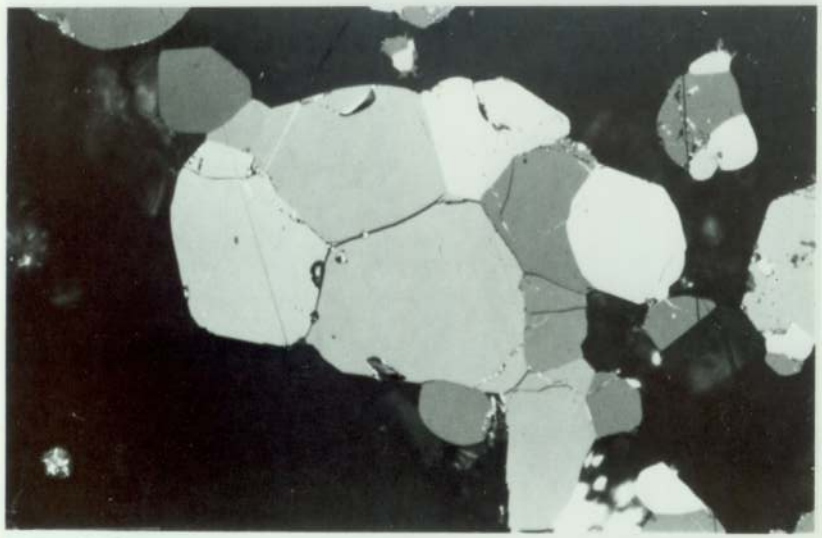

Fig. 3.1a

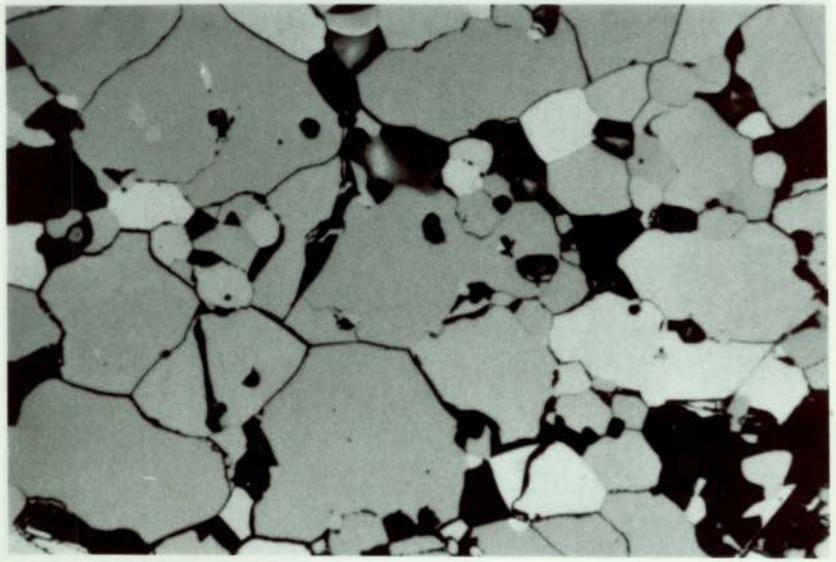

Fig. 3.1b

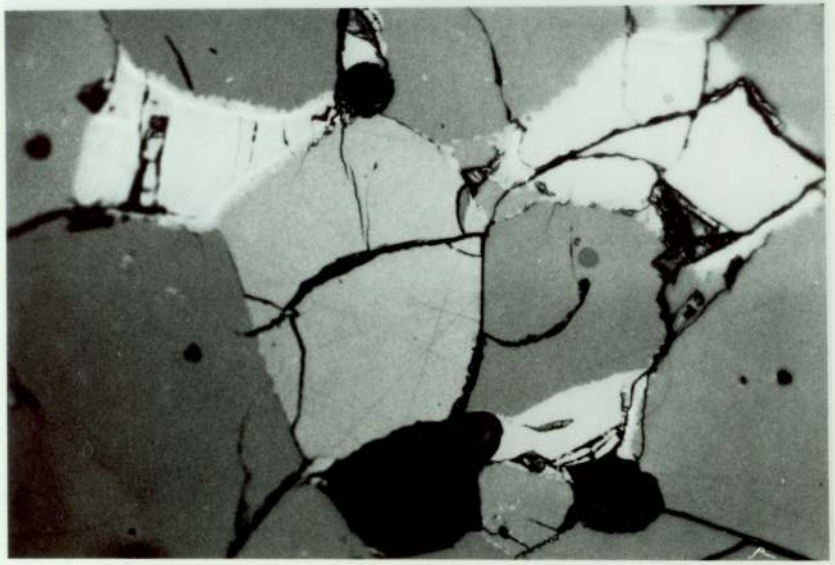

Fig. 3.1c

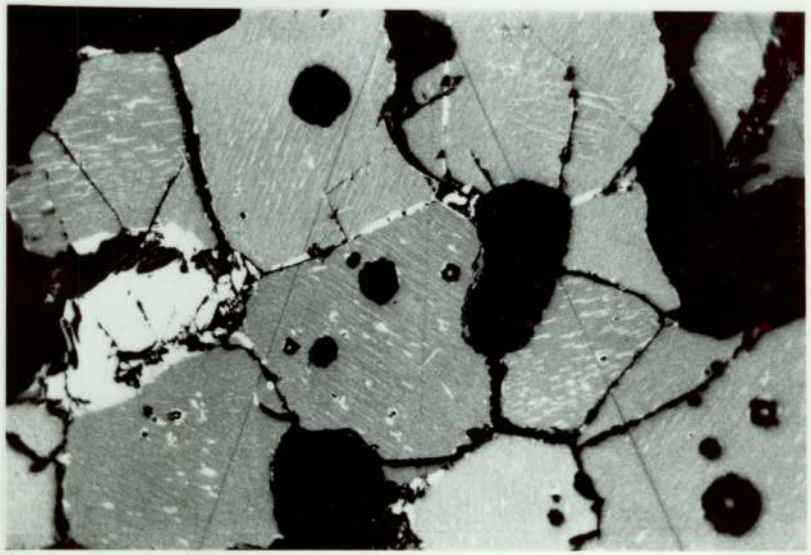

Fig. 3.1d

Fig. 3.2a Discrete, well spaced, hemispherical caps on one side of an MSS grain boundary. [Fe/Ni 5, M/S 0.966; 400°C, 10 hrs]

Fig. 3.2b Impinged and partially overgrown rectangular blebs either side of an MSS grain boundary [Fe/Ni 5, M/S 0.973; 400°C 10hrs]

Fig. 3.2c Impinged and partially overgrown hemispherical caps forming a discontinuous rim with lobate boundaries. [Fe/Ni 5, M/S 0.966; 400°C 100hrs]

Fig. 3.2d Overgrown rectangular blebs forming a continuous rim with crenellate to crenulate boundaries with the adjacent MSS grains [Fe/Ni 5, M/S 0.973, 100hrs]

Fig. 3.3a Continuous pentlandite rim with crenulate boundaries [Fe/Ni 5, M/S 0.966; 400°C, 1780 hrs]

Fig. 3.3b Coarse continuous pentlandite rim (white) with entire undulate boundaries. Almost all the indentations in the boundaries (cf Fig. 3.2d) with the adjacent MSS grains have been 'infilled' and smoothed out during growth. [Fe/Ni 5, M/S 0.973; 400°C 1780 hrs]

Fig. 3.3c Preferential growth of agglomerated pentlandite blebs resulting in deeply embayed rim with lobate boundaries [Fe/Ni 3, M/S 0.966; 400°C 100 hrs]

Fig. 3.3d Coarse continuous pentlandite rim. Preferential growth of 'portions' of the rim into one of the adjacent MSS grains results in a deeply embayed crenulate boundary, while the boundary with the other MSS grain is linear, entire. Note also coarse sub-parallel linear blades at the grain margins and the finer closer spaced blades at the fracture within the grain. [Fe/Ni 3, M/S 0.966; 400°C 1780 hrs]

(Each photograph: x1000, f.o.v. 105 μm , PPL, Oil)

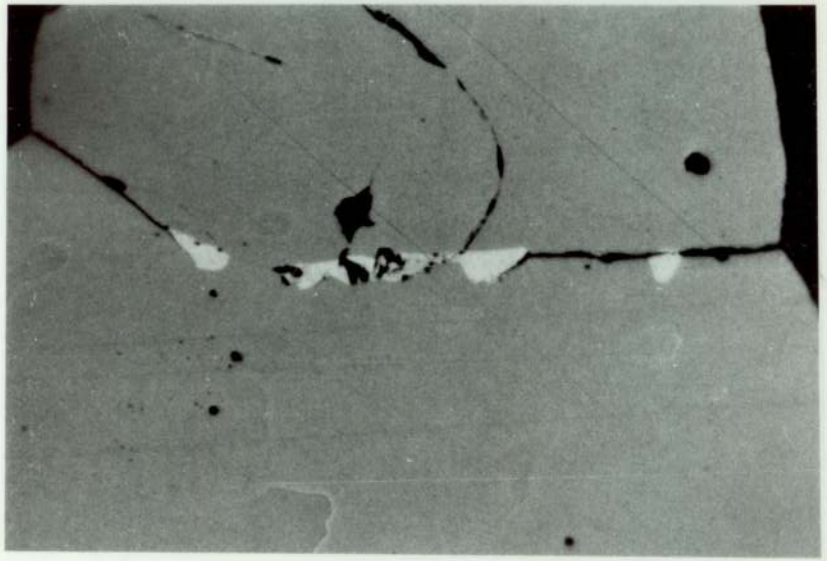

Fig. 3.2a

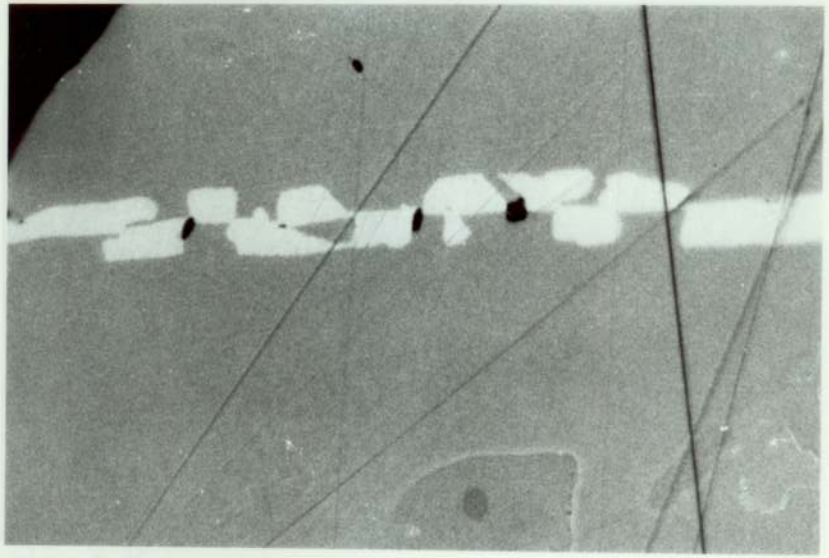

Fig. 3.2b

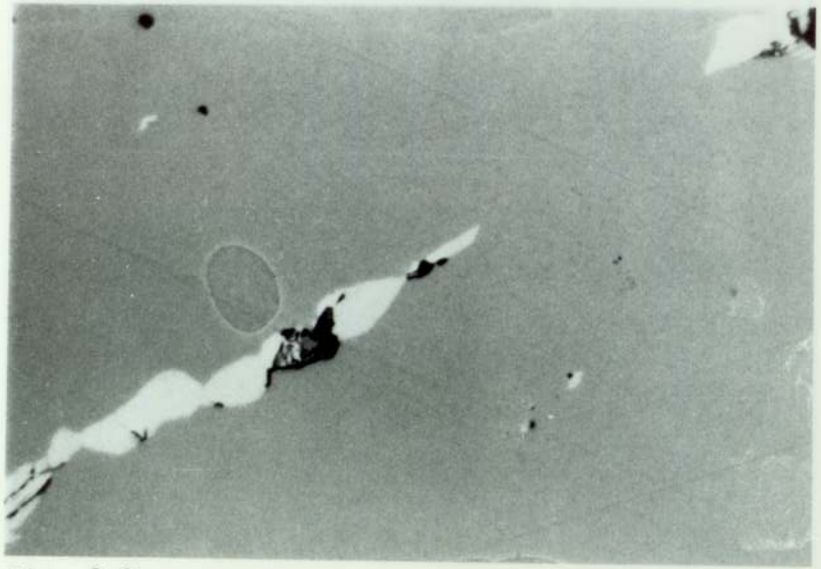

Fig. 3.2c

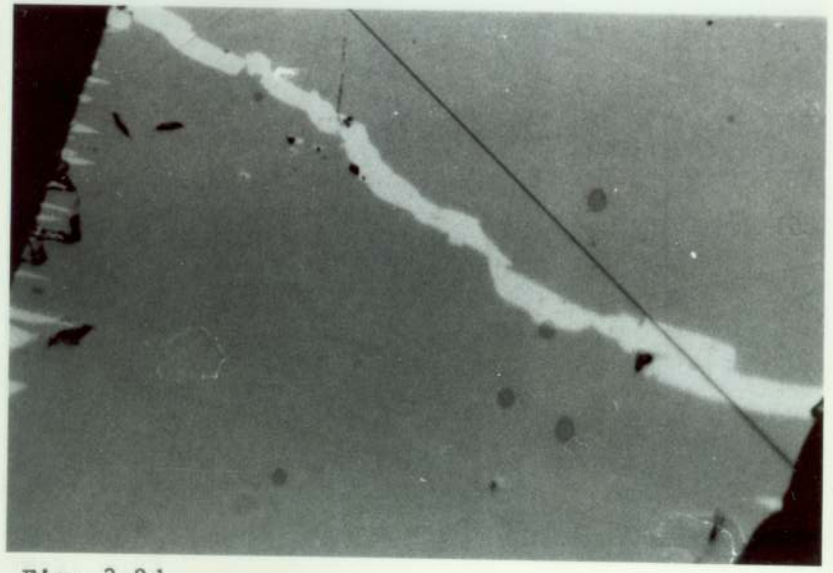

Fig. 3.2d

Fig. 3.3a

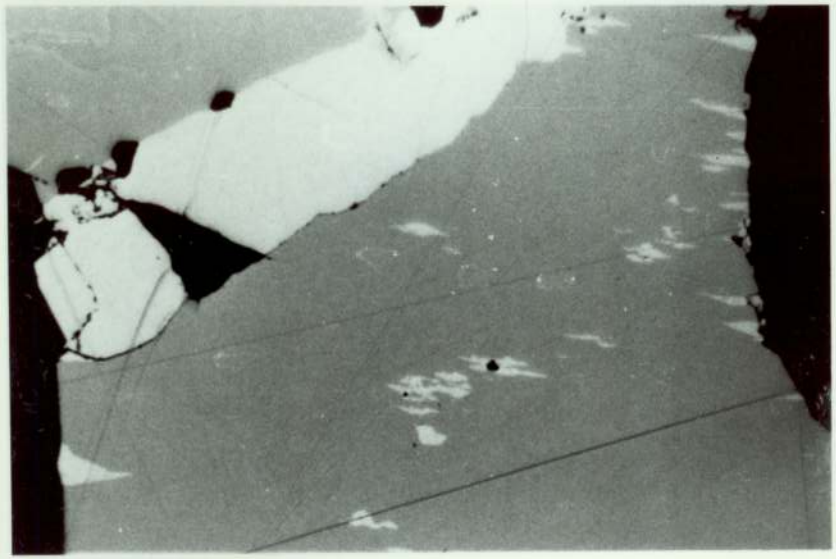

Fig. 3.3b

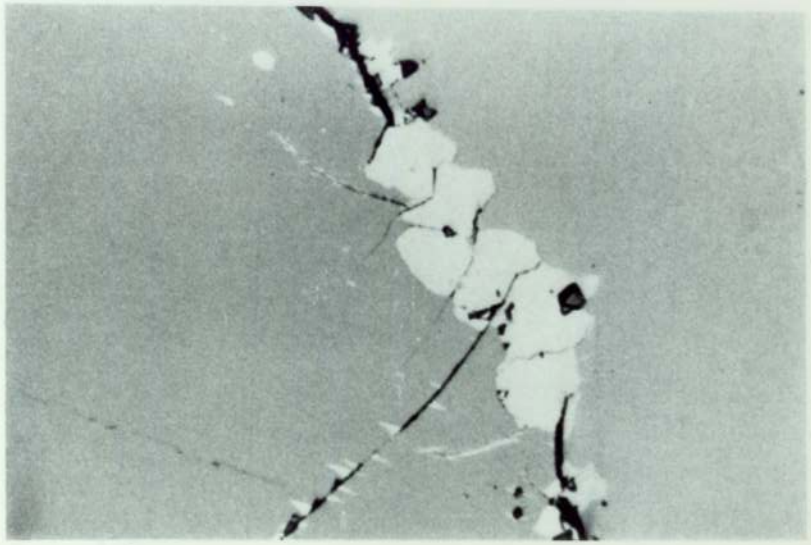

Fig. 3.3c

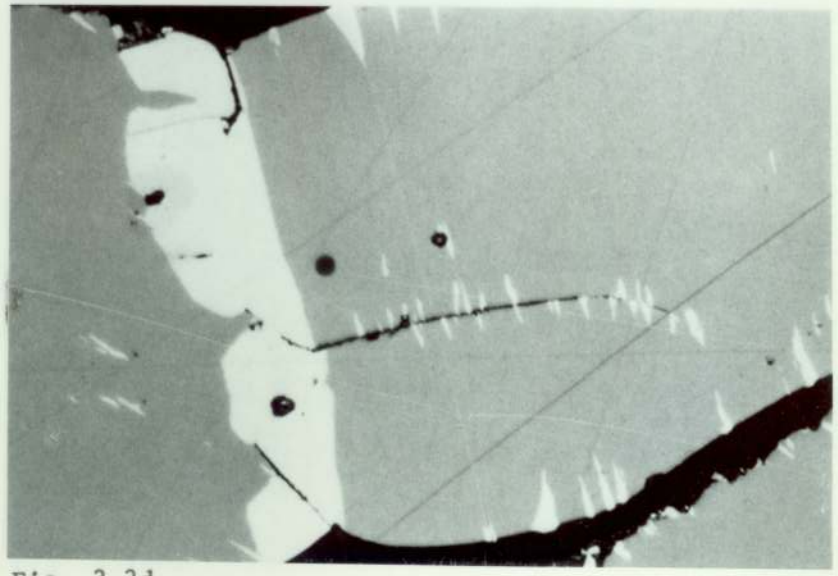

Fig. 3.3d

Fig. 3.4 Schematic diagrams illustrating stages in the development of Rim Pentlandite

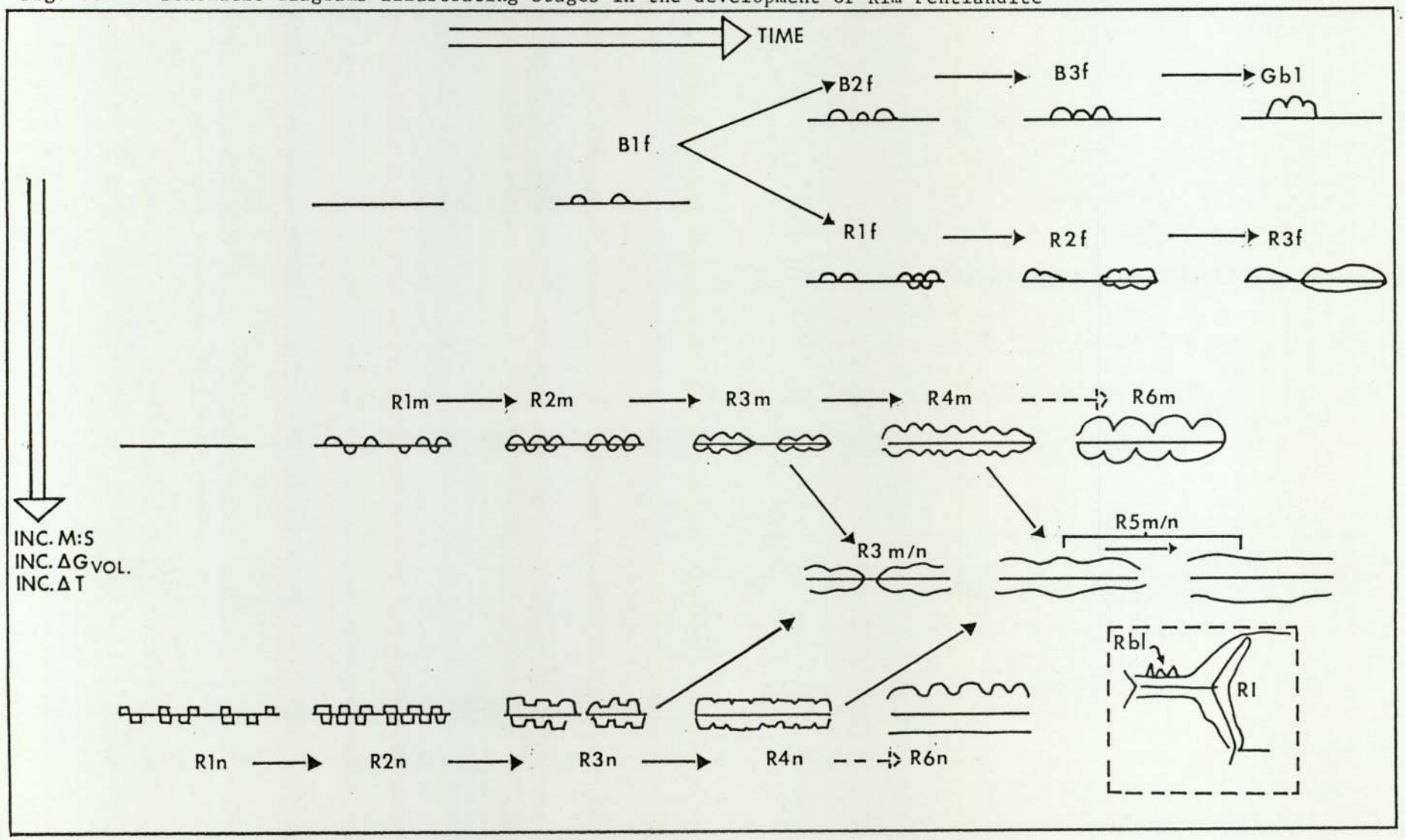

Fig. 3.5a,b Progressive 'plucking' of material at the boundaries between 'rounded' MSS 'sub grains' and coarser MSS grains [Homogeneous sample, Fe/Ni 5, M/S 0.946] (x1000, f.o.v. 70 μm , PPL, Oil)

Fig. 3.5c Interlinking of rim pentlandite with cellular rim round an interstitial sub-grain (central). Cellular rim enveloping a sub-grain located at the boundary between two coarser MSS grains (lower right). [Fe/Ni 2, M/S 0.930; 300°C 1hr] (x1000, f.o.v. 105 μm, PPL, Oil)

Fig. 3.5d Interlinking of cellular rims round adjacent MSS sub-grains (central). Moderate numbers of flame-type blades with jagged to serrated margins located at the MSS grain margins [Fe/Ni 5, M/S 0.930; 200°C 2664hrs] (x1000, f.o.v. 105 μm, PPL. Oil)

Fig. 3.5e Cellular rim enveloping a sub-grain located within a coarser MSS grain. The adjacent sub-grain has been completely converted to pentlandite. Sinuous flame-type blades with serrated margins at the MSS grain boundaries with closer spaced finer flames at a fracture [Fe/Ni 10, M/S 0.930; 200°C 2664hrs] (x1000, f.o.v. 105 μm, PPL, Oil]

Fig. 3.6a Single coarse granular blocky pentlandite (white) at MSS grain margin [Fe/Ni 5, M/S 0.966; 400°C 1780 hrs] (x600, f.o.v. 175 μm, PPL, Oil)

Fig. 3.6b Granular blocky (lower right) and granular interstitial (upper right) pentlandite (white) well dispersed within matrix of MSS grains [Fe/Ni 24, M/S 0.965; 300°C 1000hrs] (x600, f.o.v. 150 μm, PPL, Oil)

Fig. 3.6c Relatively abundant granular blocky aggregates of pentlandite (white) located at MSS grain boundaries and margins. Minor thin discontinuous lense-like rims of pentlandite also present. [Fe/Ni 3, M/S 0.930; 300°C 1000hrs]

Fig. 3.6d Extreme example of coarsening of rim pentlandite along short MSS grain boundaries resulting in coarse granular aggregates [Fe/Ni 3, M/S 0.946; 300°C 1000hrs] (x1000, f.o.v. 105 μm, PPL, Oil)

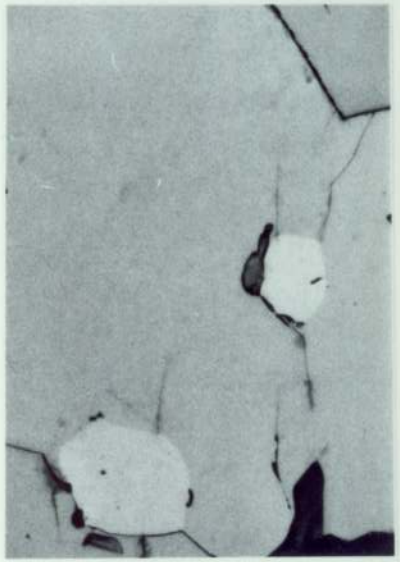

Fig. 3.5a

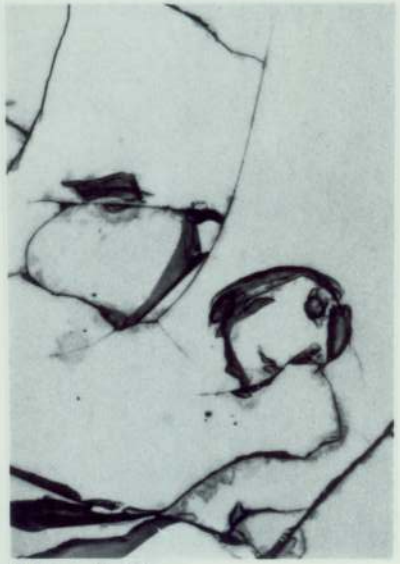

Fig. 3.5b

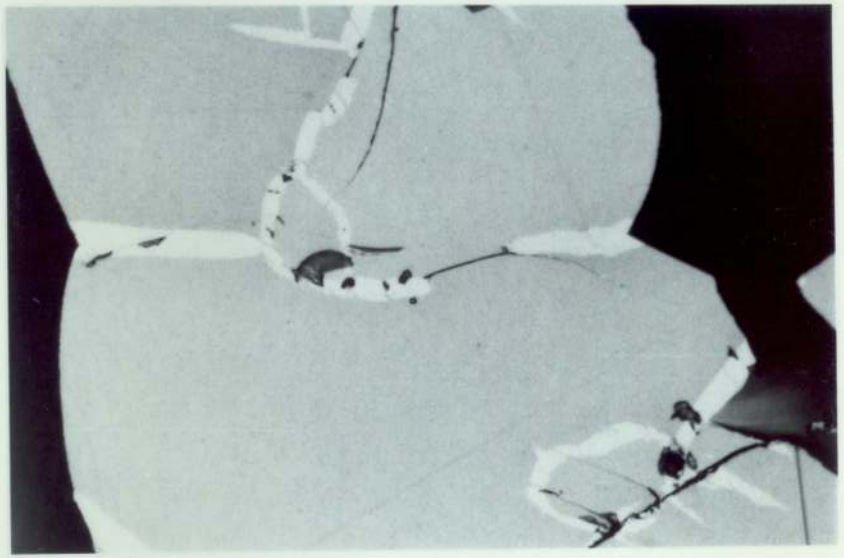

Fig. 3.5c

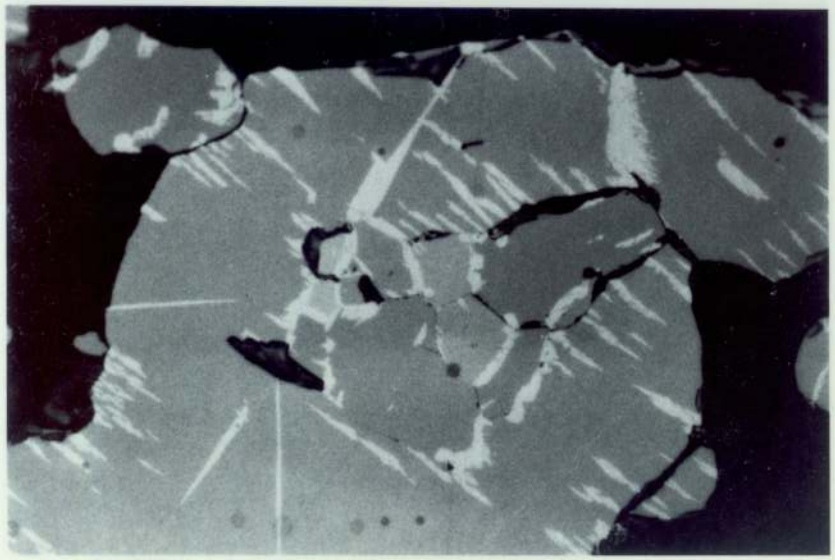

Fig. 3.5d

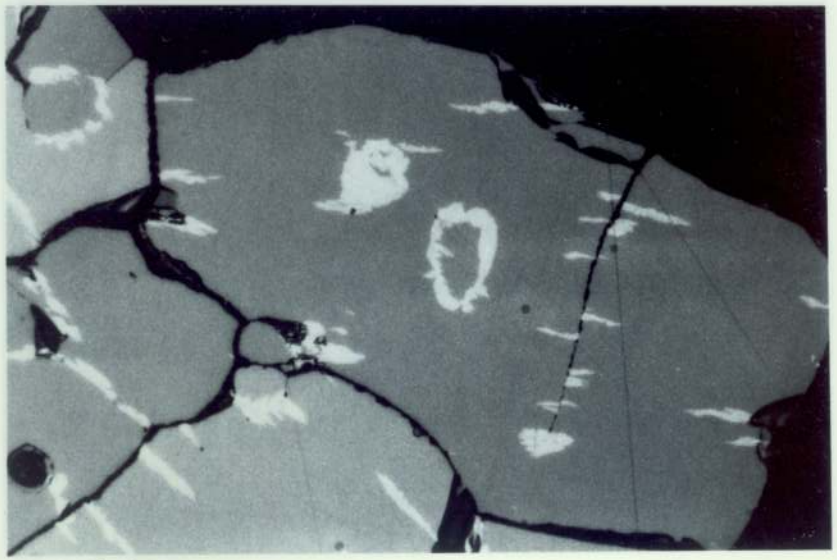

Fig. 3.5e

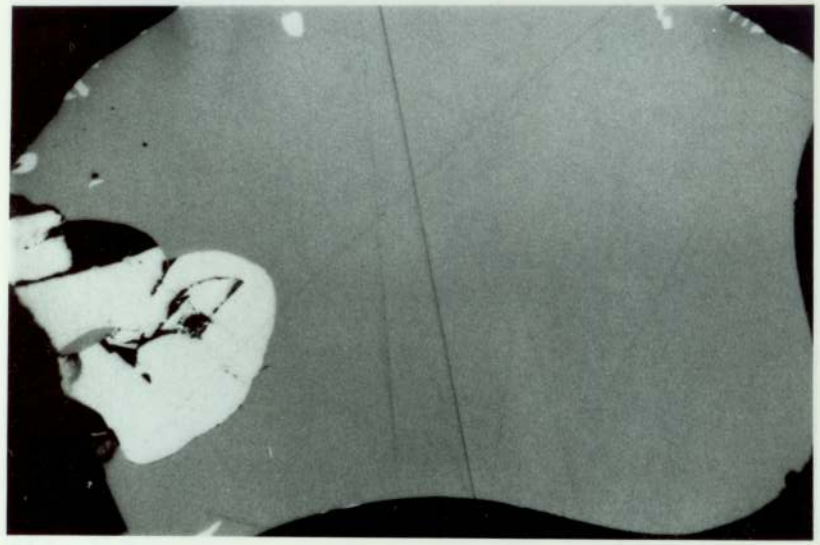

Fig. 3.6a

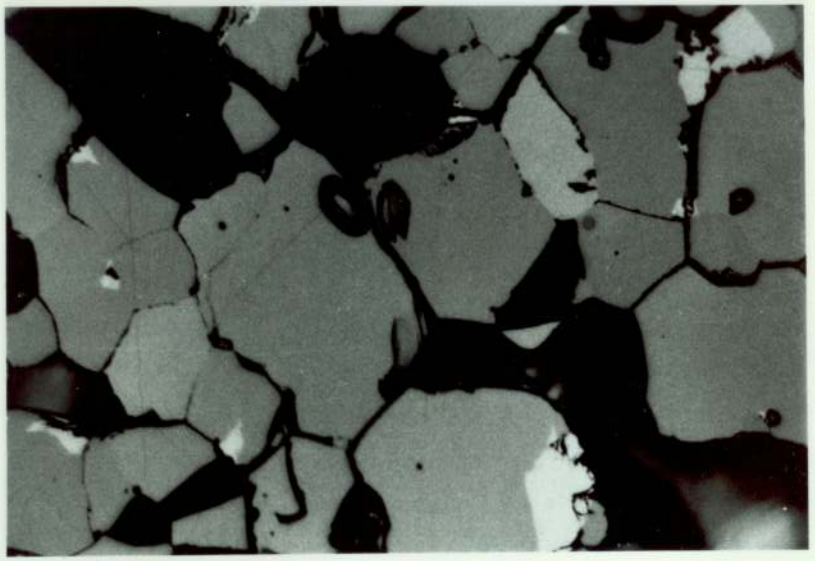

Fig. 3.6b

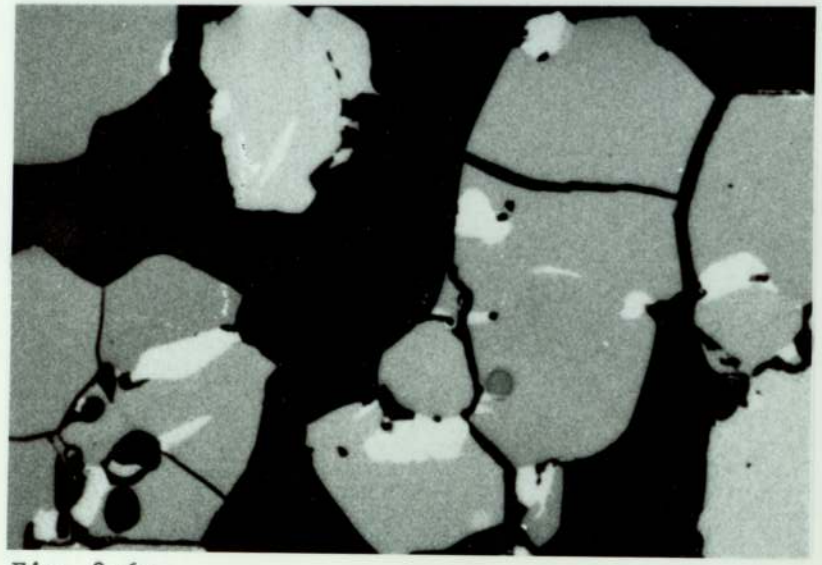

Fig. 3.6c

Fig. 3.6d

Fig. 3.7a,b Grain aggregates from MSS sample Fe/Ni 5, M/S 0.946; 300°C 100hr. (x600, f.o.v. 175 μm, PPL, Oil). Moderate numbers of regularly spaced linear blades at individual grain boundaries. A proportion of the blades have just begun to lose their linear form (and coherency), becoming more sinuous. Minor impingement between adjacent blades to form flame-type aggregates. Note also: the continuous rims with undulate to entire boundaries; clusters of partially impinged lenticular lamellae (Fig. 3.7a within grain on right hand margin) and cell pentlandite round 'sub-grain' located at the grain boundary of a coarser MSS grain (Fig. 3.7b upper right). The three large grains in the upper portion of Fig. 3.7a illustrate the variation in bladed forms with MSS grain orientation: from elongate, thin blades in the high anisotropy grain on the right hand margin; to tubbier blades in the adjacent weakly anisotropic grain; to partially impinged blebs in the basal grain on the left hand margin.

Fig. 3.7c Coarse single grain of MSS with elongate sinuous plates at the grain margin and closer spaced finer plates at fractures within the grain [Fe/Ni 3, M/S 0.946; 300°C 20mins] (x600, f.o.v. 175 μm, PPL, Oil)

Fig. 3.7d MSS sample of initial composition Fe/Ni 3, M/S 0.966 annealed 300°C 100hrs (x750, f.o.v. 140 μm, PPL, Oil). Compared with the sample of lower initial M/S ratio annealed under the same conditions (Figs. 3.7a,b) (i) The blades are more closely spaced, finer in width and more sinuous in form. Higher degree of impingement between adjacent blades (lower right). (ii) Wiry elongate lamellae in a seriate distribution occur within the MSS grain (as opposed to small clusters of lenticular lamellae). (iii) The larger grain also contains platy elongate (PE) lamellae with rounded terminations. Note the difference in orientation between the wiry lamellae (orientated sub-parallel to the basal MSS plane) and the platy lamellae. Coarse continuous rims along MSS grain boundaries also present, one with linear entire margins, the other with a single step like indentation. Within each individual MSS grain in each photograph the blades are elongate sub-parallel to each other (and sub-parallel to the basal MSS plane) hence the difference in blade orientation between different grains.

Fig. 3.7a

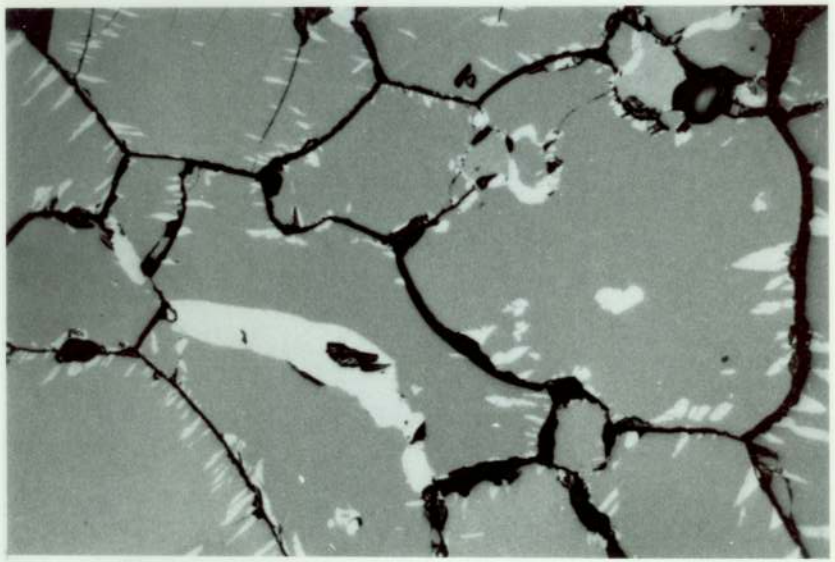

Fig. 3.7b

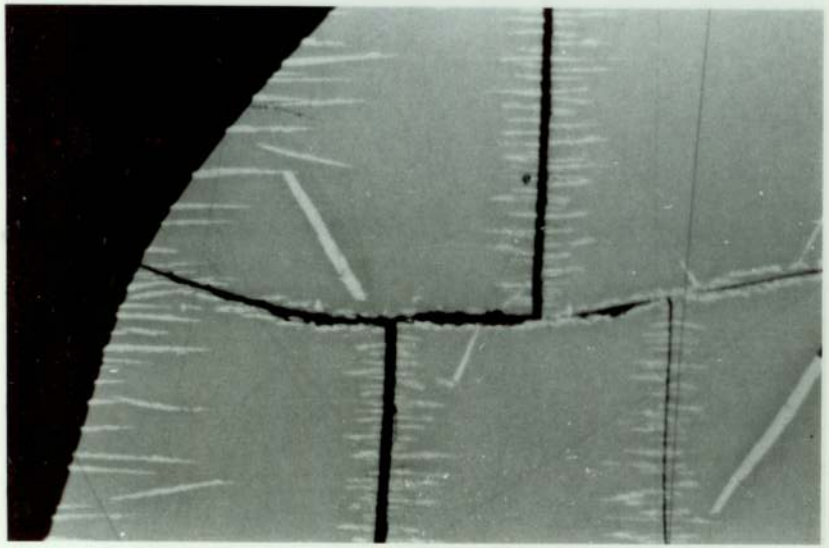

Fig. 3.7c

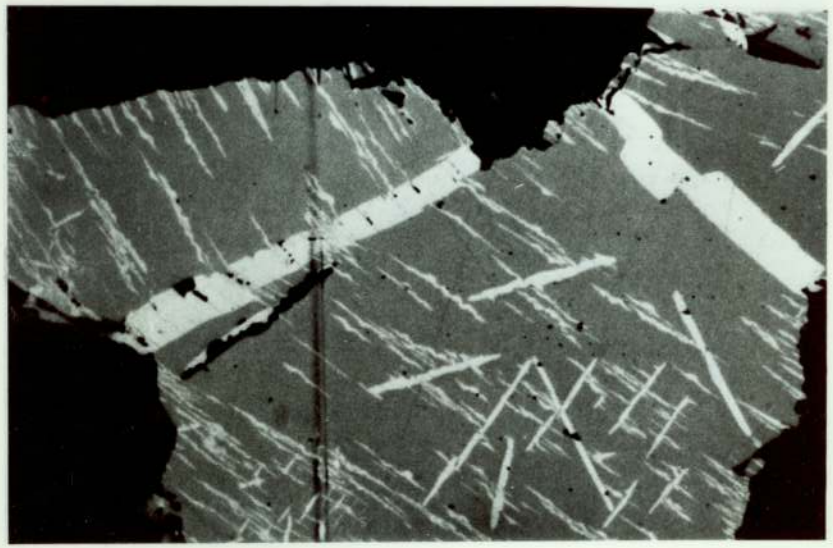

Fig. 3.7d

Fig. 3.8 Representative grain aggregates of MSS sample with initial composition Fe/Ni 5, M/S 0.966 annealed at 300°C for (a) 1hr, (b) 100hrs (both photographs x500, f.o.v. 300 μm, PPL, Oil)

Growth with increased annealing time results in

(i) an increase in the dimensions and numbers of linear blades present at MSS grain boundaries.

(ii) an increase in the width and continuity of rim pentlandite together with the development of less indented boundaries with the adjacent MSS grains.

(iii) an increase in the width of the minor cells round 'sub-grains' located at the grain boundaries and within coarser grains.

Compare Figs. 3.8a,b with textural types developed in same sample at lower temperatures, increased ΔT (Fig. 3.18b)

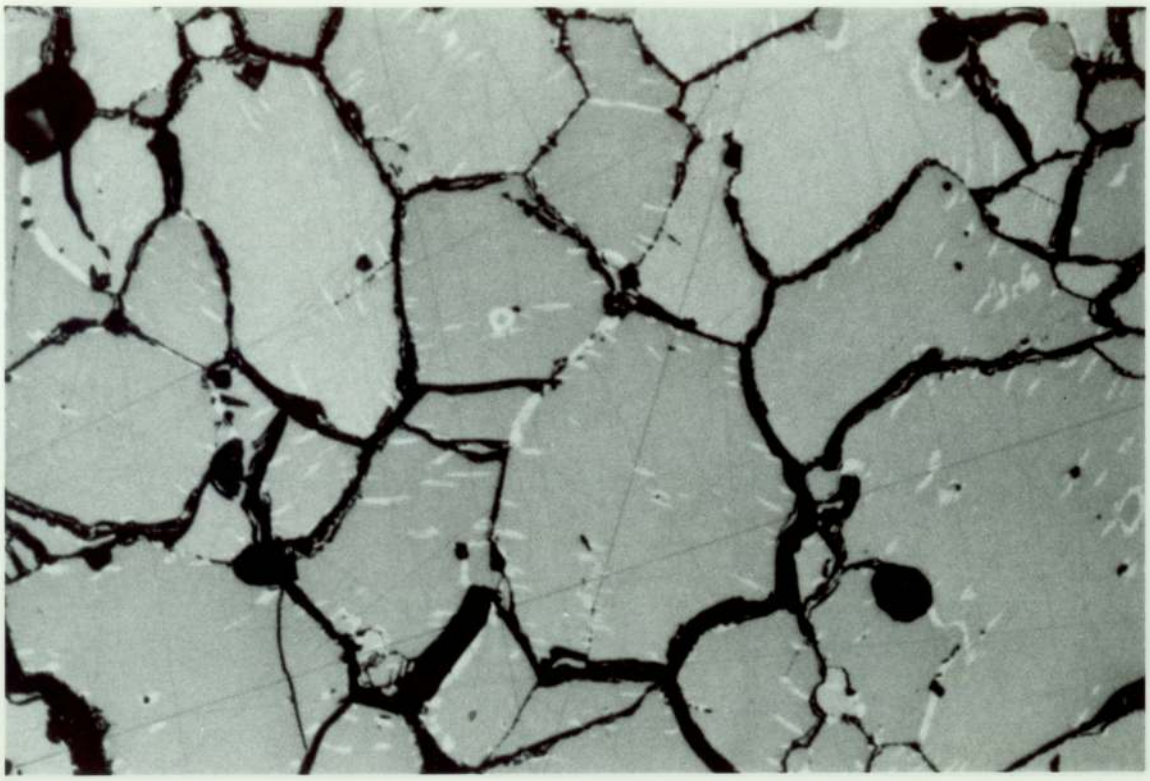

Fig. 3.8a

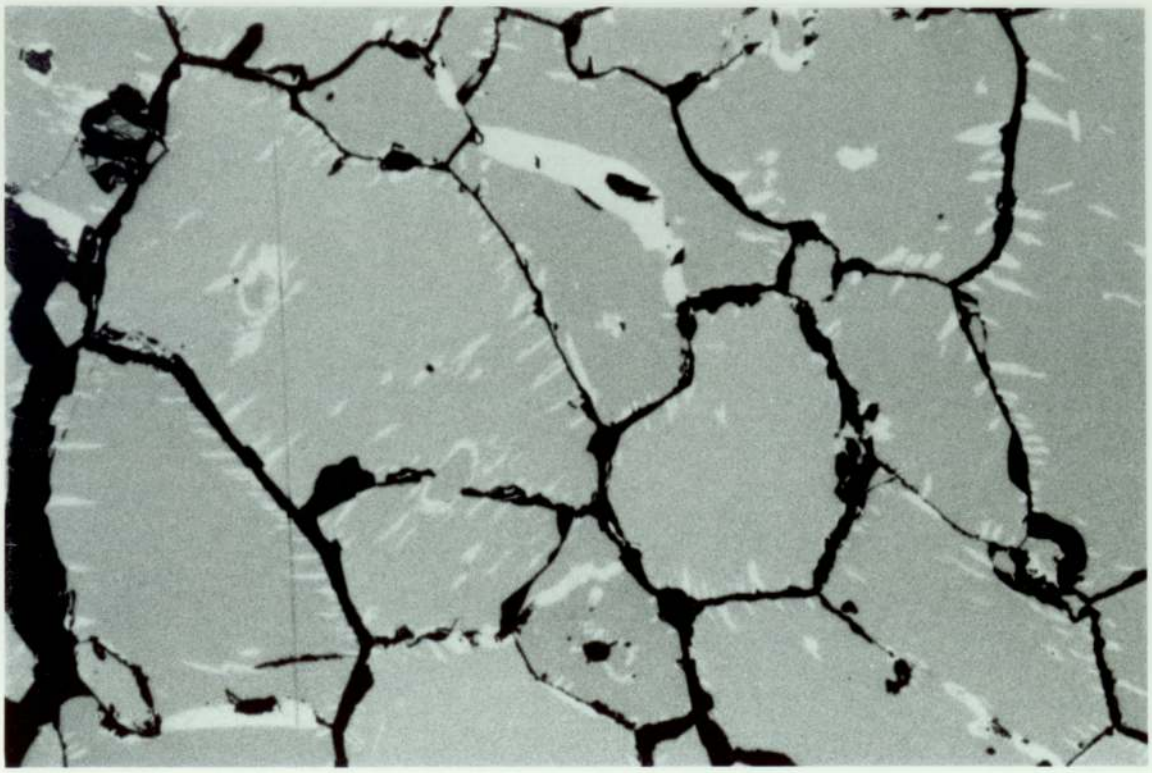

Fig. 3.8b

Fig. 3.9 Schematic diagrams illustrating stages in the development of bladed forms of Pentlandite

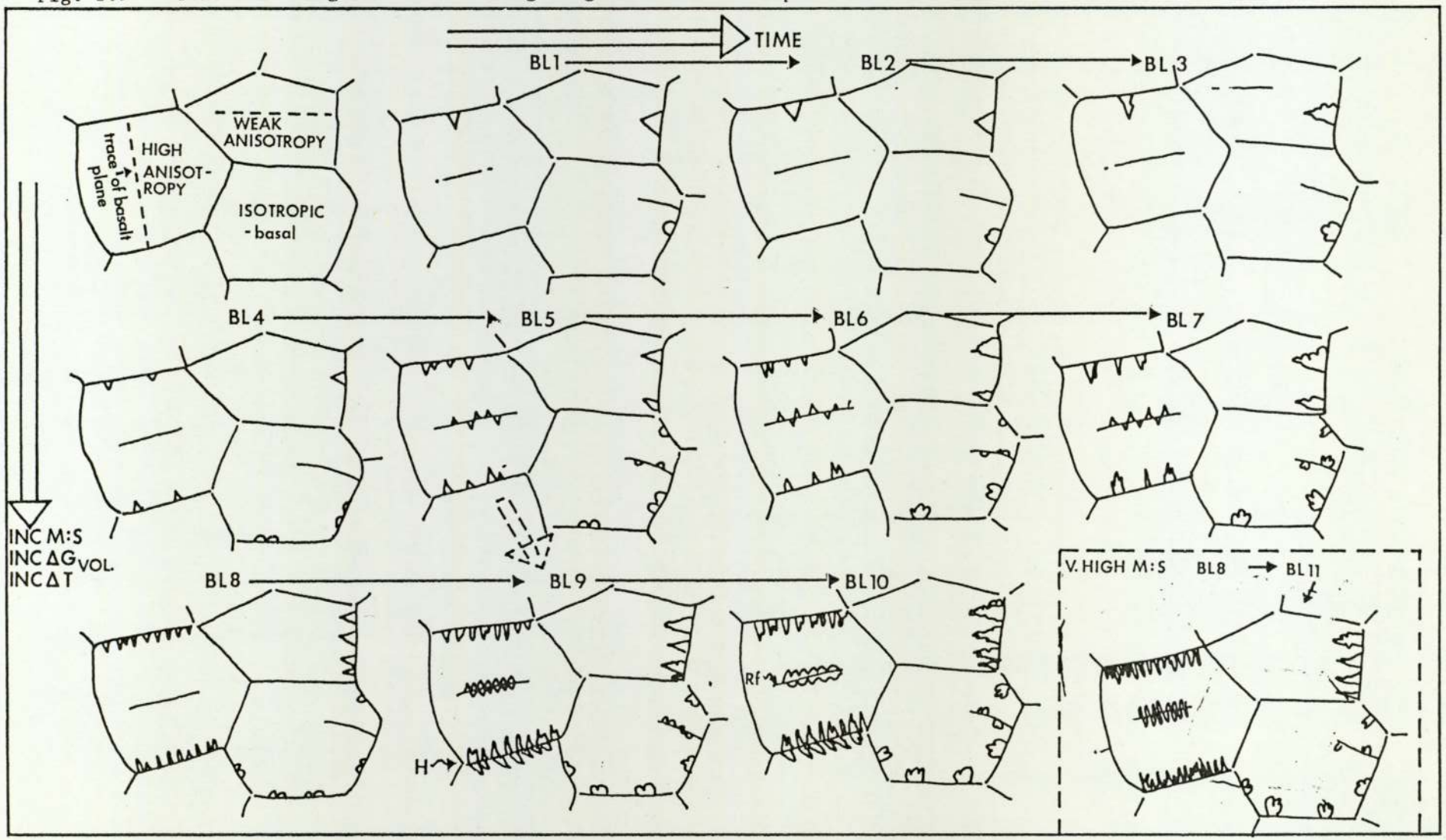

Fig. 3.10a Thin pentlandite rim with numerous bladed extensions finer than the coarse ragged flame-aggregates developed at the grain margins (lower left). [Fe/Ni 5 M/S 0.930 200°C 100hrs] (x1000, f.o.v. 70 μm PPL, Oil)

Fig. 3.10b Irregularly spaced flame-type blades with ragged margins at MSS grain boundaries [Fe/Ni 24, M/S 0.965; 200°C 2664hrs] (x1000, f.o.v. 70 μm , PPL, Oil)

Fig. 3.10c Impingement of adjacent lenticular lamellae within MSS grain resulting in flame type aggregates and more massive lenses. Flame-type blades at grain boundaries [Fe/Ni 24, M/S 0.982, 200°C 2664hrs] (x1000, f.o.v. 105 μm, PPL, Oil)

Fig. 3.10d,e Variation in form of lenticular particles 3.10d. Impinged blebs forming rosettes with embayed lobate margins irregularly distributed in basal MSS grain 3.10e clusters of numerous sinuous or sigmoidal lenticular lamellae within high anisotropy grain. Note also blades at grain margins in high anisotropy grain (3.10e) and blebs at same location in basal grain (3.10d). The basal grain (3.10d) also contains sub-grains with cellular rims - embayed lobate outer margins, entire inner margins. 3.10d Fe/Ni 5, M/S 0.946; 300°C 10hrs, (x600, f.o.v. 175 μm, PPL, Oil) 3.10e Fe/Ni 3, M/S 0.946; 300°C 20min (x1000, f.o.v. 105 μm, PPL, Oil)

Fig. 3.11a Coarsening of lenticular lamellae perpendicular to their direction of elongation to form sinuous lamellae and lenticular blebs [Fe/Ni 5, M/S 0.973; 400°C 1780hrs]

Fig. 3.11b Impingement of adjacent lenticular blebs resulting in flame-type aggregates [Fe/Ni 24, M/S 0.982; 200°C 2664hrs]

Figs. 3.11b → c → d (x1500, f.o.v. 70 μm, PPL,Oil) Figs. 3.12a → b → c → d (x1500, f.o.v. 73 μm, ,PPL, Oil) illustrate (i) the change in form and spacing of wiry lensoidal particles within MSS grains sectioned progressively closer to the basal plane, and (ii) the change in dimensions and distribution between wiry seriate forms (Figs. 3.11b,c,d) and wiry pervasive forms (Fig. 3.12) with an increase in the initial M/S ratio of the MSS. High anisotropy grains: Fig. 3.11c elongate, relatively wide, wiry seriate lamellae sub-parallel to basal plane; relatively wide interlamellar spacings between adjacent rows; numerous hemispherical caps protruding from the margins; Fig. 3.12a closer spaced, finer, more regularly distributed wiry pervasive lamellae → Fig. 3.12b moderate anisotropic grain wiry pervasive lamellae coarser, interlamellar distance increased, caps more spheroidal →Fig. 3.12c weakly anisotropic grain: wider 'dendrites', increased spacing cf 3.11d coarser wiry seriate dendrites with large spheroidal protrusions and wider more irregular spacing 3.11e, 3.11d Basal grains: clusters of blebs or impinged blebs forming embayed irregular rosettes. Fig. 3.11 Fe/Ni 5, M/S 0.966; 300°C, c) 100hrs, d,e) 10hrs. Fig. 3.11 Fe/Ni 10, M.S 1.000; 300°C, a,c,d) 10hrs, b) 1hr.

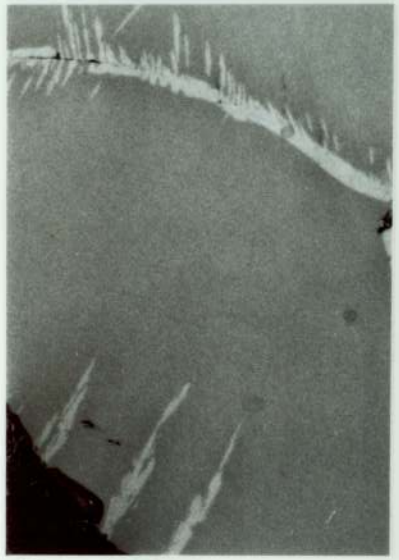

Fig. 3.10a

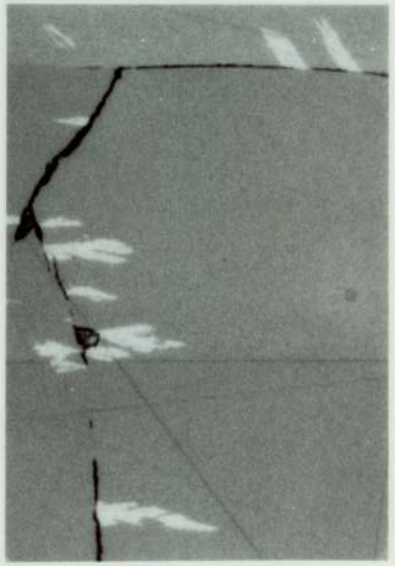

Fig. 3.10b

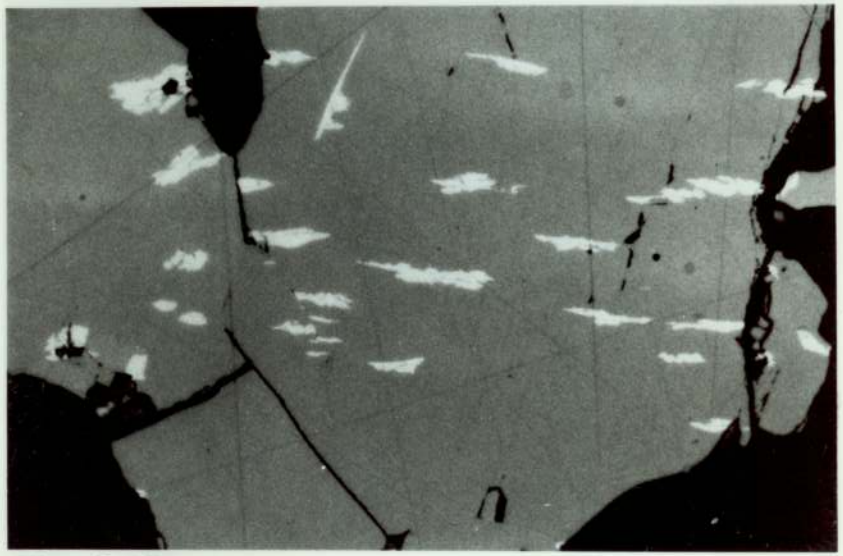

Fig. 3.10c

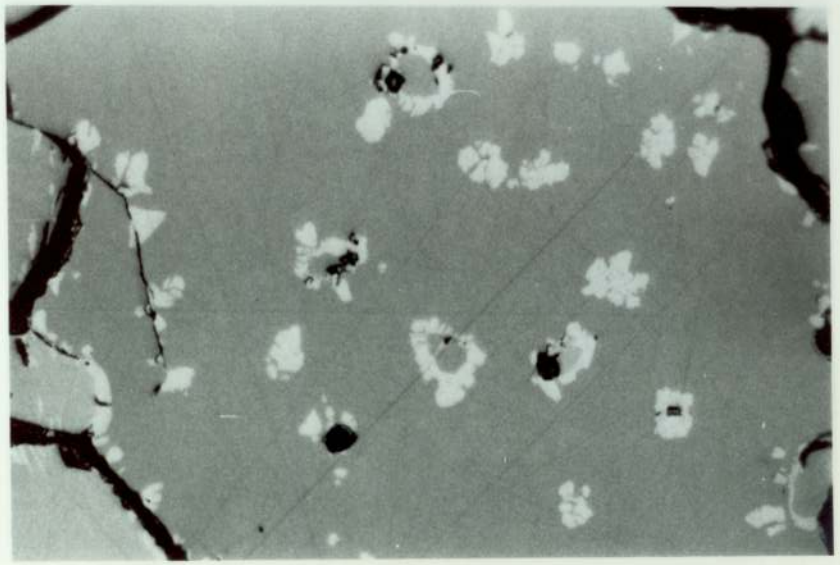

Fig. 3.10d

Fig. 3.10e

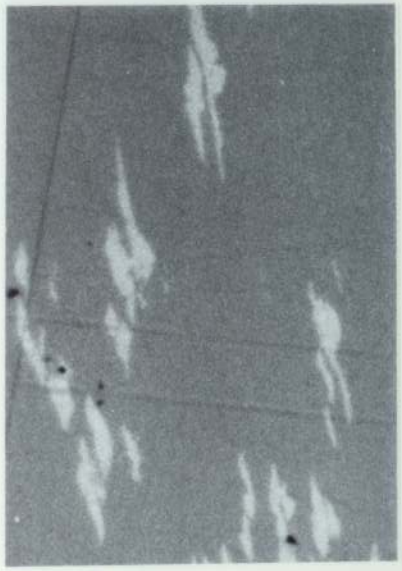

Fig. 3.11a

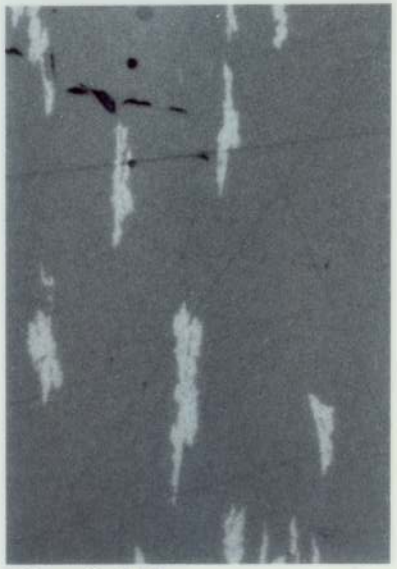

Fig. 3.11b

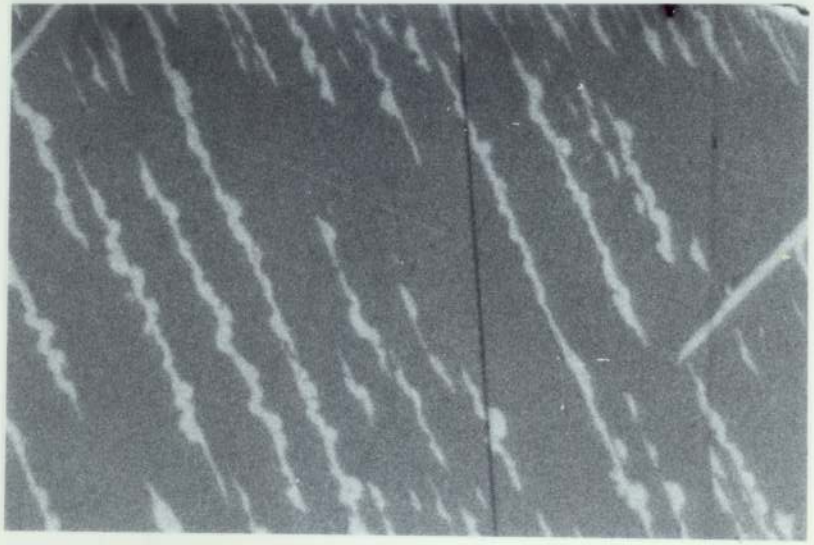

Fig. 3.11c

Fig. 3.11d

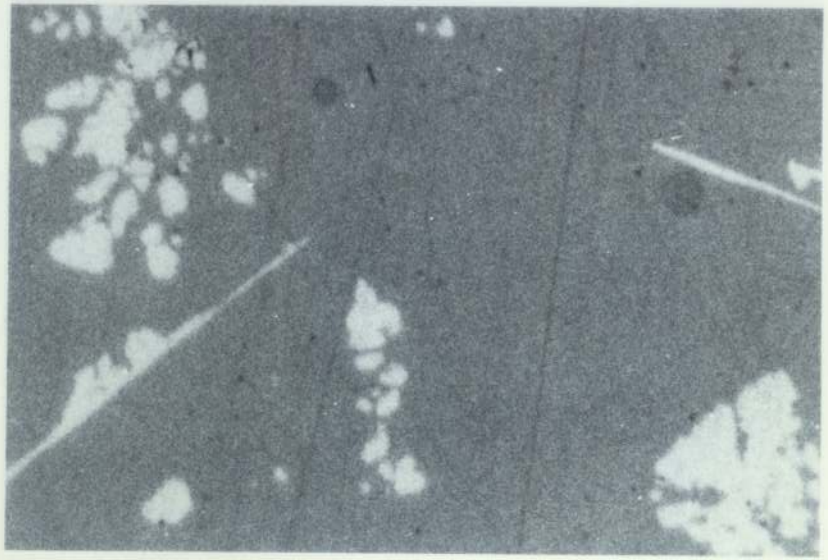

Fig. 3.11e

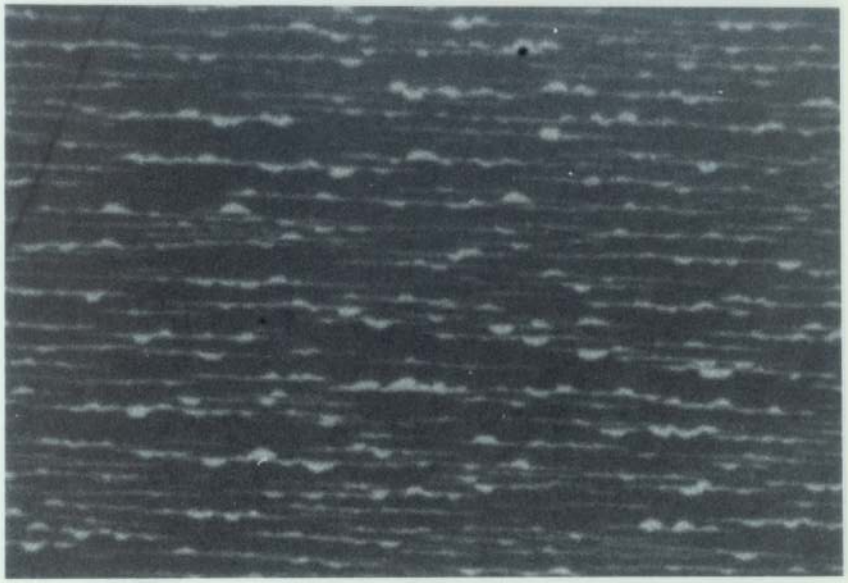

Fig. 3.12a

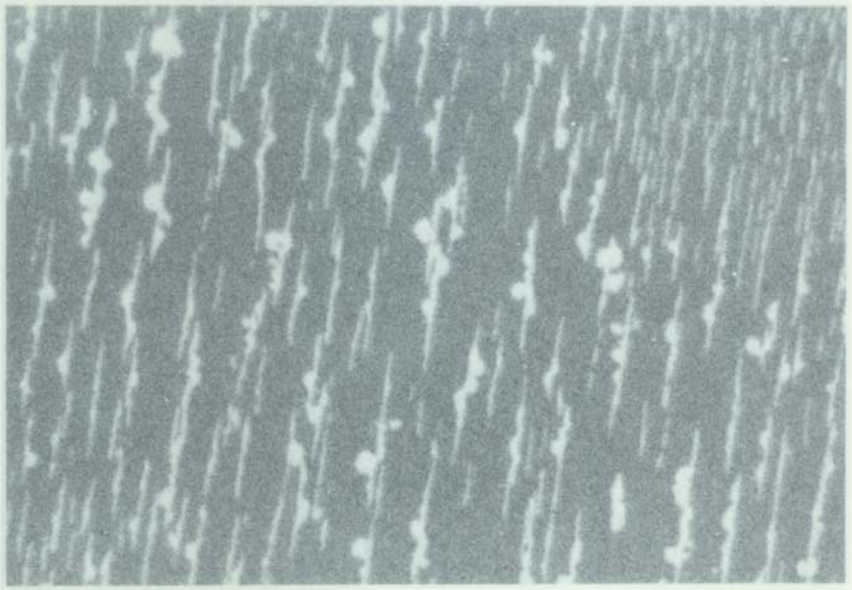

Fig. 3.12b

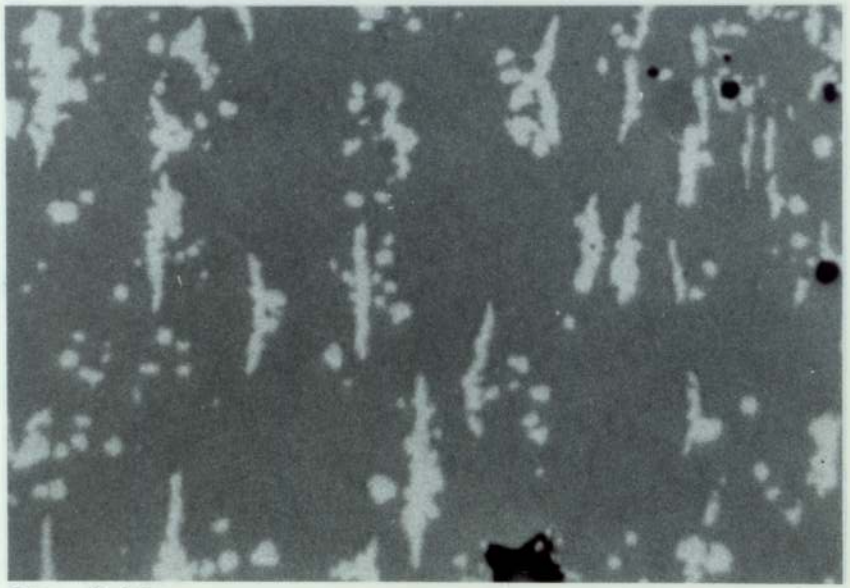

Fig. 3.12c

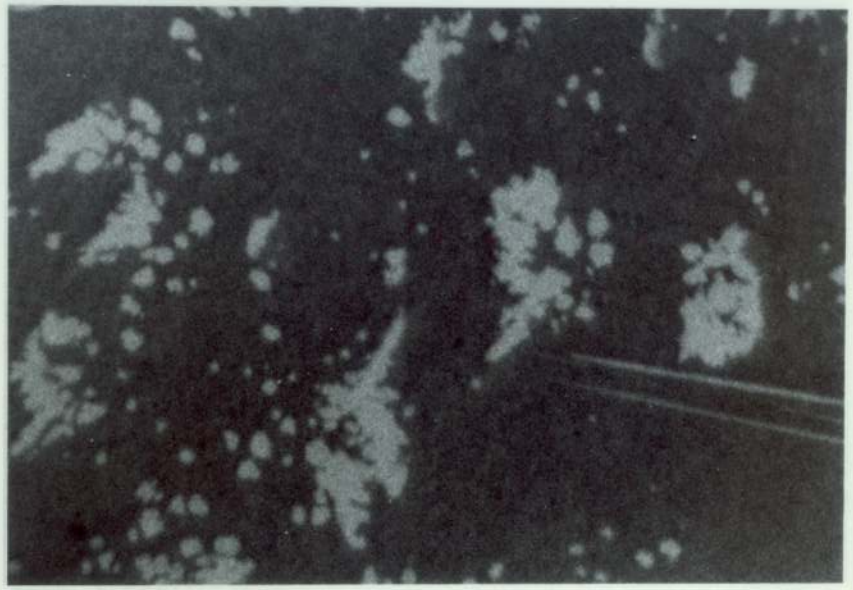

Fig. 3.12d

Fig. 3.14 MSS sample Fe/Ni 24, M/S 1.000 annealed at 300°C.

Fig. 3.14a,b (20mins) Filiar forms of lensoidal particles. Fig. 3.14a Basal MSS grain, small irregularly distributed blebs, Fig. 3.14b High anisotropy grains: extremely fine width elongate thread-like or filiar lamellae (x1500, f.o.v. 70 µm, PPL, Oil)

Fig. 3.14c (10hrs) development of filiar lamellae and clusters of partially impinged blebs (basal section, lower left) into d) (1000hrs) lenticular seriate elongate blebs and regularly distributed rosettes (basal grain upper left). Coarsening of particles perpendicular to elongation direction and increase in number of particles present. (x550, f.o.v. 190 µm, PPL, Oil)

Fig. 3.15a Fe/Ni 10, M/S 1.000, b,d.) Fe/Ni 5, M/S 0.986, c) Fe/Ni 5, M/S 0.966; All 300°C 100hrs (x500, f.o.v. 220 µm, PPL, Oil)

Fig. 3.15a cf 3.15b Increase in width and spacing of the wiry pervasive lamellae in high and moderate anisotropy MSS grains with increase in Fe/Ni ratio. (Further increase in the Fe/Ni ratio to 24 at this temperature results in development of lenticular seriate forms, Fig. 3.14) Fig. 3.15a minor platy acicular lamellae irregularly distributed within coarser grain.

Fig. 3.15d Basal MSS grain, pervasive rosettes.

Fig. 3.15c cf Figs. 3.15a,b Decrease in initial M/S ratio. Development of wiry seriate forms: coarser more irregularly distributed lamellae and coarse dendrites in weakly anisotropic grain (lower left).

Fig. 3.16a,b,c,d (all x750, f.o.v., 140 µm, PPL, Oil)
3.16a [Fe/Ni 5, M/S 0.966, 300°C 1hr] Widely spaced coarse wiry seriate dendrites with deeply embayed margins and coarse spheroidal protrusions
cf 3.16b finer more regularly and closer spaced wiry pervasive dendrites [Fe/Ni 5, M/S 0.986; 300°C 10hrs]
3.16c [Fe/Ni 3, M/S 0.966; 300°C 100 hrs] Elongate irregularly distributed (wiry seriate) rosettes in basal MSS grain.
cf 3.16d finer, closer spaced, more irregular (wiry pervasive) rosettes [Fe/Ni 3, M/S 0.986; 300°C 10hrs]
3.16c The basal grain also contains 3 sets of platy elongate lamellae orientated at exactly 60° to each other. The disruption of the platy lamellae by the rosettes suggests that the rosettes were present first.

Fig. 3.14a

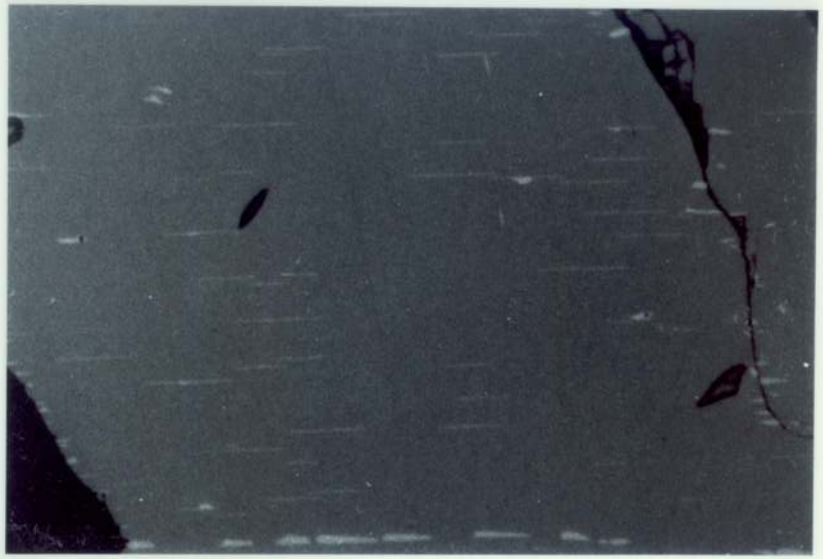

Fig. 3.14b

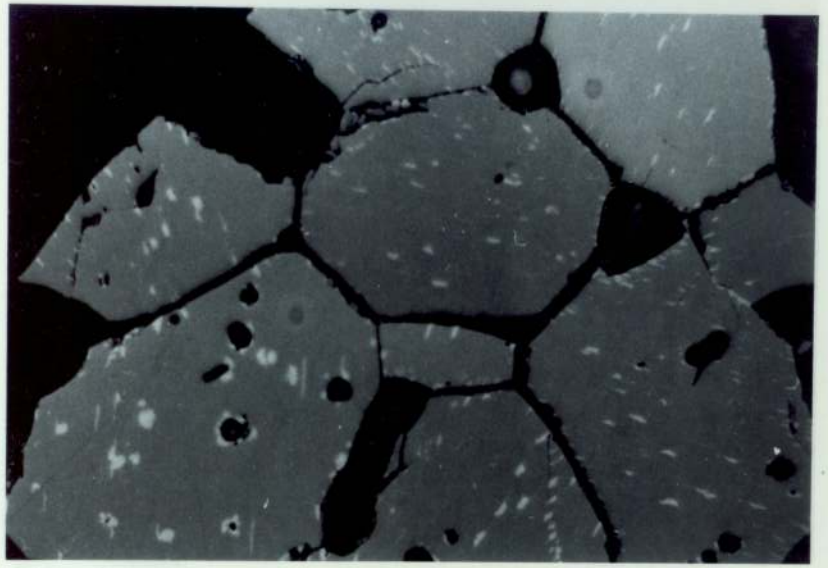

Fig. 3.14c

Fig. 3.14d

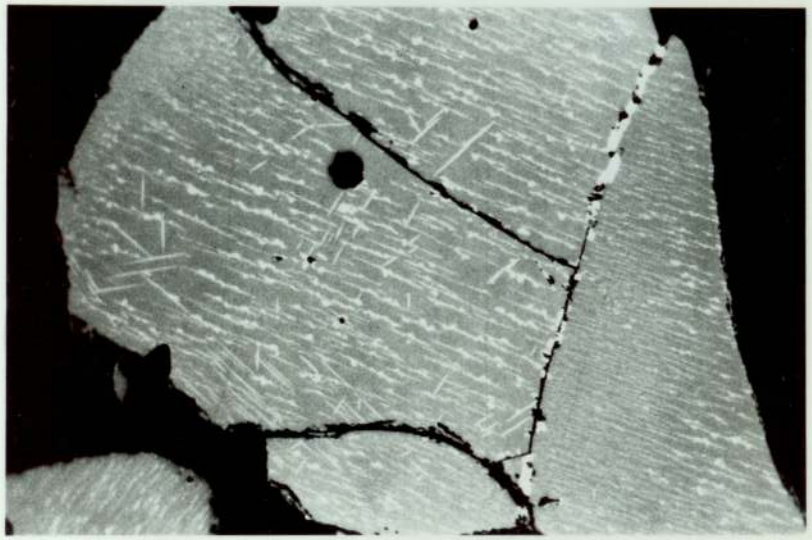

Fig. 3.15a

Fig. 3.15b

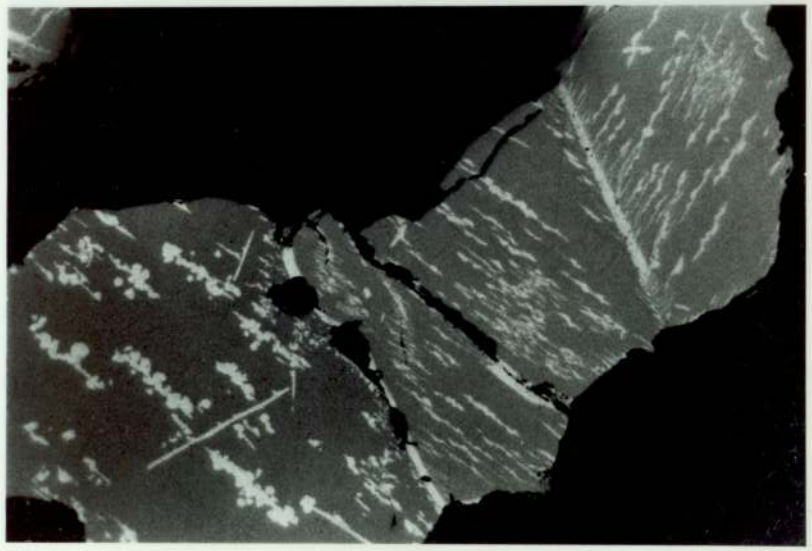

Fig. 3.15c

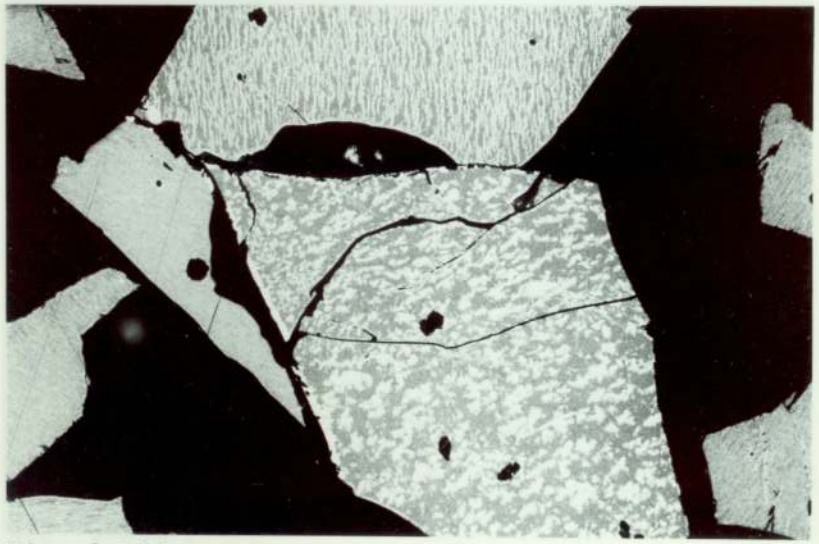

Fig. 3.15d

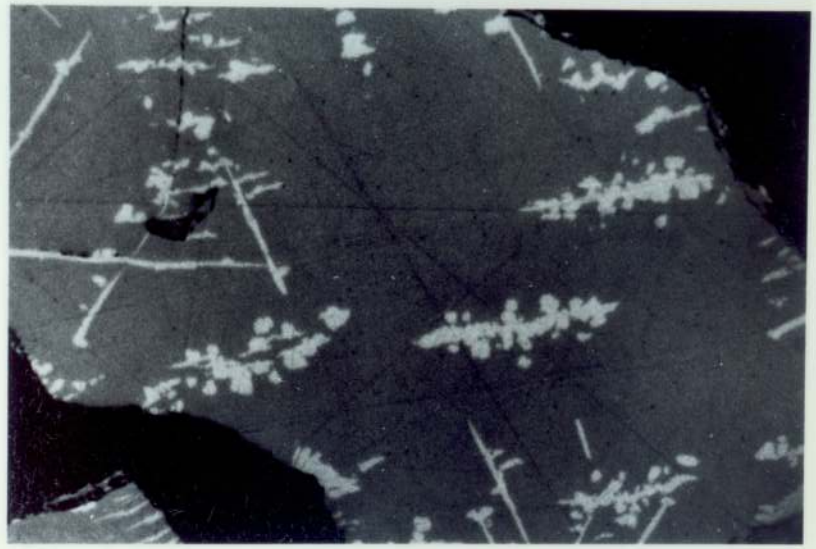

Fig. 3.16a

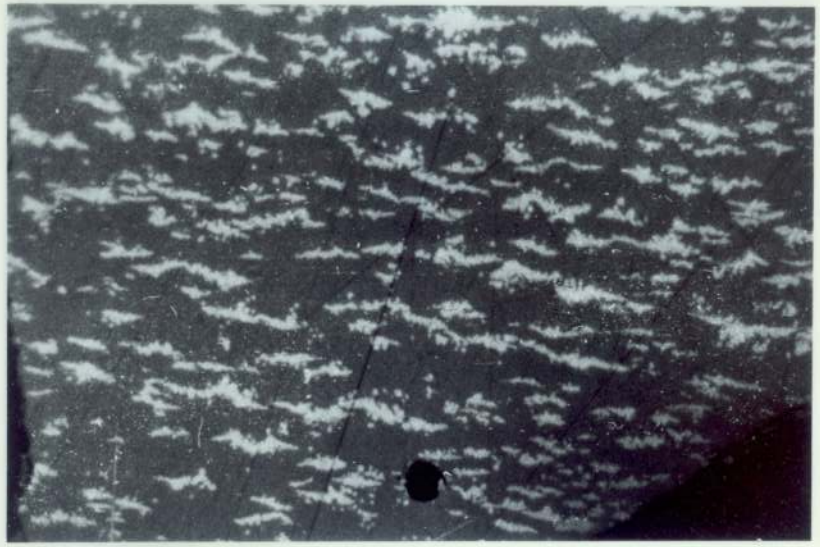

Fig. 3.16b

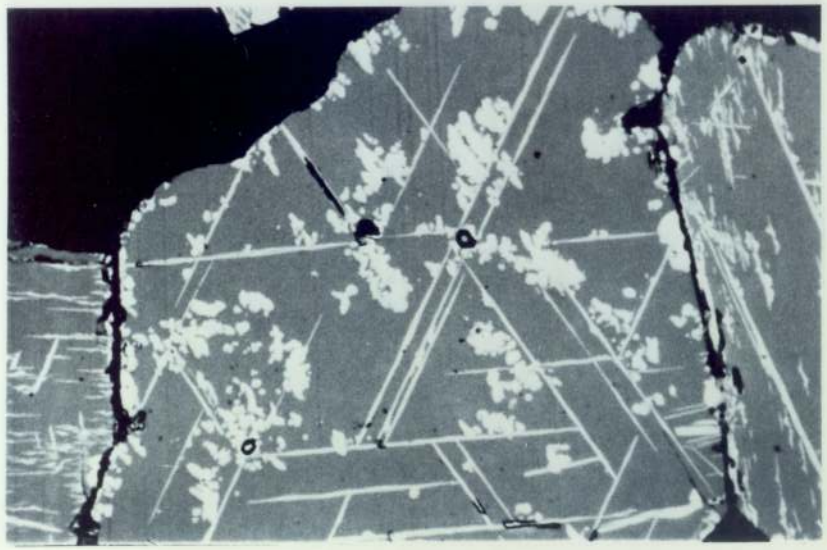

Fig. 3.16c

Fig. 3.16d

Summary: of variation in development of platy lamellae as illustrated by Figs. 3.15a, 3.16c, 3.17 to 3.19

10/1.000 300°C/100hrs
Fig. 3.15a WP >> PA

3/0.966 300°C/100hrs
Figs. 3.16c, 3.17b
PEtt<WS

3/0.946 300°C/100hrs
Fig. 3.18a PL irreg. tt

2/0.964 300°C/100hr
Fig. 3.17a PLtt

inc. Fe/Ni, dec. SSpn

inc. ΔT inc. SSpn

5/0.946 200°C/2664hrs
Fig. 3.18b
WS>PEtt

3/0.946 200°C
Figs. 3.19b,1hr;c,10hr;
d, 100hrs
PLtt>WS

Fig. 3.17a Intersecting sets of platy lamellae (PL) in a triangular trellis distribution. The lamellae have linear parallel side margins, taper at their intersections and commonly terminate against the MSS grain boundaries. Note the three wider lamellae with regular indented crenulate margins located on the right margin of the central MSS grain (x1000, f.o.v., 150 μm, PPL, Oil)

Fig. 3.17b Intersecting sets of platy elongate lamellae in a high anisotropy MSS grain. Acute angles between the sets ~80° and ~48°. The lamellae taper gently along their length to acicular terminations within the grain. Wiry seriate lamellae irregularly distributed within the 'PEtt network'. (x750, f.o.v., 140 μm, PPL, Oil)

Fig. 3.17c Coarse grained MSS sample. PNX78 annealed at 300°C for 100hrs. Very closely spaced triangular trellis of very fine PL lamellae. (?Grain sized induced nucleation of PL lamellae, see Section 4.4.8) (x750, f.o.v. 140μm, PPL, Oil)

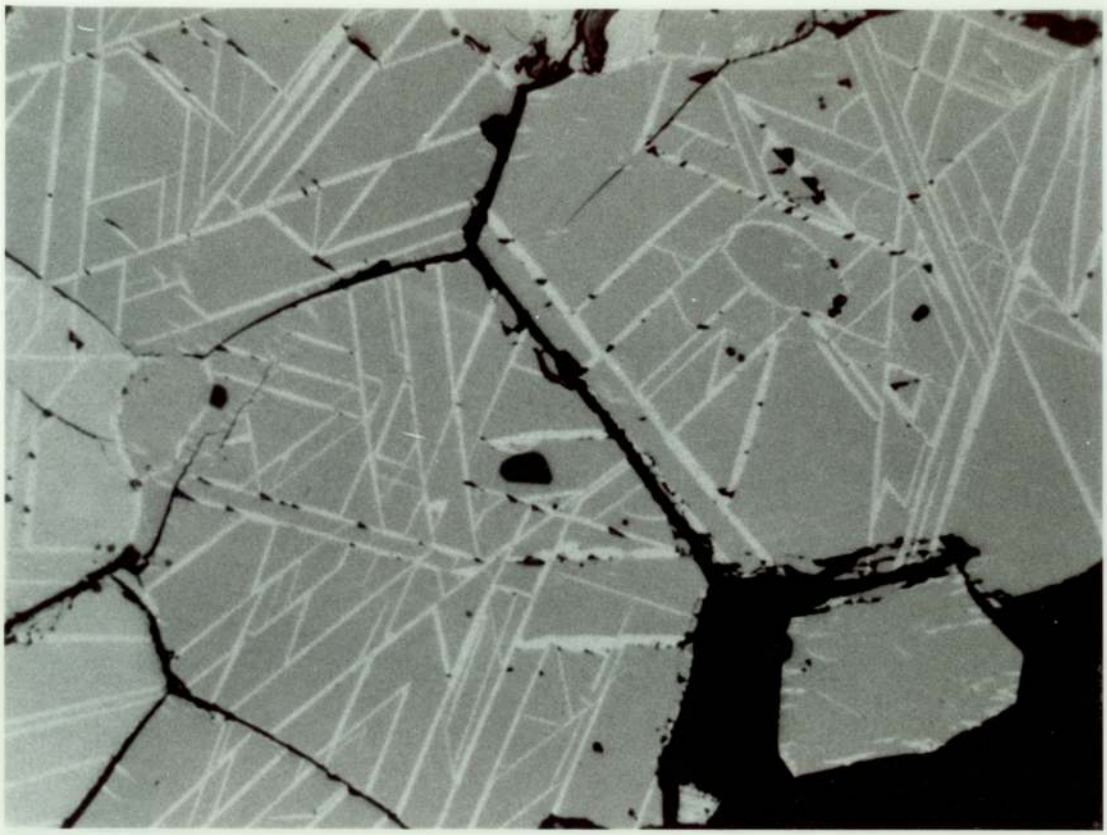

Fig. 3.17a

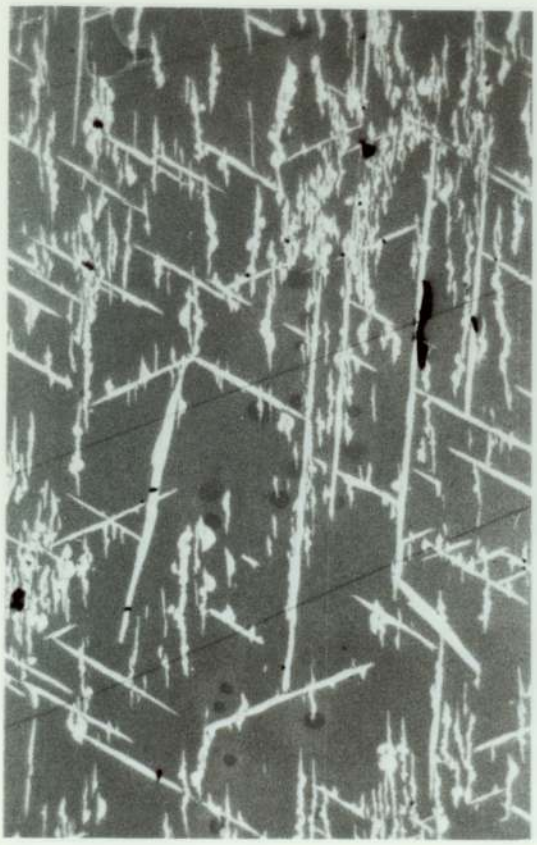

Fig. 3.17b

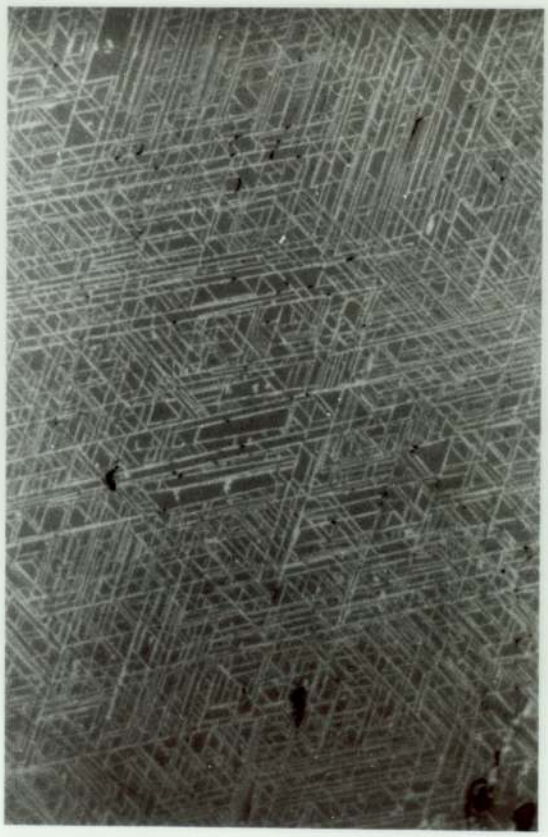

Fig. 3.17c

Fig. 3.18a Pl lamellae irregularly distributed forming an irregular triangular trellis within the host MSS grains. Variation in numbers of lamellae present in individual grains probably a function of sectioning (cf 3.19a). Clusters of numerous lenticular lamellae also present within the grains and numerous sinuous blades at the majority of grain boundaries (x500, f.o.v., 300 μm, PPL, Oil). Compare with Fig. 3.17a where the decreased Fe/Ni ratio results in the development of a regular PL triangular trellis; and with Fig. 3.17b where the increased M/S ratio results in a regular PE triangular trellis and wiry seriate lamellae, at the same annealing temperature (300°C).

Fig. 3.18b Dominantly wiry seriate forms within the MSS grains including wiry dendrites and rosettes in the two coarsest grains (lower margin). Irregular network of PE lamellae terminating within the grains also present but development restricted by the wiry seriate forms. (x500, f.o.v., 300 μm, PPL, Oil). This is the same composition as represented by Figs. 3.18a,b annealed at lower temperature 200°C (increased ΔT). This results in: (i) a decrease in the proportion of heterogeneously nucleated blades and rims, (ii) an increase in the number of homogeneously nucleated lensoidal forms, and their more even seriate distribution within the MSS grains.

Fig. 3.19a Same composition and annealing conditions as Fig. 3.18a. MSS grain sectioned at the right 'depth' to show best development of PL triangular trellis. (x600, f.o.v. 116 μm, PPL, Oil)

Fig. 3.19b,c,d Same composition as Fig. 3.18a and Fig. 3.19a but annealed at lower temperature 200°C for (b) 1hr (c) 10hrs, (d) 1000hrs. Illustrates the progressive development of a closely spaced regular triangular trellis of numerous PL lamellae. Fig. 3.19d by a marked increase in width and lesser increase in numbers of the very fine lamellae originally present. Fig. 3.19a,b. Note that on their first appearance they still traverse the MSS grains and terminate at the grain boundaries.
(Magnifications and f.o.v. (b) x750, 95 μm; (c) x500, 200 μm; (d) x500, 300μm)
Compared with Figs. 3.18a, 3.19a the decreased annealing temperature results in the development of a more regularly spaced Pltt network and a decrease in heterogeneous types such as blades.
Compared with 3.18b the decreased Fe/Ni ratio at the same annealing temperature results in the development of the PL lamellae in preference to wiry seriate forms.

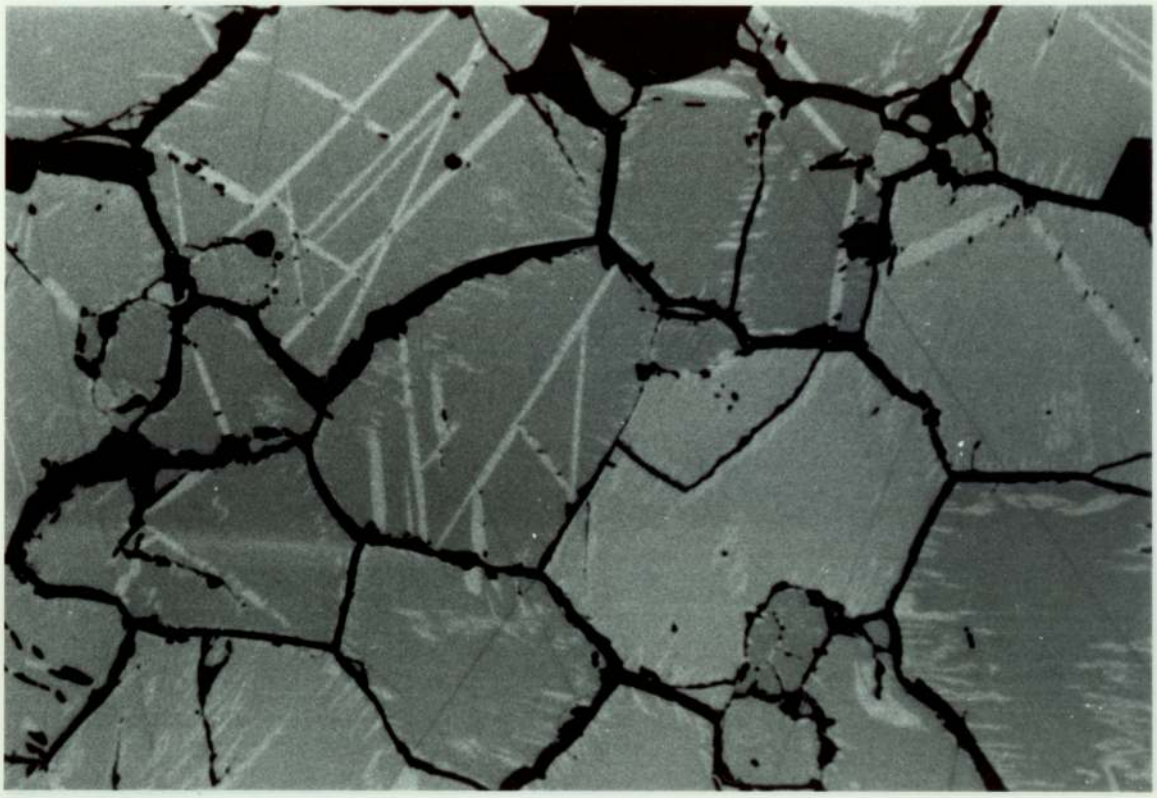

Fig. 3.18a

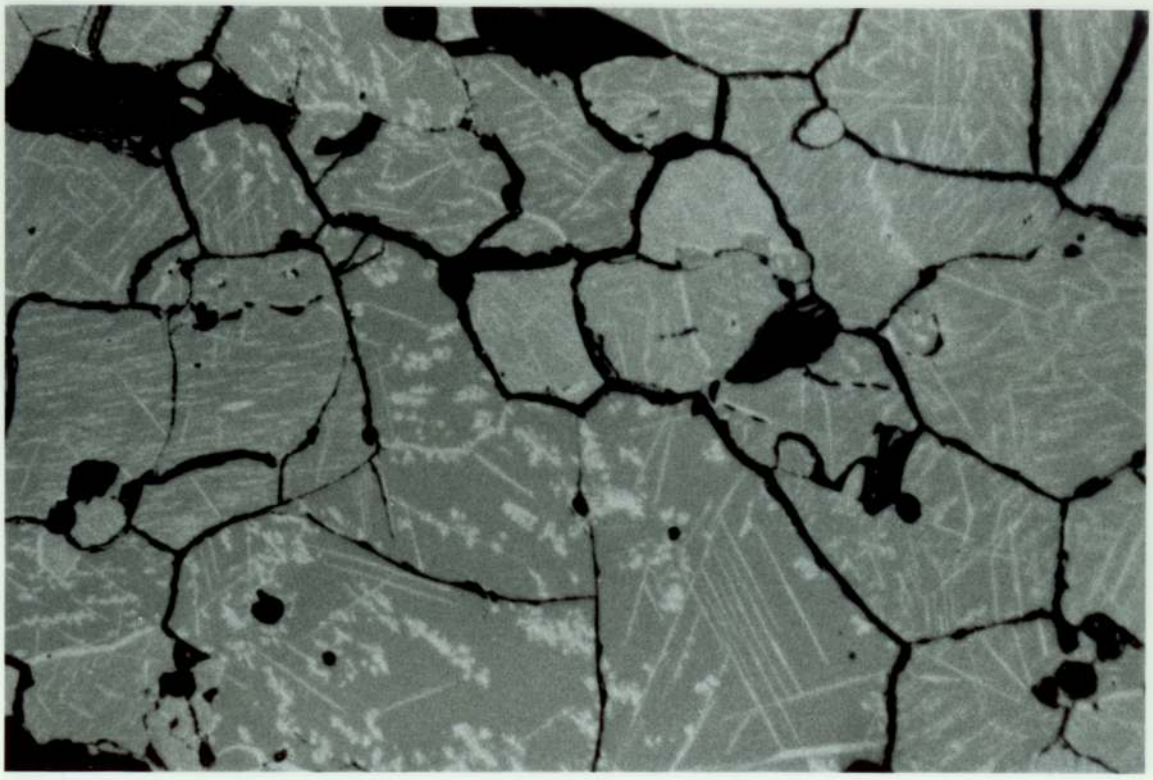

Fig. 3.18b

Fig. 3.19b

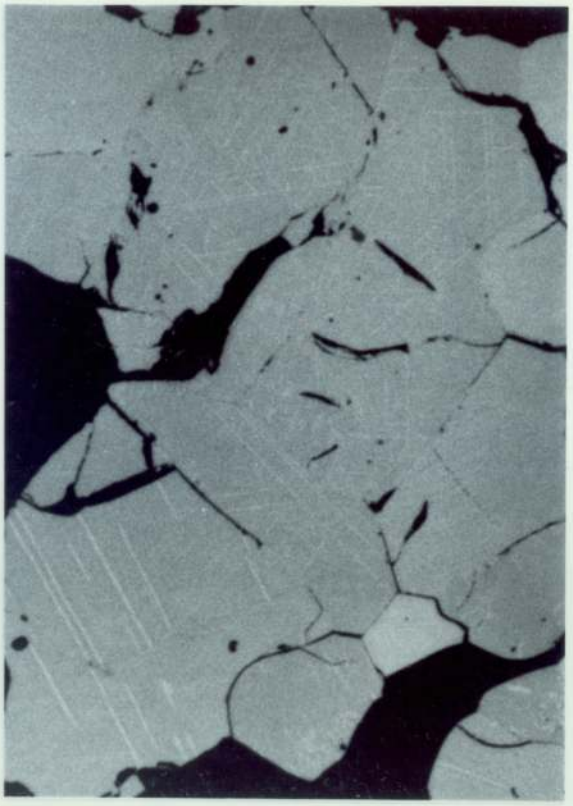

Fig. 3.19c

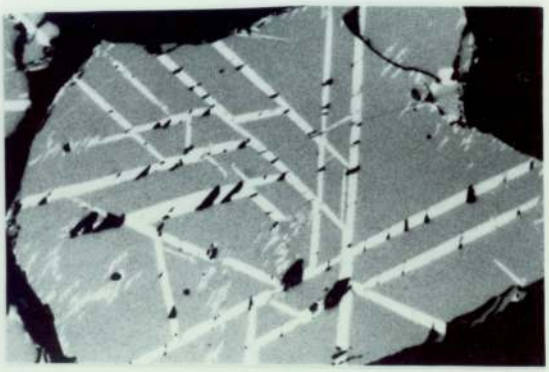

Fig. 3.19a

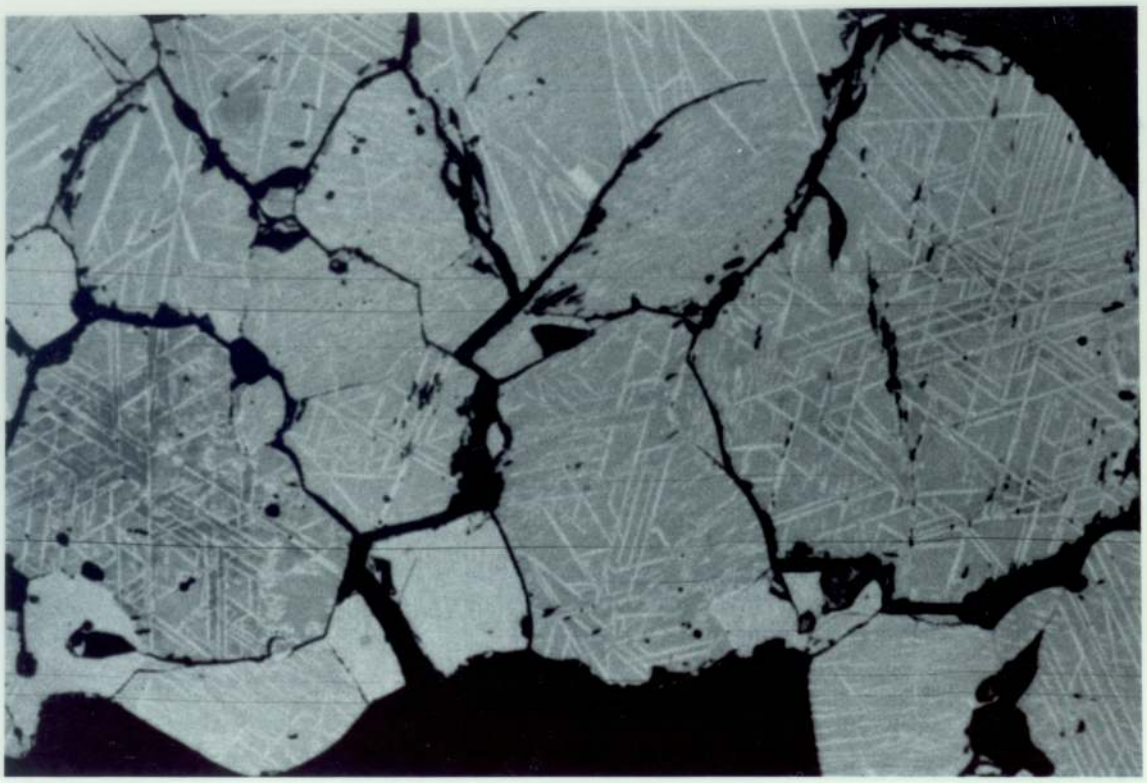

Fig. 3.19d

TABLE 3.1 Details of MSS Samples Synthesised for use in Isothermal Runs

Fe/Ni	M/S	S	Ni	Fe	Wt% At%	Synthesis and Time	Temp (days)	Time at 600°C(days)	Sample Numbers	Grain Size(μm)	Remarks
24	0.965	37.26	2.62	60.12		900°C	26	18	PNX65	30-80	tr.Fa
		50.90	1.95	47.15							
24	0.982	36.84	2.64	60.52		900°C	26	18	PNX66	30-80	tr.Fa
		50.45	1.97	47.58							
24	1.000	36.42	2.68	60.90		900°C	24	20	PNX48	50-100	
		50.00	2.00	48.00		900°C	26	18	PNX67	20-50	
10	0.934	37.96	5.90	56.14		900°C	24	20	PNX61	50-100	
		51.71	4.39	43.90							
10	0.949	37.58	5.94	56.48		850°C	20	12	PNX38	30-80	
		51.30	4.43	44.27		900°C	24	20	PNX49	50-100	
10	0.975	36.96	6.00	57.04		900°C	24	20	PNX50	20-50	
		50.64	4.49	44.87		900°C	26	18	PNX69	20-50	tr.Mt
10	1.000	36.36	6.06	57.58		850°C	20	12	PNX24	15-30	
		50.00	4.55	45.45		900°C	26	18	PNX70	100-150	tr.Pn
						850°C	16	-	PNX51	50-100	m.hzs.t.tn
5	0.930	37.96	10.76	51.28		900°C	24	20	PNX62	30-80	
		51.80	8.02	40.18							
5	0.946	37.58	10.84	51.58		900°C	24	20	PNX52	50-100	
		51.40	8.10	40.50		900°C	26	18	PNX71	50-100	tr. Mt
5	0.961	37.20	10.90	51.90		900°C	25	20	PNX15	150-250	
		50.99	8.16	40.85							

TABLE 3.1 cont'd

5	0.966	37.08	10.92	52.00	900°C	24	20	PNX53	50-100	
		50.87	8.18	40.95						
5	0.973	36.90	10.96	52.14	900°C	25	12	PNX16	150-250	tr.Mt*
		50.67	8.22	41.11						
5	0.982	36.70	11.00	52.30	900°C	25	12	PNX17	150-250	tr.Mt*
		50.46	8.26	41.28						
5	0.986	36.60	11.04	52.36	900°C	24	20	PNX54	100-150	tr.Pn
		50.35	8.29	41.35	900°C	26	18	PNX73	80-120	tr.Fa
3	0.930	37.86	16.12	46.02	900°C	24	20	PNX63	50-100	
		51.80	12.05	36.15						
3	0.946	37.48	16.22	46.30	900°C	21	12	PNX19	150-250	tr.Mt
		51.40	12.15	36.45	900°C	24	20	PNX55	50-100	tr.Mt
					900°C	26	18	PNX74	50-100	tr.Fa
3	0.961	37.10	16.30	46.60	900°C	21	12	PNX20	150-250	tr.Mt
		50.99	12.24	36.77						
3	0.966	36.98	16.36	46.66	900°C	24	20	PNX56	50-100	
		50.86	12.29	36.85						
	0.974	36.80	16.40	46.80	900°C	21	12	PNX21	150-250	tr.Mt*
		50.67	12.33	37.00						

TABLE 3.1 cont'd

3	0.986	36.50	16.46	47.04	900°C	24	20	PNX28	200-300	tr.Pn.tr.Fa
		50.35	12.40	37.35	900°C	24	20	PNX57	200-300	tr.Pn
2	0.930	37.76	21.44	40.80	900°C	26	18	PNX64	50-100	tr.Mt.
		51.80	16.06	32.13						
2	0.946	37.38	21.58	41.04	900°C	24	20	PNX58	50-100	
		51.40	16.20	32.40	900°C	26	18	PNX77	50-100	tr.Mt
2	0.966	36.88	21.74	41.38	900°C	24	20	PNX59	50-100	
		50.87	16.37	32.76	900°C	26	18	PNX78	200-300	tr.Mt.
2	0.986	36.40	21.90	41.70	900°C	24	20	PNX60	200-300	tr.Fa tr.Pn
		50.35	16.54	33.11	900°C	26	18	PNX79	200-300	tr.Fa tr.Pn

* Results from 'isothermal checking runs' indicate a shift to compositions slightly more metal rich compared with those weighed out. Comparisons of volume of Pn present indicate PNX16 equivalent in composition to PNX53; PNX17 equivalent to PNX16 (as weighed out) and PNX21 equivalent to PNX56.

TABLE 4.1 A Bibliography of useful Publications on Solid State Phase Transformations

TEXTBOOKS

Chadwick G.A. (1972) Metallography of Phase Transformations
Christian J.W. (1975) The Theory of Transformations in Metals and Alloys
Martin, J.W., and Doherty, R. D. (1976) Stability of Microstructures in Metallic Systems
Porter, D. A., and Easterling, K. E. (1981) Phase Transformations in Metals and Alloys
Putnis, A. and McConnell, J. D. C. (1980) Principles of Mineral Behaviour
Shewmon, P. G., (1969) Transformations in Metals.

REVIEW PAPERS - GENERAL THEORY

Aaronson, H. I. et al. (1974) On Differences between Phase Transformations in Metals and Silicates.
Champness, P.E. and Lorimer G. W. (1976) Exsolution in Silicates.
McConnell, J. D. C. (1971) Electron Optical Study of Phase Transformations.
McConnell, J. D. C. (1976) Microstructures of Minerals as Petrogenetic Indicators.
Yund, R. A. and McCallister, R. H. (1970) Kinetics and Mechanisms of Exsolution.

REVIEW PAPERS - DIFFUSION

Birchenhall, C. E. (1961) Mechanisms of Diffusion in Solids.
Birchenhall, C. E. (1973) Diffusion in Oxides and Sulphides.
Birchenhall, C. E. (1974) Diffusion in Sulphides.
Gjostein, N. A. (1973) Short Circuit Diffusion.
Gleiter, H. and Chalmers, B. (1972) Grain Boundary Diffusion.
Manning J. R. (1973) Theory of Diffusion.

Mechanisms and rates of Diffusion in Specific Systems

Condit, R. H. et al. (1974) Self Diffusion of Fe and S in Ferrous Sulphide.
Hobbins, R. R. (1970) Self Diffusion of Fe in Single Crystals of Ferrous Sulphide and Magnetically Saturated Fe.
Klotsmann, S. M. et al. (1963) Temperature dependence of the anisotropy of Ni and S self diffusion in Ni-MSS.

REVIEW PAPERS - NUCLEATION AND GROWTH MECHANISMS

Aaron, H. B. et al. (1970) Diffusion Limited Phase Transformations.
Aaron, H. B. and Kotler, G. R. (1971) Second Phase Dissolution.
Aaronson, H. I. et al. (1971) Origin of Microstructures from Precipitation.
Aaronson, H. I. et al. (1970) Mechanisms of Diffusional Growth of Precipitate crystals.
Hinz, W. (1977) Nucleation and crystal growth.
Nicholson, R. B. (1970) Nucleation at Imperfections.
Polmear, I. J. (1966) Nucleation from Supersaturated Solid Solutions.
Russell, K. C. (1970) Nucleation in Solids.
Uhlmann, D. R. (1977) Glass Formation.

TABLE 4.1 Continued...

REVIEW PAPERS - SPINODAL DECOMPOSITION

Cahn, J. W. (1968) Spinodal Decomposition.
Hilliard J. E. (1970) Spinodal Decomposition.

Mechanisms of Coarsening

Greenwood, C.W. (1969) Particle Coarsening.

Mechanisms of Exsolution (and ordering) in Specific Systems

Carpenter, M. A. (1980) Mechanisms of exsolution in Sodic Pyroxenes.
Champness, P. E. and Lorimer G. W. (1973) Precipitation in an Orthopyroxene.
Goldstein, J. I. and Ogilvie, R. E. (1965) The growth of the Widmanstätten Pattern in Metallic Meteorites.
Grange, R. A. and Keifer, J. M. (1941) Transformation of austentite on Continuous Cooling and its Relation to Transformation at Constant Temperature.
Putnis, A. (1974) Electron Optical Observations of the α Transformation in Troilite.
Putnis, A. (1977) Electron Microscope study of Phase Transformations in Cubanite.
Putnis, A. (1978) Talnahkite and Mooihoekite: the Accessibility of Ordered Structures in the Metal-rich Region round Chalcopyrite.
Yund, R. A. and Hall, H. T. (1970) Kinetics and mechanisms of Pyrite Exsolution from Pyrrhotite.

TABLE 4.2 Summary of the stages of evolution in each Pentlandite Textural Type.

CELL

C1 → C2 → C3 → C4
C4 → C5 → C6 → C7

RIM/GRANULAR BLOCKY

B1f
B2f → B3f → GB1
R1f → R2f
R3f
R4f
R1m → R2m→R3m→R4m
R5m
R6m
R1n → R2n → R3n→R4n
R5n
R6n

BLADED

BL1 → BL2 → BL3
BL4 → BL5 → BL6 → BL7
BL8→→→→→ BL9 → BL10
BL11

LENSOIDAL PARTICLES (LAMELLAE)

Lenticular clustered
LL1 → LL2 → LL3 → LL4
Lenticular seriate
LS1 → LS2 → LS3→ LS4
Wiry seriate
WS1 → WS2 → WS3 → WS4→ WS5→ WS6
Wiry pervasive
WP1 → WP2 → WP3 → WP4 → WP5→ WP6

CELL

M/S wrt solvus	C1	C2	C3	C4
LOW	Few, minute hem. caps or rect blebs present at sub-grn bound.	Growth of blebs. Some remain discrete, others impinge to form coarser aggregates	Overgrowth of impinged blebs to form annular lenses with smooth entire bounds to 'host' grn. Further increase in dimensions of discrete blebs.	Some adjacent annular lenses make contact to form discon. cellular rims. Discrete blebs become relatively coarse through further growth.
	C5	C6	C7	C8
INTERMED	Moderate numbers of rect blebs hem. caps more evenly dispersed along sub-grn bound. Invariably hem. caps in basal MSS 'host' grns. Blades may be present at portions of bound orientated at high angles to basal plane.	Increase in the number of particles and their dimensions results in impingement of adjacent particles. Cell boundary with host grain irregular, deeply indented.	Overgrowth of impinged particles results in cellular rims which envelop the sub-grn Bounds of individual cells with 'host' grn vary from lobate to crenulate, to serrated where bladed extensions parallel to basal MSS planes. Invariably lobate where host grn basal section.	Cell widens through continued growth. Interlinking between cells round directly adjacent sub-grns. Minor: almos complete conversion of some sub-grns present within host grns to rounded bodies of Pn.

TABLE 4.2 Continued...

M/S ratio wrt solvus					
		GRANULAR BLOCKY/INTERSTITIAL			
Very low	B1f Few minutes irregularly spaced hem. caps at low proportion of the grain boundaries available	B2f Increase in dimensions of caps, slight increase in numbers	B3f Marked increase in dimensions of individual caps results in impingement of a proportion of those closer spaced	GB1 Overgrowth of impinged blebs to form coarser blocky aggregates. Bounds with adjacent MSS grns lobated indented	GB2 Continued growth of blocky aggregates into the adjacent MSS grn. Tendency for indentations to become infilled resulting in smooth bound.
		RIM			
Low	B1f	B2f	R1f Increase in number of caps present at individual grn. bounds. Decreases distance between adjacent caps.	R2f Impingement and overgrowth of adjacent caps to form (i) discon. rims with crenulate bounds. (ii) lens-like aggregates elongate along the grn. bound, smoother contact with adjacent MSS grn. (iii) Minor proportion of con. Rims.	R3f Increase in width of discon. rims and lenses. Bounds. with adjacent MSS grns. become smooth and entire. Little increase in proportion of con. to discon. rims. R4f Overgrowth of the segments of discon. rims at individual grn. bounds results in an increase in the proportion of con. to discon. rims. Marked incraese in width accompanied by development smooth entire bounds.

TABLE4.2 Continued...

M/S ratio wrt solvus	RIM				
	R1m	R2m	R3m	R4m	R6m
Low to Intermed.	Moderate numbers of small irregularly spaced hem caps at individual grn. bounds. Moderate proportion of grn. bounds. available occupied.	Increase in number of caps present and decrease in spacing at individual grn. bounds. Increased proportion of grn bounds. occupied	Impingement and overgrowth of adjacent blebs to form discon. rims with lobate bounds.	Continued growth of rims into adjacent MSS grns, increase in width. Infilling of indentations, crenulate bounds.	Continued growth results in increase in width individual rims. Proportion of rims preferential growth of portions of the rim results in deeply embayed lobate bounds.
			R3m/n		R5m/n
	Increase in prop. of rect blebs to hem caps apart from the grn bounds of basal MSS grains		Discon. rims with smoother undulate bounds.	I - interlinking of rims along adjacent grn bounds to form discon. networks. bl - bladed extensions to rims where aligned at high angles to basal planes adjacent MSS grains	Continued growth, increase in width, development of entire undulate to linear bounds. Mirror: substantial coarsening of rims along short grain bounds to granular blocky; where adjacent grn small may result in conversion to granular interstitial
	R1n	R2n	R3n	R4n	R5n
	Numerous more regularly spaced rect. blebs at individual grn bounds. High proportion of grn bounds available occupied	Increase in number of blebs increase in dimensions of blebs. Very close regular spacing	Impingement and overgrowth of adjacent blebs to form discon rims with crenulate bounds.	Increase in width of con rims, infilling of indentations development crenulate bounds with small v-shaped indentations	Continued growth, increase in width. Proportion of rims preferential growth results in deeply embayed crenulate bounds.

Confined increase in the M/S ratio w.r.t. solvus results in a decrease in the proportion of rims formed as lamellar types of Pn increase in abundance.

TABLE 4.2 Continued...

M/S ratio	BLADED FORMS			
	Located at MSS grn bounds. Form dependent on angle at which MSS grn sectioned to basal MSS plane (degree of anisotropy). High/mod. anisotropy - linear blades narrow progressively from base to apex, linear entire margins or sinuous plates same width along most of their length, sinuous margins taper rapidly at apex to cuspidate terminations → weak anisotropy blades/plates become progressively wider. Basal (isotropic) sections blebs (hem. caps). Blades elongate subparallel to basal MSS plane.			
		BL1	BL2	BL3
LOW M/S		Single or few linear blades at individual grn bounds. Low proportion of grn bounds available occupied. Basal grns single or few hem. caps at grn bounds.	Marked increase in dimensions of blades (and blebs). Slight increase in the number of grn bounds occupied.	Continued growth in dimensions. High/mod. anis. grns: margins of blades become more sinuous and ragged. Weak anis. grns: coarse tubby blades with lobate margins. Basal grns: coarse blebs with lobate margins.
	BL4	BL5	BL6	BL7
LOW to INTERMED	Linear blades irregularly distributed in mod. numbers at individual grn bounds. Mod. proportion of grn bounds occupied. Basal grns: clusters of discrete blebs (hem. caps) at grn bounds, wide irregular spacing between clusters.	Blades become more elongate. Distance between adjacent blades decreases as the number of blades present at individual grn bounds increases. Basal sections increase in dimensions individual blebs results in impingement within clusters → hem. rosettes, deeply embayed lobate margins. Linear blades formed at fractures within grns, finer and closer spaced than blades at grn bounds (BLf).	Continued growth. Margins of blades become more sinuous. Increase in dimensions of blades results in impingement of a proportion of directly adjacent blades → formation of flame-type blades, with ragged or serrated margins. Overgrowth blebs → elongate hem. rosettes with lobate margins.	Smaller increase in dimensions of blades. Continued impingement adjacent blades/blebs → increase in proportion of flame-type blades and in basal sections rosettes. Blades at fractures: have increased in dimensions; minor impingement; majority retain their linear form.
	as M/S ratio further increases proportion of sinuous plates to linear blades initially present increases.			
	BL8	BL9	BL10	BL11
INTERMED TO HIGH	Numerous closely spaced blades/plates at individual grn bounds. High proportion of sinuous plates to linear blades. High proportion of grn bounds available occupied. Basal sections clusters of impinged blebs.	Increase in dimensions. Increase in proportion of sinuous plates. Majority of linear blades present have developed sinuous margins. High proportion of impingement of adjacent blades/plates to form flame-type blades. Basal - rosettes. Fine closely spaced blades at fractures.	Increase in proportion and dimensions of flames and rosettes. Impingement of blades at fractures → flame-type blades, or where complete overgrowth of adjacent blades → rims along fractures.	Only numerous closely spaced plates present. High degree of impingement → flame-type blades, rosettes.

TABLE 4.2 Continued...

M/S RATIO

LENSOIDAL PARTICLES (LAMELLAE) Particle habit: attenuated oblate spheroids or thin discs elongate subparallel to basal MSS plane.

1. LENTICULAR FORMS clustered irregular distribution within MSS grns. High anisotropy grns; short lenticular lamellae. Wider lamellae in weakly anisotropic grns. Blebs or clusters of blebs in basal grns. Numbers present in individual grns vary from few (f) to moderate (m) to numerous (n) both with increasing M/S ratio, wrt solvus and decreasing initial Fe/Ni ratio.

	LL1	LL2	LL3	LL4
INTERMED	fine lenses irregularly distributed in grns cut oblique to basal plane. Basal sections irregularly distributed clusters of blebs.	Increase in length and width of lenses and diameter of blebs. → initiation of particle coarsening perpendicular to their elongation. Significant proportion of lenses sigmoidal or sinuous in shape. Impingement of adjacent blebs in clusters initiated.	Growth of sigmoidal, sinuous lenses principally perpendicular to their direction of elongation results in formation of lenticular blebs. Adjacent lenticular blebs begin to impinge forming flame-type aggregates. Overgrowth of blebs to form rosettes with embayed lobate margins.	Continued growth of particles perpendicular to direction of elongation. Majority of lamellae either sinuous lenses or lenticular blebs. Increase in width and degree of impingement results in increasing proportion of flame-type aggregates. In a few cases overgrowth of adjacent lenticular blebs results in formation of 'massive' lensoidal bodies. Rosettes increase in dimensions, crenulate to entire margins.

2. FILIAR AND LENTICULAR SERIATE FORMS High anisotropy grains: initially ultrafine thread-like lamellae. Basal sections: minute blebs irregularly distributed. Lamellar distribution seriate - rows of lamellae with irregular interlamellar distances. Development restricted to narrow range of intermed. M/S ratios.

	LS1	LS2	LS3	LS4
INTERMED	Ultrafine filiar lamellae irregularly distributed in high to weak anisotropy grns. Basal grns minute blebs irregularly distributed.	Marked increase in numbers of lamellae and blebs in individual grns. Lamellae - seriate distribution relatively wide spacing between rows. Lamellae more sinuous, slightly increased in length, little increase in width. Increase in dimensions numbers of blebs results in impingement adjacent blebs.	Progressive increase in numbers of lamellae/blebs. Coarsening of a proportion of particles perpendicular to their elongation direction → development one or two small hem. caps on margins individual lamellae → increase in width, loss of filiar form → lenticular blebs → decreased in interlamellar spacing. Overgrowth blebs → irregularly distributed rosettes.	Progressive increase in number of lamellae. With hem. cap protrusions and progressive increase in size of hem. caps → decrease in proportion of filiar lamellae to lenticular blebs. Decreased interlamellar spacings. Increase in diameter of rosettes and more regular distribution.

4. WIRY FORMS

Developed at high M/S ratios wrt solvus. Particle habit: extremely attenuated oblate spheroids elongate parallel to the basal plane with 'corrugated' upper and lower surfaces. Particle forms: High anis. grns: wiry lamellae elongate sinuous lamellae with numerous hem. cap protrusions at right angles to direction of elongation. Lamellar width, spacings and size of protrusions progressively increase, as MSS grns sectioned progressively closer to basal plane. In weakly anisotropic grns elongate coarser in width 'dendrites', protrusions more spheroidal. In basal grns, clusters of blebs or elongate rosettes.

Lamellae seriate distribution, rosettes more evenly dispersed throughout basal grns. Initially, interlamellar spacings relatively large and irregular, lamellae, dendrites and rosettes relatively coarse - WIRY SERIATE FORMS. With increase in M/S ratio, particle size decreases, numbers of particles increase and more regularly and closely spaced - WIRY PERVASIVE FORMS. Apart from these differences wiry seriate and wiry pervasive forms develop in similar manner with time.

W1	WS2/WP2	WS3/WP3
Ultrafine thread-like filiar lamellae irregularly distributed in large Nos. Weakly anis grns lamellae slightly wider with more crenulate margins. Basal grns: numerous minute blebs irregularly dispersed.	Marked increase in Nos of lamellae/blebs present. Lamellae - seriate distrib slight increase in width greater increase in length, more sinuous in form. Increase in size blebs → impingement adjacent blebs.	Progressive increase in numbers of lamellae and blebs. Initiation of development of hem. caps on margins lamellae accompanied by marked increase in width. Spheroidal protrusions lamellae weakly anis.grns → dendrites. Progressive impingement and overgrowth blebs → rosettes.

WS4/WP4	WS5/WP5	WS6
Slight increase in number of particles. Continued coarsening of particles perp. to their elongation direction→progressive increase in size hem. caps protrusions on lamellae and spheroidal blebs on dendrites → progressive increase in width and decrease in spacing. No filiar lamellae now present. Increase in dimensions of rosettes.	Increase in size hem. caps, spheroidal blebs → increase in width lamellae dendrites → slight decrease in interlamellar spacing. Increase in size of rosettes.	Very minor local impingement between lamellae in adjacent rows → development minute clots. Otherwise little increase in dimensions particles.

AT ANY STAGE between W1 and W4 wiry seriate distribution may develop into wiry pervasive if sufficient increase in the number of particles present.

TABLE 4.3 Variation in the textural types observed for each MSS composition with annealing temperature and their development with time.

TABLE 4.3 (a) Fe/Ni = 24

TEMP.	SAMPLE NUMBER	20 MINS	1 HOUR	10 HOURS	TIME 100 HOURS	310 HOURS	1000/2664 HRS
			M/S = 1.000 (50.00 atl%S) Tc ~ 475°C±25°C				
500°C	48	N.D.	N.D.	N.D.	N.D.		
400°C	48		R2m BL5	R2m/3m BL5 (BLf) LL1m	R3m/4m BL6 (BLf) LL2m	R4m BL6/7 (BLf) LL3m/4m	R5m BL7 (BLf) LL4m
[350°C	48	100 hr]	R4m>BL6>LL3m				
300°C	48	2-3% LS1 R1m BL4	3-6% LS2 R1m BL4 (BLf)	5-10% LS2/3 R3m BL5 (BLf)	5-10% LS3 R3m/4m BL6 (BLf)	10-15% LS4 R4m BL7 (BLf)	15-20% LS4 R4m/5m BL7 (BLf)
[250°C	67	100 hr]	5-10% WS3>BL8>R3m				
200°C	48	N.D.	<1% BL8 R1m/f	2-5% W1/WP2 BL8 R2m/f	5-10% WP3 BL9 R3m/f	15-20% WP3 BL9 R3m/4m/f	25-30% WP3 BL9 R4m/f
			M/S = 0.982 (50.45 at % S) Tc ~ 350°C±20°C				
[350°C	66	100 hr]	N.D.				
300°C		0.5% B1f	~ 1% B2f BL1	1-3% B2f/B3f BL2	2-5% R2f/R4f BL2/5 GB1 GI	3-5% R4f BL2/5 GB2 GI	5%+ R4f BL2/5 GB2 GI
[250°C	66	100 hr]	2-5% R2f>BL5>LL2f				
200°C	66	N.D.	0.5% B1f C1	2-5% BL4 R2f C3	5-10% BL5 R2f C4	10-15% BL5/6 R2f/R4f	21%+ BL6 R4f C4
			M/S = 0.965 (50.9 at %S) Tc ~ 310°C±10°C				
[350°C	65	100 hr]	N.D.				
300°C	65	N.D.	N.D.	N.D.	N.D.	<0.5% B1f	3%+ GB2 R3f GI
[250°C	65	100 hr]	1-2% B2f>BL1> GB1				
200°C	65	N.D.	<0.5% B1f C1	1% B1f C1	2-5% B2f/R2f BL2 C2 LL1/2 v.f.	4-8% R2f BL2/5 (BLf) C3 LL2 v.f.	10%+ BL5 BLf R2f/3f C4 LL3 v.f.

For each of the individual isothermal runs the following data are listed:

1) The approximate volume of pentlandite exsolved. Estimated from enlarged photomicrographs of representative grain aggregates by computer controlled image analysis*, by point counting+; the rest are based on comparisons with known volumes from the first two methods.

2) The pentlandite textural types observed and their stage of development (see Table 4.2). Listed in order of decreasing abundance. × indicates development restricted. N.D. no visible pentlandite observed at ~ × 1000 magnification.

TABLE 4.3b (continued) Fe/Ni = 10

TEMP.	SAMPLE NUMBER	20 MINS	1 HOUR	10 HOURS	TIME 100 HOURS	310 HOURS	1000/2664 HRS
				M/S = 1.000 (50.00 at%S) Tc ~ 550°C±30°C			
500°C	70	LS1	LS1 B2f	LS2 B3f	WS2 GB2 R1f		
400°C	70		WS2	WS3	WS3	WS4	WS5
[350°C	70	100 hr]	WS3				
300°C	70	WP3	WP3 PA	WP4 PA	WP5 PA	WP5 PA	WP5/6 PA
[250°C	70	100 hr	WP4 ≫PA]				
200°C	70	N.D.	W1	WP2 PA	WP3/4 PA	WP4 PA	WP5 PA
				M/S = 0.975 (50.64 at%S) Tc ~ 450°C±25°C			
400°C	50		R1m C5	R2m BL1 C6	R2m/3m BL1/2 C7/8	R4m/3m BL2/3 C8	R4m BL3 C8
[350°C	69	100 hr]	R4m>BL4>C7				
300°C	50	5-10% R4n LL2n BL5 (BLf) C7	5-10% R4n LL3n BL5 (BLf) C8	10-15% R5nI LL3n BL6 (BLf) C8	15-20% R5nI LL4n BL6 (BLf) C8 (G.I.)	15-20% R5nI LL4n BL7 (BLf) C8 (G.I.)	21%+ R5n/6nI LL4n BL7 (BLf) C8 (G.I.)
[250°C	69	100 hr]	15-20% WS3>R4n>BL9				
200°C	50	1-2% C5 R1n	2-5% W1 R1n BL8 C6	10-15% WS3 R3n BL8 C7/8 PA	25-30% WP4 R4nI BL9 C8 PA	30-35% WP5 R5nI BL10 C8 PA	30-35% WP5 R5nI BL10 C8 PA
				M/S = 0.949 (51.3 at %S) Tc ~ 350°C±20°C			
400°C	49	N.D.	N.D.	N.D.	N.D.	N.D.	N.D.
[350°C	49	100 hr]	N.D.				
300°C	49	N.D.	1-2% R1m	8%+ R2m/3m BL4/5 BLf	5-10% R3m/4m BL5 BLf	10-15% R4m/5m BL6 BLf C.B.1	13%+ R5m/4m BL6 BLf C.B.1
[350°C	49	100hr]	5-10% R4m > BL6 > LL2m				
200°C	49	N.D.	1% BLf/R1m	1-3% R1m BLf W1	17%+ WS3 R3m BL6 (BLf) PA	15-20% WS4 R4m BL6 (BLf) PA	21%+ WS4/5 R4m/5m BL6 (BLf) PA
				M/S = 0.934 (51.7 at%S) Tc ~ 260°C±20°C			
300°C	61	N.D.	N.D.	N.D.	N.D.	N.D.	N.D.
[250°C	61	100hr]	1-2% B2f/R1f				
200°C	61	N.D.	N.D.	<1% C5 R1m	308% R3m C6 BL5 (BLf) LL2 v.f.	5-10% R4m/3m C7 BL6(BLf) LL3 v.f.	9%+ R4m/5m(b1) C8 BL6 (BLf) LL3 v.f.

TABLE 4.3c (continued) Fe/Ni = 5

TEMP.	SAMPLE NUMBER	20 MIN	1 HOUR	10 HOURS	100 HOURS	TIME 316 HOURS	1000/2664 HRS
			M/S = 0.986 (50.35 at%S) Tc ~ 600°C±10°C				
500°C	73	WS2 B1f	WS2 B2f	WS3 GB1 R2f	WS3/4 GB2 R2f		
400°C	73		WS3 (PA)	WS4 (PA)	WS4/5 (PA)	WS5 (PA)	WS5 (PA)
[350°C	54	100 hrs]	WP4 (PA)				
300°C	54	WP3/4	WP4 (PA)	WP5 (PA)	WP5 (PA)	WP5 (PA)	WP6 (PA)
[250°C	54	100 hrs]	WP4 PA				
200°C	54	WP2	WP3	WP4/5	WP5	WP5	WP5
			M/S = 0.973 (50.67 at %S)				
400°C	17		R2n BL4	2.90*0.44 R3n/4n BL5 (BLf)	4.77%*0.72 R4n BL6 (BLf) LL1f	R5n BL7 (BLf) LL2f	6.57%*1.00 R5n/6n BL7 (BLf)(Rf) G.B.
			M/S = 0.966 (50.87 at %S) Tc ~ 450°C±20°C				
400°C	17		R2n BL4	2.90* 0.44 R3n/4n BL5 (BLf)	4.77%* 0.72 R4n BL6 (BLf) LL1f	R5n BL7 (BLf) LL2f	6.57%* 1.00 R5n/6n BL7 (BLf)(Rf) G.B.
			M/S = 0.966 (50.87 at %S) Tc ~ 450°C±20°C				
400°C	16		B2f/R1m	1.02%* 0.29 R1m	1.74% 0.50 R2m GB1 BL1	R3m GB2 BL1/2	3.50%* 1.00 R3m/4m GB2 BL2
[350°C	53	100 hr]	R5m > LL3m > BL6/7 > (BLf) C8				
300°C	53	10-15% WS3 R3n BL8	15-20% WS3 R4n BL8 (PA)	20-25% WS4 R4n/5n BL9 PA	30-35% WS5 R4n/5n BL10 PA	30-35% WS5 R5n BL10 PA	39%+ WS6 R5n BL10 PA
[250°C	53	100 hr]	30-35% WP3 > BL9 > R4m > PE				
200°C	53	2-5% W1 R2m	5-10% W1 BL8 R3m	15-20% WP2/3 PE BL9 R4m	30-35% WP3 PE BL10 R5m	40-45% WP5 PE BL10 R5m	47%+ WP5 PE BL10 R5m
			M/S = 0.961 (50.99 at%S)				
400°C	15	N.D.	N.D.	N.D.	N.D.	B2f	GB1 R2f
			M/S = 0.946 (51.4 at %S) Tc ~ 390°C ±20°C				
[350°C	71	100 hr]	5-10% R4m > BL6 > (BLf) > GB1 > C7				
300°C	52	10%+ R3n BL5 (BLf) C7	13%+ R3n/4n BL6 (BLf) C7 LL2f	15%+ R4n BL7 (BLf) C8 LL2f/3f	17%+ R5n BL7 (BLf) C8 LL4f	15-20% R5n BL7 (BLf) C8 LL4f	20%+ R5nI BL7 (BLf)(Rf) C8 LL4f
[250°C	52	100 hr]	R3/4m > BL6 > LL3m > C8				
200°C	52	N.D.	2-5% R2m/3m C6 BL8 W1	15-20% WS2/3 BL9 R4m C7 PE	25-30% WS3/4 PE tt 20 BL10 R5m C8	30-35% WS4 PE tt BL10 R5m C8	42%+ WS5 PE tt 15 BL10 R5m C8
			M/S = 0.930 (51.8 at%S Tc ~ 310°C ± 20°C				
[350°C	62	100 hr]	N.D.				
300°C	62	N.D.	N.D.	N.D.	0.5% B1f	1-3% B2f R2f GB1 (GI)	5%+ GB2 R2f GI
[250°C	62	100 hrs]	5-10% R3m > BL4 > GB1 > C8				
200°C		N.D.	1% C5 R1m	1-3% C6 R3m BL4	10-15% R4m b1 BL6 (BLf) C8 LL2 v.f.	15-20% R5m b1 BL6/7(BLf) C8 LL3 v.f.	18%+ R6m/5m b1 BL7 (BLf) C8 LL3 v.f.

TABLE 4.3d continued. Fe/Ni = 3

TEMP.	SAMPLE NUMBER	20 MINS	1 HOURS	10 HOURS	100 HOURS	TIME 316 HOURS	1000/2664 HRS
			M/S = 0.985 (50.35 at %S) Tc ~ 600°C ±10°C				
500°c	28	WP2/3	WP3 B2f	WP4 GB1	WP4 GB2		
400°C	57		WP3/4	WP4	WP4	WP4/5	WP5
[350°C	28	100 hr]	WP4				
300°C	57	WP3/4	WP4	WP5	WP5	WP5	WP6
[250°C	57	100 hr]	WP4				
200°C	57	WP2	WP3	WP4/5	WP5	WP5	WP5
		M/S = 0.966 (50.85 at %S) Tc ~ 475°C±20°C					(1780 hr)
				2.76% 0.39	4.43%* 0.63		7.00%* 1.00
400°C	21		R2m/3m BL4	R3m/4m BL4	R5m(I) BL5 (BLf) GB1	R5m/6m(I) BL6 (BLf) GB2	R5m/6m(I) BL6 (BLf) GB2 GI
[350°C	56	100 hrs]	LL3n > R5m > PEtt > BL9		(BLf)		
		15-20% WS3	20-25% WS3	25-30% WS4	35-40% WS4/5	40-45% WS5/6	43%+ WS6
300°C	56	PEtt 15 BL9 (BLf) R4n C7	PEtt 15 BL9 (BLf) R4n C7	PEtt 10 BL10 (BLf) R5n C8	PEtt 10 BL10 (BLf) R5n/6n C8	PEtt 10 BL10 (BLf) R5n/6n C8	PEtt 10 BL10 (BLf) R6n/5n C8
[250°C	56	100 hrs]	WP4 > PEtt > BL10 > R5m				
		2-5%	15-20%	25-30%	40-45%	45-50%	50-55%
200°C	56	W1 R4m(f) BL8 C7 PL	WS2/3 PLtt^{x}25 BL9 R5m(f) C8	WP4 PLtt^{x}20 BL10 R5m(f) C8	WP5 PLtt^{x}20 BL10 R5m(f) C8	WP5 PLtt^{x}20 BL10 R5m(f) C8	WP5 PLtt^{x}20 BL10 R5m(f) C8
				M/S = 0.961 (50.99 at%S)		1-2%	
400°C	20	N.D.	N.D.	N.D.	N.D.	B2f/R1f	R2f
			M/S = 0.946 (51.4 at%S) Tc ~ 380°C±20°C				
400°C	19	N.D.	N.D.	N.D.	N.D.	N.D.	N.D.
[350°C	74	100 hrs]	10-15%	R5m > BL6 > (BLf)	LL3m > PL		
		10-15%	12-17%	15-20%	20-25%	20-25%	26%+
300°C	55	R4n LL2n BL5 (BLf) PL C7	R4n LL3n BL5/9(BLf) PL C7	R4n bl LL4n BL9(BLf)(Rf) PLtt 30 C8	R5n/6n LL4n BL9/10(BLf) (Rf)(GB) PLtt 25 C8	R5n/6n (GI) LL4n BL10 (BLf) (Rf)(GB) PLtt 25 C8	R6n/5n LL4n BL10 (BLf) (Rf)(GB) PLtt 25 C8
[250°C	55	100 hrs]	20-25%	PLtt > WS3/4 > BL10 > R4m			
		1-2%	10-15%	34%+	43%+	45-450%	52%+
200°C	55	PLtt 10 W1^{x}	PLtt 6 WS3^{x}	PLtt 6 WS4^{x}	PLtt 4 WS4^{x}	PLtt 4 WS4	PLtt 4 WS4^{x}
			M/S = 0.930 (51.8 at %S) Tc ~ 320±20°C				
[350°C	63	100 hrs]	N.D.				
		0.5%	1-2%	3-5%	5-10%	5-10%	9%+
300°C	63	C1 B1f	C1/2 B2f/R1f	R1f C3 B2f BL1	R2f C4 BL1 B3f/GB1	R2f/3f GB1/2 BL1/2 C4	R3f GB2 BL3 C4
[250°C	63	100 hrs]	5-10%	R4m > BL5 > (BLf)	GB1 > C8		
			0.5%	1-3%	16%+	15-20%	21%+
200°C	63	N.D.	R2m/3m C5 PL	R4m/5m BL5 (BLf) C7 PL	PL R5m bl BL6/7 (BLf) C8	PL R5m bl BL7 (BLf) C8	PL R5m bl BL7 (BLf) C8

Table 4.3e Continued... Fe/Ni 2

TEMP.	SAMPLE NUMBER	20 MINS	1 HOURS	10 HOURS	100 HOURS	TIME 316 HOURS	1000/2664 HRS
				M/S = 0.986 (50.35 at%S) Tc ~600°C ±10°C			
500°C	60	WP3	WP3/4	WP4	WP4		
400°C	60		WP3/4	WP4	WP4/5	WP5	WP5
300°C	60	WP4	WP4	WP5	WP5	WP6	WP6
200°C	60	WP2	WP3	WP4/5	WP5	WP5	WP6
				M/S 0 0.966 (50.87 at%S) Tc ~ 480°C			
400°C	59		R2/3m BL4 LL2m PL C6	R3m BL5 (BLf) LL2m PL C7	R3/4m BL5/6(BLf) LL3m PL C8	R4/5m BL7(BLf) LL3m PL C8	R5m BL7(BLf) LL4m PL C8
[350°C	59	100hr] 20.25% PLtt > WS4 > R5m > BL7 > (G.B.)					
300°C	59	WS2 BL8 R3m PL	WS3 PL BL8 R4m	WS4 PLtt BL9 R4m	WS4/5 PLtt BL10 R4m	WS5 PLtt BL10 R5m	WS5 PLtt BL10 R5m
200°C	59	WS2 PEtt^{x}	WP2 PEtt^{x}	WP3 PEtt^{x}	WP5 PEtt^{x}	WP5 PEtt^{x}	WP5 PEtt^{x}
			M/S = 0.946 (51.4 at%S) Tc ~ 380°C ±20°C				
400°C	58	N.D.	N.D.	N.D.	N.D.	N.D.	N.D.
[350°C	77	100hr]	PLtt > R4m				
300°C	58	R3m BL4 LL2m	PL R4m BL4 LL2m	PLtt R4m BL6 LL3m	PLtt 10 R5m BL7 LL4m	PLtt R5m BL7 LL4m	PLtt 6 R5m BL7 LL4m
200°C	58	PLtt BL5(BLf) W1	PLtt BL5(BLf) W1	PLtt BL6(BLf) WS2^{x}	29%$^{+}$ PLtt BL6(BLf) WS2^{x}	PLtt BL7 WS3^{x}	PLtt BL7 WS3^{x}
			M/S = 0.930 (51.8 at%S) Tc ~ 350°C ±30°C				
[350°C	64	100hr]	PLtt > R4m > BL5(BLf)				
300°C	64	PL R3m BL4(BLf) C7	PL R5m BL5(BLf) C7	16%$^{+}$ PL R5m BL5(BLf) C8	PLtt 20 R5m/6m I BL6(BLf) C8	PLtt R%m/6m BL7(BLf) C8	PLtt 15 R5m/&m BL7 C8
200°C	64	PLtt 10 R2m C7 BL4^{x}	PLtt 6 R3m C8 BL5^{x}	PLtt 4 R4m C8 BL6^{x}	PLtt 4 BL7^{x} R5m b1 C8	PLtt 4 BL7^{x} R5m C8	PLtt 4 BL7^{x} R5m C8

TABLE 4.4 Summary of the basic Pentlandite Textural Types observed in each MSS Composition at different Annealing Temperatures

Fe/Ni 24						Fe/Ni 10						Fe/Ni 5						Fe/Ni 3					Fe/Ni 2				
														TEMPERATURE °C													
M/S	400	350	300	250	200	M/S	400	350	300	250	200	M/S	400	350	300	250	200	400	350	300	250	200	400	350	300	250	200
										Rd	Rc			N.D.	GB		Rc		N.D.	Rd	Rc	PL			PLtt	PLtt	PLtt
						0.934			N.D.		C	0.930			Rd		HL			GB	HL	Rc			Rc	Rc	HL
			GB	Rd	HL						HL				(GI)		C			HL	GB	HL			HL	HL	Rc
0.965		N.D.	Rd	HL	Rd												(LL)			C	C	C				C	C
				Rd	C																						
					(LL)				Rc	Rc	WS			Rc	Rc	Rc	WS		Rc	Rc	PLtt	PLtt		PLtt			PLtt
						0.949	N.D.	N.D.	HL	HL	Rc	0.946	N.D.	HL	HL	HL	PEtt	N.D.	HL	LL	WS	WS	N.D.	Rc			HL
									GB	LL	PA			GB	C	LL	HL		PL	HL	HL						WS
			Rd	Rd	LL									C	LL	C	Rc			PLtt	Rc						
0.982		N.D.	HL	HL	HL												C			C							
			GB	LL	Rd							[0.961	400°C	GB	RD]			[400°C	Rd	GB]							
			GI		C																						
							Rc	Rc	Rc	WS	WP		Rc	Rc	Rc	WP	WP	Rc	LL	WS	WP	WP	Rc	PLtt	PLtt		WP
						0.975	HL	HL	LL	Rc	Rc	0.966	GB	LL	LL	HL	PE	HL	Rc	PEtt	PEtt	PLtt	HL	WS	WS		PLtt
	500						C	C	HL	HL	HL		HL	HL	HL	Rc	HL	GB	PEtt	HL	HL	HL	LL	Rc			
	N.D.	RC	LS	WS	WP				C	C	C			C	C	PE	Rc	GI	HL	Rc	Rc	Rc	PL	(GB)			
1.000		HL	Rc	HL	HL				(GI)			[0.966	400°C	Rc	HL	GB	LL]			C							
		LL	HL	Rc	Rc	500							500°C	400	300	250	200	500	400	300	250	200	500	400	300	250	200
							WS	WS	WS	WP	WP	WP		WS	WS	WP	WP	WP	WP	WP	WP	WP	WP	WP	WP	WP	WP
						1.000	GB			PA	PA	PA	0.986	GB	PA	PA			GB								
							Rd							Rd													

Key : GB – Granular blocky GI – Granular Interstitial Rd – Discontinuous rim Rc – Continuous rim C – Cell HL – Bladed forms PL – Platy lamellae
LL – Lenticular forms LS – Lenticular seriate WS – Wiry seriate forms WP – Wiry Pervasive forms PE – Platy elongate lamellae } tt triangular trellis
PA – Platy acicular lamellae

-51-

Table 4.5 Examples of Variations in the Total Volume of Pentlandite Exsolved with MSS Composition and Annealing Temperature

INITIAL MSS COMPOSITION			TEMP °C	TOT. VOL. OF
Fe/Ni	M/S	SAMPLE		Pn EXSOLVED
24	0.965	PNX65	300	3%
			200	11%
24	0.982	PNX66	300	5%
			200	11%
10	0.934	PNX61	200	9%
10	0.949	PNX49	300	8%
			200	14%
5	0.930	PNX62	300	6%
			200	19%
5	0.946	PNX52	300	19%
			200	42%
5	0.966	PNX16	400	3.5%*
		PNX53	300	39%
		PNX53	200	47%
5	0.973	PNX17	400	6.6%*
3	0.930	PNX63	300	9%
			200	21%
3	0.946	PNX55	300	27%
			200	50%
3	0.966	PNX21	400	7%*
		PNX56	300	43%

* Data from quantitative image anlaysis, accuracy ~ ±0.5 vol%. Other data obtained from point counting of enlarged photographs of representative grain aggregates, accuracy ~ ±10% of volume present.

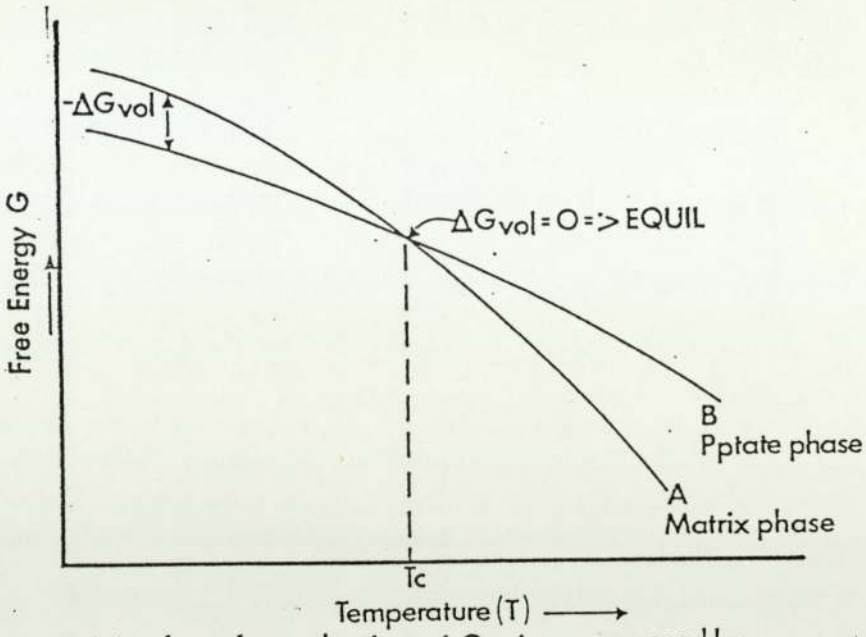

Driving force for nucleation $-\Delta G_{vol}$ opposed by

assisted by

$+\Delta G_{defect}$ -preferential heterogeneous nucleation

$+\Delta G_{strain}$ -lattice match/mismatch A-B

$\pm\Delta G_{surf}$ -morphology pptate particle

Fig. 4.1a SIMPLIFIED FREE ENERGY VS TEMPERATURE CURVES FOR MATRIX PHASE AND PRECIPITATE PHASE OF DIFFERENT STRUCTURES

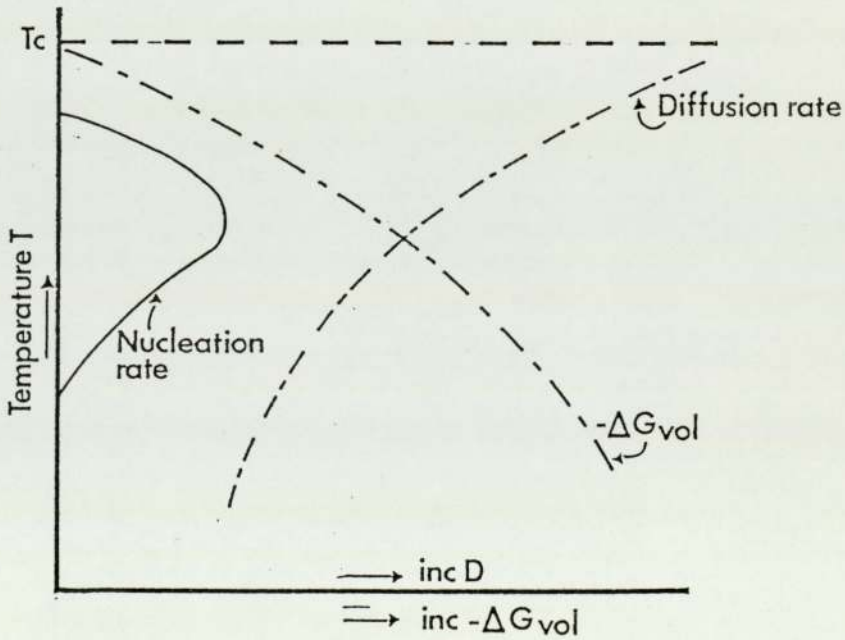

Diffusion rate D- DECREASES exponentially with decreasing temperature

Driving force for nucleation $-\Delta G_{vol}$ INCREASES with decreasing temperature

Fig. 4.1b SCHEMATIC DIAGRAM ILLUSTRATING THE DEPENDANCE OF THE DIFFUSION RATE THE DRIVING FORCE FOR NUCLEATION AND THE NUCLEATION RATE ON TEMPERATURE

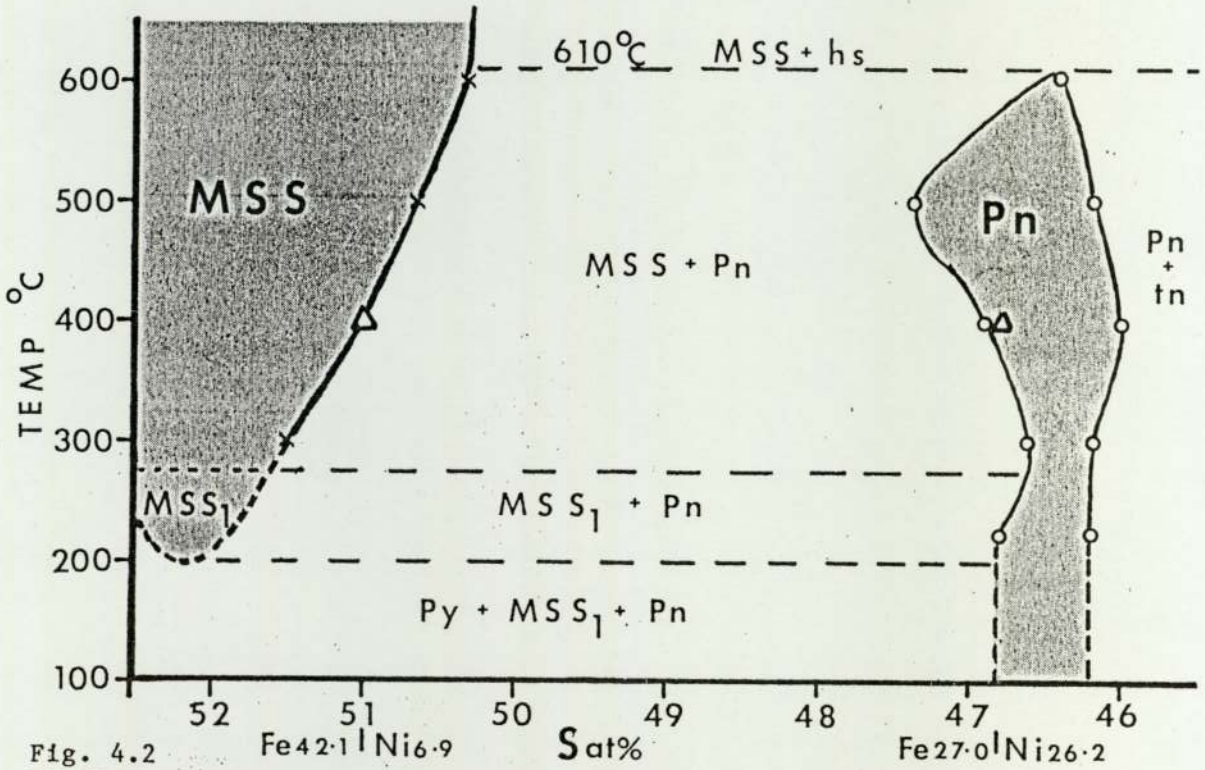

Fig. 4.2 PHASE RELATIONS IN THE CENTRAL PORTION OF THE Fe-Ni-S SYSTEM ALONG A SECTION LINKING MSS $Fe_{42\cdot1}Ni_{6\cdot9}S_{52\cdot0}$ and Pn $Fe_{27\cdot0}Ni_{26\cdot2}S_{46\cdot8}$ (at%)

Fig. 4.3 T-T-T-X diagrams for (a) Fe/Ni 5 (b) Fe/Ni 3 illustrating for each M/S ratio the approximate curves for the initiation of: heterogeneous nucleation -----; nucleation of lensoidal lamellae - - - - -; nucleation of platy lamellae -.-.-.

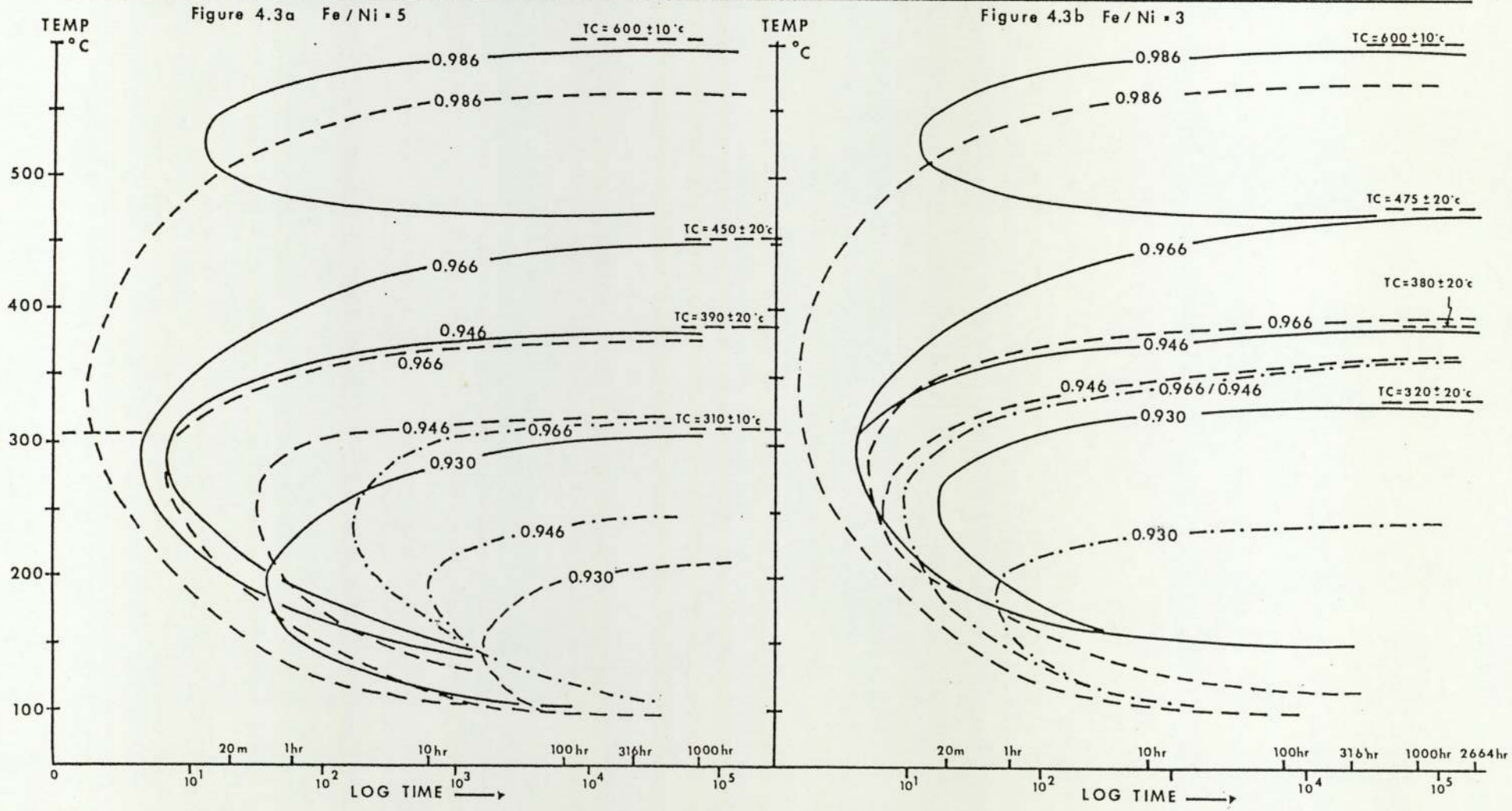

KEY to Figs 4.4 and 4.5

Fig 4.4 T-T-T-X diagrams illustrating the variation in the development of heterogeneously nucleated types.

RIMS

B – initiation of bleb nucleation

.....	discrete blebs	nucl/growth	GRANULAR BLOCKY
▬ ▬ ▬	discon Rims	impingement/ overgrowth	◠ ◠ ◠ ◠ ◠
▬▬▬▬	Con Rims	continued growth	Rc –formation of con Rims

BLADED FORMS

BL–initiation of blade nucleation

— — — —		nucl/growth	
∿ ∿ ∿ ∿	sinuous blades	growth/loss of coherence	
∿ ∿ ∿ ∿	Flame-type blades	growth/ imping.	Fbl – initiation of flames
o o o o o o	Rosettes – basal		
▬ ▬ ▬ ▬	increasing prop of aggreg. forms		

FIG 4.5 LENSOIDAL AND PLATY LAMELLAE

LENTICULAR FORMS LL – initiation of nucleation

— — — —	lenses	nucl./growth
∿ — ∿ —	sigm./sin lenses	growth/loss of coherence
∿ ∿ ∿ ∿	lenticular blebs	growth/ coarsening
o o o o o	rosettes basal	
∿ ∿ ∿ ∿	flame-type lam	growth/ impingement

WIRY FORMS

WS WIRY SERIATE FORMS

initiation of

WP WIRY PERVASIVE FORMS

— — — —	filiar lam	nucl/growth
∿ ∿ ∿ ∿	sin. filiar	nucl/growth
∿ ∾ ∿ ∾	fil./wiry lam dends	growth/loss of coherence/ initiation hem cap prot.
o o o o o	rosettes basal	imping. basal
∾ ∾ ∾ ∾	wiry lam dends	growth/coarsening/ devlp. hem cap prot.
∾.∾.∾.∾	wiry forms minor clots	growth/minor imping. adj rows

PLATY LAMELLAE

PL – initiation of platy lamellae

▲ ▲ ▲ ▲ PL tt PE triangular trellis developed

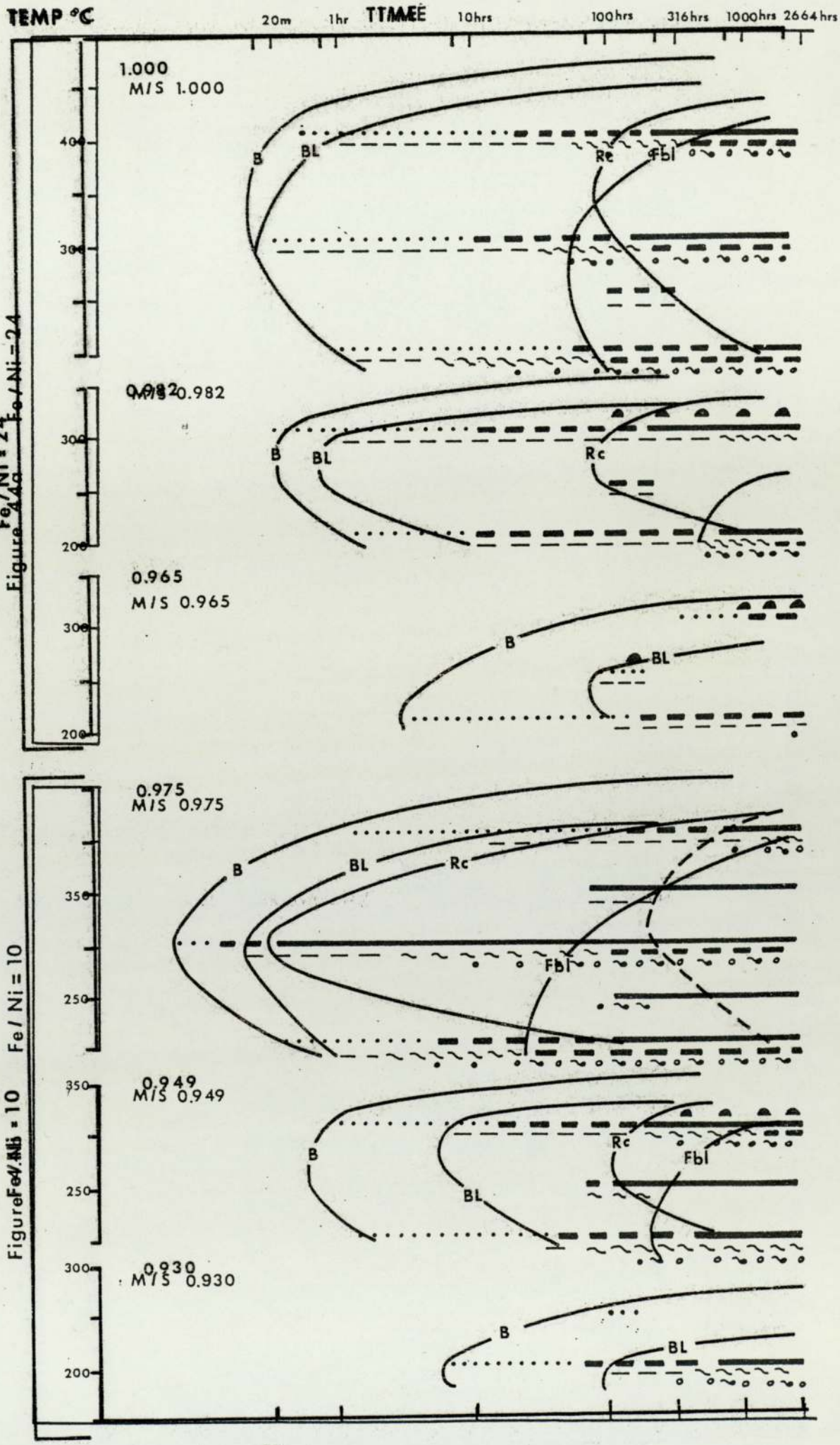

Figure 4.4a Fe/Ni = 24

Figure 4.4b Fe/Ni = 10

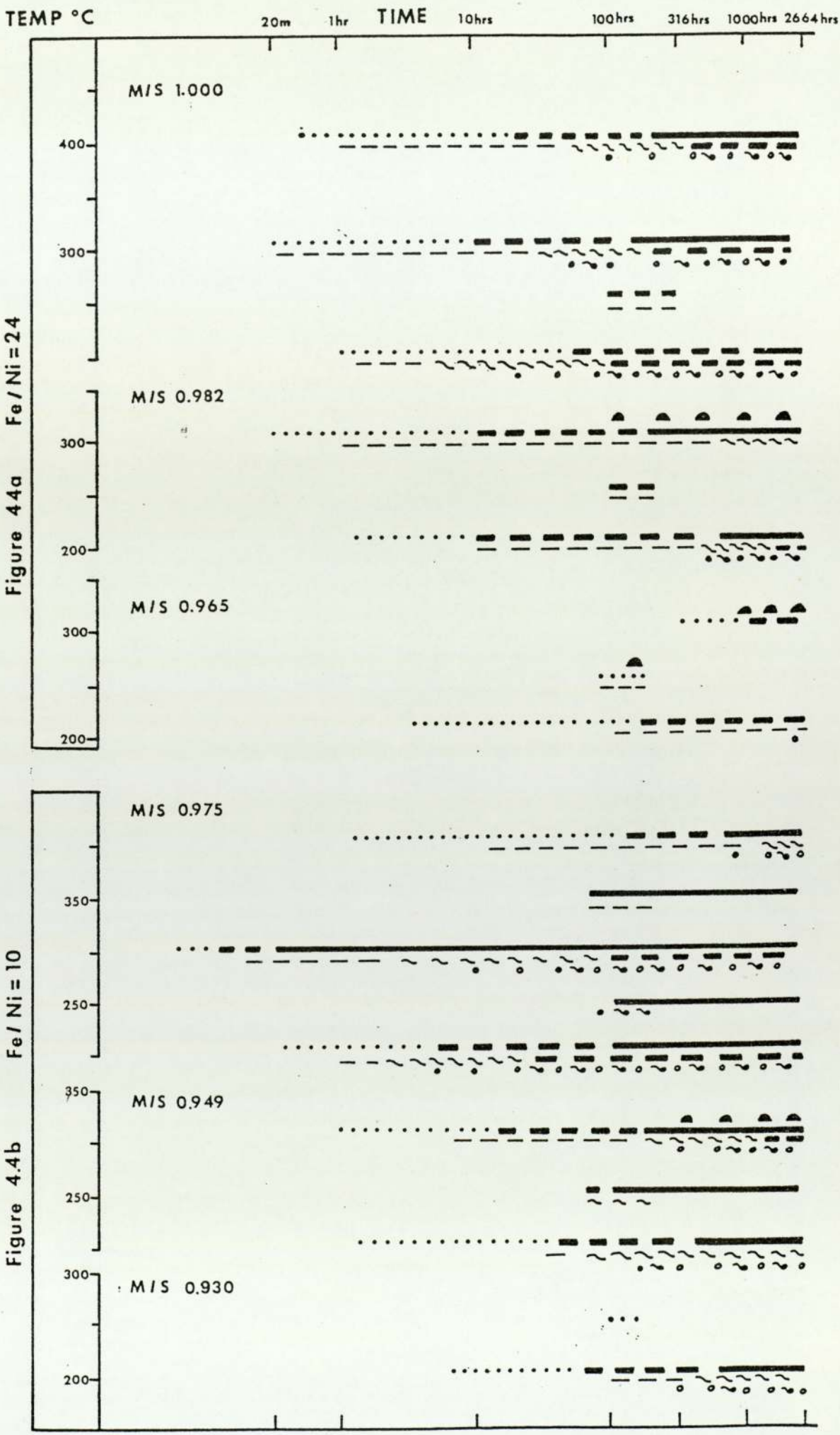
TEMP °C
TIME
20m
1hr
10hrs
100hrs
316hrs
1000hrs
2664hrs
M/S 1.000
400
300
M/S 0.982
300
200
M/S 0.965
300
200
Fe/Ni=24
Figure 44a
M/S 0.975
350
250
M/S 0.949
350
250
M/S 0.930
300
200
Fe/Ni=10
Figure 4.4b

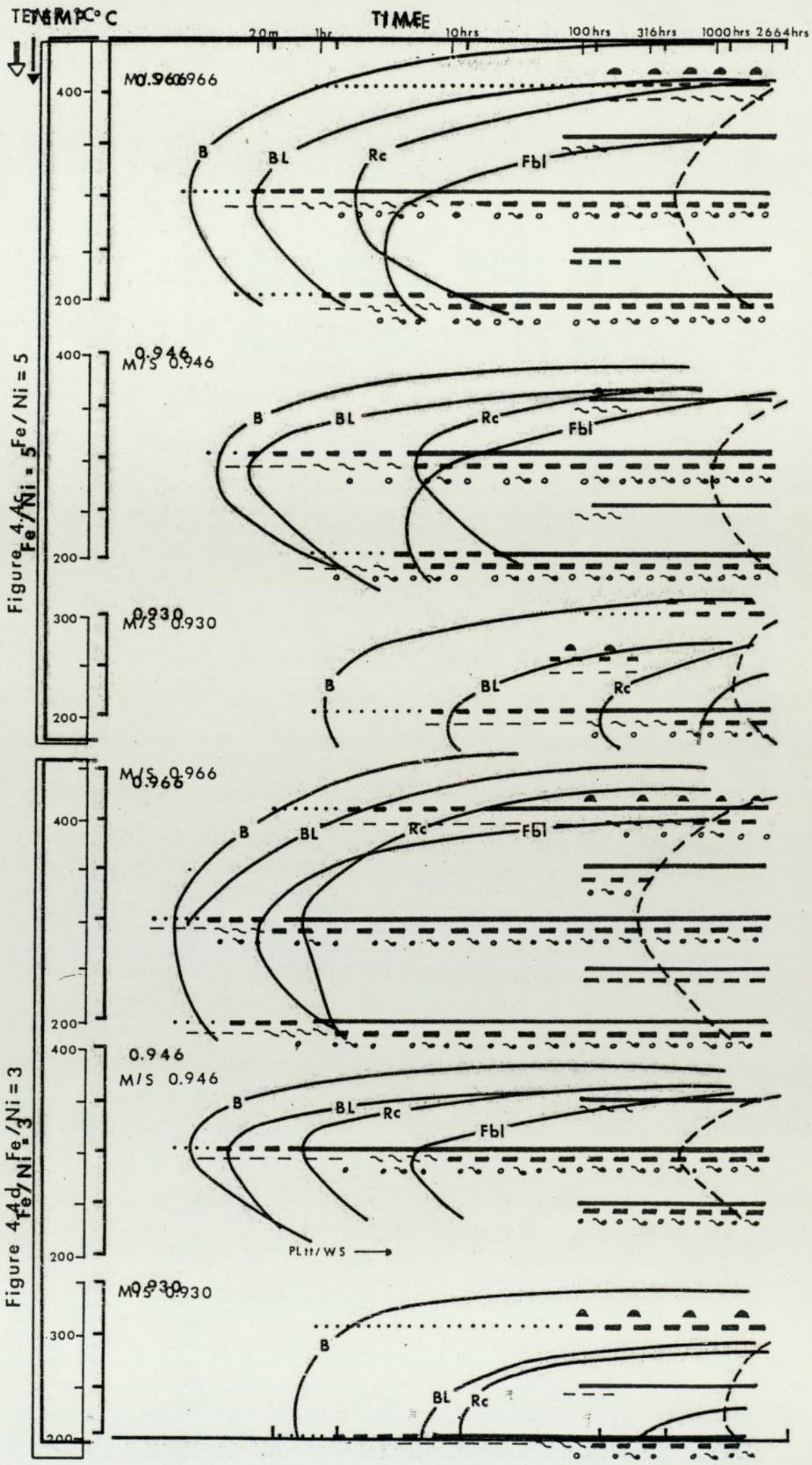

Figure 4.4c Fe/Ni = 5

Figure 4.4d Fe/Ni = 3

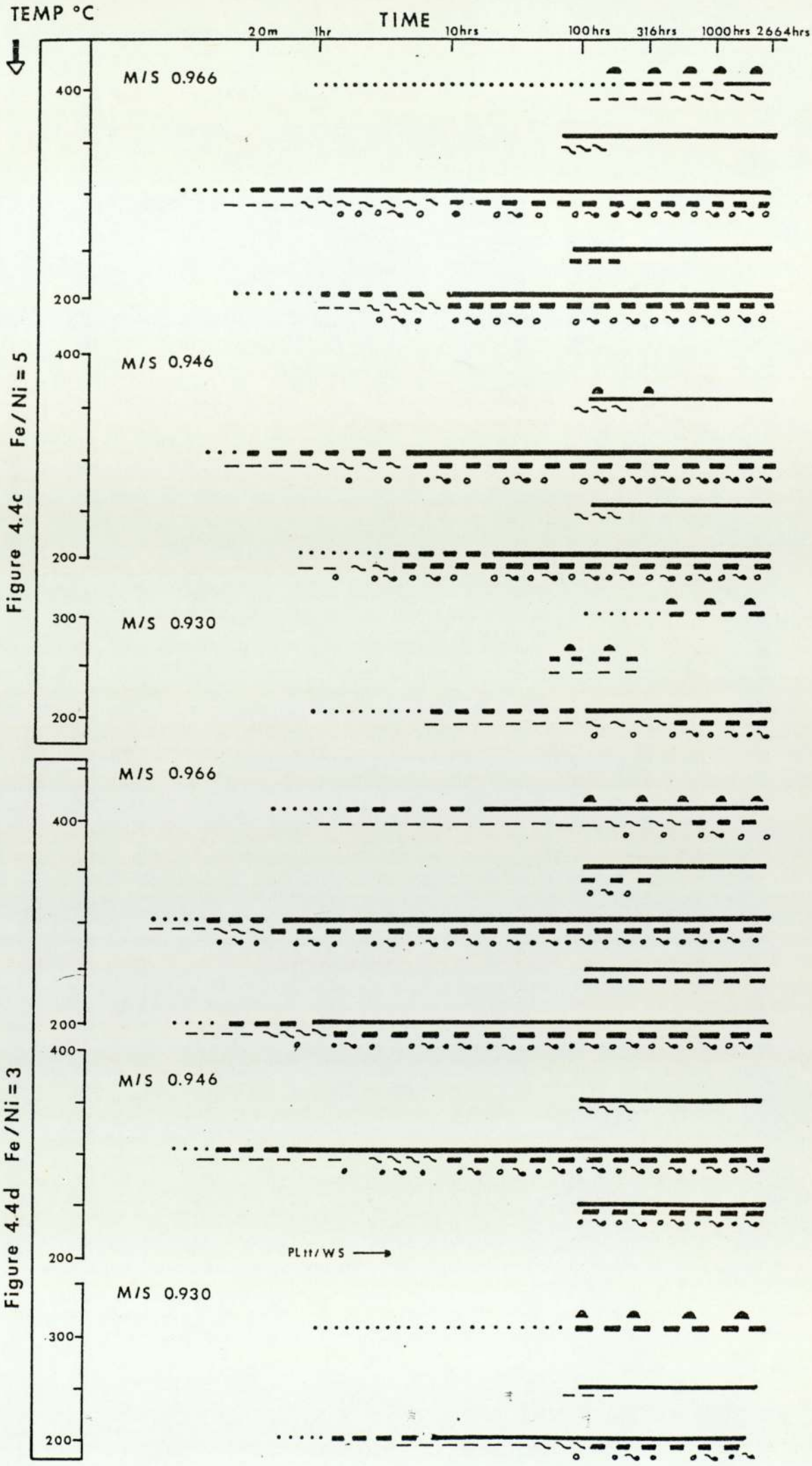
TEMP °C
TIME
20m
1hr
10hrs
100hrs
316hrs
1000hrs
2664hrs
M/S 0.966
M/S 0.946
M/S 0.930
400
200
300
Figure 4.4c Fe/Ni = 5
M/S 0.966
M/S 0.946
M/S 0.930
PLtt/WS
Figure 4.4d Fe/Ni = 3

Figure 4.5 T-T-T-X diagrams illustrating variations in the development of lensoidal and platy lamellar forms.

4.5a MSS compositions of differing M/S ratios with initial Fe/Ni ratio = 10.

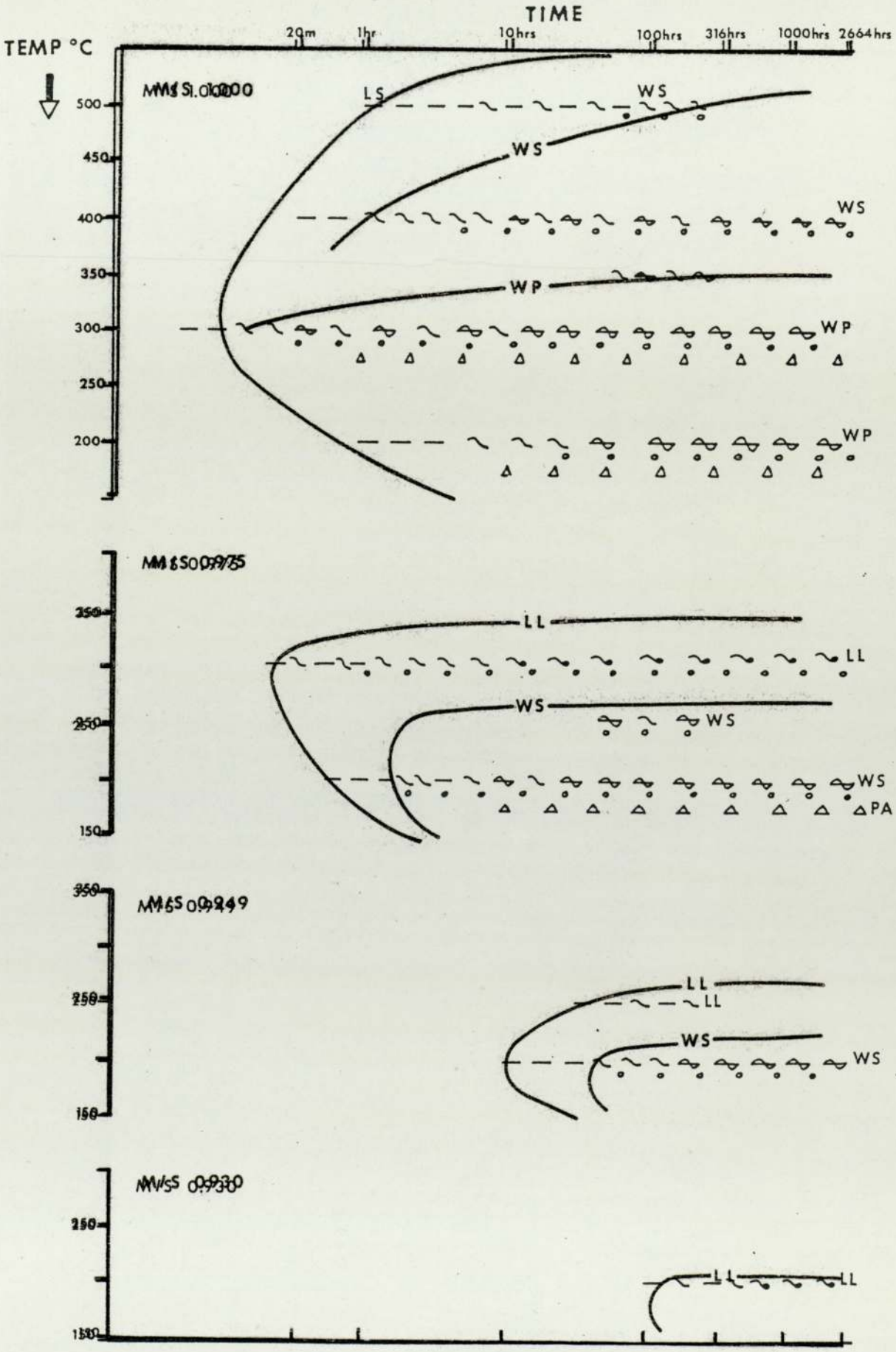

Figure 4.5 T-T-T-X diagrams illustrating variations in the development of lensoidal and platy lamellar forms.

4.5a MSS compositions of differing M/S ratios with initial Fe/Ni ratio = 10.

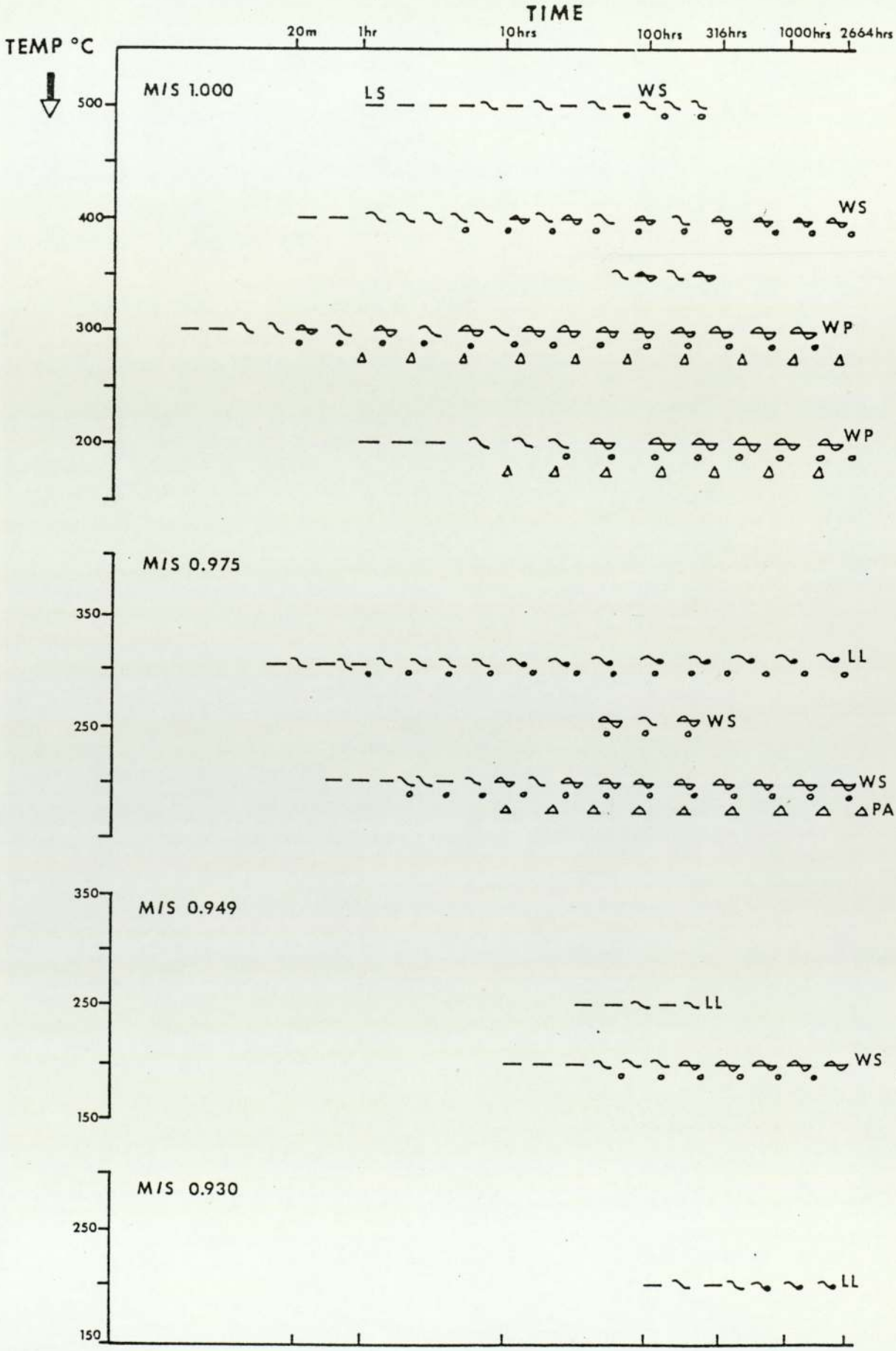

Fig. 4.5b MSS compositions of differing initial M/S ratios with initial Fe/Ni = 3.

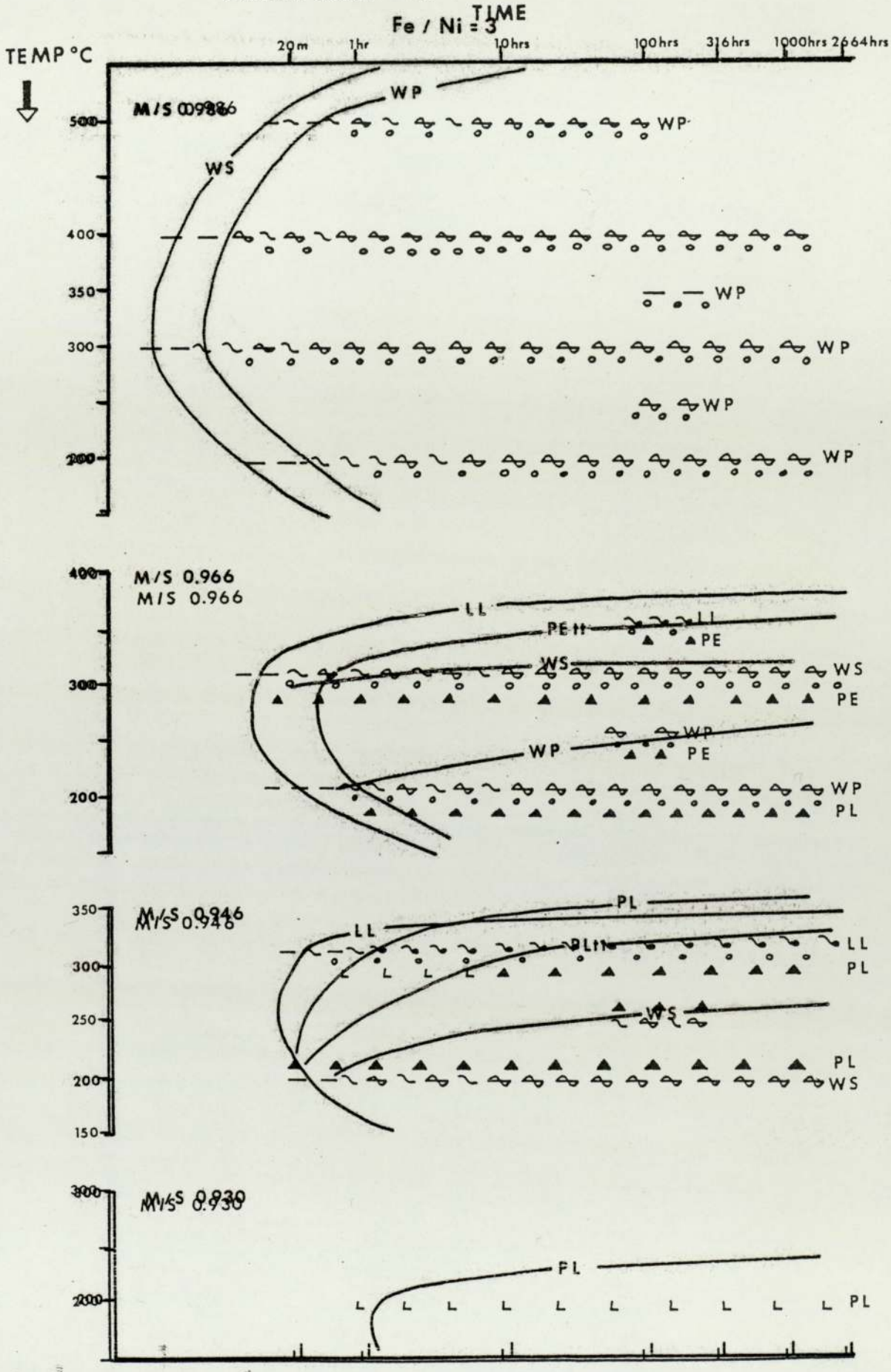

Fig. 4.5b MSS compositions of differing initial M/S ratios with initial Fe/Ni = 3.

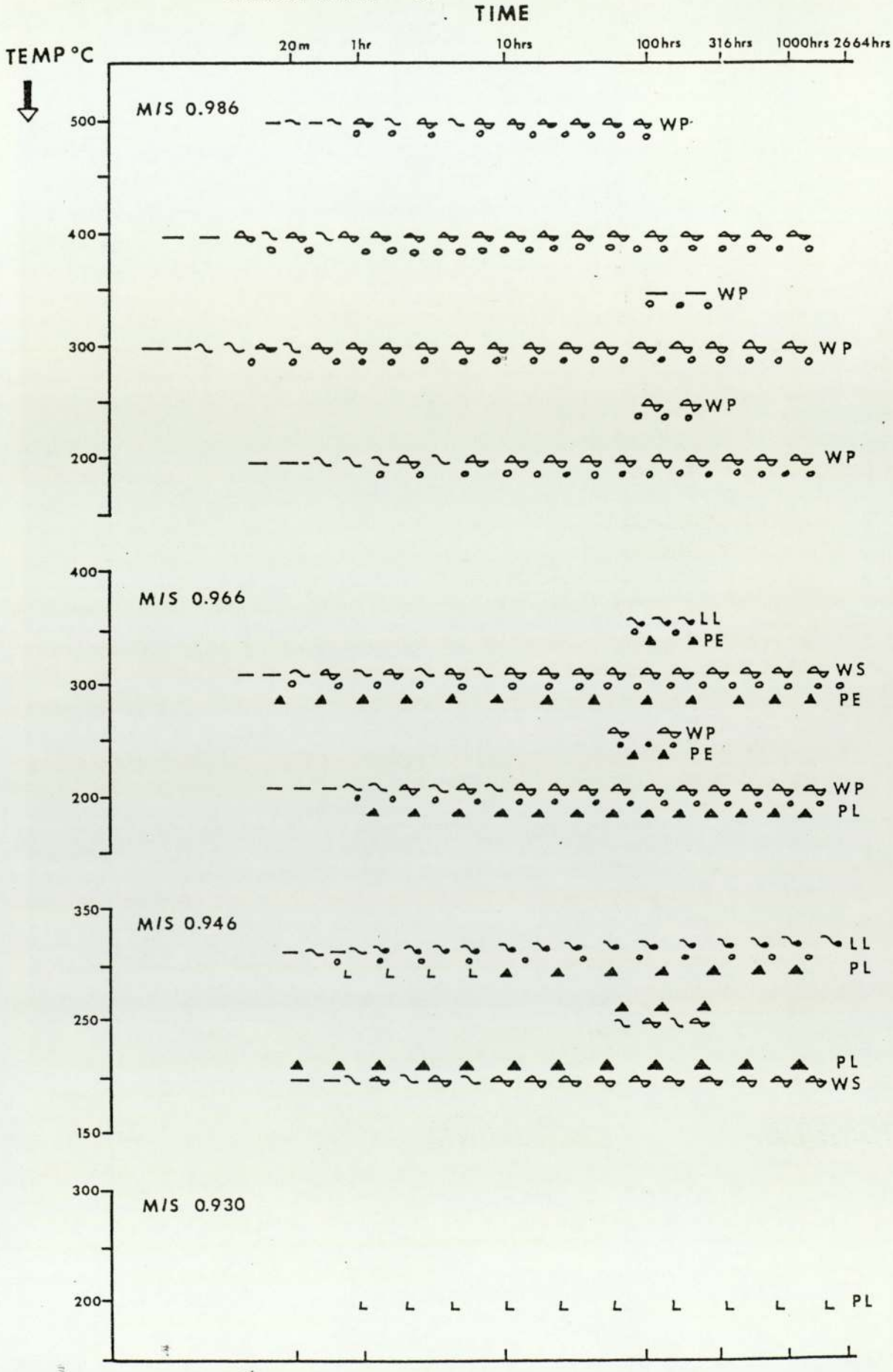

Fig. 4.6a Summary T-T-T diagram illustrating the sequence of textural types developed during isothermal annealing as ΔT increases 4.6b at higher degrees of supersaturation.

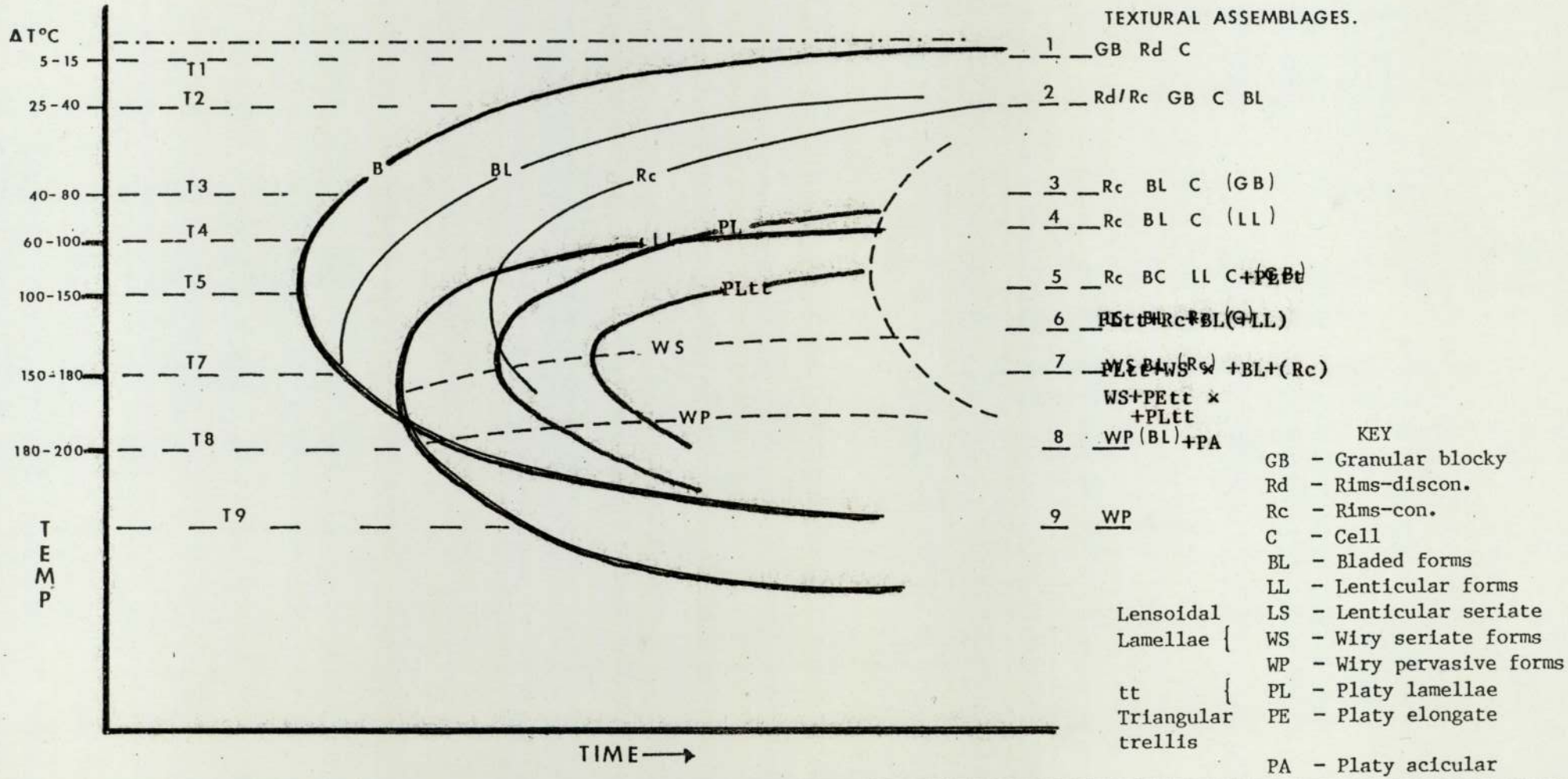

Fig. 4.6a Summary T-T-T diagram illustrating the sequence of textural types developed during isothermal annealing as ΔT increases

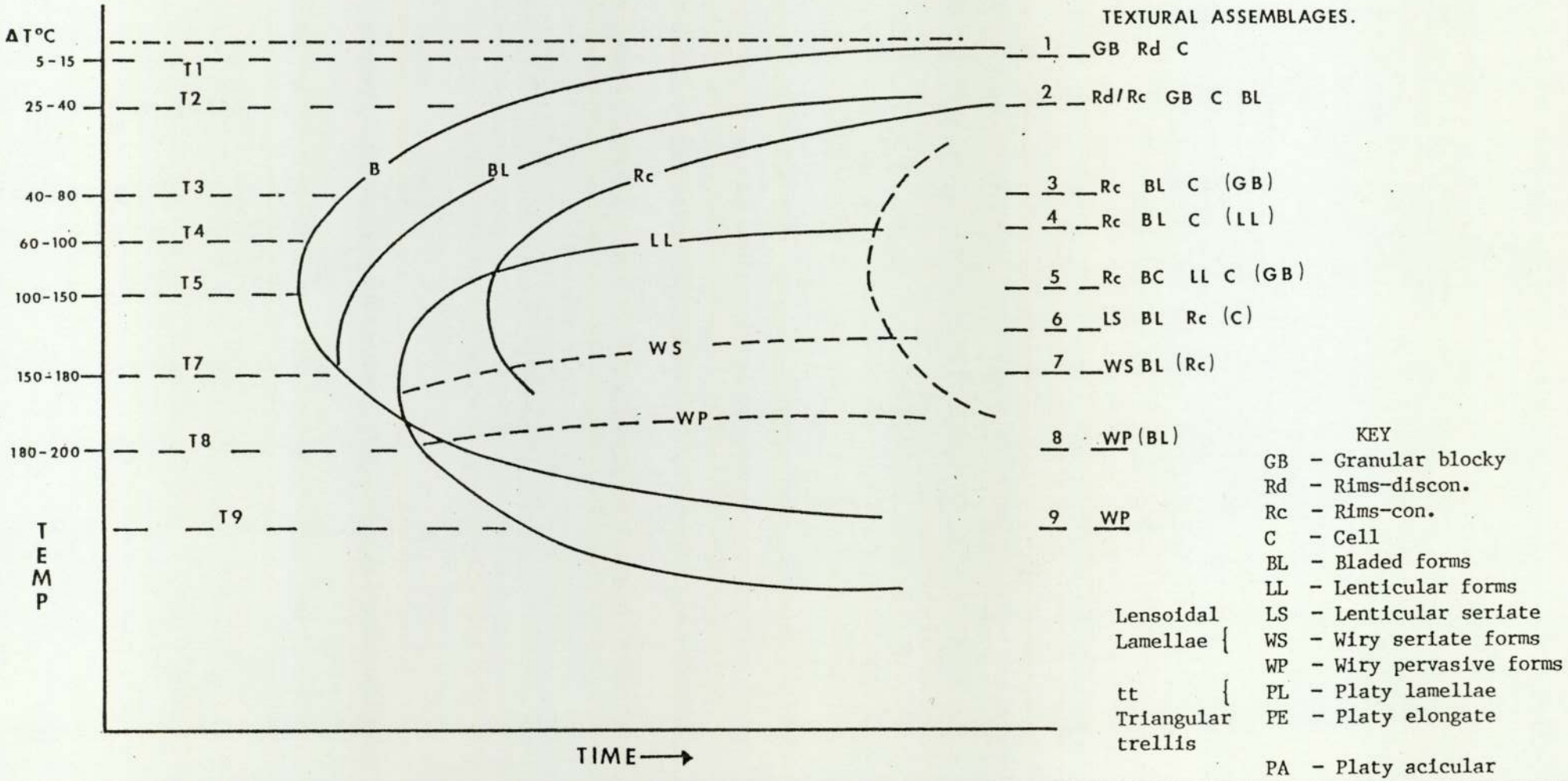

TABLE 5.2 Electron Microprobe Data* from Strathcona Mine, Sudbury

Sample No and Species		Wt % S	Wt % Fe	Wt % Ni	Wt % TOTAL	At % S	At % Fe	At % Ni	Formula
PYRRHOTITE (Mcl - monoclinic, Hex - hexagonal)									
8	Mcl	39.8	60.4	0.36	100.56	53.3	46.4	0.26	$(Fe_{6.98}\ Ni_{0.04})_{7.02}\ S_8$
8	Hex	39.1	60.9	0.68	100.68	52.6	47.0	0.50	$(Fe_{8.93}\ Ni_{0.1})_{9.03}\ S_{10}$
7	Mcl	40.7	61.2	0.38	102.28	53.5	46.3	0.25	$(Fe_{6.90}\ Ni_{0.04})_{6.94}\ S_8$
7	Hex	39.7	61.2	0.75	101.65	52.8	46.7	0.55	$(Fe_{8.85}\ Ni_{0.11})_{8.96}\ S_{10}$
4	Mcl	40.2	60.9	0.45	101.55	53.3	46.4	0.34	$(Fe_{6.97}\ Ni_{0.05})_{7.02}\ S_8$
4	Hex	39.5	61.1	0.86	101.46	52.7	46.7	0.64	$(Fe_{8.87}\ Ni_{0.12})_{8.99}\ S_{10}$
11	Bulk Analyses	39.2	60.4	0.97	100.57	52.7	46.6	0.73	$(Fe_{8.85}\ Ni_{0.14})_{8.99}\ S_{10}$
14	Mcl	39.8	59.4	0.48	99.68	53.8	45.9	0.35	$(Fe_{6.84}\ Ni_{0.05})_{6.89}\ S_8$
16	Hex	39.4	59.7	1.01	100.11	53.0	46.2	0.73	$(Fe_{8.72}\ Ni_{0.14})_{8.86}\ S_{10}$
18	Mcl	40.3	61.1	0.43	101.83	53.3	46.4	0.30	$(Fe_{6.96}\ Ni_{0.05})_{7.01}\ S_8$
18	Hex	39.4	60.5	0.85	100.75	52.9	46.5	0.60	$(Fe_{8.81}\ Ni_{0.11})_{8.92}\ S_{10}$
23	Mcl	39.8	61.1	0.39	101.29	53.1	46.6	0.30	$(Fe_{7.05}\ Ni_{0.05})_{7.10}\ S_8$
23	Hex	39.0	61.4	0.81	101.21	52.2	47.2	0.60	$(Fe_{9.02}\ Ni_{0.12})_{9.14}\ S_{10}$

TABLE 5.2 continued

Sample No	Wt % S	Wt % Fe	Wt % Ni	Wt % Co	Wt % TOTAL	At % S	At % Fe	At % Ni	At % Co	Formula
						PENTLANDITE				
Str 8	33.2	29.4	34.5	2.61	99.7	47.2	24.0	26.7	2.1	$(Fe_{4.06}\ Ni_{4.53}\ Co_{0.34})_{8.93}\ S_8$
Str 7	32.8	29.8	35.2	2.48	100.28	46.6	24.2	27.3	1.9	$(Fe_{4.17}\ Ni_{4.69}\ Co_{0.33})_{9.19}\ S_8$
Str 4	33.1	29.8	35.4	2.17	100.49	46.8	24.2	27.3	1.7	$(Fe_{4.14}\ Ni_{4.67}\ Co_{0.29})_{9.10}\ S_8$
Str 1	32.8	29.6	37.9	0.77	101.27	46.4	23.9	29.1	0.6	$(Fe_{4.12}\ Ni_{5.02}\ Co_{0.24})_{9.38}\ S_8$
Str 11	32.9	30.2	37.0	0.39	100.39	46.5	24.6	28.6	0.3	$(Fe_{4.22}\ Ni_{4.92}\ Co_{0.05})_{9.19}\ S_8$
Str 14	32.4	29.7	35.1	0.99	98.19	46.5	24.6	28.6	0.3	$(Fe_{4.20}\ Ni_{4.74}\ Co_{0.14})_{9.08}\ S_8$
Str 18	32.2	29.9	34.5	1.34	97.94	46.9	24.8	27.2	1.1	$(Fe_{4.26}\ Ni_{4.68}\ Co_{0.18})_{9.12}\ S_8$
Str 23	32.5	30.5	35.0	1.40	99.40	46.4	25.1	27.4	1.1	$(Fe_{4.33}\ Ni_{4.72}\ Co_{0.19})_{9.24}\ S_8$
Cu^+ Zone	33.4	34.0	31.2	0.44	99.0	47.6	27.8	24.3	0.3	$(Fe_{4.68}\ Ni_{4.08}\ Co_{0.06})_{8.82}\ S_8$
						PYRITE				
8	53.4	45.4	-	0.85	99.65	66.8	32.6	-	0.58	$(Fe_{0.976}\ Co_{0.016})_{0.992}\ S_{2.0}$
11	53.2	46.0	-	0.43	99.63	66.7	33.1	-	0.28	$(Fe_{0.992}\ Co_{0.008})_{1.0}\ S_{2.0}$

* All analyses from Vaughan et al. (1971) apart from $^+$Abel et al. (1979)

TABLE 5.3 Electron Microprobe Analyses of Pyrrhotite and Pentlandite from Copper Cliff Mine, Sudbury

Sample No. & Species	Wt % S	Fe	Ni	Co	Cu	TOTAL	No. of spot analyses	At % S	Fe	Ni	Co	Cu	Formula
PYRRHOTITE (Mcl - monoclinic, Hex - Hexagonal)													
CC2 Mcl	39.6	60.5	0.49	0.15	0.05	100.72	10	53.0	46.5	0.36	0.11	-	$(Fe_{7.02}\ Ni_{0.05}\ Co_{0.02})_{7.09}\ S_8$
CC8 Mcl	39.5	60.5	0.31	0.11	0.06	100.48	11	53.1	46.6	0.23	0.08	0.04	$(Fe_{7.03}\ Ni_{0.03}\ Co_{0.01})_{7.06}\ S_8$
CC8 Hex	38.8	60.8	0.73	0.13	0.06	100.53	11	52.3	47.0	0.54	0.10	0.05	$(Fe_{9.89}\ Ni_{0.11}\ Co_{0.02})_{10.02}\ S_{11}$
CC13 Mcl	40.0	60.9	0.36	0.09	-	101.35	9	53.2	46.5	0.26	0.07	-	$(Fe_{6.99}\ Ni_{0.04}\ Co_{0.01})_{7.04}\ S_8$
CC13 Hex	39.3	61.3	0.74	0.09	-	101.43	6	52.5	46.9	0.54	0.07	-	$(Fe_{9.83}\ Ni_{0.10}\ Co_{0.01})_{9.94}\ S_{11}$
CC20 Mcl	39.7	60.6	0.40	0.13	0.08	100.91	9	53.0	46.5	0.29	0.10	0.05	$(Fe_{7.02}\ Ni_{0.04}\ Co_{0.01})_{7.07}\ S_8$
CC20 Hex	39.0	61.0	0.78	0.13	0.07	100.98	6	52.3	47.0	0.57	0.10	0.04	$(Fe_{9.87}\ Ni_{0.12}\ Co_{0.02})_{10.01}\ S_{11}$
CC28 Mcl	39.6	60.5	0.35	0.13	0.06	100.62	10	53.1	46.6	0.26	0.09	0.04	$(Fe_{7.01}\ Ni_{0.03}\ Co_{0.01})_{7.05}\ S_8$
CC28 Hex	38.9	60.9	0.80	0.11	0.07	100.70	10	52.3	47.0	0.6	0.08	0.05	$(Fe_{9.87}\ Ni_{0.12}\ Co_{0.01})_{10.00}\ S_{11}$
PENTLANDITE													
CC2	33.2	30.5	35.4	1.44	0.11	100.48	20	46.8	24.7	27.3	1.09	0.09	$(Fe_{4.22}\ Ni_{4.66}\ Co_{0.19})_{9.07}\ S_8$
CC8	33.3	30.9	35.2	1.26	0.12	100.78	14	46.9	25.0	27.1	0.96	0.08	$(Fe_{4.26}\ Ni_{4.61}\ Co_{0.16}\ Cu_{0.01})_{9.04}\ S_8$
CC13	33.3	31.1	35.8	0.94	-	101.14	10	46.9	25.0	27.4	0.72	-	$(Fe_{4.27}\ Ni_{4.68}\ Co_{0.12})_{9.07}\ S_8$
CC20	33.3	30.9	35.4	1.16	0.11	100.76	11	46.8	25.0	27.2	0.89	0.08	$(Fe_{4.27}\ Ni_{4.65}\ Co_{0.15}\ Cu_{0.01})_{9.08}\ S_8$
CC28	33.0	30.9	35.3	1.12	0.15	100.47	13	46.7	25.1	27.2	0.86	0.10	$(Fe_{4.29}\ Ni_{4.66}\ Co_{0.15}\ Cu_{0.02})_{9.12}\ S_8$

TABLE 5.4 Examples of Electron Microprobe Analyses of Different Pentlandite Textural Types (Copper Cliff Mine, Sudbury)

Sample No.		CC2	CC2	CC2	CC8	CC8	CC8	CC13	CC13	CC20	CC20	CC28	CC28
Textural Type (Table 5.7)		I	IV2b	IV2b	I	IV1a	IV2b	III1a	IV1a	I	IV1b	IV1a	I
	S	33.2	33.2	33.2	33.2	33.4	33.2	33.6	33.3	33.2	33.4	33.1	33.0
	Fe	30.4	30.6	30.5	30.7	31.0	31.0	31.2	31.0	30.8	30.9	31.0	30.9
wt %	Ni	35.4	35.3	35.4	35.2	35.1	35.1	35.7	35.7	35.4	35.4	35.2	35.3
	Co	1.41	1.41	1.49	1.21	1.25	1.21	0.95	0.93	1.13	1.19	1.13	1.10
	Cu	0.11	0.11	0.11	0.11	0.12	0.12	-	-	0.12	0.10	0.13	0.13
TOTAL		100.41	100.51	100.59	100.42	100.87	100.63	101.45	100.93	100.65	100.99	100.56	100.43
		(7)	(7)	(6)	(6)	(5)	(2)	(5)	(5)	(6)	(5)	(8)	(5)
	S	46.9	46.8	46.8	46.9	47.0	46.8	47.0	46.8	46.7	46.9	46.7	46.6
	Fe	24.7	24.8	24.7	24.9	25.0	25.1	25.0	25.0	24.9	24.9	25.1	25.1
at %	Ni	27.3	27.2	27.3	27.2	27.0	27.1	27.3	27.4	27.2	27.2	27.2	27.2
	Co	1.09	1.09	1.13	0.95	0.95	0.95	0.72	0.71	0.86	0.90	0.86	0.86
	Cu	0.05	0.09	0.09	0.09	0.09	0.09	-	-	0.11	0.09	0.09	0.09

TABLE 5.5 Electron Microprobe Analyses of Chalcopyrite and Cubanite (Copper Cliff and Strathcona Mines, Sudbury).

Sample No.	Phase	Wt % S	Fe	Cu	Co	Ni	Total	( )	At % S	Fe	Cu	Co	Ni	Formula
CC8	Cp	34.9	31.5	34.2	0.07	n.d.	100.67	(8)	49.7	25.7	24.6	0.05	-	$Cu_{0.989}Fe_{1.035}S_2$
CC20	Cp	34.9	31.1	34.0	0.06	n.d.	100.06	(6)	49.9	25.5	24.5	0.05	-	$Cu_{0.983}Fe_{1.023}S_2$
CC28	Cp	35.8	31.1	34.0	-	n.d.	100.9	(5)	50.6	25.2	24.2	-	-	$Cu_{0.959}Fe_{0.997}S_2$
Cu-zone+	Cp	35.02	30.4	34.6	-	0.16	100.16		50.0	24.9	24.9	-	0.13	$Cu_{0.998}Fe_{0.996}S_2$
CC20	Cub	35.6	40.9	20.8	-	-	97.3	(3)	51.2	33.8	15.1	-	-	$Cu_{0.885}Fe_{1.979}S_3$
Cu-zone+	Cub	34.8	40.9	23.4	-	0.13	99.3		49.6	33.5	16.8	-	0.10	$Cu_{1.02}Fe_{2.03}S_3$

+ From Abel et al. (1979)

TABLE 5.6 Electron Microprobe Analyses of Pyrite (Copper Cliff Mine, Sudbury)

Euhedral Zoned Pyrite (Fig. 5.11b)

Analyses No.		1	5	4	3	2	6	13	14	7	8	9	10	12	11
Distance From Grn. Margin (µm)		10	30	50	85	110	130	Grn. Core	Grn. Core	150	180	190	200	220	250
	S	53.6	53.5	53.5	53.4	53.6	53.6	53.5	53.5	53.6	53.6	53.4	53.5	53.7	53.5
wt %	Fe	46.3	46.6	46.4	46.6	44.7	44.7	44.8	44.8	45.8	45.5	45.0	45.7	45.8	45.9
	Co	1.07	0.64	0.94	0.59	2.49	2.40	2.39	2.47	1.62	1.99	2.06	1.55	1.27	1.12
TOTAL		100.97	100.74	100.84	100.59	100.79	100.70	100.77	100.77	101.02	101.09	100.46	100.75	100.77	100.52

Ni present in trace amounts ~0.05 wt %

'Pinker darker patches' at Pyrite Grn. Bounds (Fig. 5.11c)

wt %	S	Fe	Co	Ni	TOTAL	
	53.5	43.8	3.45	0.07	100.82	(3)

Sieve-like Pyrite Associated with Magnetite (Fig. 5.15)

	53.5	47.0	0.11	0.07	100.68	(9)

TABLE 5.7 Summary of Pentlandite Textural Types in the Sudbury Ores

	Mode of Occurrence/Location	Average Dimensions (mm), Diameter(D) Width(W), Length(L)	Other Pn Types in Direct Association	Abundance
I RIM Pn	Aggregates of equant Pn particles forming discon. to con. stringers			
	1) Along individual Po grn. bounds. Boundaries with adjacent Po generally indented, lobate to crenulate.	W and continuity of individual rims decreases as Po grn. size decreases	Bladed flame extensions	Very common in massive and intermediate ore. Abundance decreases as abundance of Mt. increases and Po grn. size decreases.
		Po / Pn		
		6-20 / 0.4-0.6	Cell Pn (II2)	
		1-6 / 0.1-0.3	Irregular angular masses where interlink (III2a)	Rare in disseminated ore
		0.4-1 / 0.02-0.075	Coarsen to triangular rounded granular masses where adjacent rims interlink (III1a)	
	2) Along twin boundaries	W 0.04-0.1		Rare, confined to coarse Po grains (>4mm) with well developed twinning.
II CELL Pn	Continuous rims enveloping finer Po grains (0.2-0.8mm). Located:			
	1) Contact between coarse or medium grained Po mosaics and finer Po mosaics	W 0.05-0.075	Elongate blocky Pn (III2b)	Common in massive ore and coarser blebs intermediate ore. Most abundant where conc. Mt. moderate and Po matrix consists fine grained mosaics abutting medium or coarse grained mosaics.
	2) Where fine Po grains interstitial to medium or coarse grains	W 0.1-0.2	Coarse blocky Pn (III3a)	

TABLE 5.7 Continued...

	Mode of Occurrence/Location	Average Dimensions (mm), Diameter(D) Width(W), Length(L)	Other Pn Types in Direct Association	Abundance
IIIa BLOCKY INTERSTITIAL Pn	Where adjacent Pn rims intersect 1a) at Po T-junctions - regular rounded or triangular granular masses	D0.2-0.4	Fine Pn rims	In massive ores moderate More common in fine-grained Po mosaics
	2a) Contact between fine and medium grained Po - irregular angular masses not confined to Po T-junctions	D 0.4-0.8	Pn rims, Cell Pn (II1)	Few. Confined to massive/ intermed ore.
	3a) Coarse granular masses associated with cell Pn interstitial to coarse Po	D 0.7 × 0.3 to 1 × 0.5	Cell Pn (II2)	Rare. Confined to massive/ intermed ore.
IIIb DISCRETE INTERSTITIAL Pn	Discrete masses interstitial to Po grains	D 0.3-0.8	Discrete	Rare in massive ore. Located within rare very fine grained (0.1-0.4mm) Po mosaics
	1b) Po T-junctions in fine grained Po mosaics - discrete ovoid or ellipsoid masses	D 0.1-0.2	Discrete	Few in intermediate ore, within fine grained Po mosaics close to sulphide/silicate contact.
	2b) On margins fine Po grains where abut coarser grains - regular elongate masses	D 0.2-0.4	Cell Pn	Massive/intermediate ore. Rare
IIIc LOBATE BLOCKY Pn	Discrete lobate masses located at silicate/sulphide contact in disseminated ore	D 0.02-0.1		Common in disseminated ore

TABLE 5.7 Continued...

	Mode of Occurrence/Location	Average Dimensions (mm), Diameter(D) Width(W), Length(L)	Other Pn Types in Direct Association	Abundance
IV GRANULAR BLOCKY PENTLANDITE	Located at contact between Po grains and (a) Magnetite, (b) Coarse granular Cp.			
	1a) Irregular granular masses abutting Mt grains located at Po grn. bounds	D increase as Po grain size increases Po: 0.4-1, 1-4 mm Blocky Pn: D 0.2-0.4, D 0.4-0.8	Occasionally with Rim Pn	Common in massive/ intermediate ore. Abundance increases as proportion of Mt present increases.
	1b) Coarse angular Pn stringers at Cp/Po contact. Angular boundaries protrude into cusps between adjacent Po grns.	L 3.5-1.5 W 1.2-0.6	Adjacent Po matrix depleted in Pn	Found in massive ore where coarse granular segragations Cp common. Otherwise rare.
	2b) Discrete more equant masses at Cp/Po contact	D 0.2-1	Massive ore associated coarse	granular Cp. More rarely intermediate ore associated with Cp selvages.
	[3b) Pn collars at Cp/Po contact. Smooth interface with Po, bladed interface with Cp]			
V COARSE Pn VEINLETS	Located contact fine grained/coarse grained Po mosaics. Consist of coarse angular stringer along contact and network of granular interstitial masses within adjacent fine grained Po mosaic.	upto L 7 mm W 1.2 mm		Very rare
VI FLAME-TYPE Pn AGGREGATES	-aggregates of finer pentlandite particles (blades, lamellae, elgonate blebs). Shape of aggregate and type of pentlandite particle depends on location within Po matrix and orientation of host Po grain. Particles and aggregates elongate sub-parallel to basal Po plane.			

TABLE 5.7 Continued...

	Mode of Occurrence/Location	Average Dimensions (mm), Diameter(D) Width(W), Length(L)	Other Pn Types in Direct Association	Abundance
1. BLADED AGGREGATES	Consist of partially agglomerated elongate subparallel plates or blades in moderate to high anisotropy Po grains. More feathery aggregates of tubbier blades in weakly anisotropic grains and hemispherical rosettes in basal grains.			
	Located:			
	1a) At Po grain boundaries. Where present either side grn. bound. → herringbone texture	L 0.04-0.1 W 0.05-0.2		Common in massive/ intermediate ore
	1b) as flame extensions form Pn rims	L 0.02-0.06		Common in massive/ intermediate ore
	1c) extending from margins of Mt grains or less commonly Py grains			Moderate in massive/ intermediate ore
	1d) within Po grains at fractures or less commonly twin boundaries	L 0.04-0.1 W 0.03-0.05		More common in coarser (>4 mm) Po grains
	1e) at sulphide-silicate contact in disseminated ore. Aggregates more acicular in form.	L0.02-0.1		Disseminated ore
2. 'LAMELLAR' AGGREGATES	Located wtihin Po grains at defect free areas. In Po sections cut oblique to basal plane appear as rod-like or ellipsoid aggregates consisting of lamellae or blebs elongate subparallel to elongation direction aggregate.	L0.08-0.25 W 0.002-0.02		Common within coarser Po grains (>4 mm) in massive ore
	Basal Po sections aggregates appear as aborescent rosettes	D 0.1-0.2		
VII Pn LENSES	Massive elongate lenses either			Rare. Confined to few samples of massive ore
	(a) extending from rim Pn	L 0.2-0.8		
	(b) within Po grains at defect free areas appear as massive 'ovoids' in basal Po sections.	W 0.05-0.15		

TABLE 5.9a Electron Microprobe Analyses of Zoned Magnetite and Coexisting Ilmenite (Sample CC2, Copper Cliff)

	MAGNETITE									ILMENITE
	1	2	3	4	5	6	7	8		
FeO	32.9	33.6	34.2	34.7	34.3	33.0	33.0	33.2		38.7
Fe_2O_3	62.6	59.1	58.1	57.8	58.8	59.9	62.9	61.7		7.8
TiO_2	2.76	4.06	4.67	5.05	4.59	3.55	2.75	3.29		47.3
MnO	0.26	0.35	0.43	0.47	0.42	0.33	0.27	0.32		4.2
Cr_2O_3	0.10	0.12	0.12	0.12	0.11	0.12	0.11	0.11		-
TOTAL	98.6	97.2	97.5	98.0	98.2	96.9	99.0	98.6		98.0
O	32	32	32	32	32	32	32	32		6
Fe^{2+}	8.577	8.871	8.991	9.063	8.967	8.758	8.571	8.664		1.539
Fe^{3+}	14.682	14.042	13.760	13.595	13.817	14.277	14.689	14.477		0.566
Ti^{4+}	0.647	0.964	1.105	1.187	1.079	0.846	0.642	0.748		1.178
Mn^{2+}	0.069	0.094	0.115	0.125	0.111	0.089	0.071	0.084		0.178
Cr^{3+}	0.025	0.030	0.030	0.030	0.027	0.030	0.027	0.027		
Mol %									Mol %	
usp	8.1	12.1	13.8	14.8	13.5	10.6	8.0	9.3	Ilm_{SS}	92.5
mt	91.9	87.9	86.2	85.2	86.5	89.4	92.0	90.7	$Haem_{SS}$	7.5

TABLE 5.9b Electron Microprobe Analyses of Unzoned Magnetites

Sample No.	CC20	CC8(1)	CC8(2)		CC8(3)	CC8(4)
No. of spot analsyses	10	9			6	8
FeO	31.1	30.7	30.6 -	30.6	31.0	31.2
Fe_2O_3	69.2	68.3	67.9 -	66.4	67.2	66.3
TiO_2	0.03	0.03	0.16-	0.61	0.58	0.97
MnO	0.12	0.06	0.16-	0.35	0.31	0.43
	100.5	99.0	98.0	98.0	98.8	98.9
O	32	32	32	32	32	32
Fe^{2+}	7.977	7.991	7.995	8.051	8.055	8.114
Fe^{3+}	15.985	15.986	15.925	15.712	15.727	15.545
Ti^{4+}	0.007	0.007	0.037	0.144	0.136	0.227
Mn^{2+}	0.031	0.016	0.042	0.093	0.082	0.113
Mol % usp	0.1	0.1	0.5	1.8	1.7	2.8
mt	99.9	99.9	99.5	98.2	98.3	97.2

CC20 Subhedral magnetite

CC8 (1) Subhedral magnetite containing few u/fine ilmenite lamellae

(2) Subhedral magnetite containing few u/fine ilmenite lamellae, bulk analyses

CC8 (3) Segmented magnetite containing numerous u/fine ilmenite lamellae, bulk analyses

(4) Disrupted magnetite containing numerous u/fine ilmenite lamellae, bulk analyses.

TABLE 5.10 Electron Microprobe Analyses of Sphalerite (Copper Cliff)

		CC28 SINGLE GRN.			CC8 SINGLE GRN.						CC20 3 GRN. AGGRG.		
		MARGIN	CORE		MARGIN	MARGIN		CORE	MARGIN		GRN 1 (avg 3)	GRN 2 (avg 4)	GRN 3 (avg 3)
	S	33.2	33.4	33.3	33.4	33.2	33.3	33.5	33.5	33.5	33.6	33.9	34.1
	Zn	59.5	60.0	60.5	59.3	59.7	60.6	61.1	60.3	59.7	59.7	60.4	59.8
WT%	Fe	6.73	6.42	6.20	6.86	6.64	6.36	6.17	6.72	6.94	7.13	6.49	7.17
	Cu	-	-	-	-	0.43	0.29	0.28	0.27	0.62	0.63	0.51	0.61
TOTAL		99.5	99.81	100.0	99.6	99.9	100.6	101.0	100.8	100.8	101.2	101.3	101.7
	ZnS	88.3	88.9	89.3	88.1	87.9	88.7	89.1	88.1	87.2	86.9	88.1	86.9
Mol%	FeS	11.7	11.1	10.7	11.9	11.4	10.9	10.5	11.5	11.9	12.2	11.1	12.2
	CuS	-	-	-	-	0.7	0.4	0.4	0.4	0.9	0.9	0.8	0.9

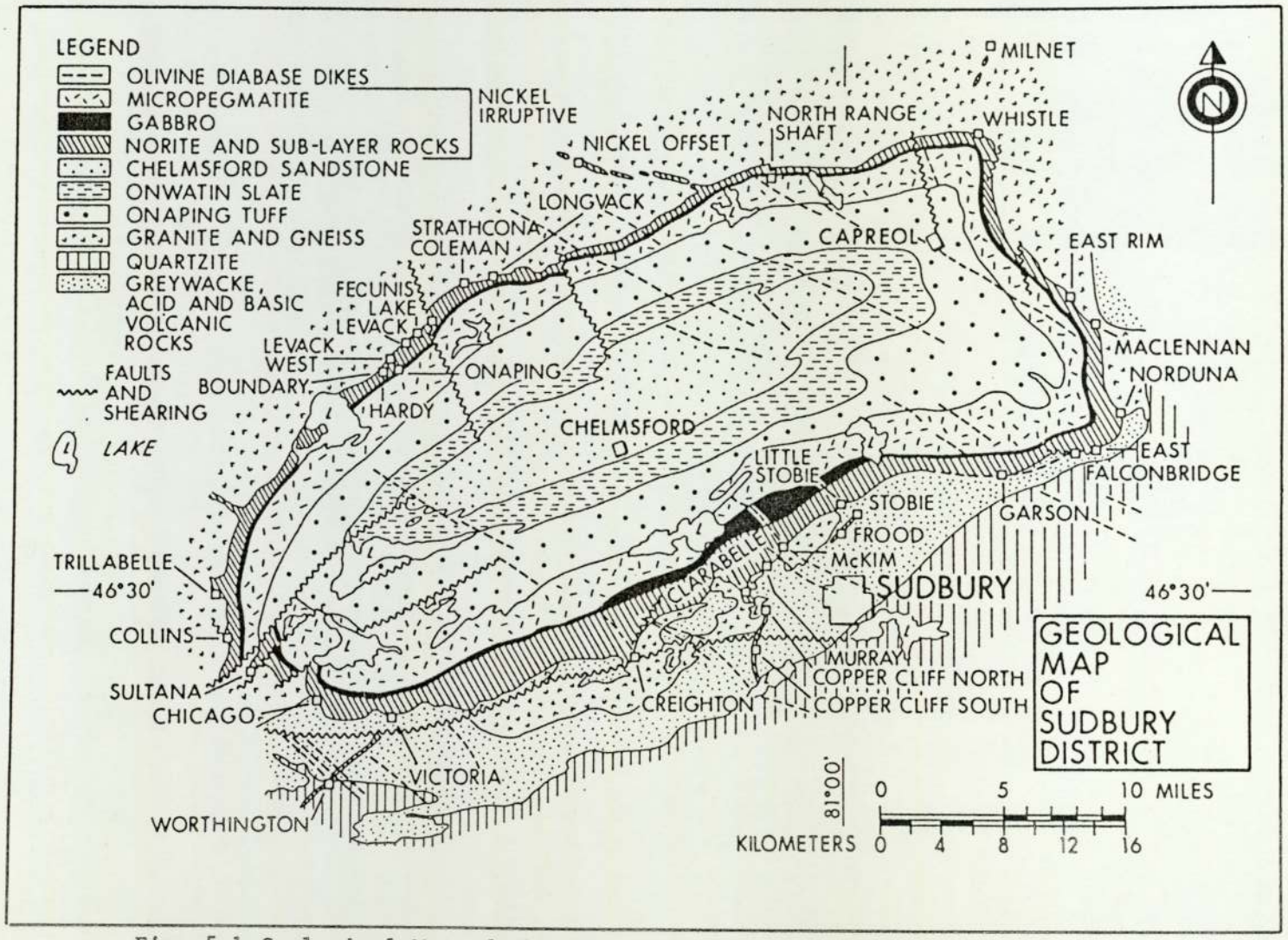

Fig. 5.1 Geological Map of the Sudbury district (after Naldrett, 1981b).

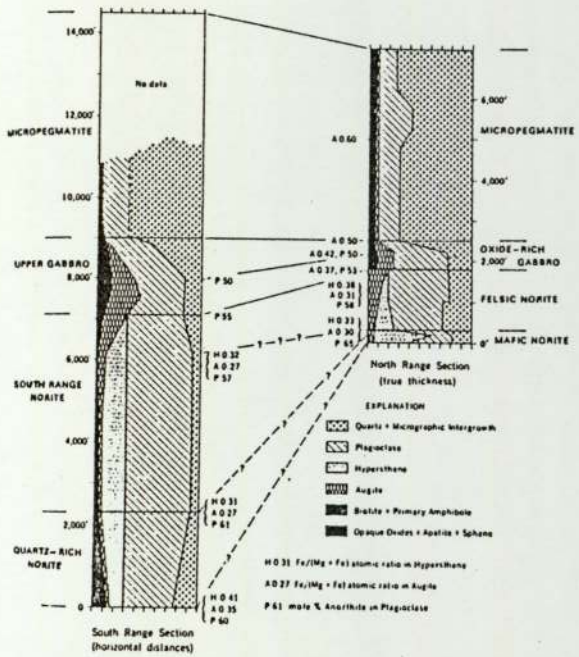

Fig. 5.2 Mineralogical variation in sections through the North and South ranges of Sudbury Irruptive (after Naldrett and Gasparrini, 1972).

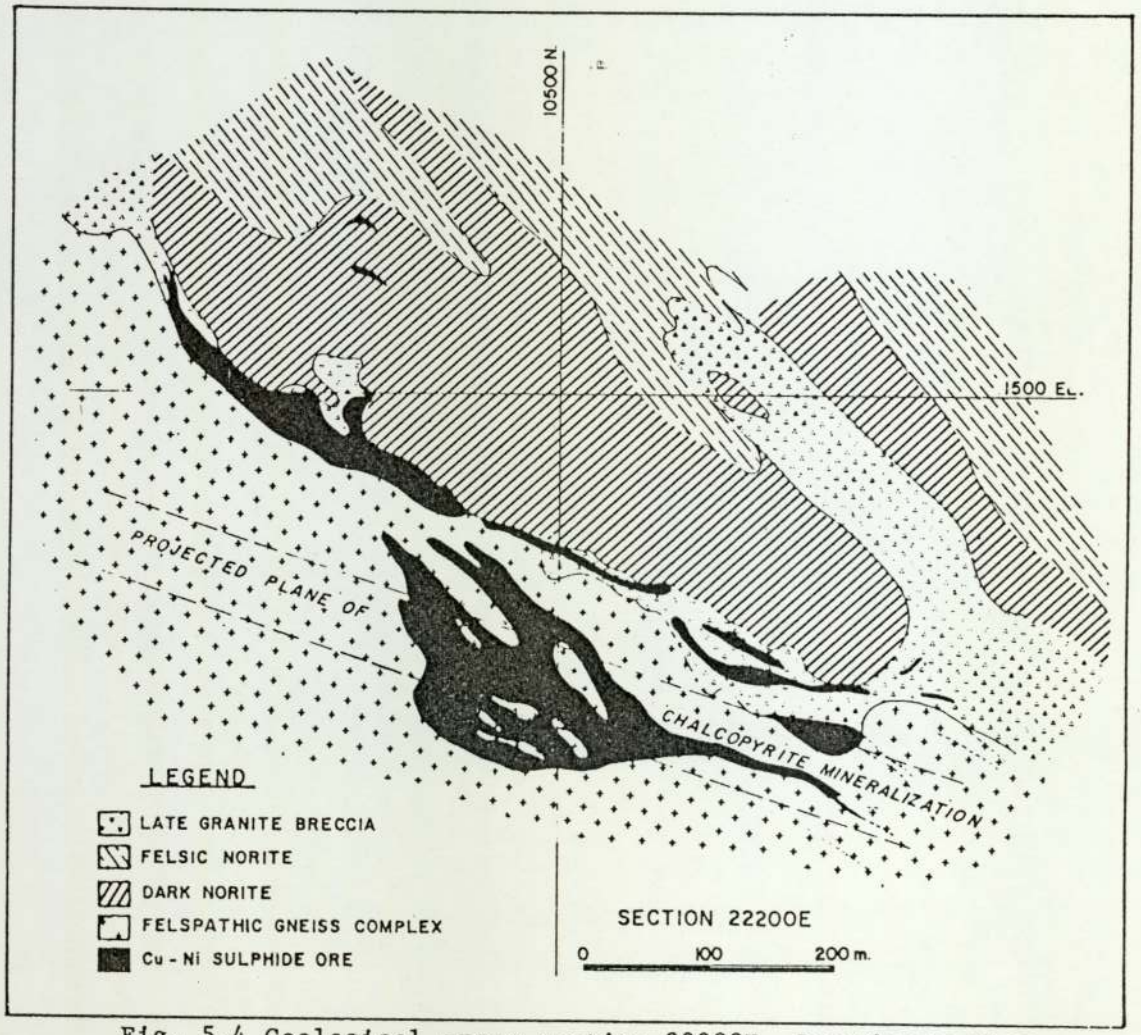

Fig. 5.4 Geological cross section 22200E, Strathcona Mine (modified after Strathcona Mine Staff).

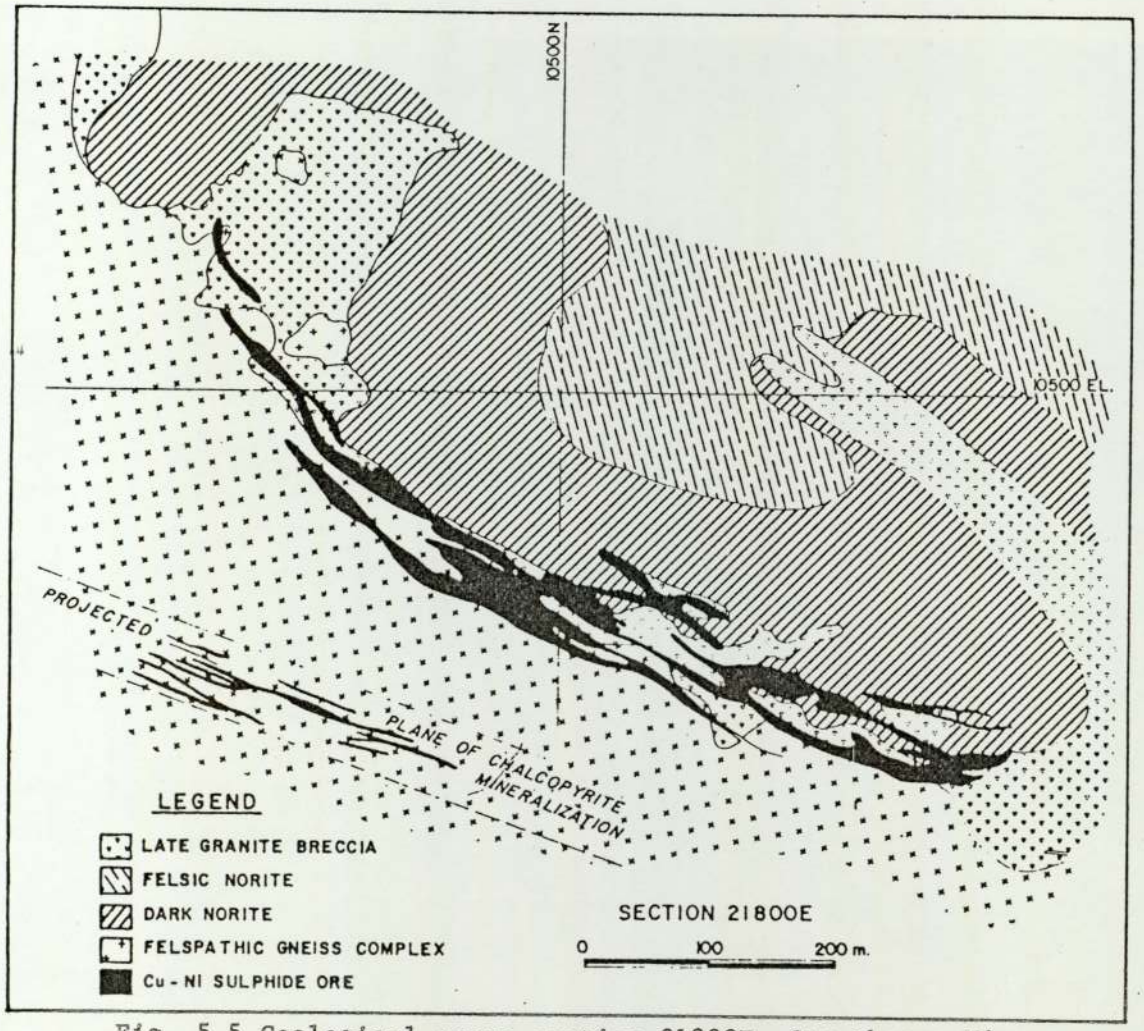

Fig. 5.5 Geological cross section 21800E, Strathcona Mine (modified after Strathcona Mine Staff).

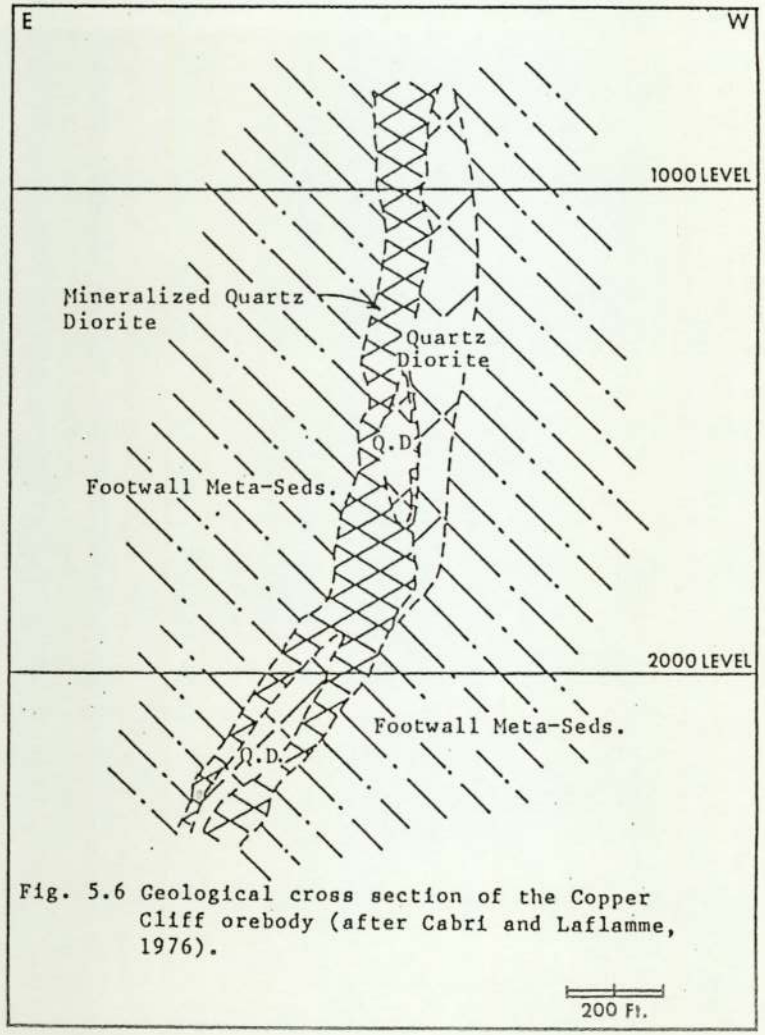

Fig. 5.6 Geological cross section of the Copper Cliff orebody (after Cabri and Laflamme, 1976).

Fig. 5.7 to 5.9 Monoclinic/'hexagonal' pyrrhotite intergrowths within the Sudbury Ores.

Fig. 5.7 Concentration of Mcl Po (dark grey) adjacent to rim Pn (in extinction, right hand margin) at the Po grain boundary. The core of the grain consists predominantly of 'hex Po' (light grey) with minor lamellae and patches of Mcl Po (see Figs. 5.9, 5.10) (f.o.v., 2mm, XP)

Fig. 5.8 Lamellar intergrowth of Mcl Po (dark grey) and (?) hex Po (light grey). The Po grain is rimmed by granular cubanite (white). Note the angular irregular nature of the Po/Cub contact (Massive ore sample, Strathcona Copper Zone) (f.o.v., 2mm, unXP)

Fig. 5.9 Concentration of Mcl Po enveloping flame Pn (in extinction) located at a fracture, within predominantly hex Po (light grey). (f.o.v., 0.32mm, XP, Oil)

Fig. 5.10 Sub-parallel elongate lamellae of Mcl Po (dark grey) within hex Po (light grey). Rod-like flames of Pn (in extinction) 'sheathed' in Mcl Po (f.o.v., 0.5mm, XP, Oil)

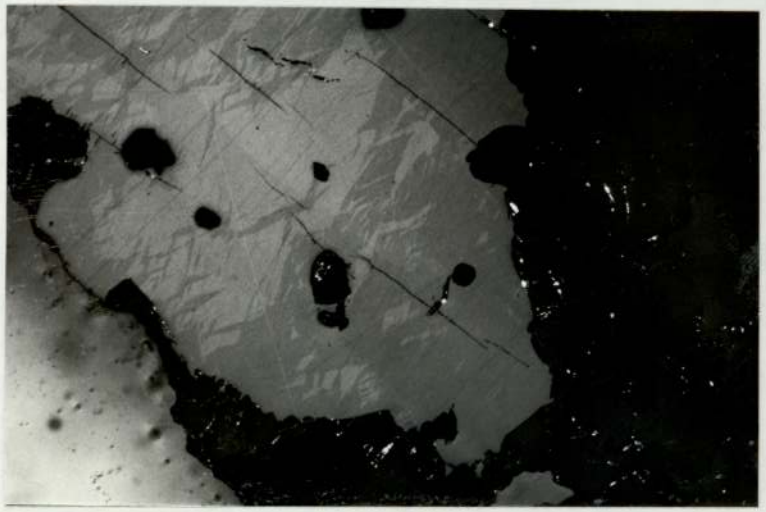

Fig. 5.7

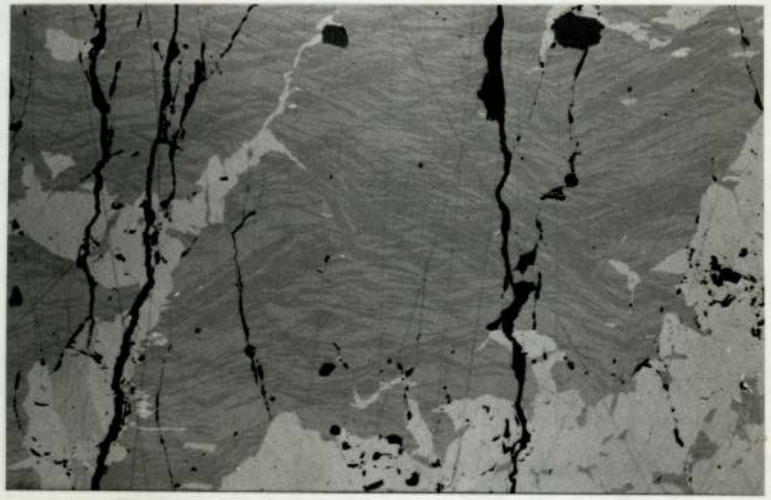

Fig. 5.8

Fig. 5.9

Fig. 5.10

Fig. 5.11a Line concentration profile of Co across zoned euhedral py. grain (Fig. 5.11b).

Fig. 5.11b Euhedral py. xtal. (white) located at Po (dark grey)/silicate (black) contact in dissem. ore bleb (f.o.v., 0.5mm, PPL, Oil).

Fig. 5.11c Subhedral py. xtals. (white) at Po (dark grey)/silicate (black) contact, dissem. ore. Light grey areas within the py. xtals. are zones of Co enrichment at grn. bounds. of individual py. grains. (see Table 5.6) (f.o.v., 0.2mm, PPL, Oil)

Fig. 5.12 Part of coarse bleb of interm. ore. Silicate contact (black) visible upper right. Composite stringer of interlocking euhedral py. xtals. (white) enveloped in Cp (lighter grey, higher relief cf Po), within matrix of interlocking Po grains (light grey). Mt/Ilm inclusions (dark grey) within the stringer, shredded and replaced by Cp. (f.o.v. 3.4 mm, PPL)

Fig. 5.13 Rim Pn (white, pitted) at boundary between two Po grains (grey). Small euhedral py. xtals. (white, higher relief) located at Po/Pn contact or partially enveloped by Pn. (f.o.v., 2mm, PPL).

Fig. 5.14 Coarse subhedral py. grains (white) partially enveloping Mt. grains (dark grey), located on margin large Po grain (grey). Smaller py. grains (upper right) contain numerous silicate inclusions (dark grey). (f.o.v. 3.4mm, PPL)

Fig. 5.15 Sieve-like py. (white) moulded about corroded Mt (dark grey). Located within silicate matrix (black) dissem. ore. Local sulphidation of Mt within silicate (f.o.v. 0.5mm, PPL, Oil)

Fig. 5.11a Line concentration profile of Co across zoned euhedral pyrite grain (Fig. 5.11b) (sample CC2, Copper Cliff).

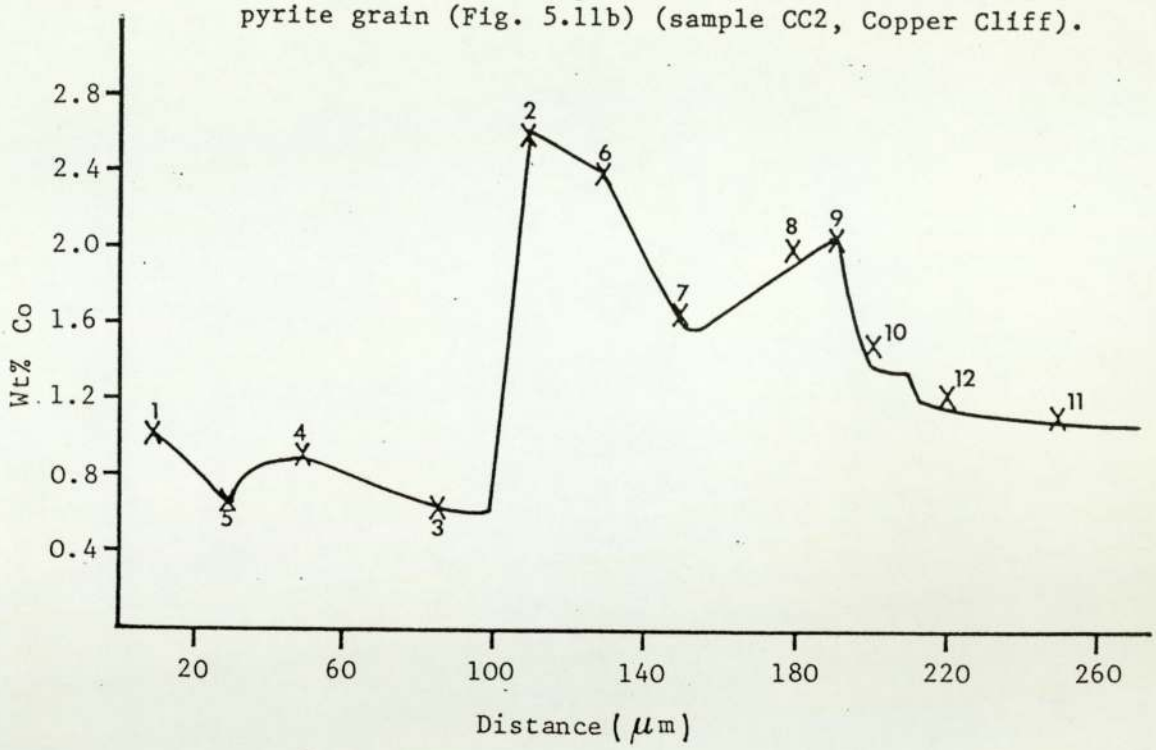

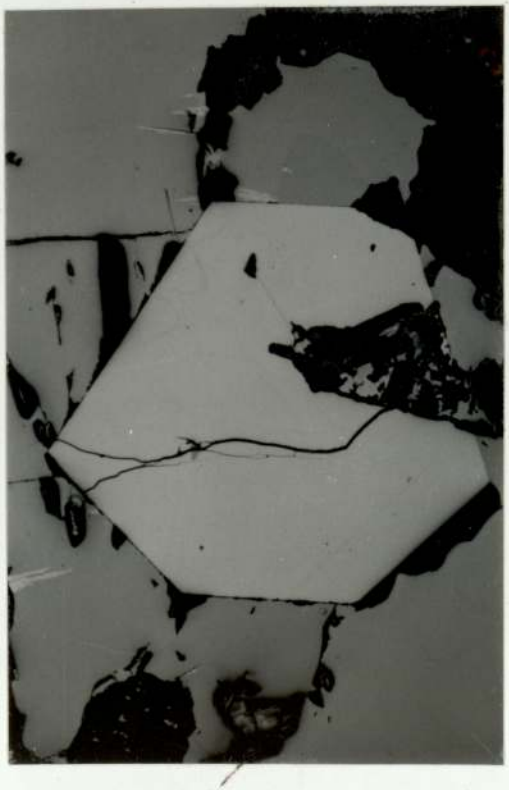

Fig. 5.11b

Fig. 5.11c

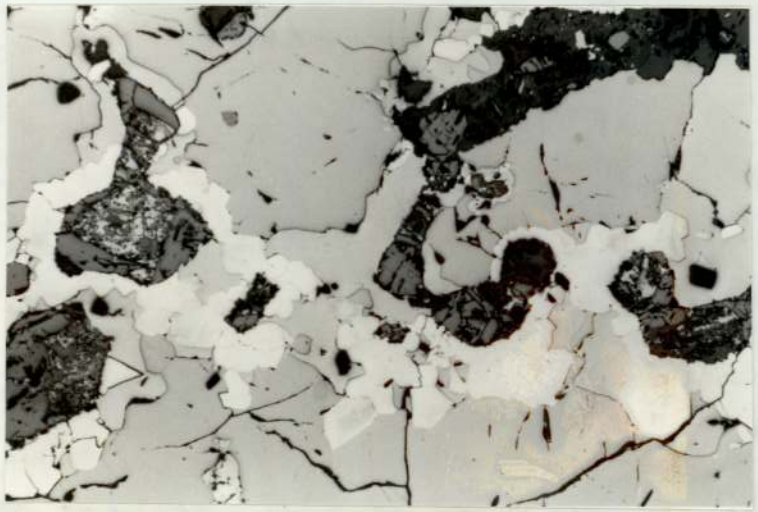

Fig. 5.12

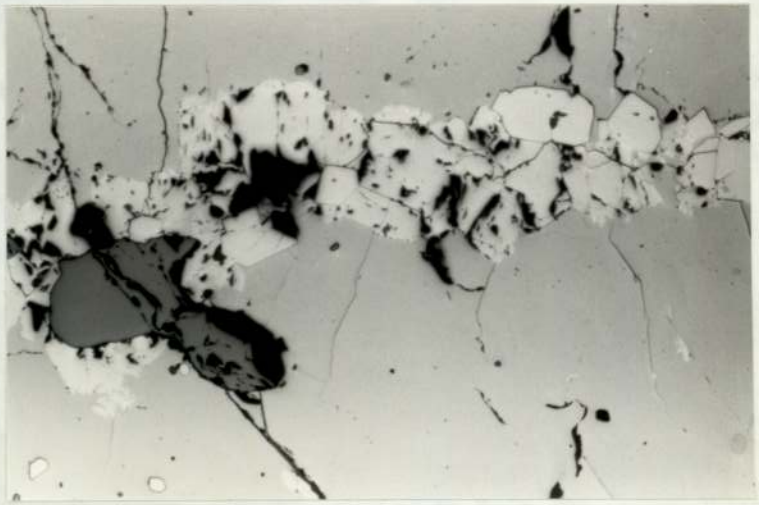

Fig. 5.13

Fig. 5.14

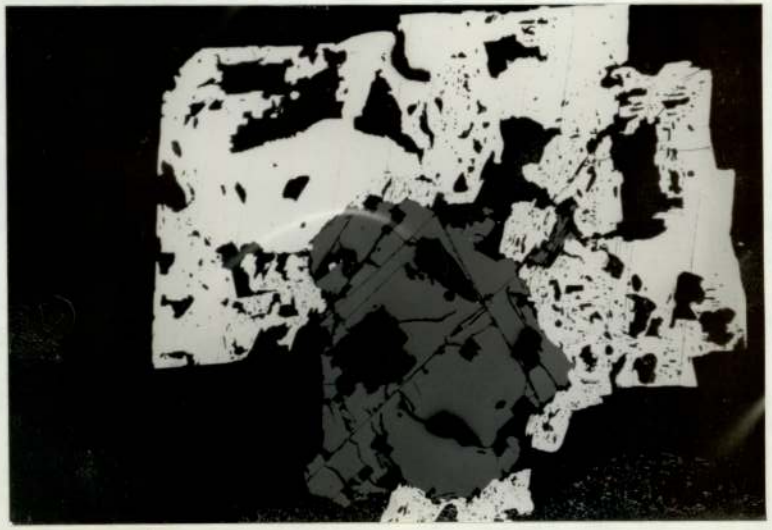

Fig. 5.15

Fig. 5.16 Coarse Pn rim (white) relatively continuous along the grain boundary between a medium sized Po (light grey) grain and adjacent Po grains, massive ore. Rim consists of impinged and overgrown equant Pn grains (bounds between them picked out by fine fractures) resulting in lobate indented bounds with adjacent Po grains. Basal parting within Po visible (f.o.v. 3.4mm, PPL)

Fig. 5.17 Finer grained 'Po mosaic' within massive ore: interlocking rounded to angular Po grains in different orientations (various shades grey). Pn rims (white) more discontinuous and finer in width (cf coarser Po mosaics, Fig. 5.16) thickening to triangular blocky interstitial Pn where intersect at Po triple-junctions. Subhedral rounded Mt grains (black) interstitial to or straddling Po grain boundaries (f.o.v., 3.4mm, PPL)

Fig. 5.18 Part of fine grained Po mosaic within massive ore. Fine Pn rims (white), along grain boundaries fine Po grains, partially interlink to form discontinuous network. Numerous bladed-flame extensions to rims orientated sub-parallel to basal plane of individual Po grains. Note the smooth nature of the Po grain boundaries and ~120° triple-junction. (f.o.v., 1.3mm, PPL)

Fig. 5.19 Rim Pn (white) along twin planes in coarse Po grain (grey) with well developed 'lamellar' twinning. Rim consists of agglomerated Pn blebs, indentations between adjacent blebs still visible (upper right). (f.o.v., 0.5mm, PPL)

Fig. 5.20 Interlinking of moderate width Pn rims (white) along adjacent boundaries. Medium sized Po grains (light grey). Little coarsening where rims intersect (cf Fig. 5.17). Individual relatively equant Pn grains picked out by fine fractures along their grain boundaries. (f.o.v., 1mm, PPL).

Fig. 5.21 Example of variation in nature of rim Pn/Po boundaries (contacts) with orientation of Po grain. Lobate/undulate boundary where Pn/Po contact aligned sub-parallel to basal Po parting (Po grain to the right). Boundary with Po grain to left aligned at high angles to basal Po parting, ragged nature due to flame extensions. Changes to more linear entire boundary where aligned at lower angles to basal Po parting after triple junction (f.o.v., 1.6mm, PPL)

Fig. 5.22 Interlinking of coarse Pn rims (white) with cellular Pn enveloping small Po grains which are interstitial to coarser grains. Note the coarsening to blocky Pn where rims and cells meet. (f.o.v., 3.4mm, unXP)

Fig. 5.23 Contact between finer grained Po 'mosaics' (to right and bottom) with medium sized Po grains (left and upper margin) massive ore. Cell Pn enveloping finer Po grains directly adjacent to the contact. (f.o.v., 2mm, unXP).

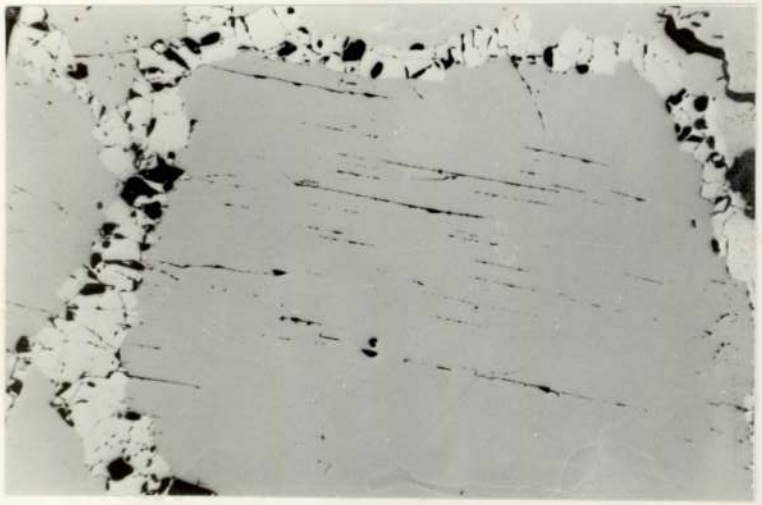

Fig. 5.16

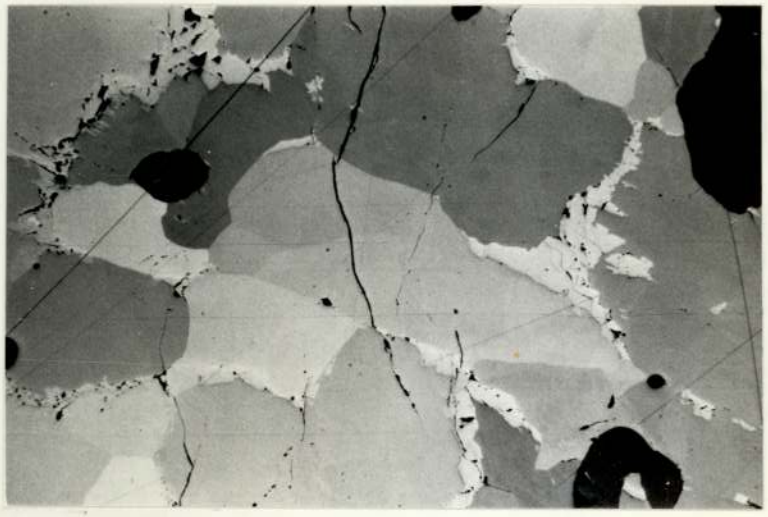

Fig. 5.17

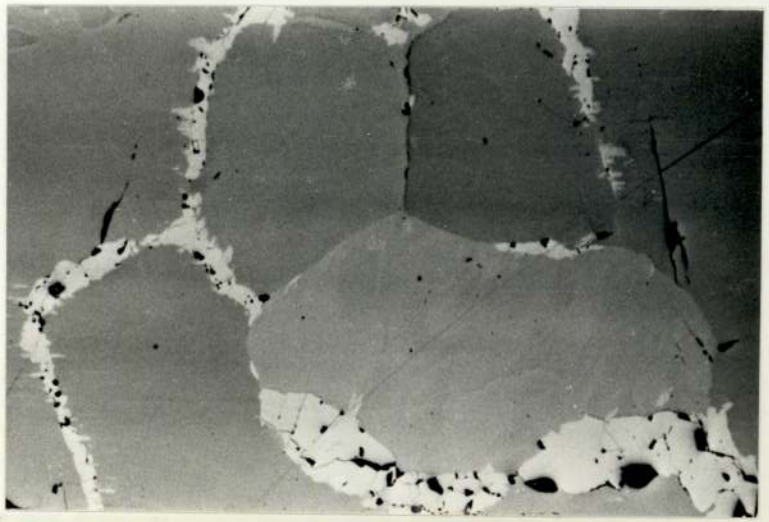

Fig. 5.18

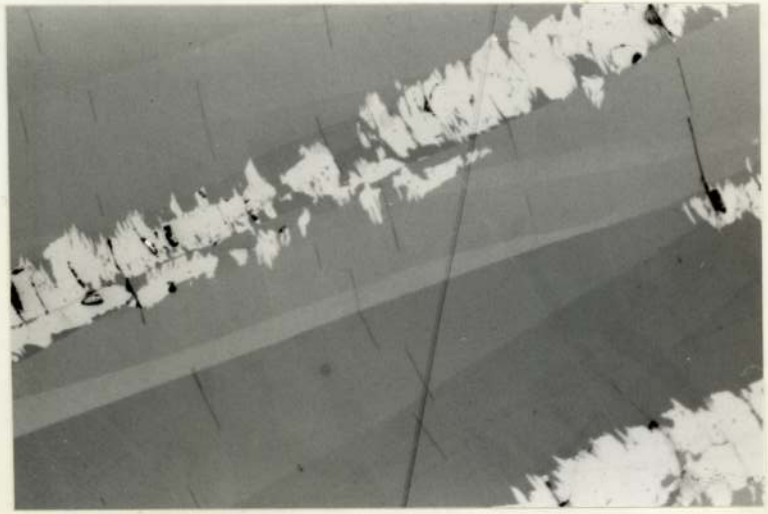

Fig. 5.19

Fig. 5.24 Contact between medium sized Po grains (light grey) and finer Po grains, massive ore. Irregular angular blocky Pn where Pn rims intersect, linked to Cell Pn enveloping boundaries finer Po grains. (f.o.v., 2mm, unXP)

Fig. 5.25 Substantial coarsening to triangular or rounded blocky interstitial Pn where Pn rims along boundaries of adjacent fine Po grains intersect. (f.o.v., 2mm, unXP)

Fig. 5.26 Very fine grained matrix of Po grains (various shades grey), located adjacent to silicate contact of interm. ore bleb. Discrete Pn aggregate (white) with smooth boundaries interstitial to Po. Note also fine bladed aggregates of Pn, located at Po grain boundaries. (f.o.v., 0.5mm, unXP, Oil)

Fig. 5.27 Very fine grained Po matrix in massive ore from Strathcona deep zone. (Individual Po grains, various shades light grey). Discrete ovoid of blocky Pn (white, lower right) interstitial to Po grains. Subhedral Mt grains (dark grey) interstitial to Po.
(f.o.v., 1mm, PPL)

Fig. 5.28 Elongate discrete interstitial Pn (white) along grain boundaries between two finer Po grains (light grey, to right) and medium sized Po grains (to left) (f.o.v., 2mm, unXP).

Fig. 5.29 Irregular granular blocky Pn (white) abutting subhedral Mt grain (dark grey), located at Po (light grey) grain boundary (f.o.v., 1.6mm, unXP)

Fig. 5.30 Network of Mt grains (dark gray) within very fine grained matrix Po grains (various shades, light grey), located close to silicate contact (black, upper margin) of interm. ore veinlet. Pn (white) present as granular blocky aggregates abutting Mt. grains and intergranular to Po. (f.o.v., 2mm, unXP)

Fig. 5.31 Concentration of subhedral Mt (dark grey) within fine grained Po matrix (light grey) in massive ore. Granular blocky Pn (white) associated with Mt. (f.o.v., 2mm, PPL)

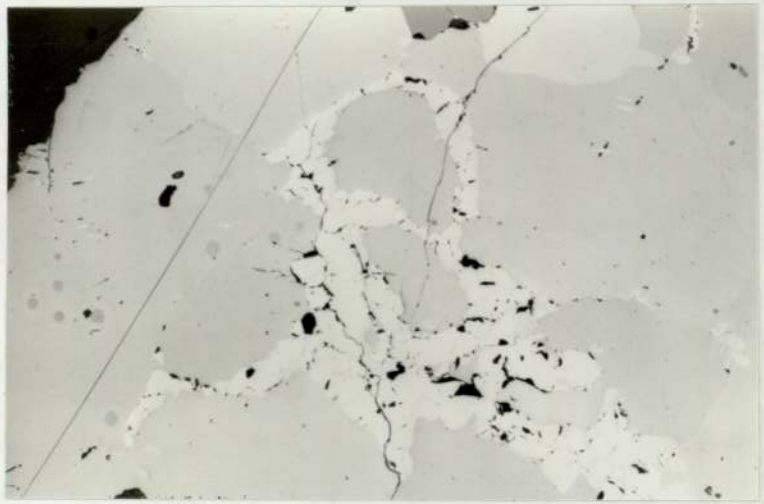

Fig. 5.24

Fig. 5.25

Fig. 5.26

Fig. 5.27

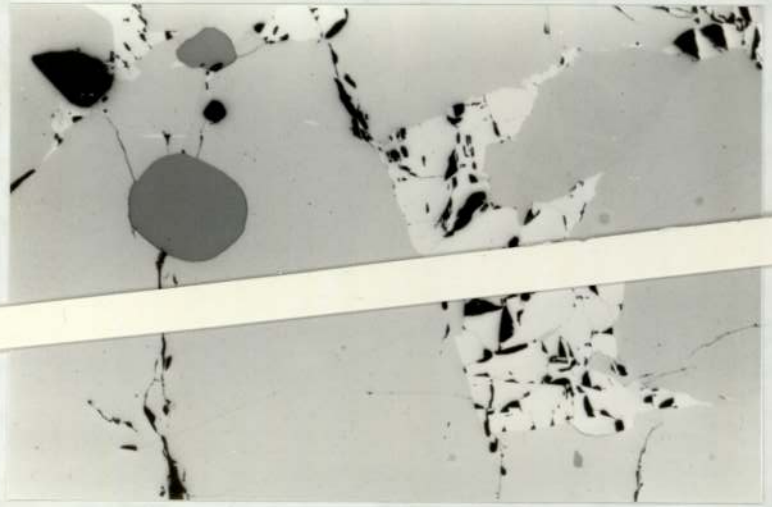

Fig. 5.28

Fig. 5.29

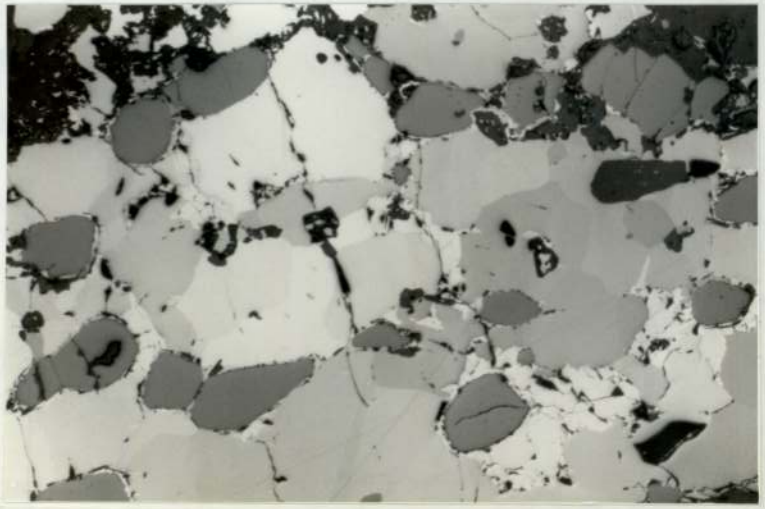

Fig. 5.30

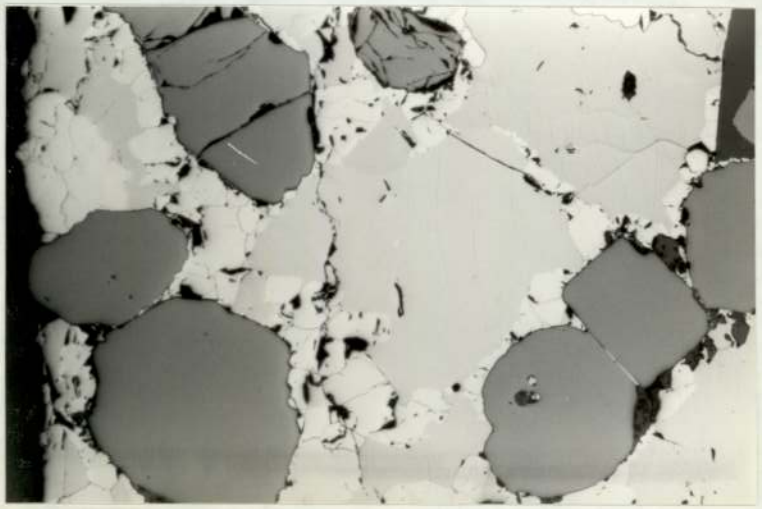

Fig. 5.31

Fig. 5.32 Contact between coarse granular Cp segregation (just visible upper margin, light grey) with adjacent matrix of Po grains (slightly darker grey). Coarse angular stringer of Pn (white) along the contact. Pn protrudes into cusps between adjacent Po grains giving angular Pn/Po contact. Smooth contact with Cp. Adjacent Po matrix relatively depleted in Pn. Grain aggregates of sphalerite (dark grey) located at Cp/Pn contact. (f.o.v., 3.4mm, unXP)

Fig. 5.33 Discrete blocky Pn (white) located at contact between coarse granular Cp (upper margin, light grey) and fine Po grains (darker grey). Patchy Mcl/hex Po intergrowth within Po grains just visible. (f.o.v., 1.6mm, unXP).

Fig. 5.34 Graphic intergrowth of Cp (light grey) and Po (darker grey) at margin of coarse angular Pn stringer (white, edge just visible upper central) (f.o.v., 0.5mm, PPL, Oil)

Fig. 5.35 Pn collars (white) at Cp (light grey), Po (dark grey) contact. Pn/Po contact relatively smooth. Pn/Cp contact ragged due to bladed Pn extensions. (f.o.v., 0.5 mm, PPL, Oil)

Fig. 5.36 Bleb of dissem. ore consisting predominantly of Po grains (light grey). Note corroded sieve-like nature of the silicate contact (black). Euhedral Py (white) located at Po/silicate contact and at Po grain boundaries. Single lobate blocky Pn aggregate (duller white, upper right margin) located at Po/silicate contact (f.o.v., 1mm, PPL)

Fig. 5.37 Two Po grains (light grey) within dissem. ore bleb. Lobate blocky Pn (white) at Po/silicate contact (f.o.v., 0.4mm, PPL, Oil)

Fig. 5.38 Coarse composite Pn veinlet at contact between fine grained Po (light grey) mosaic and coarse Po grain (upper right margin). Veinlet consists of 'massive' stringer of Pn at contact and interlinking network of interstitial granular Pn within fine Po mosaic. Massive ore Str. D. Z., (f.o.v., 3.4mm, unXP).

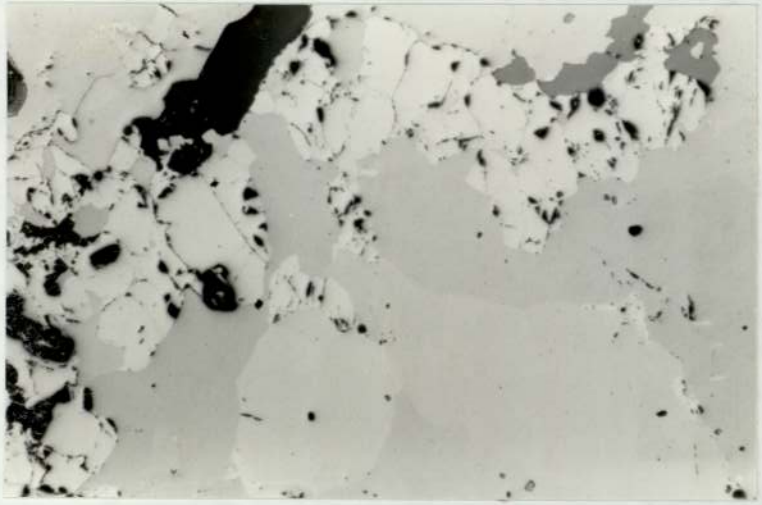

Fig. 5.32

Fig. 5.33

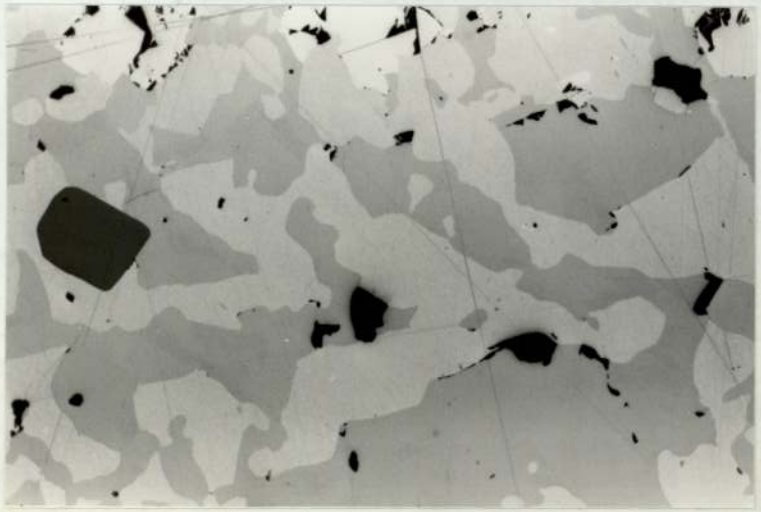

Fig. 5.34

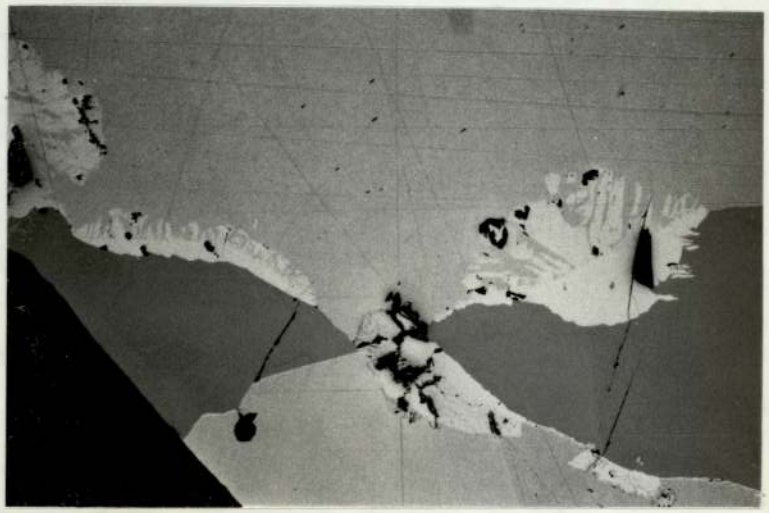

Fig. 5.35

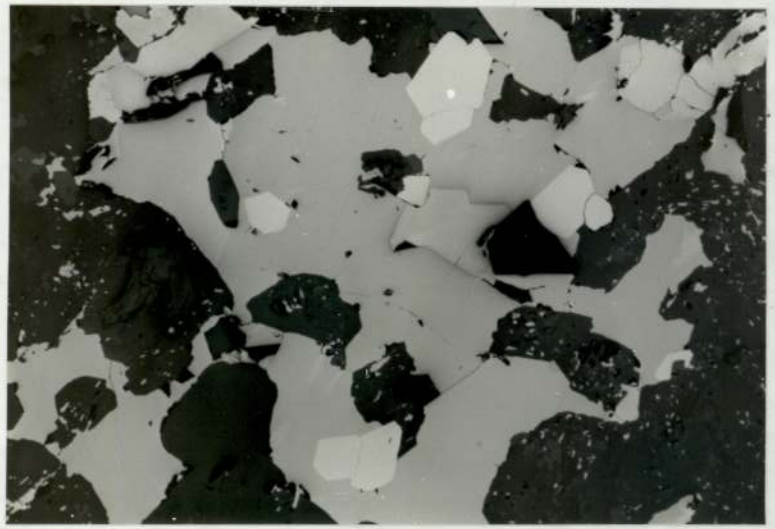

Fig. 5.36

Fig. 5.37

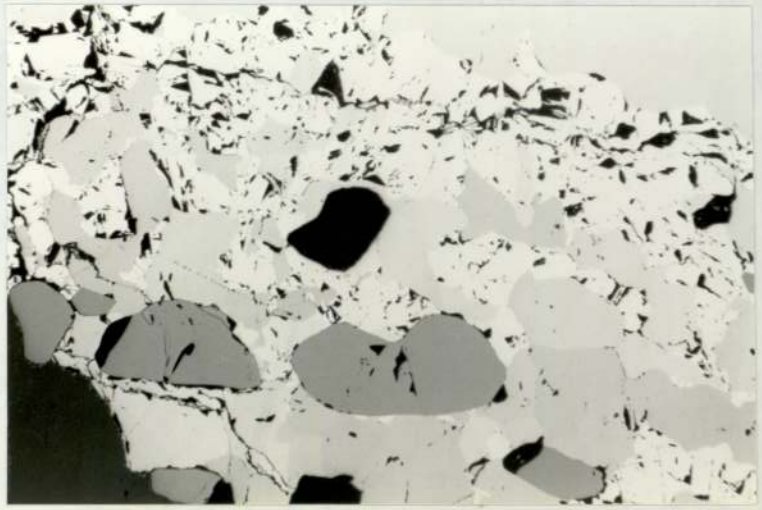

Fig. 5.38

Fig. 5.39

Fig. 5.39 'Acicular' flame-type Pn aggregates at silicate (black)/Po (light grey) contact, dissem. ore. Aggregates consist of a series of sub-parallel partially agglomerated blades with ragged margins. (f.o.v., 0.3mm, PPL, Oil)

Fig. 5.40 Flame-type Pn (white) aggregate at Po (light grey) grain boundary. Aggregate consists of sub-parallel elongate blades with ragged or sinuous margins, which have impinged and overgrown at their base. (f.o.v., 0.16mm, PPL)

Fig. 5.41 Series of individual 'linear' Pn blades (white) or small clumps of blades at Po (grey) grain boundary. Further along the grain boundary (lower right) they pass into more continuous flame-type aggregates (f.o.v., 0.5 mm, PPL, Oil)

Fig. 5.42 Laterally continuous series of partially agglomerated Pn blades (white), present either side of a Po grain boundary, forming a 'herringbone texture'. Within the individual Po grains, the blades are elongate sub-parallel to the basal Po plane. Hence the difference in orientation of the blades either side of grain boundary. Just visible within the right hand Po grain is a patchy Mcl Po (light grey)/hex Po (darker grey) intergrowth. (f.o.v., 0.5mm, PPL, Oil)

Fig. 5.43 (f.o.v., 0.5mm, PPL, Oil) Flame-type Pn (white) aggregates consisting of partially agglomerated blades located at fractures within a moderately anisotropic Po grain. Individual blades and the aggregates are elongate sub-parallel to the basal plane. As the Po grain is sectioned progressively closer to the basal plane the flames become progressively tubbier and more feathery → Fig. 5.44 feathery flames in weakly anisotropic Po grain. (f.o.v. 0.4mm, PPL, Oil). In basal Po sections (rarely observed) the aggregates appear as elongate aborescent rosettes similar to Fig. 5.50.

Fig. 5.47 Elongate flame-type Pn aggregates emanating at ~ right angles from Po twin planes. Note the difference in orientation between flames present in adjacent twins (f.o.v., 1mm, unXP)

Fig. 5.45 Lamellar 'flame-type' Pn aggregates located within defect free area of a moderately anisotropic Po grain. Aggregates elongate sub-parallel to basal Po plane (f.ov., 0.5mm, PPl, Oil)

Fig. 5.46 The aggregates consist of partially impinged and overgrown Pn lamellae or blebs elongate at low angles to the elongation direction of the aggregates (f.o.v., 0.08mm, PPL, Oil).

Fig. 5.48, 5.49 (f.o.v., 0.5mm, PPL, Oil) Figs. 5.50, 5.51 (f.o.v., 0.2mm, PPL, Oil) In basal Po sections flame-type aggregates within defect free areas of the grains appear as aborescent rosettes with deeply embayed serrated or feathery margins. Figs. 5.49 to 5.51 represent progressive serial sections parallel to the basal Po plane, towards the 'core' of the rosette.

Fig. 5.40

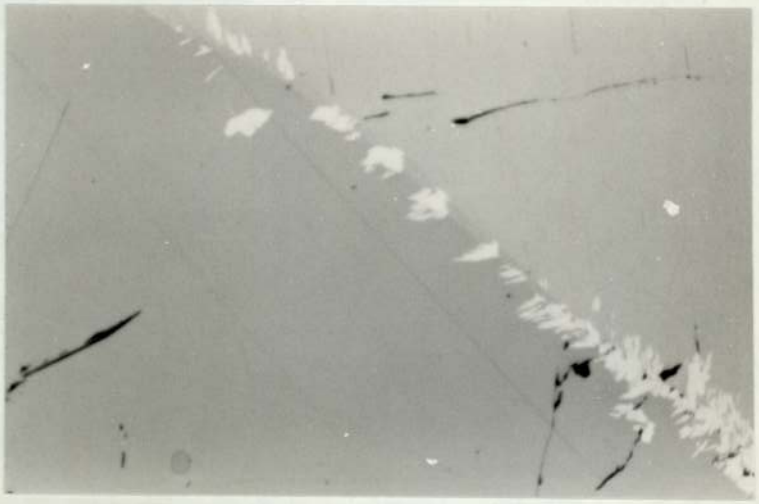

Fig. 5.41

Fig. 5.42

Fig. 5.43

Fig. 5.44

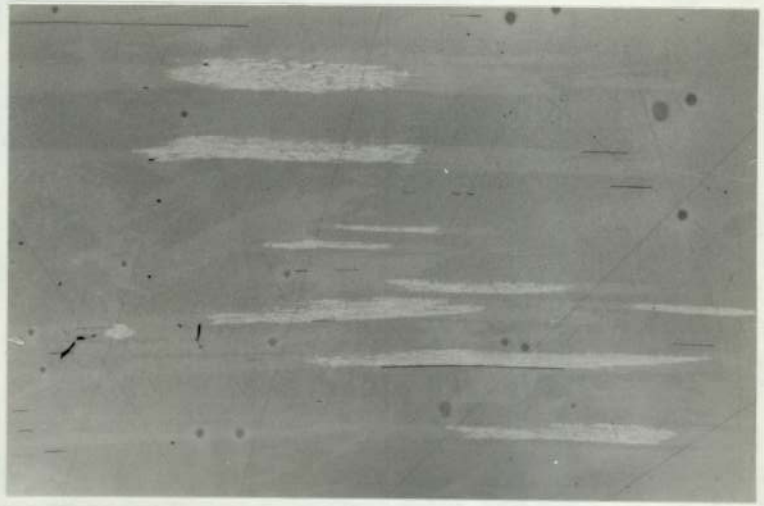

Fig. 5.45

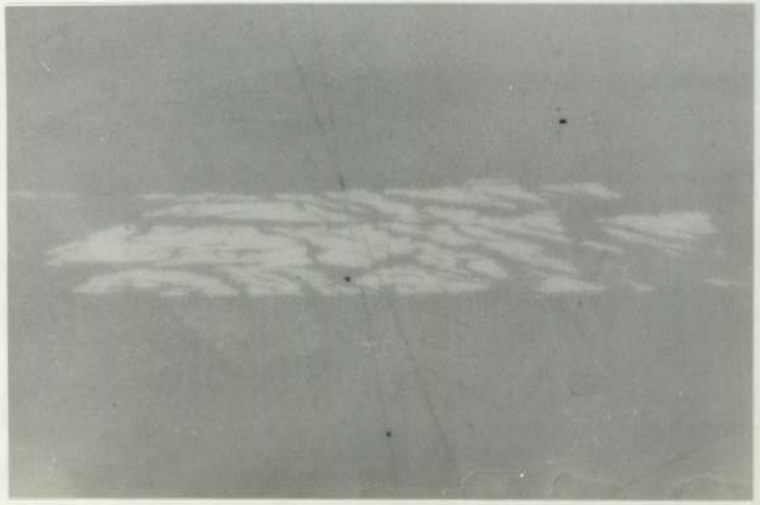

Fig. 5.46

Fig. 5.47

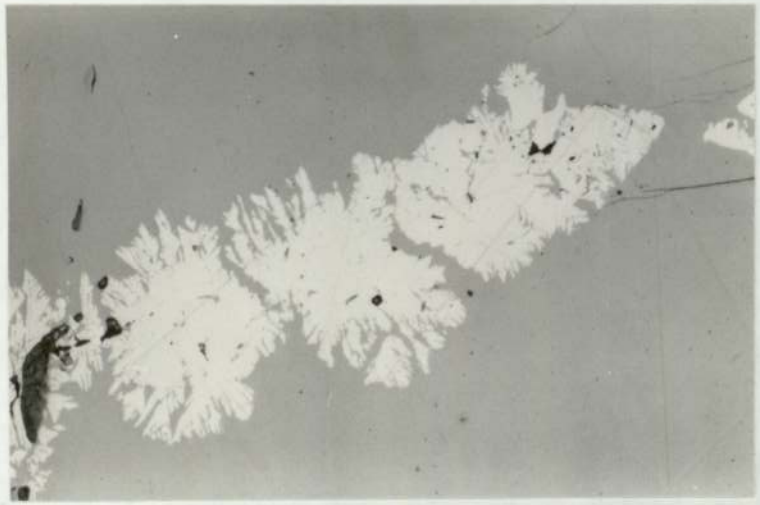

Fig. 5.48

Fig. 5.51

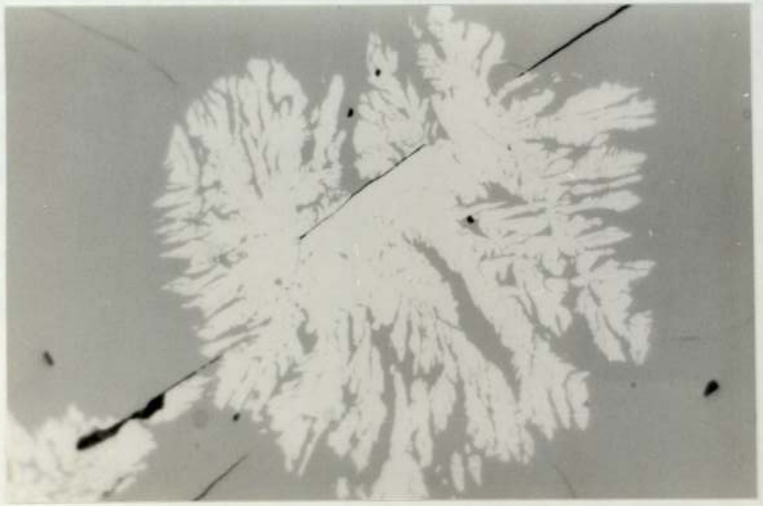

Fig. 5.50

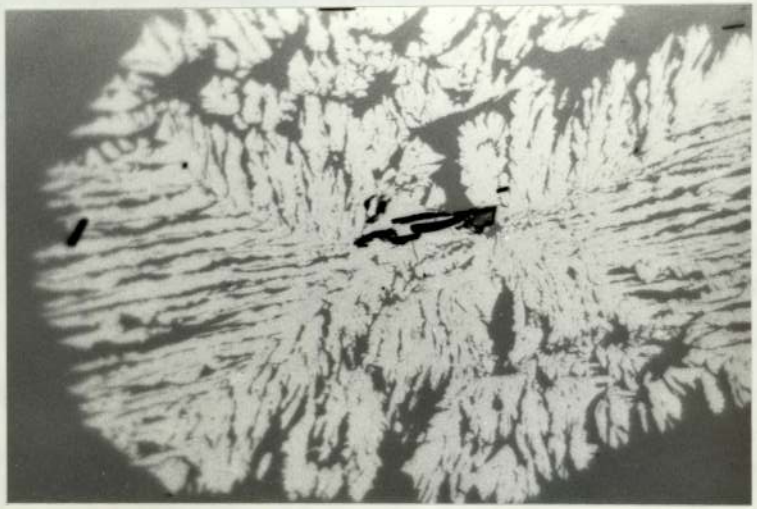

Fig. 5.49

Figs. 5.52, 5.53 (f.o.v., 0.5mm, PPL, Oil). Unusual spindle (Fig. 5.52) and butterfly-shaped flame Pn aggregates (white) within defect free Po (grey). Rare in occurrence. Possibly represent 'lamellar' flame aggregates sectioned at very low angles to the basal Po plane.

Figs. 5.54, 5.55 Massive Pn lenses as extensions to rim Pn (Fig. 5.54) and within defect free areas of Po grain (Fig. 5.55) Formed by coarsening and complete overgrowth of particles in flame-type aggregates. Rare in occurrence (f.o.v. 3.4mm and 2mm respectively, PPL).

Fig. 5.56 'Lozenge' of Cp (light grey) abutting Mt grain (very dark grey) at the margin of a Po grn (darker grey cf Cp). Bladed flame-type Pn aggregate located at Cp/Po contact. (f.o.v., 0.5mm, PPL, Oil).

Fig. 5.57 Mt. grain (dark grey) rimmed by very thin selvage of Ilm. Located close to the silicate (black, upper left)/Po (light grey) contact of a coarse bleb of interm. ore. Partially corroded and replaced by fine grained Po (mottled grey). Feathery flame-type Pn (white) located at contact between Ilm selvage and adjacent Po grain. (f.o.v., 0.3mm, PPL, Oil).

Fig. 5.58 Mt. grain (grey) with thin lamellae and selvage of Ilm. (darker grey) located close to Po (white)/silicate (black, lower left) contact of interm. ore bleb. Mt. corroded and partially replaced by Po. (f.o.v., 0.4mm, PPL, Oil).

Fig. 5.59 External composite intergrowth of Mt and granular Ilm. (both grey) located at contact between silicate inclusion (black) and Po (white) in massive ore. The Ilm. contains a patchy intergorwth of a darker grey phase, possibly pseudobrookite. Discrete grains of Mt. and Ilm. also visible (right hand margin). (f.o.v., 1mm, PPL)

Figs. 5.61, 5.62 (f.o.v., 1mm and 0.65mm, PPL) Illustrate the progressive veining and segmentation of Mt. (dark grey) by Po (light grey) where Mt. occurs close to the (black) silicate/Po contact in coarse blebs of interm. ore or small lenses of massive ore containing large silicate inclusions. In Fig. 5.61 the Mt. is partially segmented by small wedge shaped veinlets and wider more continuous veinlets of very fine grained Po. In Fig. 5.62 the Mt. has been completely disrupted into smaller angular fragments enveloped by fine grained Po. In both cases the outline of the original grain preserved by selvage of Ilm. and silicate (black). In Fig. 5.61 grain aggregate of Sph (darker grey) abuts upper margins Mt. and 'seals' wedged shaped Po veinlets. Similar occurrence of rim Pn (white) just visible on upper left Mt. margin.

Fig. 5.63 Grain aggregates of Sph (very dark grey) abutting silicate (black) within veinlet of Cp (light grey), intermed. ore. (f.o.v., 0.5mm, PPL)

Fig. 5.64 Sph grains (black) interstitial to Po (grey) in massive ore. (f.o.v., 0.5mm, unXP, Oil).

Fig. 5.65 Sph grains (black) enclosed by rim Pn (white). Thin rim of Cp (light grey) at Sph/Po (darker grey) contact (f.o.v., 0.2mm, PPL, Oil)

Fig. 5.66 Lamellae of cub. (dark grey) within Cp (lighter grey) (massive ore Str. Cu-Zone) (f.o.v., 0.5mm, PPL, Oil)

Fig. 5.52

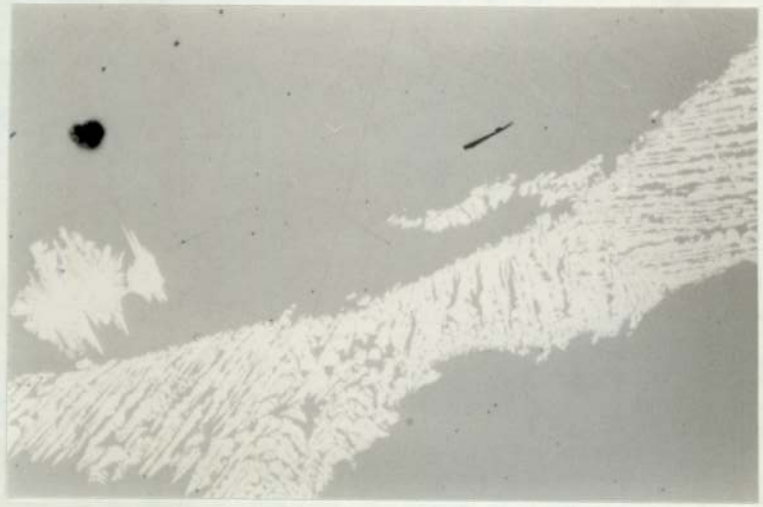

Fig. 5.53

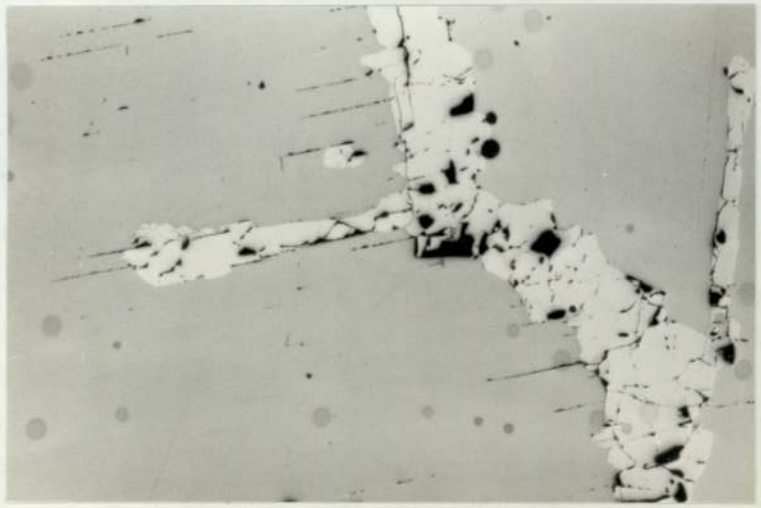

Fig. 5.54

Fig. 5.55

Fig. 5.56

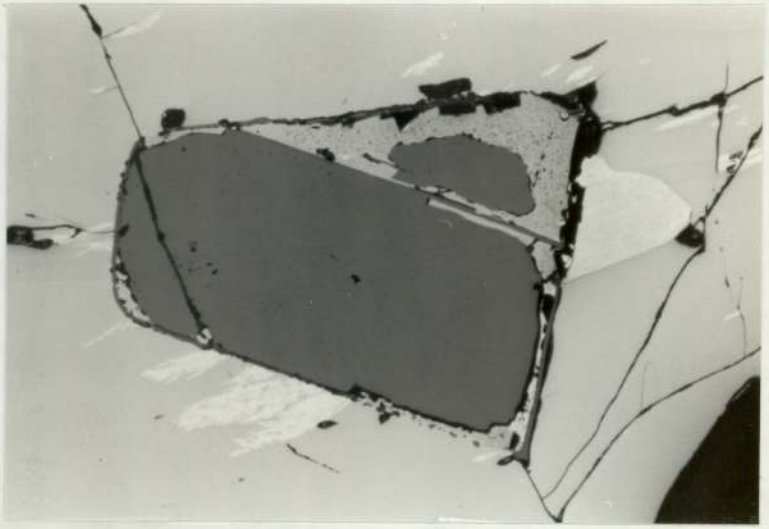

Fig. 5.57

Fig. 5.58

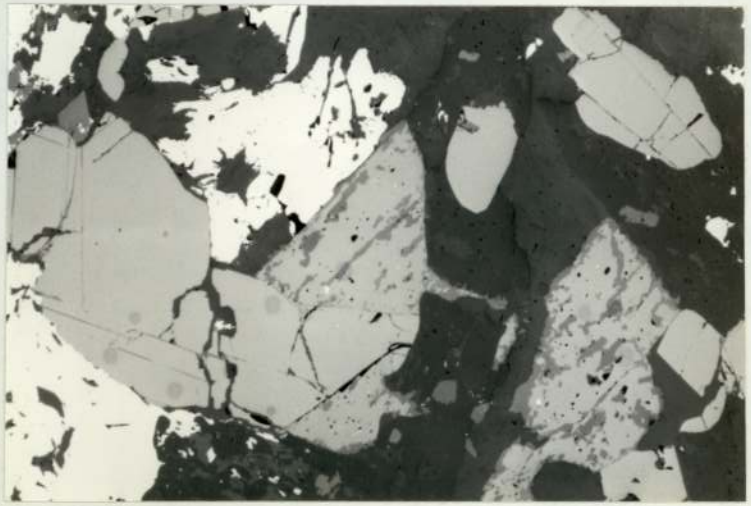

Fig. 5.59

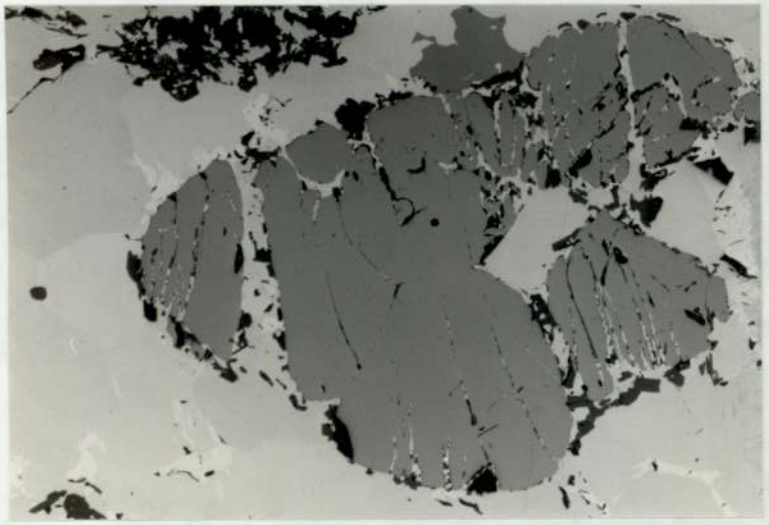

Fig. 5.61

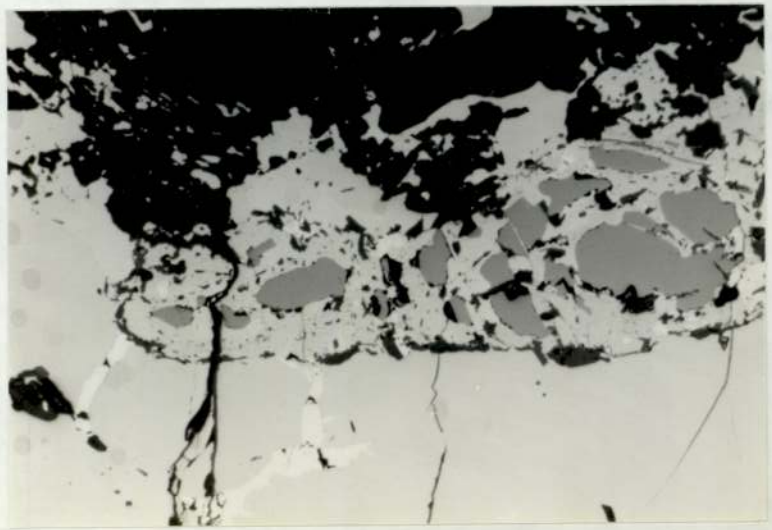

Fig. 5.62

Fig. 5.63

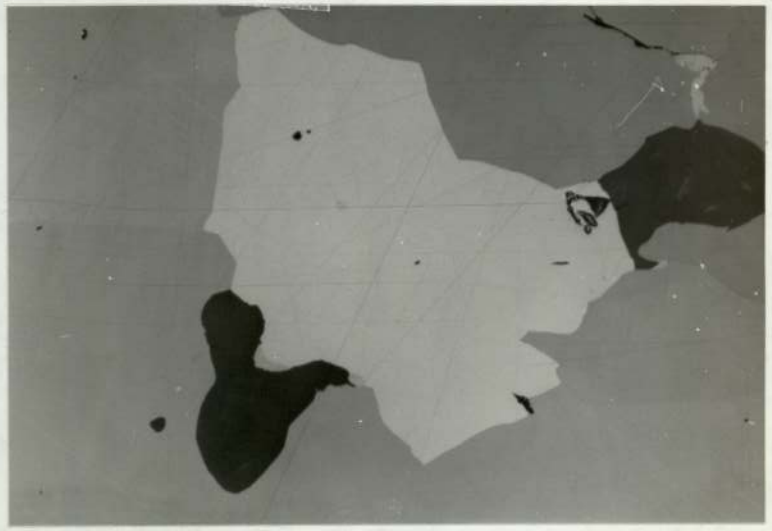

Fig. 5.64

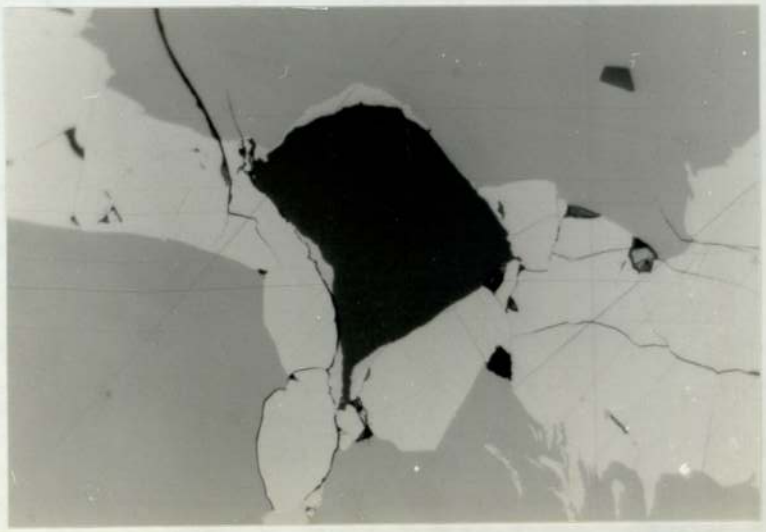

Fig. 5.65

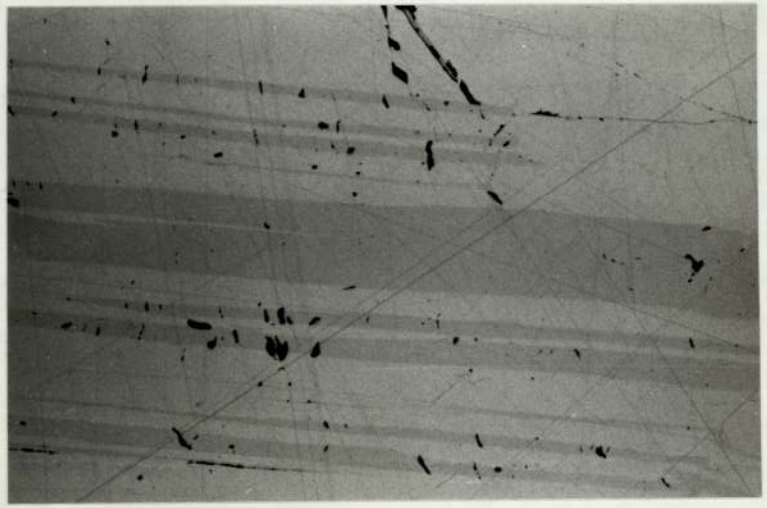

Fig. 5.66

TABLE 6.1 Volumetric Composition of Base Metal Sulphides in the Merensky Suite.

Rock Type, Locality	Po	Pn	Cp	Py	Cub.	Mck.	Ref.
Rustenburg							
Hangingwall norite	51.9	25.8	17.1	4.7			(1)
Merensky pyroxenite							
upper part	53.0	28.8	17.4	1.3			(1)
lower part	42.3	32.8	23.4				(1)
Pegmatitic pyroxenite	45.4	31.8	13.8	4.3			(1)
'reef'	38.8	30.4	22.1	2.0			(1)
Chromitite	43.7	34.6	25.0	1.4			(1)
Mean 1	45.9	30.7	19.8	2.7			(1)
Mean 2	46.9	32.3	17.1	3.4	0.5	0.2	(2)
Mean 3	44.0	33.4	19.7	2.8	0.3	0.1	(3)
Atok.							
Mean	8	13	30	45			(4)
Impala.							
Mean	41	37	18	4			(5)

References: (1) Liebenburg (1969)
(2) Kingston (1977)
(3) Vermaak and Hendricks (1976)
(4) Schwellnus et al. (1976)
(5) Mostert et al. (1982).

TABLE 6.2 Electron Probe Microanalyses of Merensky Reef Sulphides from Rustenburg Mine

Phase	S	Fe	Ni	Co	Cu	Total	( )	S	Fe	Ni	Co	Cu	Structural Formula
				wt %							at %		
Coarse													
Angular Po	38.85	61.17	0.50	0.13	-	100.65	(10)	52.28	47.26	0.37	0.09	-	$(Fe_{9.94}Ni_{0.08}Co_{0.02})_{10.04}S_{11}$
'Hex' Po													
Mosaic Po													
'Hex' Po	38.86	61.17	0.43	0.14	-	100.60	(7)	52.31	47.28	0.32	0.10	-	$(Fe_{9.94}Ni_{0.07}Co_{0.02})_{10.03}S_{11}$
Coarse Granular Pn	33.12	32.01	34.39	0.71	-	100.23	(4)	46.87	26.00	26.58	0.55	-	$(Fe_{4.44}Ni_{4.54}Co_{0.09})_{9.07}S_{8}$
Blocky Pn Stringer	33.02	31.74	34.81	0.73	-	100.30	(4)	46.74	25.79	26.91	0.56	-	$(Fe_{4.41}Ni_{4.61}Co_{0.10})_{9.12}S_{8}$
Blocky Inter-granular Pn	33.11	31.55	35.04	0.68	-	100.38	(7)	46.81	25.61	27.06	0.52	-	$(Fe_{4.38}Ni_{4.62}Co_{0.09})_{9.09}S_{8}$
Pyrite+	52.01 n.d.	47.38 0.2	n.d. 0.2	n.d. 0.2	n.d.	98.73	(8)	65.66	34.34	-	-	-	$Fe_{1.05}S_{2}$
(Vermaak and Hendricks, 1976)													
Hex Po	37.9	59.9	0.2	0.1	-	98.1		52.31	47.46	0.15	0.08		
Pn	31.85	32.95	33.55	0.9	-	99.25		45.78	27.19	26.33	0.70		

Po - pyrrhotite; Mcl - Monoclinic; Hex - hexagonal; Pn - Pentlandite; ( ) No. of individual spot analyses; + energy dispersive analyses.

TABLE 6.3 Electron Probe Microanalyses of Merensky Reef Sulphides from Published Sources

Phase	S	Fe	wt % Ni	Co	Cu	Total	S	Fe	at % Ni	Co	Cu	Structural Formula
(Western Mine, Marikana; Brynard et al. 1976)												
Mcl Po	40.1	60.4	0.6	0.3		101.4	53.28	46.07	0.43	0.22		$(Fe_{6.92}Ni_{0.06}Co_{0.03})_{7.02}S_8$
Mcl Po	40.0	61.3	0.6	0.4		101.5	52.35	46.22	0.36	0.29		$(Fe_{6.96}Ni_{0.05}Co_{0.04})_{7.05}S_8$
Mcl Po(?)	39.2	61.3	0.6	0.3		101.4	52.35	46.99	0.44	0.22	{	$(Fe_{7.18}Ni_{0.08}Co_{0.03})_{7.29}S_8$
												$(Fe_{9.81}Ni_{0.09}Co_{0.05})_{9.95}S_{11}$
Hex Po	39.1	61.4	0.6	0.3		101.4	52.24	47.10	0.44	0.22		$(Fe_{9.92}Ni_{0.09}Co_{0.05})_{10.06}S_{11}$
Hex Po	38.5	62.9	0.5	0.3		102.2	51.30	48.12	0.36	0.22		$(Fe_{10.32}Ni_{0.08}Co_{0.05})_{10.45}S_{11}$
Hex Po	39.0	62.0	0.5	0.3		101.8	51.98	47.44	0.36	0.22		$(Fe_{10.04}Ni_{0.08}Co_{0.05})_{10.17}S_{11}$
Pn	32.1	33.3	34.3	0.8		100.5	45.61	27.16	26.61	0.62		$(Fe_{4.76}Ni_{4.67}Co_{0.11})_{9.54}S_8$
Pn	31.6	35.8	32.3	0.8		100.5	45.00	29.26	25.12	0.62		$(Fe_{5.20}Ni_{4.47}Co_{0.11})_{9.77}S_8$
Pn	31.8	32.8	35.2	0.8		100.6	45.24	26.79	27.35	0.62		$(Fe_{4.74}Ni_{4.84}Co_{0.11})_{9.09}S_8$
Py	53.0	47.5	0.4	0.3		101.2	65.72	33.81	0.27	0.20		$(Fe_{1.03}Ni_{0.01}Co_{0.01})_{1.05}S_2$
Py	52.7	47.6	0.4	0.3		101.0	65.54	33.99	0.27	0.20		$(Fe_{1.04}Ni_{0.01}Co_{0.01})_{1.06}S_2$
(Impala Pt. Mine; Mostert et al. 1982)												
Mcl Po	39.6	59.3	0.1	0.1		99.1	53.69	46.16	0.08	0.07		$(Fe_{6.88}Ni_{0.01}Co_{0.01})_{6.90}S_8$
Mcl Po	39.2	60.9	-	-		100.1	52.86	47.14	-	-		$Fe_{7.14}S_8$
Mcl Po	39.2	60.1	-	0.1		99.4	53.15	46.78	-	0.07		$(Fe_{7.04}Co_{0.01})_{7.05}S_8$
Mcl Po	39.8	60.1	-	0.1		100.0	53.53	46.46	-	0.07		$(Fe_{6.94}Co_{0.01})_{6.95}S_8$
Pn	33.7	31.4	33.9	0.7	0.5	100.2	47.55	25.43	26.12	0.54	0.36	$(Fe_{4.28}Ni_{4.40}Cu_{0.06}Co_{0.09})_{8.83}S_8$
Pn	32.9	32.6	34.3	0.7	-	100.5	46.52	26.46	26.48	0.54	-	$(Fe_{4.55}Ni_{4.55}Co_{0.09})_{9.19}S_8$
Pn	33.7	31.2	33.9	0.7	0.2	99.7	47.73	25.37	26.22	0.54	0.14	$(Fe_{4.20}Ni_{4.40}Cu_{0.02}Co_{0.09})_{8.76}S_8$
Pn	33.7	31.7	34.0	0.8	-	100.2	47.53	25.67	26.19	0.61	-	$(Fe_{4.32}Ni_{4.41}Co_{0.10})_{8.83}S_8$
Cp	34.7	30.6	-	0.1	34.8	100.2	49.91	25.05	-	-	25.04	$(Cu_{1.01}Fe_{1.01})_{2.02}S_2$
Cp	35.0	30.7	-	-	34.3	100.0	50.05	25.20	-	-	24.75	$(Cu_{0.98}Fe_{1.00})_{1.98}S_2$
Cp	33.8	30.6	-	-	34.8	99.2	49.04	25.48	-	-	25.48	$(Cu_{1.04}Fe_{1.04})_{2.08}S_2$
Cp	34.9	31.0	-	-	34.0	99.9	49.96	25.48	-	-	25.56	$(Cu_{0.98}Fe_{1.00})_{1.98}S_2$

Po - pyrrhotite, Mcl - monoclinic, Hex - 'hexagonal'; Pn - Pentlandite; Py - Pyrite; Cp - Chalcopyrite.

TABLE 6.4 Pentlandite Textural Types in the Rustenburg Ore

Textural Type	Mode of Occurrence	Dimensions (mm) (W - width, L - length)	Associations
1. Blocky Pn stringers or rims (Fig. 6.11)	(i) on margin dissemination as continuous → discontinuous rim abutting silicate walls. Very Common.	Variable W ~ 0.075 - 0.4	Abuts coarser Po on inner margin (interface lobate). May enclose Cp (interface mutual) or more rarely thin rims of mosaic Po (interface embayed due to penetration of Pn into cusps adjacent to fine Po grains). Where silicate walls encroach and dissem narrows passes into coarse granular Pn.
(Fig 6.10)	(ii) at contact between areas of mosaic Po and coarse angular Po grains. Common.	Variable W ~0.1 - 0.4	Embayed interface mosaic Po. Lobate interface coarse Po.
	(iii) along margins of pyrite grains. Rare.	Variable W ~0.05-0.15	Encloses fine grained Po and thin Cp rims. Mutual interface Cp, embayed fine Po.
2. Coarse Granular Pn (Fig. 6.12)	(i) where silicate walls encroach and dissemination narrows. Common.	Max ~2	May contain inclusions of Po. Veined by chlorite - serpentine.
(Figs. 6.13 to 6.15)	(ii) in rectangular or V-shaped sulphide terminations. Very Common.	~0.6 - 1 (W)	Enclose coarser Cp patches - scalloped interface.
3. Finer Pn Textural Types			Always associated with areas of fine grained mosaic pyrrhotite
(i) Blocky Pentlandite Cores (Fig. 6.16)	Centre of Py free mosaic Po areas Rare	~ 0.2	- on margins Py/Po intergrowths

TABLE 6.4 (Continued)

Textural Type	Mode of Occurrence	Dimensions (mm) (W - width, L - length)	Associations
(ii) Intergranular Blocky Pentlandite (Fig. 6.17)	Discrete Pn grains in fine grained Po mosaics. Common.	~ 0.05 - 0.1	- Py free mosaic Po in sulphide terminations. Smooth mutual interface with Po.
(iii) Interstitial pentlandite rounded blebs. (Fig. 6.18)	T-junctions in fine grained Po mosaics	~ 0.002	Py free mosaic Po in sulphide terminations
triangular or star shaped blebs.	T-junctions in fine grained Po mosaics	~ 0.005 - 0.010	Py free mosaic Po in sulphide terminations
discrete Pn grains	'	~0.02	Py free mosaic Po in sulphide terminations grades into intergranular blocky Pn
(iv) Pn lozenges	along Po grain boundaries in fine grained mosaics	~ 0.005 - 0.010 (W)	Py free mosaic Po in sulphide terminations grades into intergranular blocky Pn
Elongate blebs	along Po grain boundaries in fine grained mosaics	~ 0.002 (W)	Py free mosaic Po in sulphide terminations grades in intergranular blocky Pn
4. Pn Lamellae (Fig. 6.19)	Within coarse angular Po grains	~0.01 - 0.02 (L) ~0.001 - 0.002 (W)	Smaller-smooth interface Po: larger - more crenulate interface. Orientated ⊥ to trace 'C' axis.
5. Flame-type pentlandite. Very Rare	(i) extensions to blocky Pn stringers (ii) Herringbone Pn. Po. twin bound (iii) Pn flames. silicate margin.	~ 0.02 (L)	

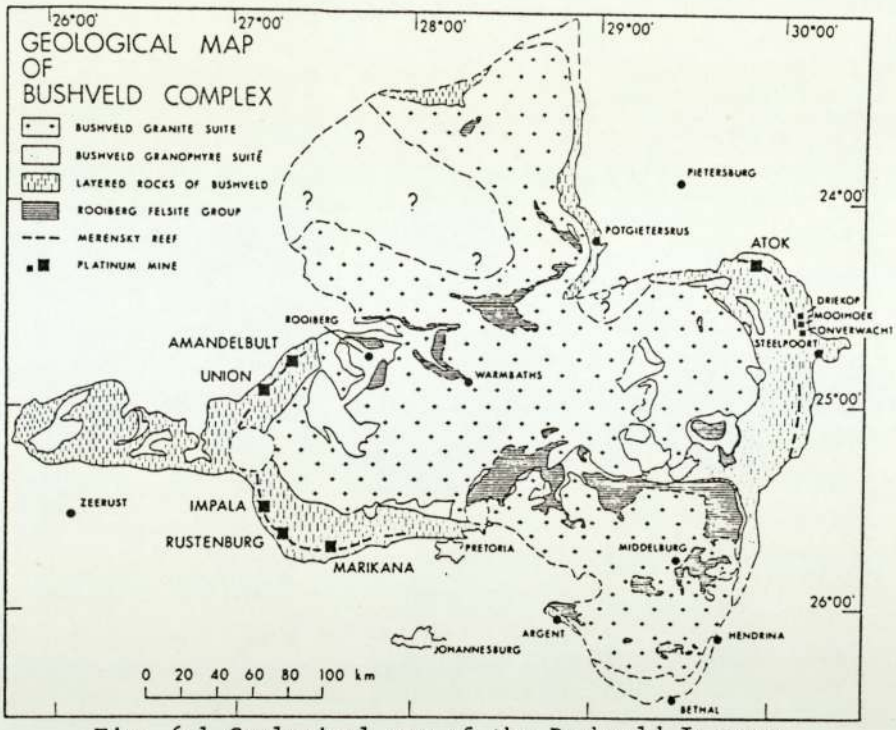

Fig. 6.1 Geological map of the Bushveld Igneous Complex (after Naldrett, 1981b)

Fig. 6.2 Generalised stratigraphic column of the layered mafic rocks of the Bushveld Complex (after Naldrett 1981b)

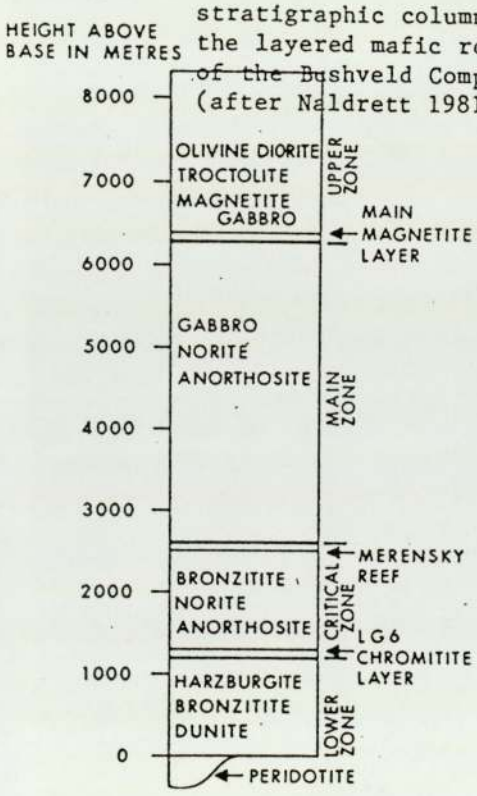

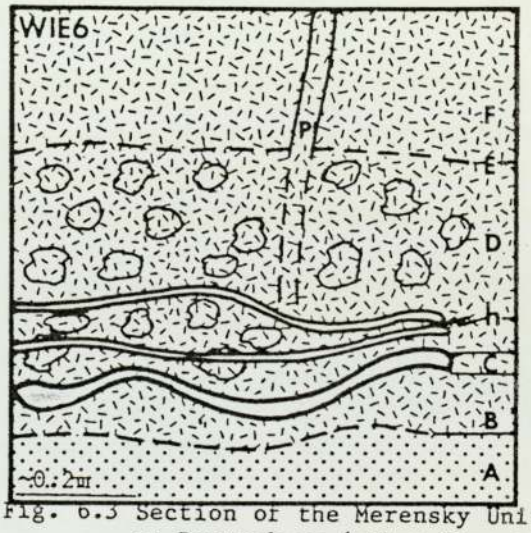

Fig. 6.3 Section of the Merensky Unit at Rustenburg (after Kingston, 1977).

A - F/W spotted anorthosite
B - thin white anorthosite
C - basal chromite band
D - Reef pegmatitic pyroxenite
E - top chromite band
F - Merensky Pyroxenite
P - Qtz-mica-feldsp. vein
H - curving chloritic fractures

Fig. 6.4 Part of an angular sulphide bleb interstitial to the enclosing silicate grains (black). Dominated by a coarse angular Po grain (dark grey) with a more bireflecting/anisotropic twin lamellae (white). Silicate contact relatively straight and 'uncorroded'. Note also coarse granular Pn (white, lower right). (f.o.v., 2mm, PPL)

Fig. 6.5 'Mosaic' of interlocking fine-grained Po (various shades grey) protruding into coarse angular Po grain (dark grey). Coarse grain in optical continuity either side of 'mosaic'. (f.o.v., 3.4 mm, unXP)

Fig. 6.6 Subhedral aggregate of Py grains (white) enveloped by Po grns (grey). Fine-grained Po veinlets penetrate along Py grn bounds and segment the aggregate. Blocky Pn stringer (white pitted) along the contact with the enclosing silicate (black). Partially envelopes the Py and fine-grained Po (along the upper margin; see Fig. 6.7) (f.o.v., 2mm, PPL)

Fig. 6.7 Margins of Py grains (white) corroded by fine-grained Po (grey). Cp (lighter grey, upper right) 'sandwiched' between enveloping Pn (white) and 'follows' Po into fine veinlet separating 'corroded' Py grns. (f.o.v., 1mm, PPL)

Fig. 6.8 Angular Py fragments (white) preserving 'ghost outline' of original square xtal aggregate, enveloped by 'mosaic' of very fine grained interlocking Po grns (various shades grey). Silicate contact (black) just visible, lower margin. Where relatively Py free (left hand margin) Po 'mosaic' coarser grained and in contact with coarse angular Po grain (light grey, edge just visible lower left margin) (f.o.v., 3.4 mm, PPL)

Fig. 6.9 Angular pyrite fragment (white lower right) within 'mosaic' very fine grained Po (various shades grey). Individual Po grains contain 'sub-grains' with angular boundaries, which interlock in a 'jigsaw fashion' giving the appearance of undulose extinction (f.o.v., 2mm, unXP)

Fig. 6.10 Py-free mosaic of fine grained Po (various shades grey) occupying a 'depression' in the enclosing silicate wall (black). Note the regular lobate silicate protrusions and uncorroded nature of the Po/silicate contact. Mosaic Po in contact with coarse angular Po (more even grey, just visible upper margin). Part of this contact occupied by granular Pn rim (white with cross-cutting fractures, upper left). (f.o.v., 2mm, unXP)

Fig. 6.11 Continuous stringer or rim of Pn (white) located at contact between coarse angular Po grain (light grey) and enclosing silicate (black) (f.o.v., 2mm, PPL).

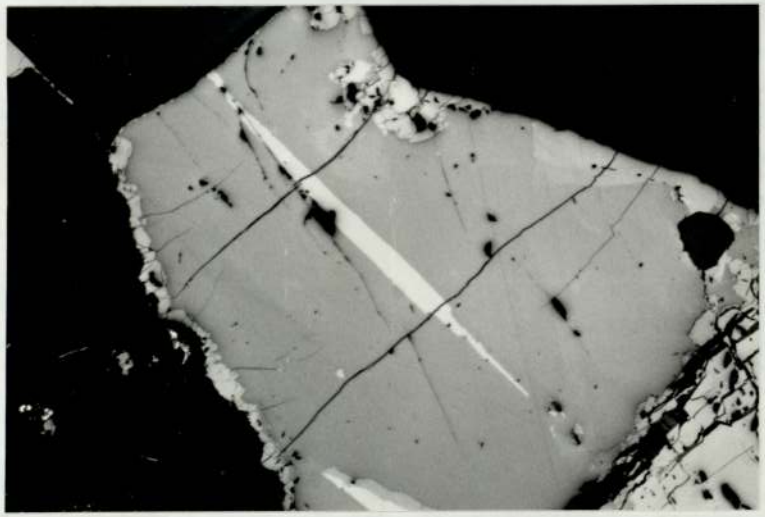

Fig. 6.4

Fig. 6.5

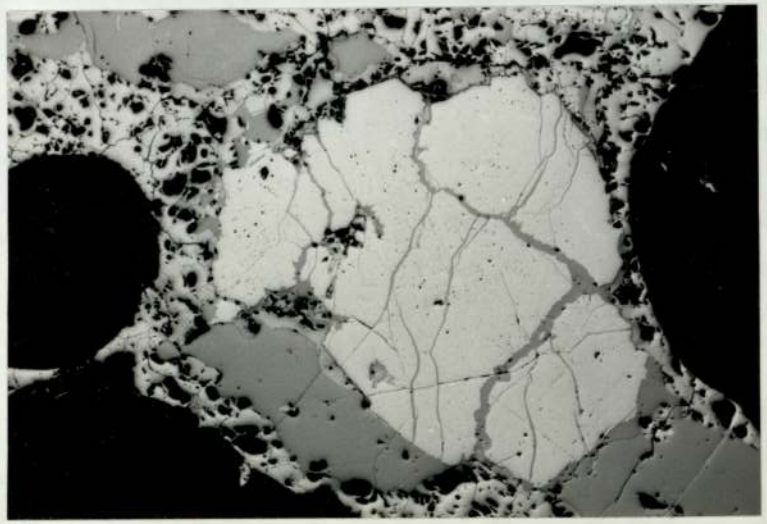

Fig. 6.6

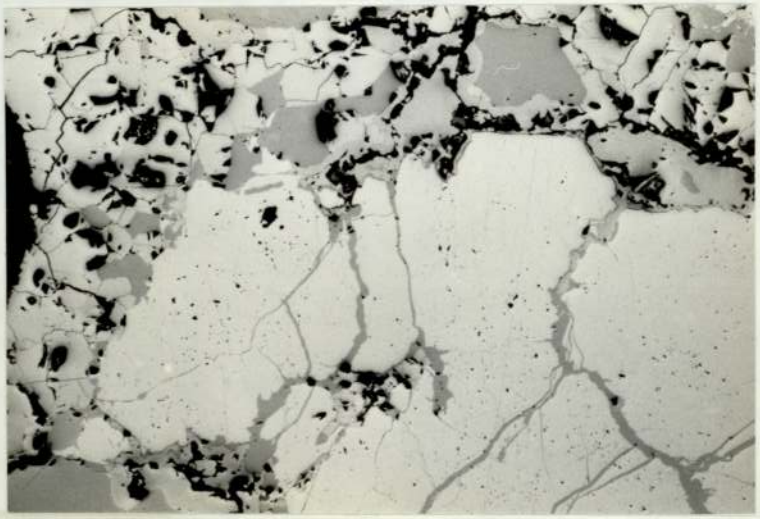

Fig. 6.7

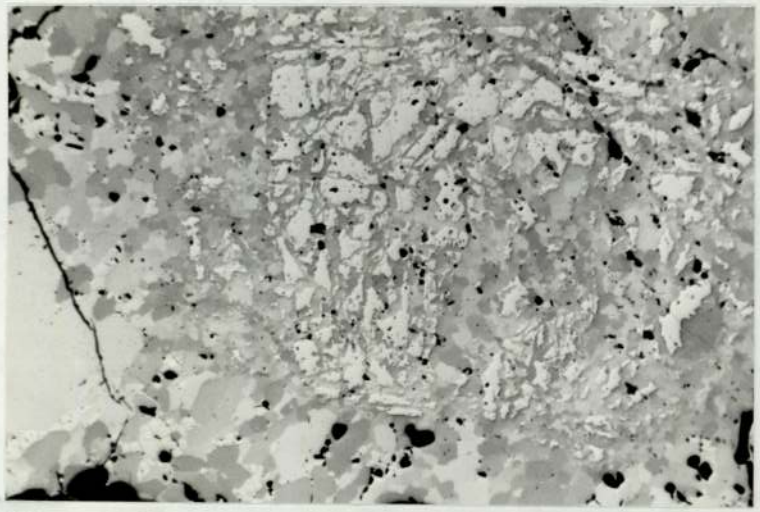

Fig. 6.8

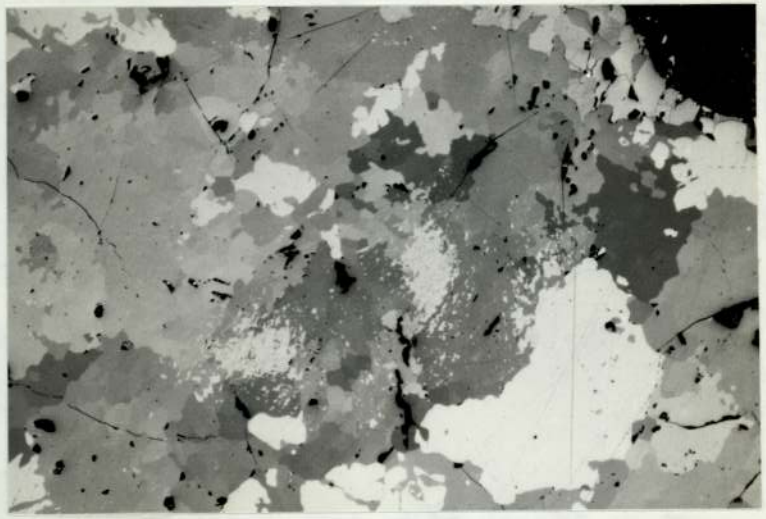

Fig. 6.9

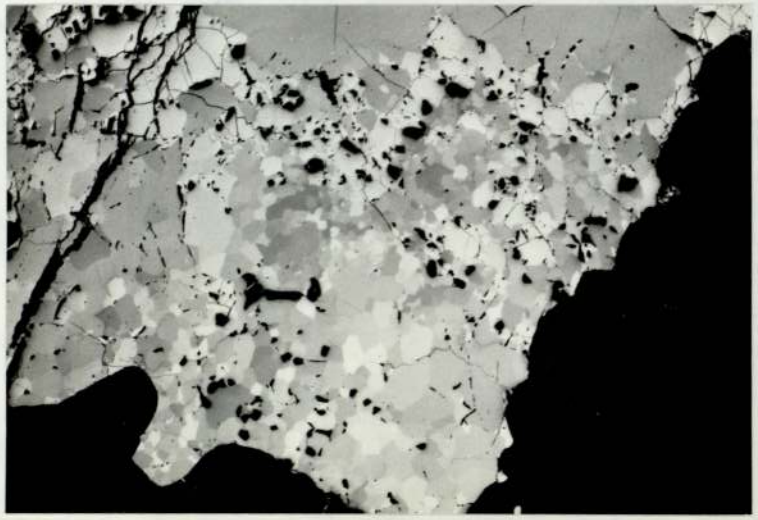

Fig. 6.10

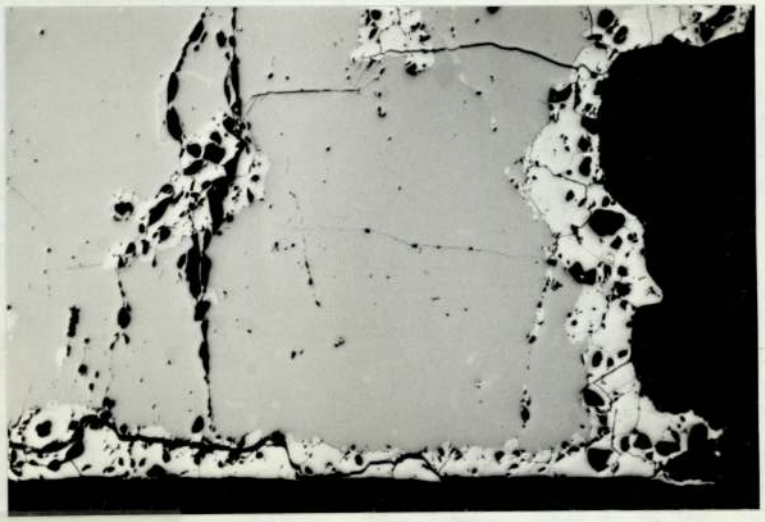

Fig. 6.11

Fig. 6.12 Coarse granular Pn (white) located where the 'walls' of the enclosing silicate (black) encroach and dissem. narrows. Contains inclusions of Po grains (light grey) and irregular cross-cutting silicate 'alteration' veinlets (black). (f.o.v., 3.4mm, PPL).

Fig. 6.13 Rectangular terminations to dissem. sulphide bleb penetrating between into cusps between enclosing coarse silicate grains (black). Terminations occupied by blocky masses of Cp (light grey, upper left, right margin) which are enclosed by granular blocky Pn (white). Granular Pn in contact with coarse angular Po which occupies 'core' of the sulphide bleb (grey, lower central) (f.o.v., 3.4mm, PPL)

Fig. 6.14 Blocky granular Pn (white) in 'rectangular termination' to sulphide bleb lensing out along silicate wall (black). Coarse angular Po grain (grey). (f.o.v., 2mm, PPL)

Fig. 6.15 Small rectangular sulphide bleb in silicate (black). Section cut at right angles to rectangular termination of larger sulphide bleb (cf 6.13, 6.14), hence dominated by granular blocky Pn (white) rather than Po (light grey) (f.o.v., 1mm, PPL)

Fig. 6.16 Rectangular termination to dissem. sulphide bleb occupied by mosaic of fine grained Po (mottled, various shades light grey, left). In contact with coarse angular Po grn (light grey, to right) occupying core of dissem. Blocky Pn stringer (white) along Po/silicate contact (black). Pn/Po contact angular. Blocky Pn at core of mosaic Po. Small (bright white) P.G.M. at silicate contact (lower right), enclosed by Pn stringer. (f.o.v., 2mm, PPL)

Fig. 6.17 Fine grained 'mosaic' of polygonal Po grains in different orientations (various shades grey). Blocky Pn (white) intergranular to Po. Numerous small Pn blebs and fine rims at Po grain boundaries or interstices. (f.o.v., 11m, PPL)

Fig. 6.18 Fine grained mosaic of Po (various shades grey). Interstitial triangular or 'star shaped' blebs of Pn (white). Minute elongate Pn blebs or larger Pn 'lozenges' along Po grain boundaries. No cross-cutting of Po grains by Pn (f.o.v., 0.5mm, unXP, Oil)

Fig. 6.19 Orientated 'lenticular lamellae' of Pn (white) within coarse angular Po grain (dark grey). Little impingement between adjacent lamellae. Rare in occurrence. (f.o.v., 0.2mm, PPL, Oil)

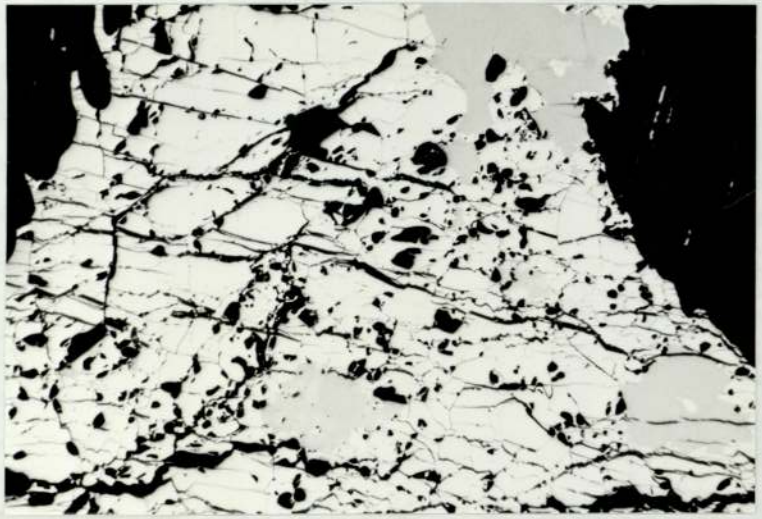

Fig. 6.12

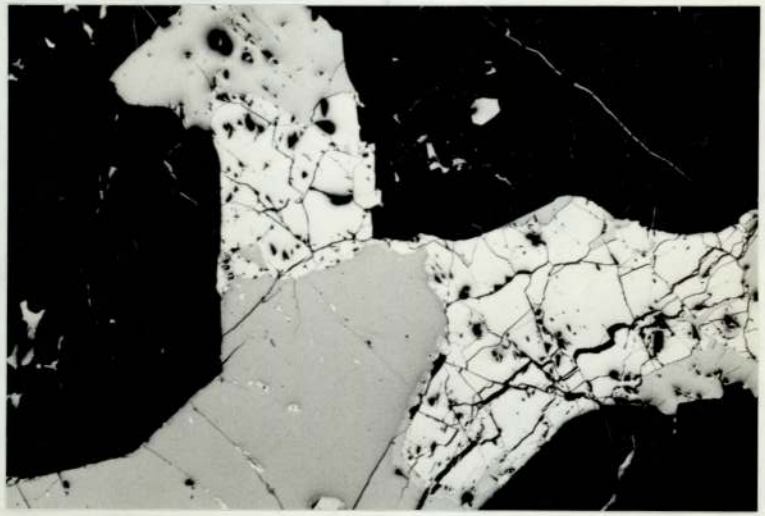

Fig. 6.13

Fig. 6.14

Fig. 6.15

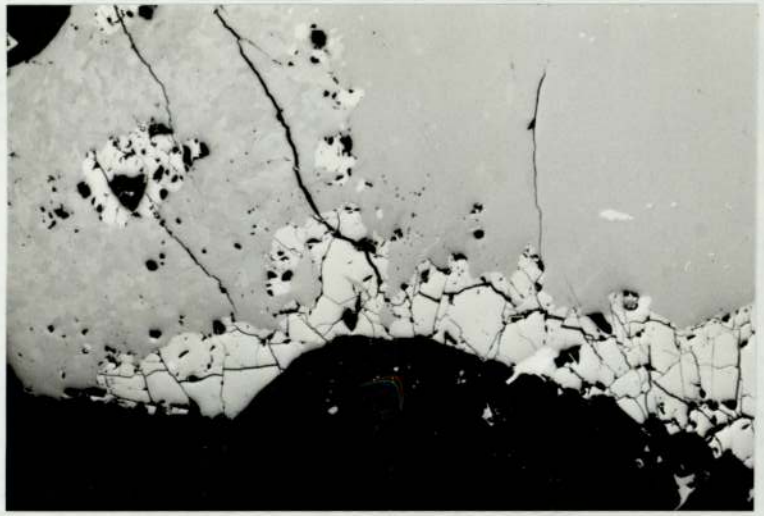

Fig. 6.16

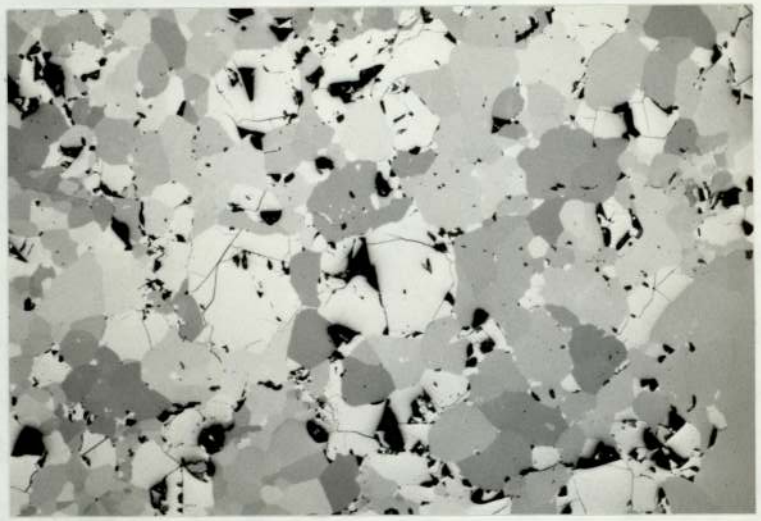

Fig. 6.17

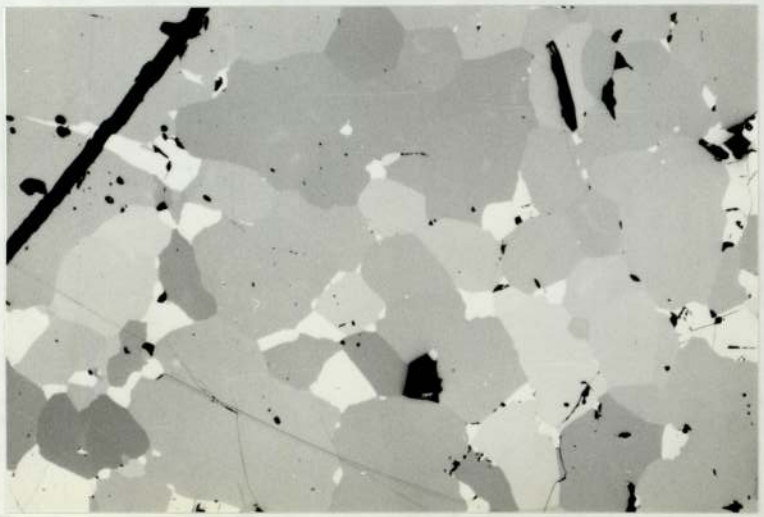

Fig. 6.18

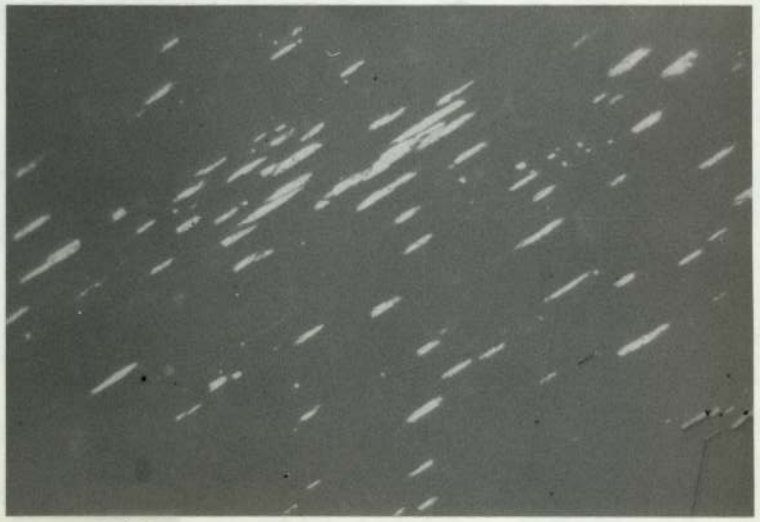

Fig. 6.19

TABLE 7.1 Electron Probe Microanalyses of Minerals in the Sarqa Intrusion, South Greenland

Sample No.	Phase	Wt % S	Fe	Ni	Co	Cu	Total	At % ( )	S	Fe	Ni	Co	Cu	Structural Formula
SQ1	Tr*	36.48	63.59	n.d.	0.12	n.d.	100.19	(11)	49.94	49.97	-	0.09	-	$(Fe_{1.001}Co_{0.002})_{1.003}S$
SQ1	Tr×	34.52	63.70	n.d.	n.d.	n.d.	98.22	(6)	48.56	51.44	-	-	-	$Fe_{1.06}S$
SQ1	Mck*	35.84	60.79	3.60	0.34	0.35	100.92	(6)	49.05	47.76	2.69	0.25	0.24	$(Fe_{0.973}Ni_{0.055}Co_{0.005}Cu_{0.005})_{1.038}S$
SQ1	Mck×	33.85	59.55	3.44	n.d.	0.43	97.37	(7)	48.26	48.75	2.68	-	0.31	$(Fe_{1.01}Ni_{0.06}Co_{0.01})_{1.08}S$
SQ3	Pn×	30.67	34.42	30.05	0.77	n.d.	95.91	(4)	45.60	29.38	24.40	0.62	-	$(Fe_{5.15}Ni_{4.28}Co_{0.11})_{9.54}S_8$
SQ3	Pn+	32.67	34.42	30.05	0.77	n.d.	97.91		47.17	28.53	23.70	0.60	-	
SQ4	Cp×	32.97	31.45	n.d.	n.d.	34.63	99.05	(5)	48.13	26.36	-	-	25.51	$Cu_{1.06}Fe_{1.20}S_2$
SQ4	Cub×	33.15	42.27	n.d.	n.d.	22.79	98.21	(4)	48.10	35.21	-	-	16.69	$Cu_{1.00}Fe_{2.20}S_3$
		Mg	Fe	Co	Ni	Cu	S	OH						
SQ3	Val	7.70	32.06	0.3	0.2	17.37	21.87		20.99		(9)			

* wavelength dispersive analyses; × energy dispersive analyses; +corrected for error in S; ( ) No. of individual spot analyses;

Tr - troilite, Mck - Mackinawite, Pn - Pentlandite, Cp - Chalcopyrite, Cub - Cubanite, Val - Valleriite

TABLE 7.2 Pentlandite Inclusions in Granular Chalcopyrite from the Sarqa Intrusion

Morphology of inclusion		Occurrence	Average Dimensions (μm)	Contact with Chalcopyrite	Other Associations
Pn lenses	- regular	rare	~600 × 200	interface step-like crenulate	worm-like Mck lamellae concentrated in medial portion lense.
	- feathery	common	variable from ~20 × 5 to ~75 × 20	embayed by Cp in relatively regular fasion	Irregular lenticular bodies of Mck or bundles Mck lamellae directly abutting Pn, relatively common
	- irregular	common	variable from ~5 × 1 to 150 × 25	embayed by Cp. Microveinlets of Cp (1μ wide) penetrate inclusion. Extreme cases microveinlets crosscut and segment inclusion - shredded appearance.	Irregular lenticular bodies of Mck or bundles Mck lamellae directly abutting Pn, relatively common.
Angular Pn	- irregular	common	variable from ~5 to ~100	Embayed by Cp. Microveinlets of Cp (1μ wide) penetrate inclusion. Extreme cases microveinlets crosscut and segment inclusion - shredded appearance.	Coarser 'shredded' inclusions (~50 μm to 150 μm) may directly abut the silicate margin
Pn lozenges	- irregular	common	variable from ~5 × 20 to ~20 × 100	embayed by Cp intergrown with irregular Cp veinlets	Also found at contact between Cub lamellae and Cp
Linear Pn stringers	- irregular	common	variable length~20 to ~100 consist of strings of blebs and blades ~5		Also found at contact between Cub lamellae and Cp or intergrown with Cub lamellae
Pn 'collars' at Cp/tr contact	irregular	less common	vary from discon. collars ~10 to 20 wide to lozenges ~300 × 100	Pn very embayed by Cp, irregular caries-like contact	Larger lozenges contain at pervasive worm-like Mck lamellae

Pn - pentlandite; Cp - chalcopyrite; Cub - cubanite; Mck - Mackinawite

Table 7.3 Qualitative Optical Properties of Sarqa Cubanite and Unknown $Pd(Bi_{1-x}Te)$ Phase.

1. **Cubanite**

In Air	In Oil
Colour: pale grey-green against chalcopyrite. Distinctly greenish against troilite and pentlandite	pale greenish tint more distinct
Bireflectance: distinct in cub. lamellae, from slightly lower than cp to slightly higher. Weak in granular masses associated with chalcopyrite.	more distinct
Anisotropy: moderate in lamellae brown → grey. Weak in granular masses associated with cp ~ same as cp.	more distinct but considerably lower than troilite. Deep brown → bluish grey.

Internal reflections not present

VHN_{50g} range 218-250 avg 227 $kgmm^{-2}$.

2. **Unknown $Pd(Bi_{1-x}\ Te_x)$ Phase**

Colour: light golden yellow

Reflectivity > cobaltite - gersdorffite estimate 60-65%

Bireflection/Pleoichroism: not observed

Anisotropy: very weak, greenish brown tint (in oil)

Other Characteristics: euhedral grains, takes good polish, scratch free.

TABLE 7.4 Energy Dispersive Electron Microprobe Analyses of Zoned Chromite from the Sarqa Intrusion (see Figure 7.22)

	CORE			OUTER CORE	INNER MARGIN		OUTER MARGIN		
Analysis No. wt % oxide	1	2	3	4	5	6	7	8	9
S_1O_2	0.60	0.53	0.62	0.87	0.72	0.72	0.62	0.53	0.59
TiO_2	0.27	0.43	0.28	0.45	1.37	1.97	1.20	1.20	1.35
MgO	2.47	2.77	2.14	1.68	0.70	0.96	0.65	0.83	1.14
CaO	n.d.	n.d.	n.d.	n.d.	n.d.	n.d.	0.27	0.32	n.d.
MnO	0.68	0.67	0.67	0.39	0.68	0.45	0.28	0.39	0.44
ZnO	0.72	0.44	1.12	1.13	0.39	0.39	n.d.	n.d.	n.d.
FeO	31.64	31.83	31.99	31.50	33.21	33.09	32.66	28.85	32.12
Fe_2O_3	5.36	4.95	5.46	5.84	21.93	23.15	44.28	48.82	39.82
Cr_2O_3	49.65	49.74	50.09	46.34	39.10	37.90	20.89	20.07	24.59
Al_2O_3	13.45	14.28	13.06	12.02	3.99	2.66	1.34	1.36	1.64
V_2O_3	0.27	0.44	0.34	n.d.	0.31	0.27	0.16	n.d.	0.32
TOTAL	105.11	106.08	105.77	100.22	102.4	101.56	102.35	102.37	102.01

TABLE 7.5 Qualitative Optical Properties of Mackinawite and Valleriite from the Sarqa Intrusion

	Mackinawite	Valleriite
Colour:	strongly pleoichroic, brown to pale creamy yellow; (in oil) dark greyish brown to pale creamy white	pleoichroic, brown to yellow brown;(oil) deeper bronzy brown to yellow brown. Colours appear more 'dirty' than mackinawite colours.
Bireflectance:	strong Bireflectance and pleoichroism more marked than in valleriite.	moderate
Anisotropy:	Very strong. Greyish white to dark bluish grey (in oil - same) With polars slightly uncrossed ~5° and high level incident illumination distinctive bright light blue colour	Strong. More distinct in oil than in air, distinct bronzy yellow colours. Fine aggregates within lamellae give patchwork appearance. On rotation stage adjacent platelets go into extinction consecutively giving appearance undulose extinction.

TABLE 7.6 Mode of Occurrence of Mackinawite and Valleriite in the Sarqa Mineralisation.

Morphology	Average Dimensions, Mode of Occurrence and Associations
MACKINAWITE	
1. Worm-like lamellae	~5-10μm long ~1μm wide (i) Pervade granular Pn in myrmeketic intergrowth; very common. Proportion varies from 30-50%. Appears to be three different elongation directions at 60°, but not well defined. Extinguish in different positions within adjacent 'grains' of Pn. Rare - linear zones (~40μm) of Pn full of Mck lamellae alternate with Mck free Pn. Rare or absent in 940m level Pn - where present orientated in one direction close to margin. Where intense alteration Pn to vl. - irregular patchy zones Mck free vl intergrown with vl and Mck. (ii) Pervade coarser Pn inclusions within Cp. (iii) Rarely as strings of lamellae associated with fine Pn stringers within Cp. (iv) Associated with Cub lamellae either protruding from Cub/Cp contact into Cp or as bundles of lamellae intergrown with and orientated subparallel to Cub. lathes.
2. Irregular lenticular bodies	vary from ~20 to 75μm long and ~5 to 20μm wide. Under XP observe fine irregular lamellae crossing lenticle at right angles to direction elongation. (i) Within Cp most commonly directly associated with Pn inclusions, more rarely associated with Cub lathes. (ii) Rare - associated with Mck lamellae in granular Pn.
3. Irregular 'patches'	vary from ~50μm to ~100μm. Relatively rare. Occur on margins granular Pn where it directly abuts Cp. Cub lamellae may also be present.
VALLERIITE	
Discontinuous veinlets	~5 - 40μm wide. Occurs in trace amounts cf Mck. Margins of veinlets may have fine rims of mt. Either (i) discontinuous veinlets cross cutting granular Pn-Mck-vl, or (ii) thin discontinuous veinlets and small elongate aggregates in silicate close to margins suphide aggregates.

TABLE 7.7 Mode of Occurrence and Compositions of Associated* PGM Telluride and Sulpharsenide Phases in Sarqa Ore

Phase	Morphology	Dimensions (μm)	Pd	Pt	Ag	Te	Bi	As	Tot	( )	STRUCTURAL FORMULA
Sperrylite	Euhedral	~30	-	56.04	-	-	-	43.26	99.30	(5)	$Pt_{0.99}As_2$
Hessite	Anhedral roughly elongate ovoid	~80 × 9-40	-	-	57.68	35.03	-	-	94.47	(5)	$Ag_2Te_{1.08}$
(?)Merenskyite	Irregular lamellae within hessite	up to 14 × 5	26.37	-	10.00	62.19	-	-	97.03	(3) (?)	$Pd_{0.85}Ag_{0.18}Te_2$ $Pd_{1-x}Ag_xTe_2$
Unknown	Euhedral	~40 × 21	34.51	-	-	6.49	55.63	-	96.63	(11)	$Pd_1Bi_{0.82}Te_{0.13}$
Unknown	Replicate anlayses		34.32	-	-	6.48	55.42	-	96.22	(4)	
Cobaltite -Gersdorffite	Euhedral	~50 ~17 × 10	(see Table 7.8)								

* Occur as inclusions within granular chalcopyrite (Fig. 7.25). Unknown phase also found within chalcopyrite replacing pentlandite.

TABLE 7.8 Energy Dispersive Electron Microprobe Analyses of Zoned Cobaltite -Gersdorffite Grain (See Figure 7.26).

Analysis No.		5	4	1	3	2	7	6	8	
Distance from GRN Margin µm		4	16	26	35	43	margin	core	margin	avg 2 σ
	S	17.49	16.79	16.44	16.73	17.34	17.12	16.30	15.57	0.2
	As	48.19	47.67	46.72	47.01	46.42	44.47	45.98	45.45	1.2
	Fe	5.51	5.16	4.75	4.78	5.51	4.87	4.55	4.76	0.2
Wt %	Ni	13.07	13.00	12.41	11.23	10.63	9.15	11.63	10.96	0.4
	Co	17.15	15.09	14.48	14.77	16.98	20.19	13.81	13.73	0.4
	Cu	n.d.	0.51	0.47	n.d.	0.40	0.39	n.d.	0.46	0.3
	Rh	n.d.	2.08	3.08	3.42	0.99	n.d.	3.08	3.85	0.3
	Pt	n.d.	n.d.	1.40	n.d.	n.d.	n.d.	n.d.	n.d.	0.7
	Pd	1.58	1.88	1.74	2.28	1.08	0.63	1.66	2.42	0.3
TOTAL		102.08	102.2	101.50	100.11	99.35	96.81	97.00	97.22	
	S	30.04	29.48	29.48	30.13	30.83	30.95	30.11	29.17	
	As	35.42	35.82	35.85	36.24	35.32	34.41	36.34	36.45	
	Fe	5.43	5.20	4.89	4.94	5.62	5.05	4.82	5.12	
At %	Ni	12.26	12.46	12.15	11.05	10.32	9.03	11.73	11.21	
	Co	16.03	14.42	14.13	14.48	16.42	19.86	13.88	14.00	
	Cu	-	0.49	0.43	-	0.36	0.36	n.d.	0.43	
	Rh	-	1.14	1.72	1.92	0.55	n.d.	1.77	2.25	
	Pt	-	-	0.41	-	-	n.d.	n.d.	n.d.	
	Pd	0.82	0.99	0.94	1.24	0.58	0.34	1.35	1.37	

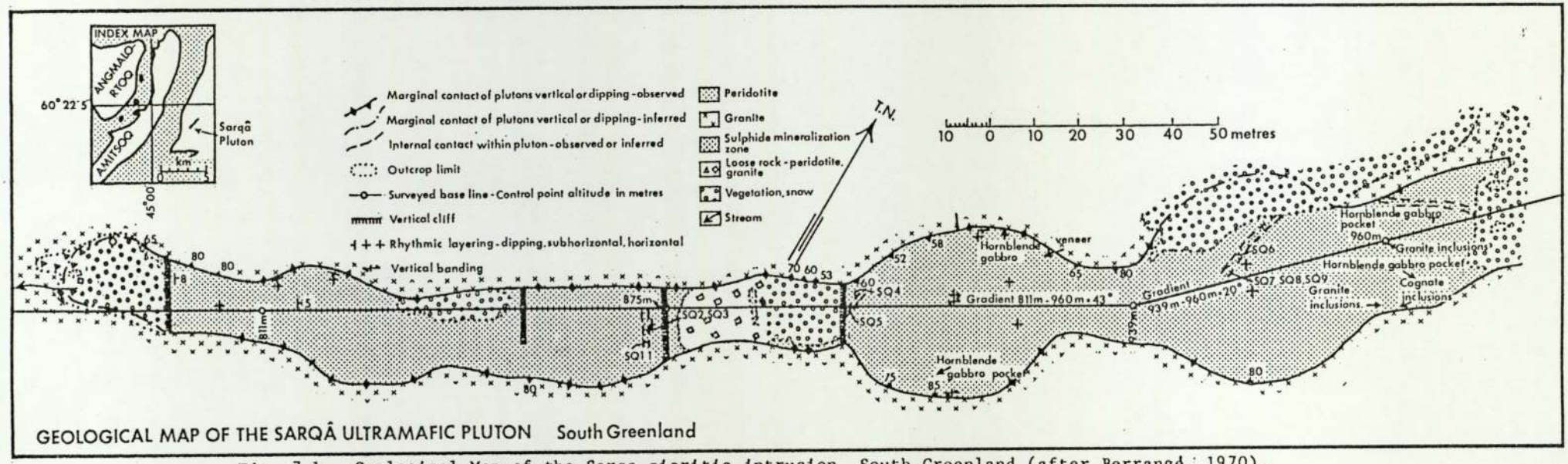

Fig. 7.1 Geological Map of the Sarqa picritic intrusion, South Greenland (after Berrangé, 1970).

Fig. 7.2 Angular sulphide dissem. interstitial to enclosing silicates (black). Dissem. dominated by coarse angular tr grain (light grey). Blocky Pn (white) located at silicate/tr contact (left). Coarse chromite grain (very dark grey, upper right) rimmed by Mt. (lighter grey). Discontinuous porous Mt. veinlet rimming (upper) silicate/Po contact (f.o.v., 2mm, PPL)

Fig. 7.3 Rounded 'droplet' of ore entirely enclosed within host silicate grain (black). Cp (light grey) rims sulphide/silicate contact and contains minor inclusions of Pn (white). Tr (darker grey) occupies the rest of the droplet. (f.o.v., 0.2mm, PPL)

Fig. 7.4 Bladed and lamellar tr. twins (f.o.v., 0.5mm, XP)

Fig. 7.5 Coarse granular Pn (white) located at tr (light grey)/silicate contact (black lower margin). Subhedral Pn xtal faces developed against Po. Contains rounded inclusions of Cp (light grey, central) (f.o.v., 1mm, PPL)

Fig. 7.6 Coarse angular Pn mass, partially replaced from the margins by vl, enclosing small Cp segregation against silicate 'wall' of dissem. (black, upper right). Tr in contact with Pn towards 'core' of dissem. (lower left) (f.o.v., 1mm, PPL)

Fig. 7.7 Part of a coarse granular Pn aggregate (white) located close to silicate contact (black, right margin). Pn contains numerous minute wormlike Mck. lamellae (light grey) in myrmeketic intergrowth. Small Cp segregation (light grey) 'sandwiched' between Pn and silicate contact, contains numerous fine, Mt lamellae (very dark grey) which terminate at Cp/Pn contact. Cp/Pn contact 'shredded'. Pn inclusions with Cp penetrated by microveinlets of Cp. (f.o.v., 0.5mm, PPL, Oil)

Fig. 7.8 Part of the contact between a coarse granular Pn and tr. Pn partially rimmed by Cp, containing very fine Mt lamellae (very dark grey). Contact of Pn with Cp very irregular and embayed. Bright white phase located at Pn/tr contact (on right) is the unknown Pd bismutho-telluride (see Table 7.7) (f.o.v., 0.5mm, PPL, Oil)

Fig. 7.9 Margin of a coarse Pn segregation (edge visible lower margin) in contact with tr (left) and Cp (right). Patchy Mck intergrowth at Cp/Pn contact (lower left). Cub lamellae containing numerous irregular Pn inclusions (white) emanates from Cp/Pn contact. Cp contains numerous very fine Mt lamellae (dark grey)

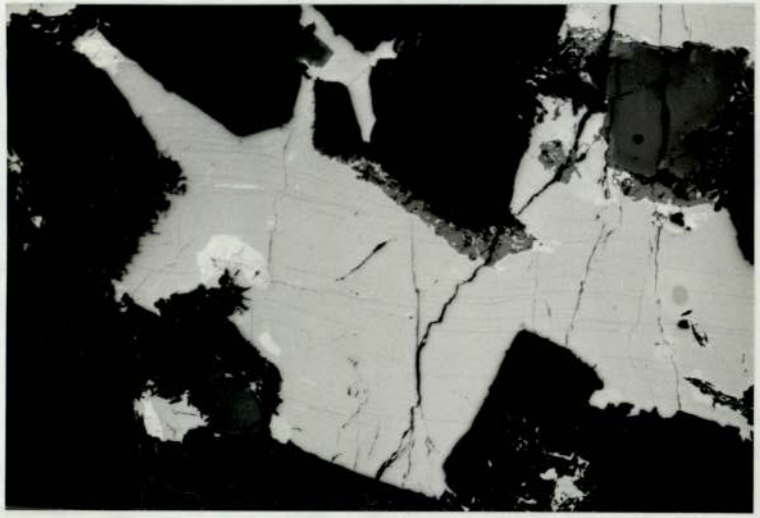

Fig. 7.2

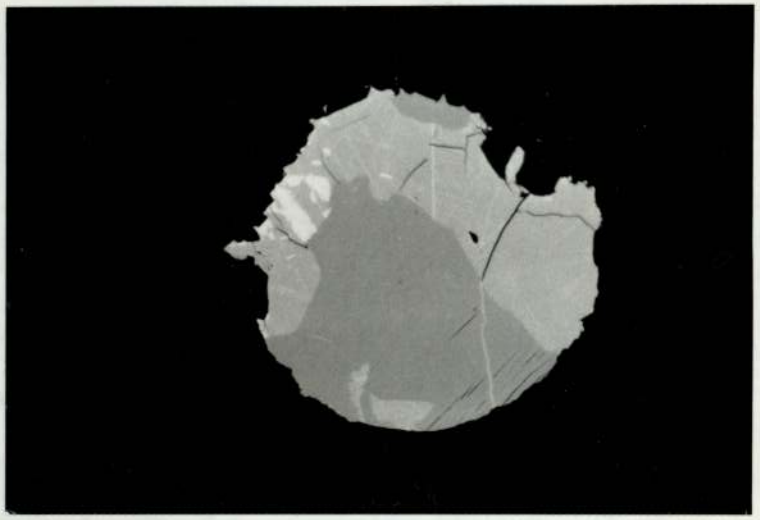

Fig. 7.3

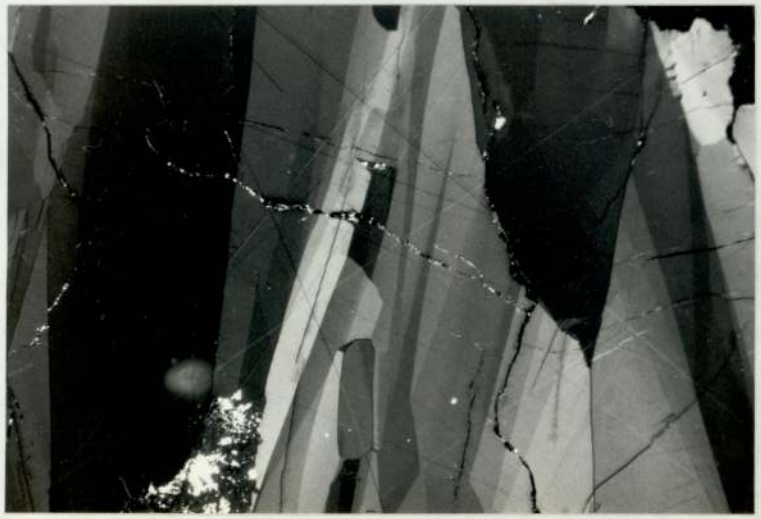

Fig. 7.4

Fig. 7.5

Fig. 7.6

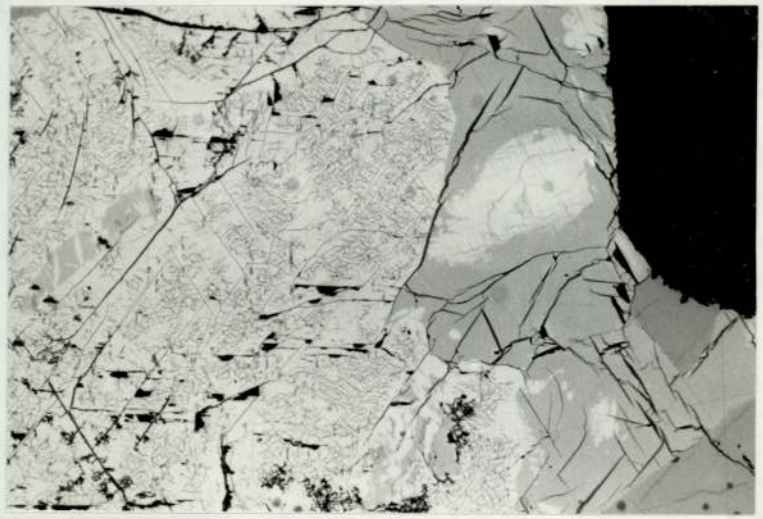

Fig. 7.7

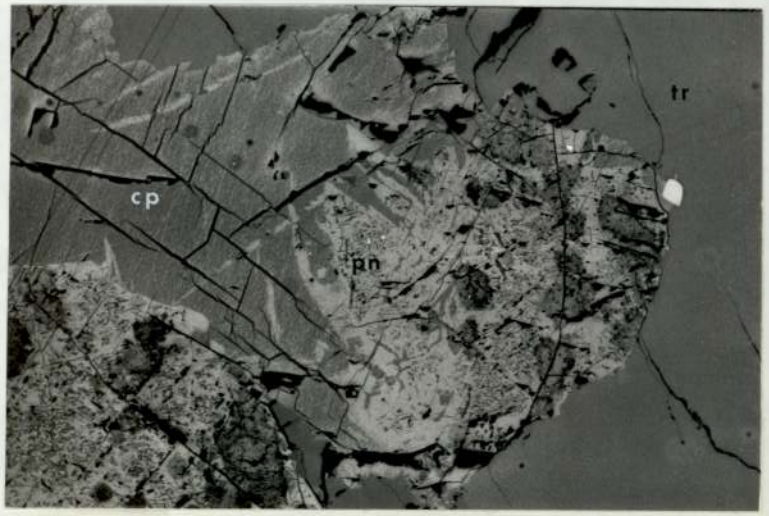

Fig. 7.8

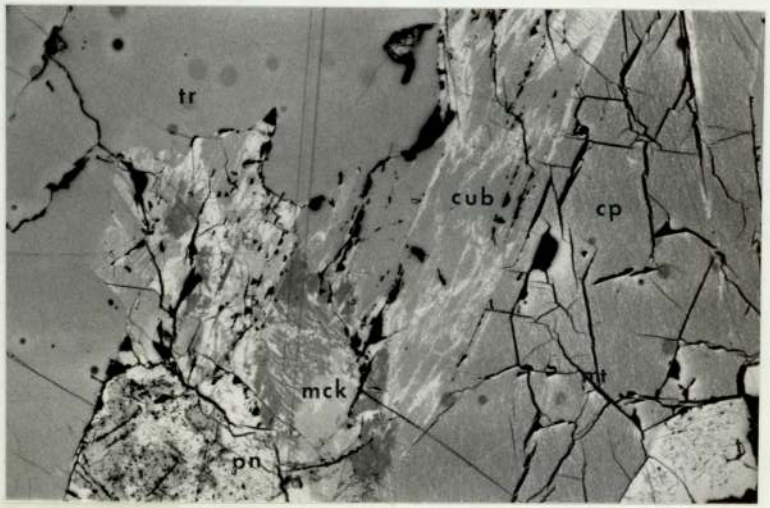

Fig. 7.9

Fig. 7.10 Orientated worm-like lamellae of Mck (light grey) in myrmeketic intergrowth with Pn (white). Tr (light grey)/Pn contact just visible (lower left). Grey phase on extreme left hand margin is vl, replacing Pn (f.o.v., 0.16mm, PPL, Oil)

Fig. 7.11 Worm-like Mck lamellae (light grey) associated with linear fractures in Pn (white), separated by Mck free 'zones' of Pn. Tr (light grey)/Pn contact just visible (extreme lower left) (940m level mineralised zone) (f.o.v., 0.2mm, PPL, Oil)

Fig. 7.12 and 7.13 Same f.o.v., 0.5mm, in PPL (7.12) and under XP (7.13) illustrating replacement of Pn-Mck by vl. Contact of original Pn mass with tr (light grey) just visible extreme upper left. Mck-free vl occurring closer to this contact, contains remnants of Pn (white) along fractures and separates areas of vl containing numerous Mck lamellae. These show up better in XP (Fig. 7.13) as bright white patchy areas separated by vl in extinction.

Fig. 7.14 Coarse granular Cp segregation located at silicate contact (black, lower margin) of dissem. ore bleb. Tr occurs towards core of bleb (upper margin). The Cp contains fine Mt. lamellae (very dark) orientated in an irregular octahedral pattern. These terminate at the Cp/tr contact. Irregular lozenge of Pn (white) at Cp/tr contact. (f.o.v., 1mm, PPL)

Fig. 7.15 Coarse granular Cp segregation containing Mt. lamellae (dark grey) in irregular octahedral pattern, located at silicate contact (black). Coarse ovoid of granular Pn (white) partially replaced by vl (patchy grey) located at Cp/tr contact (upper margin). (f.o.v., 2mm, PPL).

Fig. 7.16 Coarse Cp segregation in rectangular termination to dissem. sulphide bleb. Angular tr grain occurs towards core of dissem. (right). Bundles of lathe-shaped (?autometamorphic silicates) penetrate Cp. (f.o.v., 1.6mm, PPL)

Fig. 7.17 Cp (light grey) at contact between granular Pn (white, just visible extreme left) and tr (darker grey, right margin). The Cp contains numerous 'feathery'-'shredded' inclusions of Pn (white). Directly associated with the Pn inclusions are lozenges of Mck (darker grey cf Cp) (f.o.v., 0.5mm, PPL, Oil)

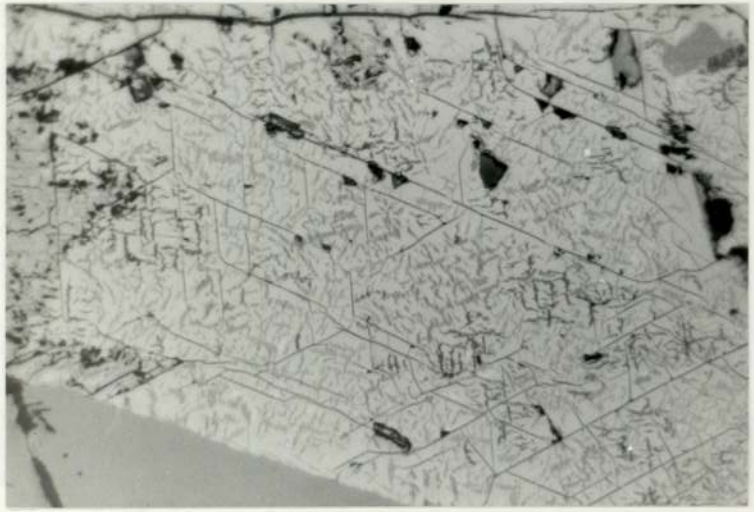

Fig. 7.10

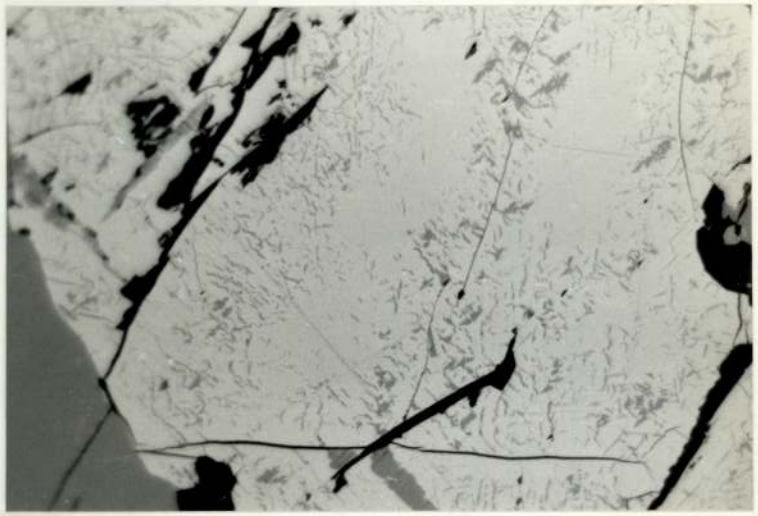

Fig. 7.11

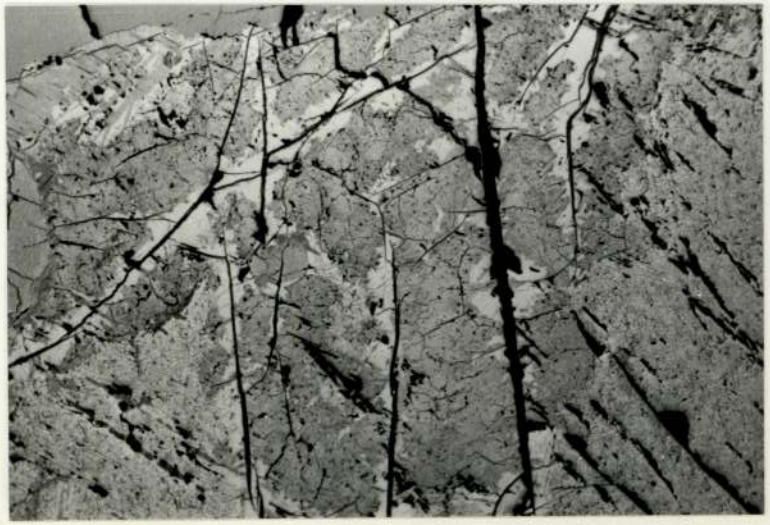

Fig. 7.12

Fig. 7.13

Fig. 7.18 Composite granular Pn (white)/Cp (grey, to the left) mass, located at (black) silicate/tr contact (grey, upper margin) (f.o.v., 0.5mm, PPL, Oil)

Fig. 7.19 Margin of small sulphide dissem. dominated by coarse angular tr grain (grey). Granular blocky Pn (white), Mck free, located at (black) silicate/tr contact (f.o.v., 1mm, PPL)

Fig. 7.20 Composite granular mass of cub (even grey) and Cp (mottled grey). Cub/Cp contact angular and irregular. Cp contains Mt. lamellae (very dark grey) which terminate at the Cub/Cp contact and at the Cp/tr contact. (f.o.v., 0.5mm, PPL, Oil)

Fig. 7.21 Part of a granular Pn aggregate segmented into individual Pn grains (light even grey) by veinlets of Mt (very dark grey). Fine grained Po (Polygonal 'mosaic', various shades of grey, central) is associated with the Mt. Individual Pn grains contain worm-like lamellae of Mck (white and black) in a myrmeketic intergrowth. (f.o.v., 0.5 mm, unXP, Oil)

Fig. 7.22 Replacement of small granular Pn mass (white) located at (black, upper margin) silicate/tr contact, by cub. Cub envelops Pn and penetrates in small microveinlets. Granular area of cubanite (right) contains numerous 'shredded' inclusions of Pn. Very fine irregular veinlets of Mt (very dark grey) within cubanite terminate at cub/tr contact. (f.o.v., 0.5mm, PPL, Oil)

Fig. 7.23 Replacement of small granular Pn located at (black) silicate contact by fine grained 'mixture' of Po and Cub (mottled grey, central). Only shredded remnants of Pn (white) remain, at silicate contact. Very dark granular masses of Mt associated with Cub and Po. Tr grain (grey, to upper right) unaltered. (f.o.v., 0.5mm, unXP, Oil)

Fig. 7.24 Chromite grain with zoned ferrochromit 'reaction mantle' located within silicate (black) close to contact with tr (white). Three distinct successively lighter grey zones just visible on the left hand margin of the chromite. (see Table 7.4) (f.o.v. 0.5mm, PPL, Oil)

Fig. 7.25 Microassemblage of P.G.M., Telluride and sulpharsenide phases present as inclusions within Cp (mottled dark grey): euhedral cobaltite-gersdorffite (light grey, lower grain); anhedral hessite (dark grey) intergrown with brighter ?Merenskyite; euhedral unknown $Pd_1Bl_{0.82}Te_{0.13}$ phase (bright white). Mt lamellae (very dark grey) in Cp terminated against these inclusions.

Fig. 7.18

Fig. 7.19

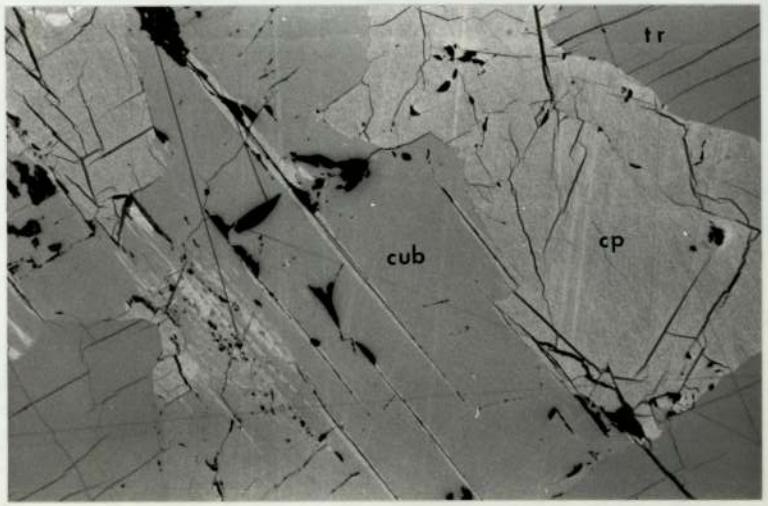

Fig. 7.20

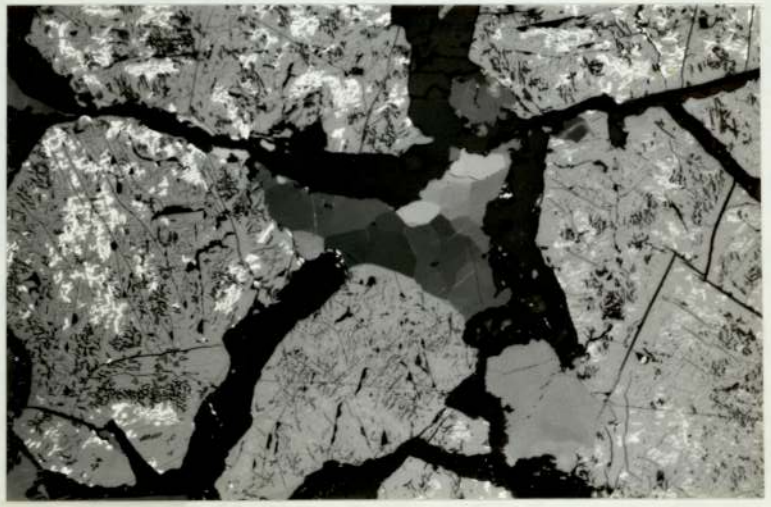

Fig. 7.21

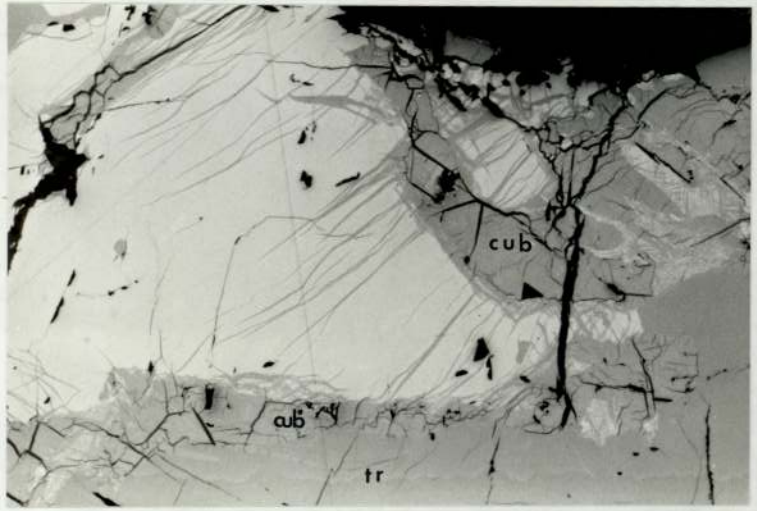

Fig. 7.22

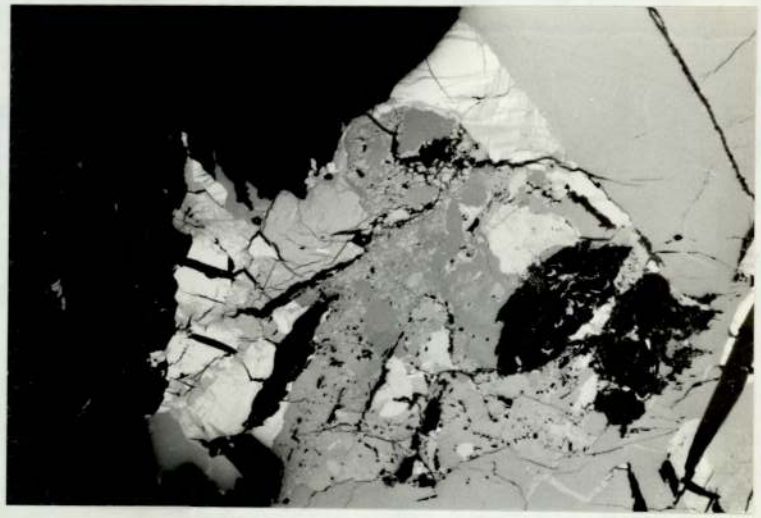

Fig. 7.23

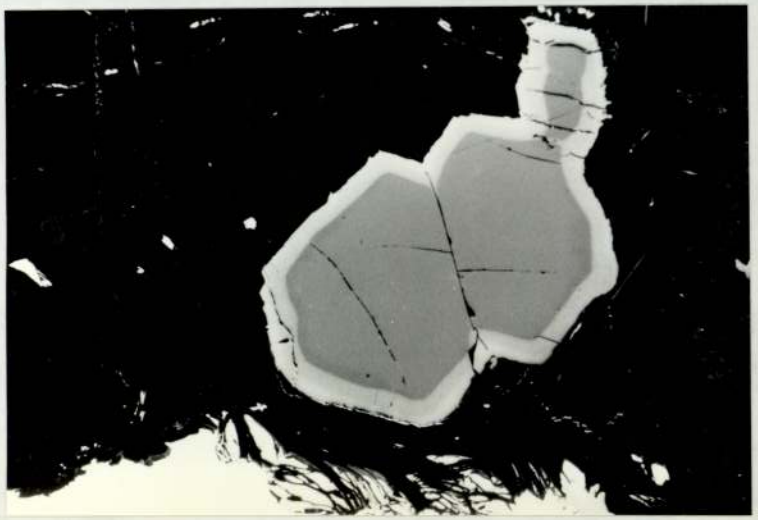

Fig. 7.24

Fig. 7.25

Fig. 7.26 Zonation in Cobaltite-Gersdorffite grain (see Table 7.8)

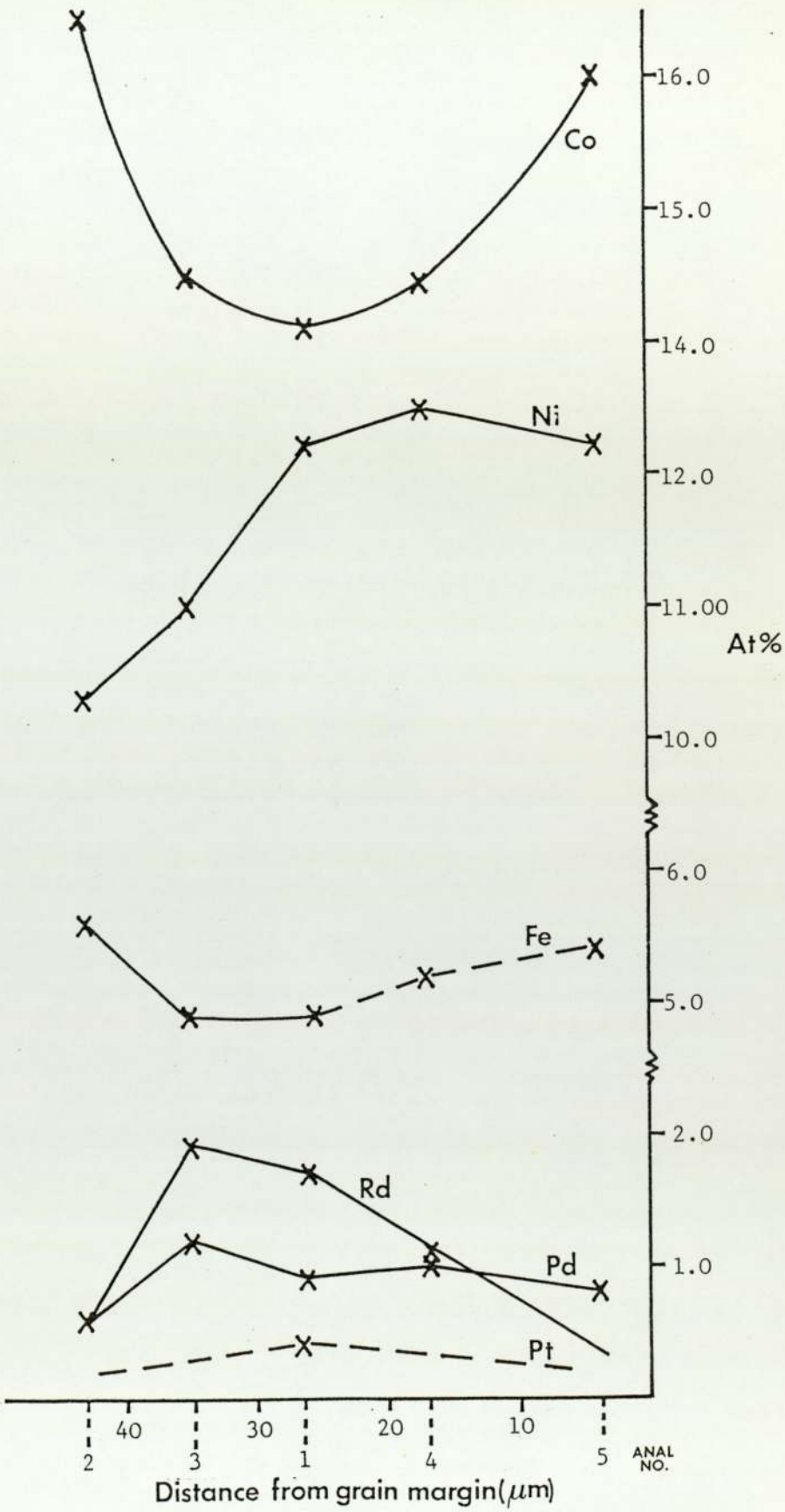

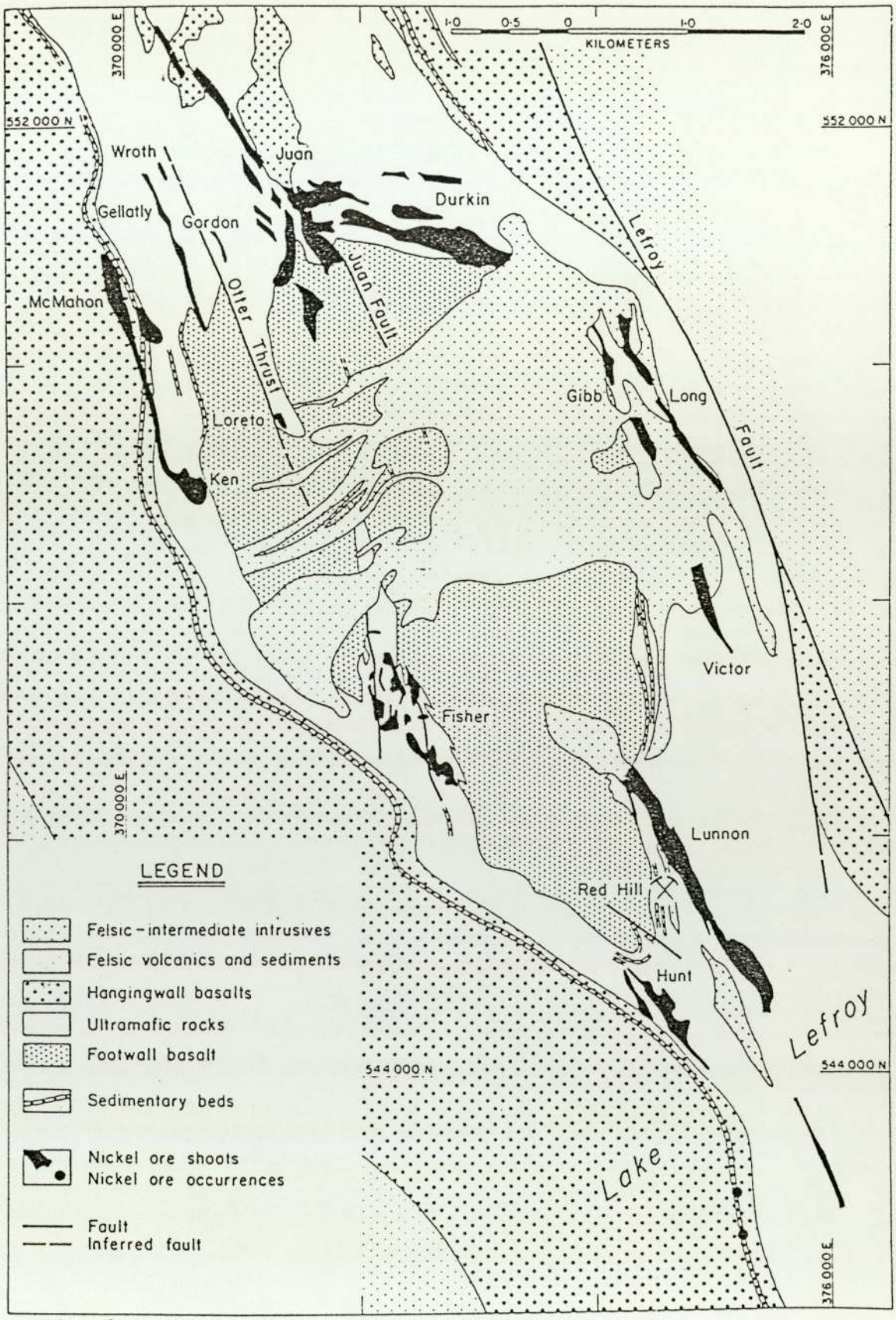

Fig. 8.1 Geological plan of the Kambalda dome showing the nickel sulphide ore shoots in plan projection (after Gresham and Loftus-Hills, 1981).

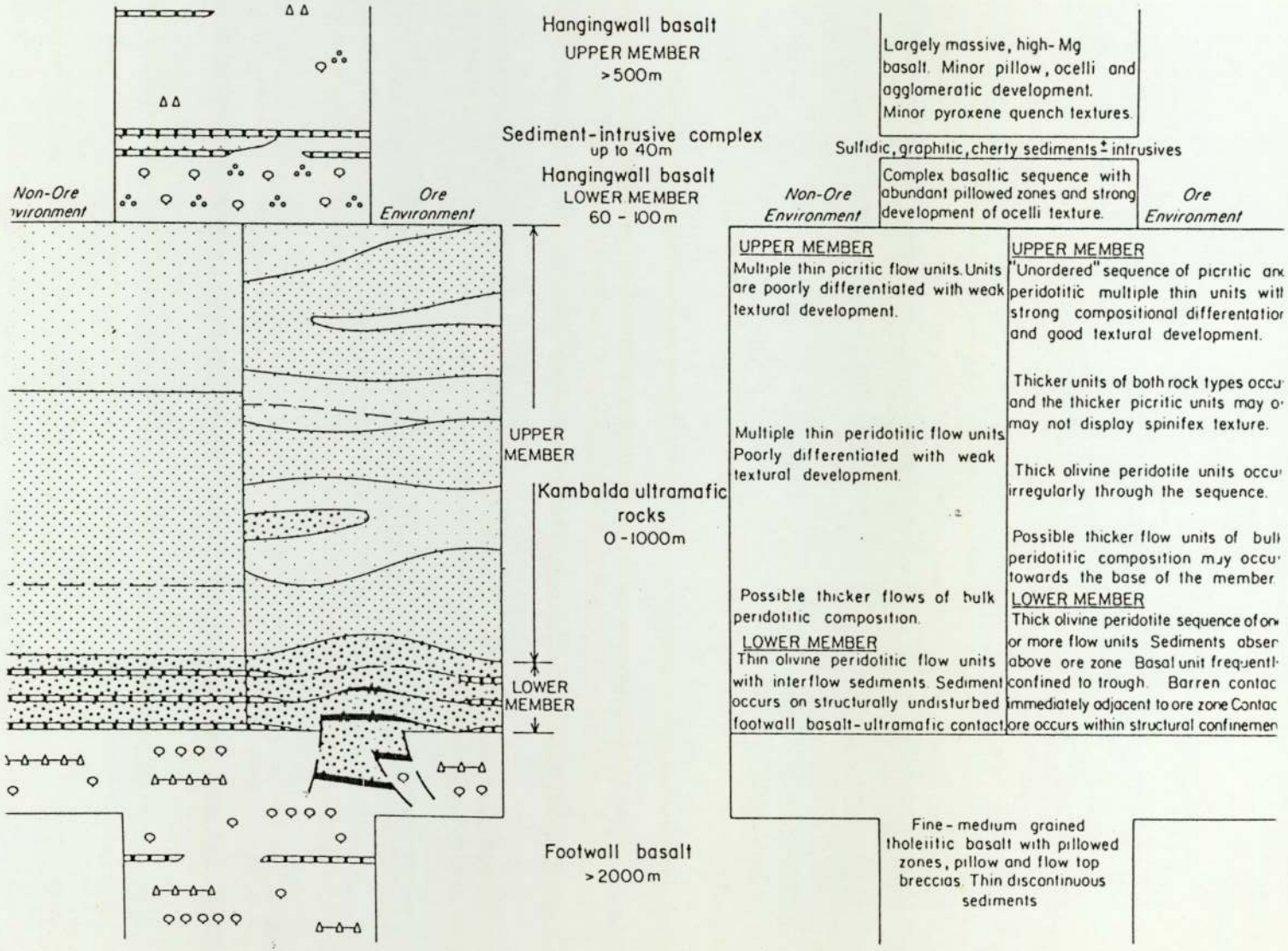

Fig. 8.2 Stratigraphic column of the Kambalda sequence illustrating the location of the ore and its relationship to the host rocks (after Gresham and Loftus-Hills, 1981).

TABLE 9.1 Pentlandite Textural Types in Massive Breccia Sulphide Ore, Thompson Mine.

Textural Type	Mode of Occurrence, Dimensions, Association
1. COARSE GRANULAR CLOTS (Fig. 9.7)	Discrete masses of Pn within Po matrix. Shape varies from irregular ovoids to more elongate. Well developed cleavage and fracture. Size variable ~2mm - 10mm, majority 4-6mm. Irregular concentrations associated with areas of finer grained (~0.4mm - 0.8mm) Po mosaics. Boundary with adjacent Po embayed due to: fine grained nature Po, development subhedral lobate Pn protrusions, extensions of Pn into cusps between Po. Actual interface with individual Po grains relatively smooth. Inclusions: irregular grain aggregates of Po and Cp (up to ~0.4 mm); small ragged inclusions Py (~0.05 mm); laths or elongate masses of valleriite. May partially or wholly envelop large biotite lathes.
2. BLOCKY Pn	Discrete Pn masses intergranular to adjacent Po grains or on margins silicate inclusions. Variable in morphology and dimensions (i) ovoid shaped (~0.3 mm) (Fig. 9.8) , (ii) irregular masses (~0.8 mm) associated with very fine grained (~0.1 - 0.2 mm) Po mosaics interstitial to coarser Po grains, irregular extensions along grain boundaries adjacent Po (Fig. 9.9), (iii) coarser irregular granular masses (~ 1mm) often associated with silicate fragments and lathes, (iv) small (~0.05 - 0.1 mm) lobate Pn on margins silicate fragments. Occasionally coarser irregular types have irregular granular aggregates of Cp on margins. Coarser types grade towards coarse granular 'clots'.
3. RIM Pn (Fig. 9.10)	Discontinuous veinlets along Po grain boundaries. Width of rim dependent on Po grain size, (i) in coarser grained Po mosaics vary from ~0.05 mm to 0.2 mm wide, interface generally smooth undulating, flame extensions relatively uncommon. (ii) in finer grained Po mosaic ~0.02 - 0.05 mm wide, small flame extensions more common.

TABLE 9.1 continued

Textural Type	Mode of Occurrence, Dimensions, Association
4. FLAME TYPE PENTLANDITES	Aggregates of finer pentlandite particles. Morphology variable dependent on: proportions of different Pn particles, location in Po matrix. More common in coarse grained Po mosaics free from coarse granular Pn 'clots'. Listed in decreasing order of abundance. (i) Grain boundaries - vary from acicular aggregates up to ~75μm by ~5μm to triangular aggregates of partially agglomerated plates, up to ~50μm by 20μm . (Fig. 9.11). (ii) Flame extensions to Pn rims. More common on rims ≤0.1mm wide (rarely observed as extensions to blocky Pn or coarse granular Pn clots). Consist of partially agglomerated blades, plates and wedges. Aggregates vary from few μm long to ~ 30μm long (Fig. 9.10). (iii)Margins silicate lathes and fragments. Vary from relatively coarse ragged blades up to ~100μm by 10μm to acicular aggregates ~20μm to 75μm long up to ~10μm wide (Fig. 9.13). (iv) Flames within Po grains. Occur predominantly in coarser Po grains in small orientated groups. Vary in morphology from elongate rods to elongate ellipsoids size ~20μm - 50μm long. Consist of elongate blebs and lamellae. (v) Flames from fractures, rarity reflection of limited occurrence of fine orientated fractures within individual Po grains. Roughly acicular to triangular aggregates from ~10μm to 70μm long (Fig. 9.14).
5. INTERSTITIAL PENTLANDITE	Rare in occurrence. Found within fine grained Po mosaics associated with concentrations of coarse granular 'clots' of Pn where other Pn textural types are rare. Convex triangular grains (~20μm) at Po triple junctions.

TABLE 9.2 Electron Probe Microanalyses of Pentlandite from Thompson Mine

	Coarse Granular Pn 'clot'		Coarse Granular Pn 'clot'	Rim Pn	Rim Pn
Wt %		Replicate Analyses			Replicate Analyses
S	32.94	33.09	33.11	32.98	33.08
Fe	30.07	30.17	30.10	29.24	29.52
Ni	37.25	37.05	37.26	37.80	37.71
Co	0.67	0.67	0.66	0.65	0.64
Total	100.93	100.98	101.13	100.67	100.95
At %					
S	46.45	46.60	46.57	46.61	46.61
Fe	24.35	24.39	24.31	23.72	23.88
Ni	28.69	28.50	28.62	29.17	29.02
Co	0.51	0.51	0.50	0.50	0.49
( )	5	5	2	6	5

( ) No. of individual spot analyses

TABLE 9.3 Electron Probe Microanalyses of Pyrrhotites from Thompson Mine

		Pyrrhotite abutting coarse granular pentlandite clot														Pyrrhotite with rim Pn at grain boundary				
		'Line' Profile 1								'Line' Profile 2										
							Grn. Bound ↓													
Anal.No.		14	15	16	17	18	19	20	21	12	5	4	3	2	1	10	9	8	7	6
Dist. from contact µm		90	240	420	780	900	1170	1300	1420	80	125	600	800	1050	1300	150	525	800	1050	1450
	S	39.78	39.78	39.62	39.70	39.70	39.67	39.68	39.74	39.71	39.68	39.63	39.64	39.69	39.71	39.65	39.78	39.75	39.76	39.77
	Fe	60.76	60.44	60.17	60.25	60.04	60.08	60.20	60.15	60.69	60.35	59.81	59.93	59.90	60.07	60.20	59.89	60.13	59.89	59.87
WT %	Ni	0.67	0.86	0.94	1.15	1.28	1.21	1.06	1.27	0.66	0.89	1.21	1.17	1.24	1.22	0.91	1.05	1.03	1.03	1.03
	Co	0.13	0.13	0.11	0.13	0.12	0.13	0.11	0.12	0.11	0.12	0.12	0.12	0.12	0.14	0.12	0.13	0.12	0.11	0.13
TOTAL		101.34	101.22	100.85	101.23	101.14	101.09	101.07	101.28	101.16	101.05	100.76	100.86	100.95	101.13					
	S	52.97	53.03	53.11	52.94	52.98	52.97	52.99	52.95	52.95	52.99	53.06	53.03	53.05	52.99	53.03	53.18	53.07	53.18	53.19
AT %	Fe	46.45	46.25	46.12	46.13	46.00	46.06	46.16	46.02	46.47	46.27	45.97	46.03	45.96	46.02	46.22	45.96	46.09	45.99	45.97
	Ni	0.49	0.63	0.69	0.84	0.93	0.88	0.77	0.94	0.60	0.65	0.88	0.85	0.90	0.89	0.66	0.77	0.75	0.75	0.75
	Co	0.09	0.09	0.08	0.09	0.09	0.09	0.08	0.09	0.08	0.09	0.09	0.09	0.09	0.10	0.09	0.09	0.09	0.08	0.09

Table 9.4 Examples of the variation in Bulk Metal Content, Pentlandite Compositions and Residual Ni Content of Pyrrhotite in Deposits of Different Petrotectonic Associations.

Deposit	Bulk Metal Content (wt %)			Residual Ni (at %)		Pn Compositions (at %)		
Petrotectonic Setting	Cu	Ni	Tr	Mcl Po	Hex Po	S	Ni	Co
Komatiitic Volcanics								
Kambalda ore shoots								
Lunnon (altered)			-	0.4-0.5(4)	-	46.8(4)	24.3(4)	0.6(4)
unaltered	0.8(1)	~7-12(2)	-	0.2-0.6(5)	-	?	26.4-28.2(5)	0.3-0.6(5)
Durkin (altered)	1.3(1)	~14-16(1)	-	0.4(4)	-	47.4-48.6(4)	27.6-24.6(4)	0.3-0.4(4)
Marbridge	0.4(1)	~6.5(1)	-	0	0	47.3(6)	27.4-27.8(6)	0.3(6)
(altered)				?	?	46-49.4(7)	18.7-20(7)	0.1(7)
Komatiitic dunite intrusives								
Mt. Keith-Betheno	0.6(1)	35(1)	-	?	-	?	26.5-28.8(8)	?
		-	-	(Pn+hz)	?	26.6-28.2(8)	?	
		-	-	(Pn+ml)	?	32.5-34.5(8)	?	
Spargoville			-		0.2-0.7(9)	46.5-47.4(9)	23.3-26.9(9)	0.3-0.9(9)
?Thompson ? (Tables 9.1, 9.2)		~8(3)	-	0.5-0.9(3)	-	46.5-46.6(3)	28.7-29(3)	0.5(3)
Minor picritic intrusion								
Sarqa (Table 7.1)	~7(3)	n.d.	-	-	47.2(3)	24(3)	0.6(3)	
Intrusives related to flood basalts								
Duluth (Minnamax)	17.2(1)	3.91(1)	n.d.	-	0.2(10)	47-48(10)	23-33(10)	1-1.5(10)
Merensky Reef (Bushveld)								
Rustenburg (Table 6.2)	~5(3)	~8.5(3)	-	-	0.4(3)	46.7(3)	25.6-26(3)	0.3-0.4(3)
Western		-	-	0.3(11)	45.2-46(11)	25.1-27.3(11)	0.6(11)	
Impala		-	?	?	46.5-47.7(12)		26.1-26.5(12)	0.5(12)
Sudbury Deposits								
Strathcona (Table 5.2)	1.2(1)	3.6(1)	-	0.4(13)	0.5-0.7(13)	46.4-47.6(3)	26.7-29.1(13)	2.1-0.3(13)
Copper Cliff (Table 5.3)			-	0.3-0.4(3)	0.5-0.8(3)	46.7-46.9(3)	27.1-27.4(3)	0.7-1.1(3)
Falconbridge	1.5(1)	5.4(1)	-	0.3(6,7)	0.3-0.8(7)	46.1-47.1(6,7)	28.7-28.9(6,7)	0.6(6,7)

References (1) Naldrett 1981a, (2) Gresham and Loftus-Hills 1981, (3) This study, (4) Keele et al 1974, (5) Marston and Kay 1980, (6) Misra and Fleet 1973a, (7) Harris and Nickel 1972, (8) Groves and Keays 1979, (9) Ramsden 1975, (10) Pasteris 1984, (11) Brynard et al. 1976, (12) Mostert et al. 1982, (13) Vaughan et al. 1971.

Fig. 9.1 to 9.4 Photomicrographs illustrating the occurrence of granular Pentlandite within Pyrrhotite in massive ore from Kambalda

Fig. 9.1 'Lensoid layer' of 'massive' granular Pn (white) 'giving way' to discrete blocky Pn interstitial to matrix of interlocking Po grains (various shades grey; ignore green tint) (f.o.v., 7.8mm, PPL) [Lunnon ore shoot]

Fig. 9.2 Layer of continuous 'massive' granular Pn (white) grading into anastomising network of granular Pn within matrix of interlocking fine-grained Po (various shades grey). Contact between massive Pn and fine-grained Py rich layer containing angular fragments of Pn (slightly higher relief) just visible on right hand margin. (f.o.v., 9.7mm, PPL) [Ken ore shoot]

Fig. 9.3 Anastomising netowrk of granular Pn (white) interstitial to matrix of Po grains (various shades grey) grading (to right) into Po matrix containing only discrete interstitial Pn grains. (f.o.v., 3.2mm, unXP) [Lunnon ore shoot]

Fig. 9.4 Example of Po matrix layer 'midway' between adjacent continuous massive Pn layers. Interlocking fine Po grains (various shades of grey). Discrete interstitial Pn grains which decrease in size and abundance (upwards) until only very fine interstitial Pn blebs and fine Pn rims are present.

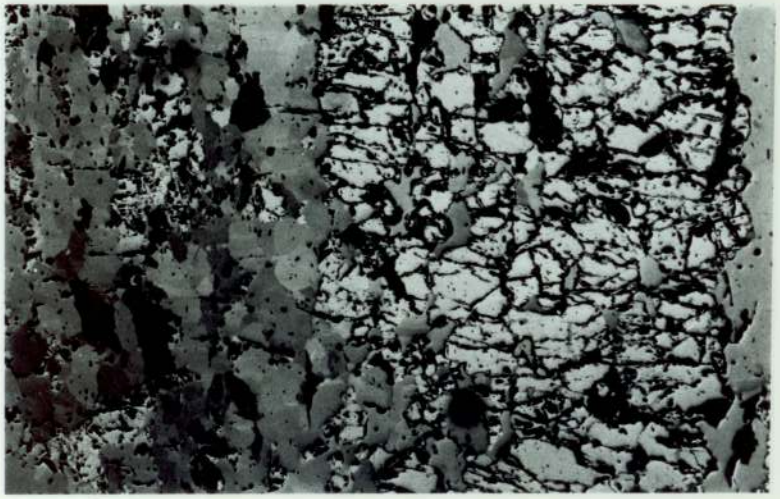

Fig. 9.1

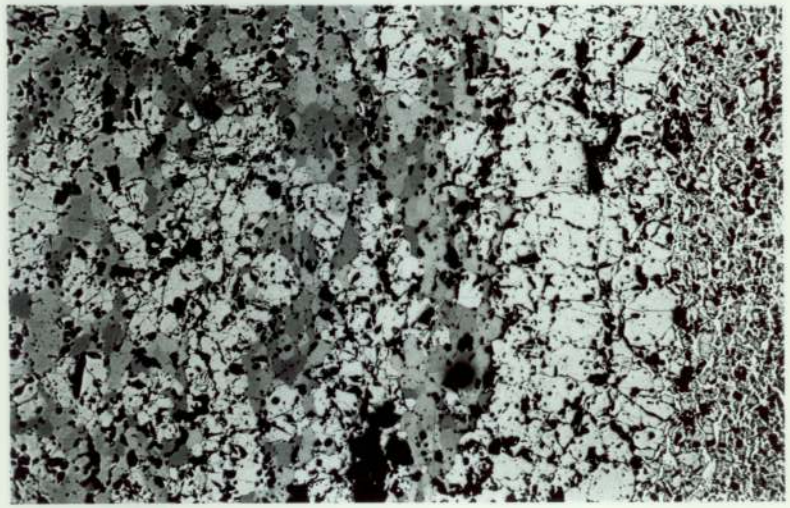

Fig. 9.2

Fig. 9.3

Fig. 9.4

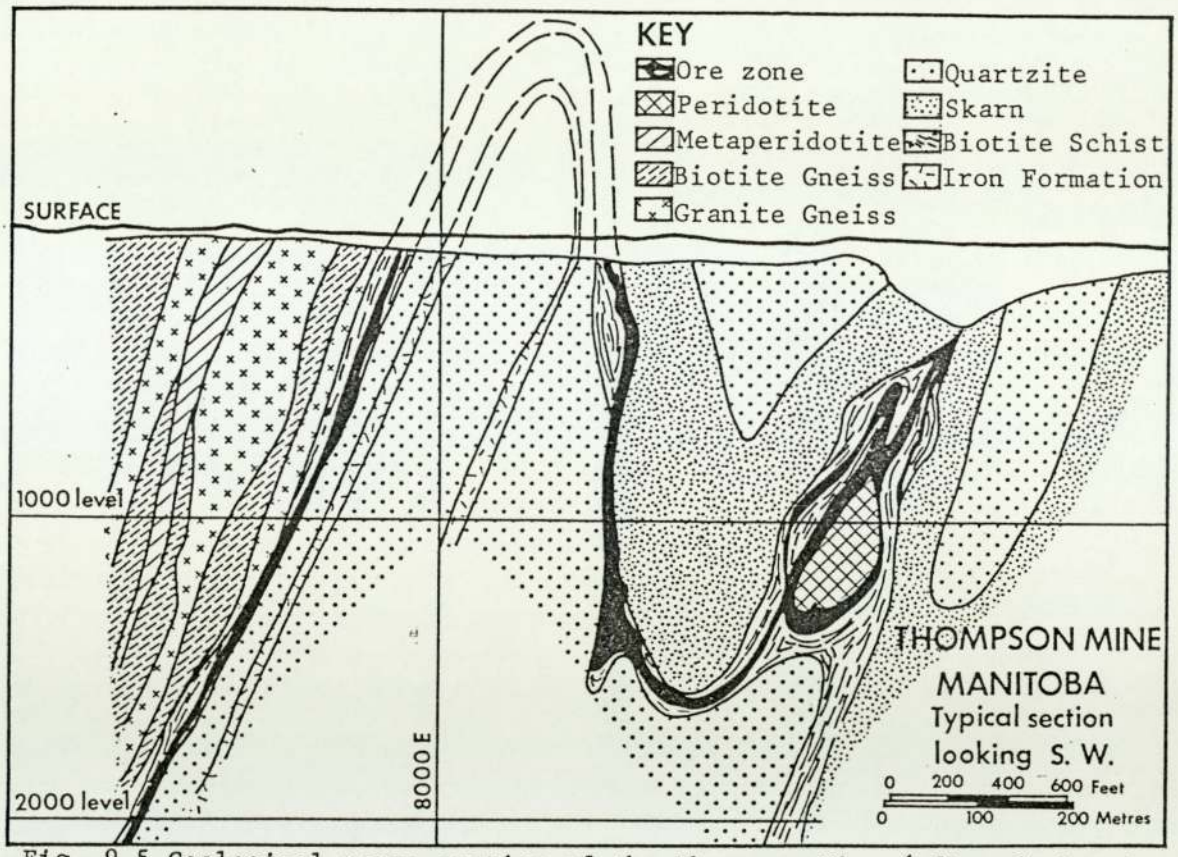

Fig. 9.5 Geological cross section of the Thompson Mine (after Coats et al., 1972).

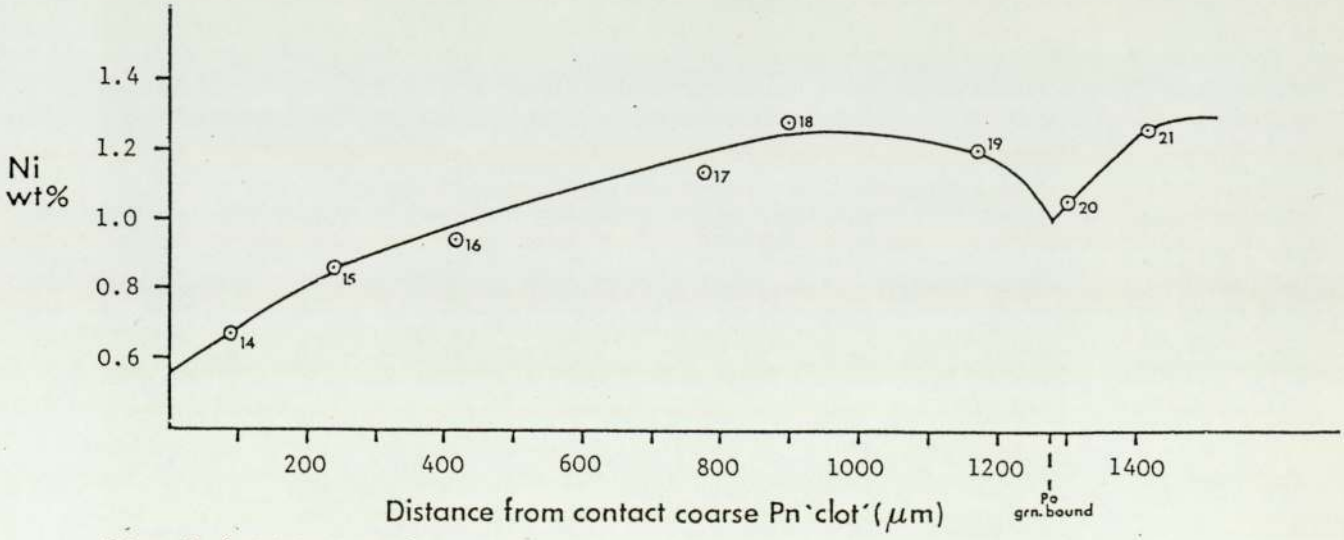

Fig. 9.6 Nickel line profile across Pyrrhotite grains directly adjacent to a coarse granular Pentlandite 'clot' (massive breccia ore, Thompson Mine).

Fig. 9.7 to 9.10 Photomicrographs illustrating the occurrence of granular and rim Pentlandite in massive breccia ore from the Thompson Mine, Manitoba

Fig. 9.7 Two very coarse granular Pn 'clots' (white with fractures, left and right margins) within very fine grained matrix of Po grains (various shades of grey), depleted in Pn. (f.o.v., 7.8mm, unXP)

Fig. 9.8 Discrete blocky Pn (white) interstitial to adjacent relatively coarse Po (grey) grains (f.o.v., 1mm, unXP)

Fig. 9.9 Blocky granular Pn (white) located on the boundaries of fine Po grains (grey, central) which are interstitial to coarser Po grains (f.o.v., 2m, unXP).

Fig. 9.10 Discontinuous Rim Pn with numerous flame extensions along the boundaries between relatively fine Po grains (f.o.v., 1mm, unXP)

Fig. 9.11 to 9.14 Flame-type Pentlandite aggregates within the Kambalda and Thompson ores.

Fig. 9.11 and 9.12 Isolated bladed flame type Pn aggregates at Po grain boundaries. Note ~120° Po triple junctions. Fig. 9.11 Thompson; f.o.v., 0.5mm, unXP, Oil. Fig. 9.12 Hunt ore shoot, Kambalda; f.o.v., 0.31mm, PPL.

Fig. 9.13 Acicular bladed flame Pn aggregates (white) located at contact between a silicate inclusion (black) and Po (light grey) (Thompson; f.o.v., 0.5mm, unXP, Oil)

Fig. 9.14 Bladed flame type Pn aggregates (white) located at a fine fracture within a Po grain (grey) (Thompson; f.o.v., 0.5mm, unXP, Oil)

Fig. 9.7

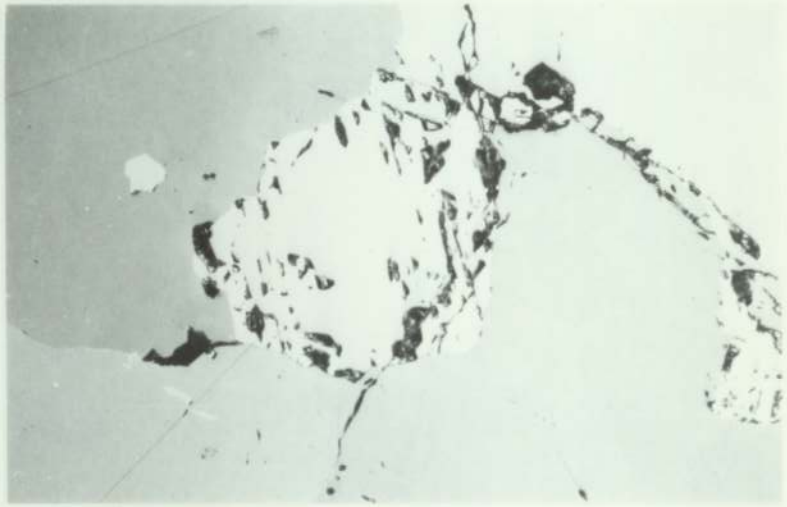

Fig. 9.8

Fig. 9.9

Fig. 9.10

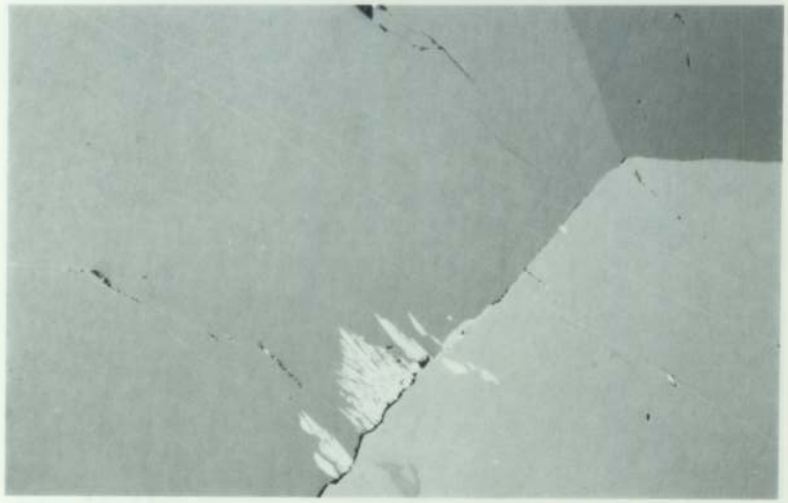

Fig. 9.11

Fig. 9.12

Fig. 9.13

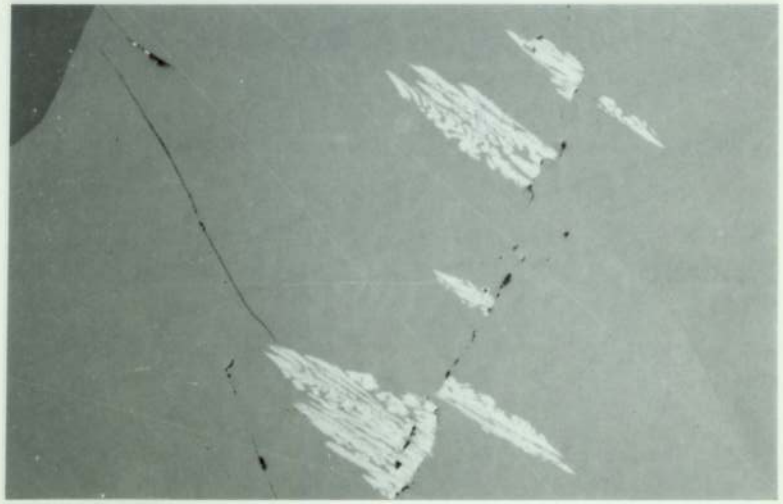

Fig. 9.14

TABLE IA List of Standards used in Electron Microprobe Analysis.

	Element and Standard											
Phase	S	Fe	Ni	Co	Cu	Zn	As	Sb	Ag	Ti	Mn	Cr
MSS	FeS_{syn} NiS_{syn}	FeS_{syn}	NiS_{syn}	$Cu_{0.5}Co_{2.5}S_4$ syn	CuS	----	----	----	----	----		
Pn	-"-	-"-	-"-	-"-	-"-	——	$FeAsS_{syn}$	——	$AgBiSe_2$			
Hex Po	-"-	-"-	-"-	-"-	-"-	——	-"-	Sb_2S_3	——	——		
Mcl Po	-"-	-"-	-"-	-"-	-"-	——	-"-	Sb_2S_3	——	——		
Tr	-"-	-"-	-"-	-"-	-"-	——	——	——	——	——		
Mck	-"-	-"-	-"-	-"-	-"-	——	——	——	——	——		
Py	-"-	-"-	-"-	-"-	-"-	——	FeAsS	Sb_2S_3	——	——		
Cp	FeS_{syn} CuS_{syn}	-"-	-"-	-"-	-"-	ZnS_{syn}	——	——	——	——		
Cub	-"-	-"-	-"-	-"-	-"-	——	——	——	——	——		
Sph	FeS_{syn} CuS_{syn}	-"- -"-	-"-	-"-	-"-	ZnS_{syn}	FeAsS	Sb_2S_3	——	——		
Mt } Ilm }	---	Fe_3O_4	Ni metal	Co metal	Cu metal	——	——	——	——	Ti metal	Mn_3O_4	Cr metal

APPENDIX I ELECTRON MICROPROBE ANALYSIS.

The majority of the analyses reported from this study are wavelength dispersive, determined on a Cambridge Instruments Microscan V. The accelerating voltage was 15KV and the specimen/probe current ∿0.05μA. This reduced both the possibility of 'beam damage' causing vaporization of sulphur and the fluorescence effects. A carbon coat of '∿250μm' was applied to the samples to eliminate 'charging up' of the areas analysed. Care was taken to ensure that the specimens and standards had a carbon coat of the same thickness. The standards used for each phase are listed in Table IA. A P.E.T. crystal was used to detect and select the S, Ti, Cr, and Sb peaks. Other metals were detected using an LiF. crystal. Each individual spot analysis was an average of ten second peak counts for each element. Background readings for each element were taken at 2° either side of the peak. The number of individual spot analyses averaged for each reported mineral analysis are given in the tables.

Peak and background counts were corrected for counter dead time before calculation of the unknown value by comparison with standard counts. The apparent weight percentages obtained were then computer corrected for Z.A.F. matrix effects using the methods devised by Sweatman and Long (1969). Because the standards were close in composition to the minerals analysed, matrix corrections were small, apart from the correction for fluorescence of Fe by Ni in nickel-rich phases.

Operating errors were kept to a minimum by using the following procedures. Areas of analysis for each phase were selected beforehand using reflected light microscopy. Analysis spots were then located using the probe's optical system, backscattered electron imaging and X-ray mapping by reference to sketches or photomicrographs. This was particularly important when analysing fine grained intergrowths such as monoclinic/hexagonal pyrrhotite in the

natural ores and pentlandite/MSS in the synthetic grain mounts. Small inclusions within grains of the phase to be analysed, such as flame pentlandite within pyrrhotite or MSS were avoided by using X-ray mapping of selected elements; in this case nickel. Contamination spots produced by the vacuum pump hydrocarbons were useful for checking the exact location of each spot analysis. The calibrated co-ordinate system on the specimen drive was also used to locate each analysis using a fixed reference point in the sample. This was particularly important when analysing pentlandite and pyrrhotite or MSS since cross-boundary fluorescence of Fe in the Fe-rich monosulphide phases by nickel in the pentlandite occurs close to the mineral boundaries. For this reason analyses of synthetic pentlandite were restricted to the coarser varieties such as rim pentlandite.

The probe current was monitored using the Faraday cage and a drift of approximately ±3 parts in 500 of the probe current was allowed before taking another set of standard counts. The spectrometer peak positions were then rechecked and the beaming centring and focus realigned if necessary, prior to taking another set of standard analyses. Generally between five and ten complete analyses were obtained between each set of standard counts. Within each set of analyses two minerals were analysed to ensure that systematic errors between the results obtained for the same elements in each phase due to slight variations in the operating conditions did not occur. Long analytical runs of up to ten hours were used since once the filament warmed up after operating for 1 or 2 hours, the probe remained relatively stable and only minor corrections for beam drift were required thereafter.

Analytical error was estimated:

i) from the counting statistics

ii) from the variance within the corrected set of analyses obtained for individual (unzoned) phases in the same sample

iii) by taking replicate analyses of each mineral from the same areas in

analytical sessions days or weeks apart.

These methods indicated that the errors in each of the phases analysed were ∿1% of the amount reported for major elements and within ∿10% of the amount reported for minor elements. The minimum detection level was taken at 2δ above the background and varied from ∿0.05wt% to ∿0.1wt% depending upon the atomic weight of the element.

The minor number of energy dispersive analyses were carried out on a Cambridge Instruments S150 S.E.M. with an on-line Link 850 analytical unit. The accelerating voltage was 20KV and count times of 100secs were used. Full Z.A.F. corrections were carried out by the on-line computer using a program patented by Link Systems Limited. Wavelength dispersive and energy dispersive analyses on the same phases from the same samples can be compared in Table 7.1 and are discussed in Chapter 7.

APPENDIX II PROCEDURE FOR PRODUCING GOOD QUALITY POLISHED SECTIONS OF SYNTHETIC MATERIAL

In this method cold setting epoxy resin (Araldite HY753, Hardener HY913) is used to mount the specimens. Up to 15 individual labelled samples can be mounted in a 3 cm diameter araldite block. This is the largest size block which fits the sample holder on a Cambridge Instruments Microscan $\overline{\underline{V}}$ electron probe. The advantages of the method are outlined in Section 3.4.

METHOD

i) Mix up araldite and hardener in required proportion (10:1 by weight) in a clean container.

ii) Place container in an ultrasonic bath and leave for ~10 mins . This moves all the air bubbles to the surface where they can be scraped off with a glass slide. It also has the advantage of temporarily reducing the viscosity of the araldite (see below).

iii) Fill standard 3 cm diameter mould to a depth of between 0.6 cm and 1 cm. The mould should be lightly pre-greased with a contact release agent, such as vaseline.

iv) After allowing to set for a day remove block from mould and champfer off any excess araldite.

v) With block firmly held in metal die drill a series of 4 mm holes, equidistant from the centre of the block, right through the block.

The outer edge of each hole should be ~3-4 mm from the edge of the block. This allows 10 conveniently spaced holes to be drilled, although up to 12 can be made to fit. Drill a further 5 holes closer to the centre of the block. It is easiest to have the surface which will become the polished surface uppermost when drilling, since the small 'lip' around the base of the block prevents fracturing when the drill penetrates to the base.

vi) Replace block in lightly greased mould so that surface is in contact with the bottom of the mould.

vii) Place individual samples into separate holes in the block. The easiest method is to use small funnels of high gloss paper inserted in each hole. This helps prevent cross contamination between samples. Insert label for sample into each hole.

viii) Make up quantity of araldite. It is especially important to ultrasonic to reduce the viscosity.

ix) Pour araldite into each individual hole a portion at a time. Fill the holes to the top.

x) Allow araldite to set for ~24 hours, remove block from mould and leave for a few days to cure thoroughly.

xi) Drill a hole in the base of the block for locating pin on lapping machine. Bevel edges on surface to be polished so that material is easily removed during grinding and polishing.

xii) Remove excess araldite from surface by grinding on a glass plate using 600 mesh carborundum (or silicon carbide) in a light water slurry. It is important at this stage to ensure that most of the surface of the grains or grain aggregates in each sample has almost all the araldite removed.

xiii) After washing and cleaning in an ultrasonic bath, repeat grinding on a glass plate with 800 mesh and 1200 mesh carborundum, carefully washing and cleaning between each stage and especially after the 1200 mesh stage.

xiv) The sample is now placed on lapping machine (Kent MkIIa) on a paper lap with a small amount of diamond paste on surface of lap. Polish at this stage until almost all pluck marks are removed and edge of grain aggregates are clearly visible. Use slow speeds to prevent plucking. It was found to be better not to use weights although inevitably this means it takes longer (~10 to 20 hours). It is important that at no stage in the polishing is a lap that has been previously used to polish silicates used to polish the synthetics.

xv) After cleaning in an ultrasonic bath, polish on 1μm lap until all plucks removed from any pentlandite that is present and 6μm scratches removed. Final polishing on $\frac{1}{4}$ μm lap removes any 1μm scratches in ~30 mins- 1 hr.

xvi) Mount specimen on glass slide using plasticine and specimen press so that polished surface level. This is particularly important since the material is relatively fine-grained and when using high power objectives, all of field of view needs to be in focus, especially for

photomicroscopy.

This method can easily be adapted to other situations where large numbers of 'grain mounts' are required. If the material is coarser grained than in this system (~50 - 250μm) or if larger numbers of grains are required for examination simply drill larger holes and mount fewer specimens on the same block.

APPENDIX III

IMAGE ANALYSIS IN THE STUDY OF PENTLANDITE EXSOLUTION RATES

James R. Craig*, David P. Kelly**, David J. Vaughan**, Robert M. Haralick* and Ting Chuen Pong*

* Spatial Data Analysis Laboratory, Virginia Polytechnic Institute and State University, Blacksburg, Virginia 24061, U.S.A.

** Dept. of Geological Sciences, University of Aston in Birmingham, Birmingham B4 7ET, ENGLAND

The General Image Processing System (GIPSY) has been employed to provide quantitative rate measurements of the amounts of pentlandite $(Fe,Ni)_9S_8$, which have exsolved from the $(Fe,Ni)_{1-x}S$ monosulfide solid solution (mss) in the Fe-Ni-S system. These measurements provide the basic data in a larger study of the kinetics and mechanisms of exsolution reactions. Initially homogeneous mss compositions of differing metal/metal and metal/sulfur ratios have been annealed at varying temperatures from 1 to nearly 2000 hours. The products have been sectioned, polished, and analyzed using GIPSY to define the amount and rate of exsolution. The application of GIPSY has been found to be superior to other methods of charting the progress of the exsolution.

The scientific and economic importance of classification and interpretation of ore textures has been recognized in numerous studies of the textures observed in individual ore deposits at the macroscopic and microscopic levels as summarized in various texts (1,2) More recent textbooks have emphasized the importance of studies of phase equilibria in relevant systems to textural interpretation (3). However, phase equilibrium studies provide a very incomplete and idealized picture of mineral behavior since they characterize only the final, hopefully equilibrium, state in a system. In natural ore mineral systems, the mechanisms and rates (kinetics) of the reactions involved have important influences upon the textures which develop. This detailed quantitative textural analysis can provide information on the amounts of the various phases and yield information useful in the interpretation of the kinetics and mode of exsolution. The data should also enable a much more rigorous application of textural studies in the estimation of rates of cooling and of diffusion within and throughout orebodies. Conversely, greater knowledge of theories of textural development should enable predictions to be made of textural variations which will benefit the mineral technologist.

Two of the authors (D.P.K. and D.J.V.) have been engaged in experimental studies of the Fe-Ni-S system and comparative studies of natural pentlandite-pyrrhotite ores which are characteristic of the so-called "sulfide nickel" deposits. The Fe-Ni-S system is especially appropriate for this type of study because the corresponding natural ores are economically important, are widespread, nearly always contain exsolution textures, and because the general phase relations of the system are well established (4-8)

The mechanisms and kinetics of the exsolution process as deduced from these studies are being described in detail elsewhere (9) The objective of this paper is to demonstrate the application of automated image analysis, GIPSY, in this work to determine the relative amounts of host and exsolved phases and to chart the progress of exsolution as a function of time or of temperature changes. The advantages of image analysis in comparison with alternative methods for charting exsolution are also assessed.

Pyrrhotite-Pentlandite Intergrowths and the Fe-Ni-S System

The so-called "Sulfide nickel" orebodies are the major world source of nickel and often contribute significant amounts of copper, cobalt and platinum group metals. They occur in a variety of geological environments and include such famous examples as the Sudbury Basin, Ontario, Canada (10); the Noril'sk-Talnakh deposits of Northern Siberia, USSR (11) and the Kambalda deposits of Western Australia (12). It is now apparent that most, or all, of the sulfides have crystallized from an immiscible sulfide melt which separated from the parent mafic or ultramafic magma during the early stages of cooling. The sulfide melt and its subsequent crystallization can be very well described in terms of the Fe-Ni-S system.

The various experimental studies noted previously have demonstrated that the dominant feature of the Fe-Ni-S system is the monosulfide solid solution which spans from $Fe_{1-x}S$ to $Ni_{1-x}S$ from above 900°C to below 300°C. Pentlandite becomes a stable phase only when the temperature drops below 610°C; it spans a considerable Fe/Ni range but exhibits only a slight variation in metal/sulfur ratio (see Fig. 1). The bulk compositions of the sulfide fraction of many sulfide nickel orebodies plot within the mss, generally towards more Fe-rich compositions (from 3.6 wt% Ni at Strathcona,

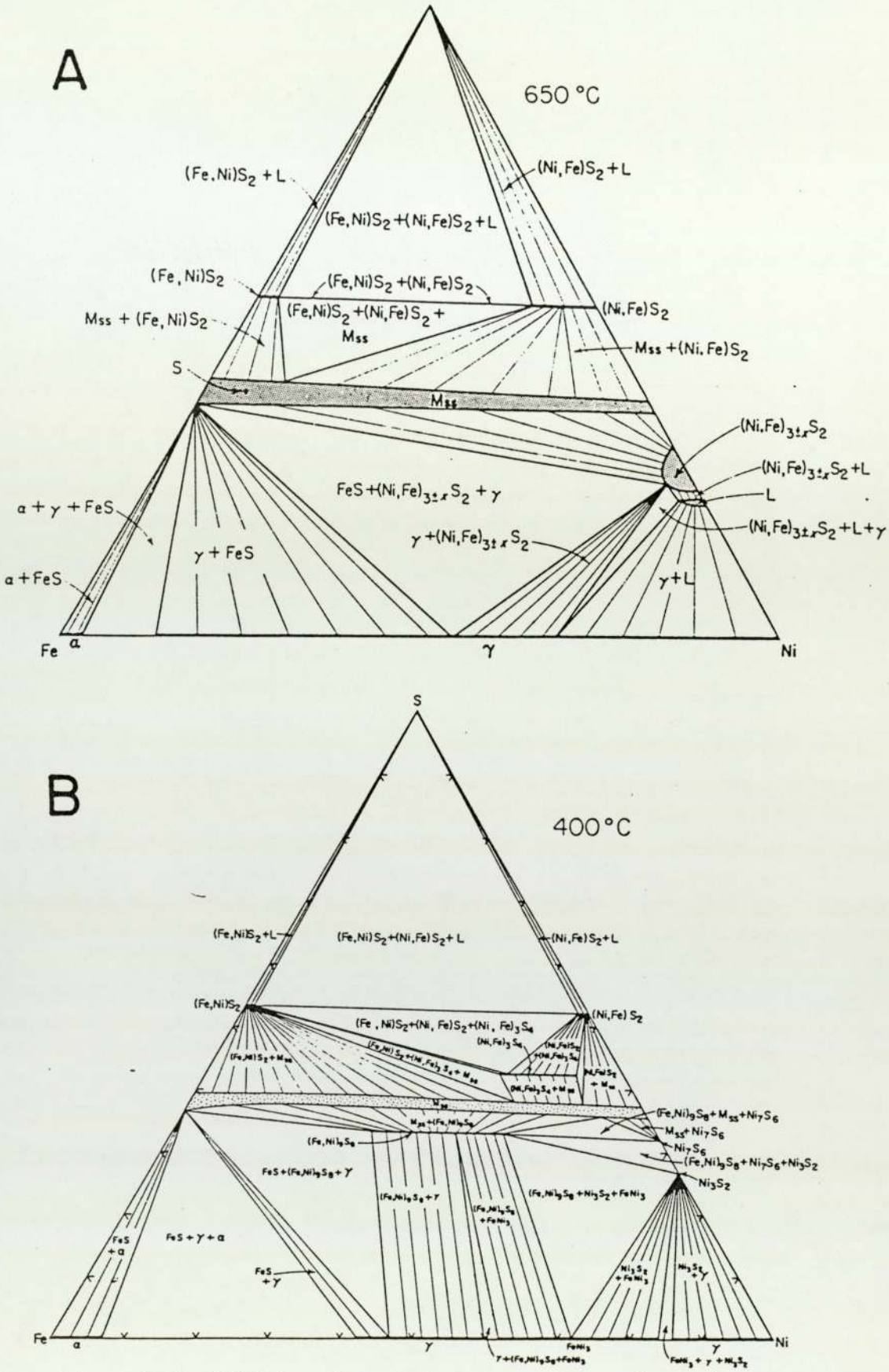

Figure 1. Equilibrium phase relations in the Fe-Ni-S system at: (A) 650°C, and (B) 400°C; from (15).

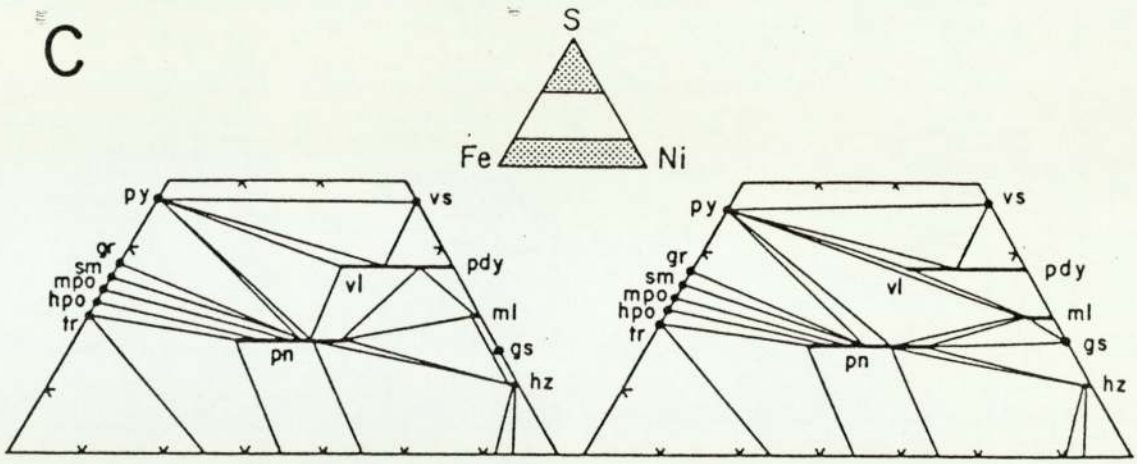

Figure 1(C) Alternative interpretations of low temperature phase equilibria in the Fe-Ni-S system; from (15).

Sudbury to 14.4 wt% Ni at Juan Shoot, Kambalda) when plotted in terms of the Fe-Ni-S system (5,13). Accordingly, original crystallization of the sulfide melt resulted in the formation of mss which remained homogeneous on cooling to temperatures at least as low as 500-600°C. Further cooling resulted in shrinkage of the limits of the mss field such that originally homogeneous sulfide compositions could not be accomodated within the mss. At this point pentlandite began to exsolve from the mss as a separate phase. The exsolution of pentlandite from the mss can be illustrated with reference to Fig. 2 which shows the iron-rich and sulfur-poor portion of the mss. Here have been plotted a series of mss compositions which were synthesized in this work, along with the boundaries showing he sulfur-poor limits of the mss at 600°C, 400°C and 300°C (data from 5). These show that as the temperature decreases below 600°C, the sulfur-poor boundary retreats to more sulfur-rich compositions. Thus, the series of homogeneous samples of varying Fe:Ni and Metal:Sulfur (M:S) ratios synthesized in this study at 600°C (Fig. 2), when annealed at 400°C exsolved a more nickel-rich

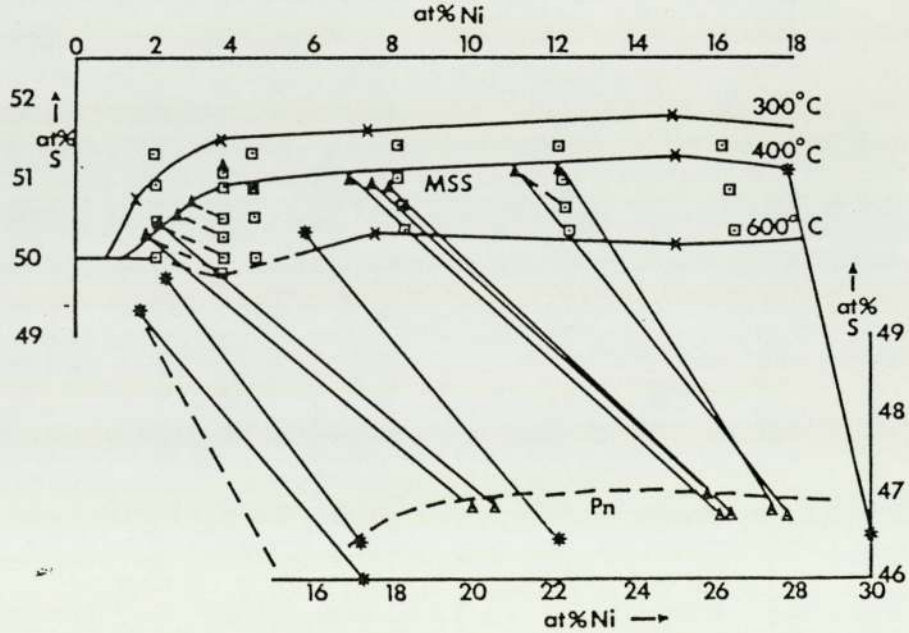

Figure 2. Experimental compositions in the iron-rich mss and pentlandite fields plotted as S and Ni atom percent; note the offset of the Ni scales. Squares are initial compositions at 600°C; triangles are compositions determined by probe at 400°C; stars are from (7); solid lines are S-poor limit of mss from (5).

pentlandite and moved towards a more nickel-poor and iron- and sulfur-rich mss composition. As cooling and exsolution proceed, the residual mss matrix becomes progressively more iron- and sulfur-rich until eventually stabilizing as pyrrhotite.

In order to study the kinetics and mechanisms of pentlandite exsolution, the series of mss compositions illustrated in Figure 2 were synthesized and then divided into batches for annealing in isothermal runs for times varying from 1 to nearly 2000 hours. A variety of annealing temperatures between 500°C and 200°C were used, results reported here are from 400°runs. In this way the rate of reaction and evolution of the textures produced could be monitored. Figure 3 shows the similarity of natural and synthetic pyrrhotite/pentlandite intergrowths.

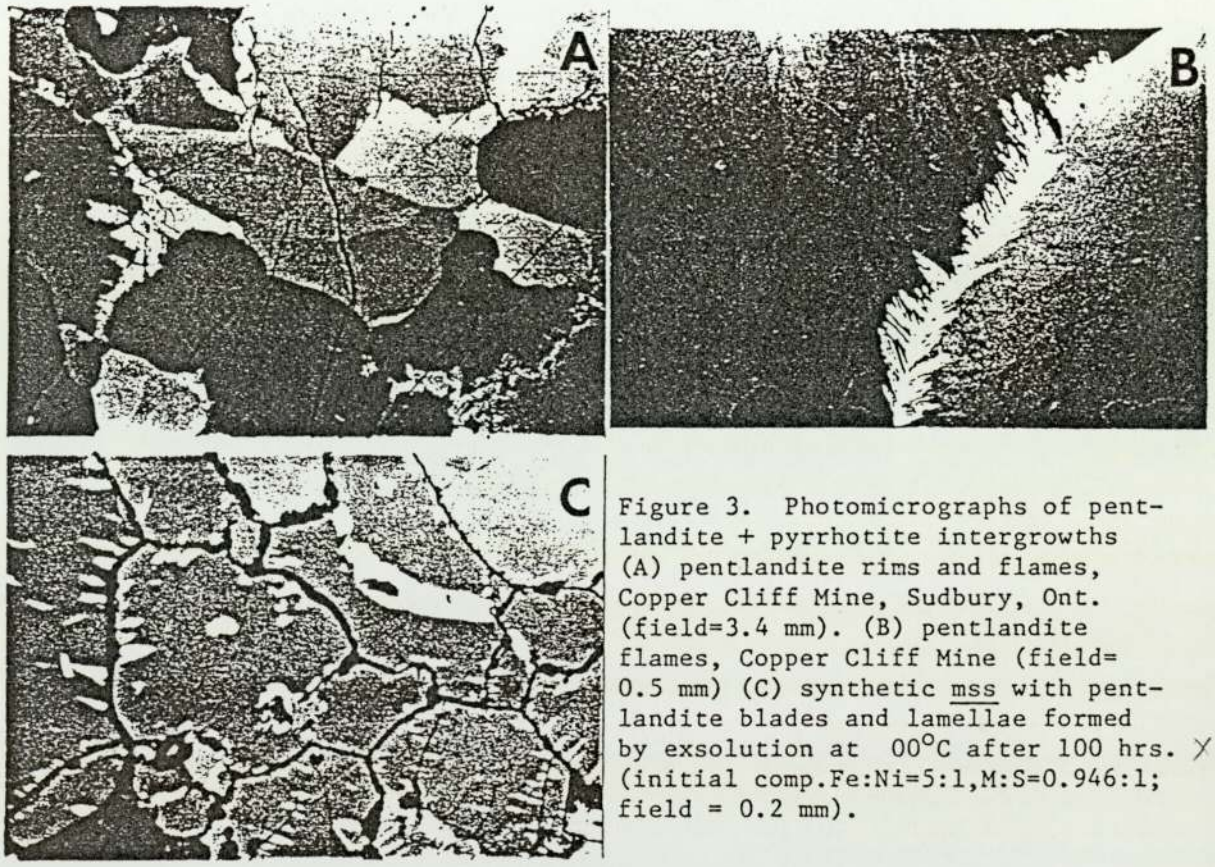

Figure 3. Photomicrographs of pentlandite + pyrrhotite intergrowths (A) pentlandite rims and flames, Copper Cliff Mine, Sudbury, Ont. (field=3.4 mm). (B) pentlandite flames, Copper Cliff Mine (field= 0.5 mm) (C) synthetic mss with pentlandite blades and lamellae formed by exsolution at 00°C after 100 hrs. (initial comp.Fe:Ni=5:1,M:S=0.946:1; field = 0.2 mm).

Image Analysis Using the General Image Processing System (GIPSY)

Accurate determination of the relative amounts of exsolved pentlandite and host mss (or pyrrhotite) is a crucial aspect of this study. For this purpose, image analysis employing the General Image Processing System (GIPSY) was used. GIPSY is a general interactive image processing software package designed to be easily used, easily learned, easily modified, and easily transported from one computer to another. It operates with single or multiband images, in integer or real format, and includes more than 180 operations to do image filtering, classification, geometric spatial transformations, numeric and symbolic recursive neighborhood operations, spatial clustering, region growing, and property file generation. GIPSY is user friendly and has all its documentation on-line and available through GIPSY commands.

In order to carry out image analysis, GIPSY, like most other systems, subdivides the original image into an N by N (N in the range 100 to 5000)

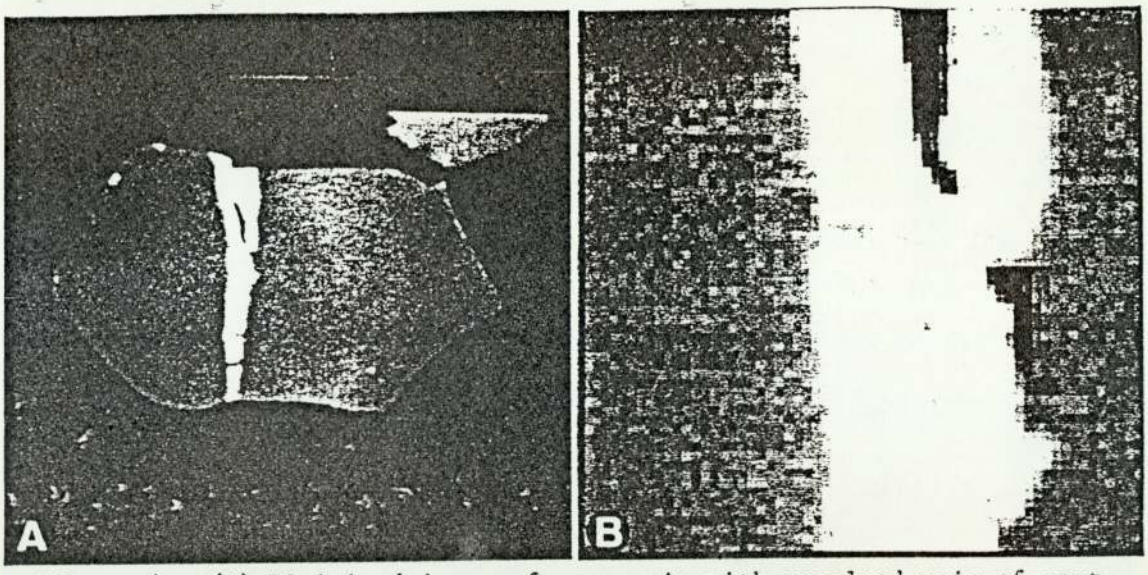

Figure 4. (A) Digitized image of mss grain with exsolved vein of pentlandite (white) (field of view = 0.5mm). (B) Enlargement of a central portion of the image in (A) to show the individual pixels of the image.

array of individual squares (pixels), as shown in Figure 4. The original image, derived from a 35 mm film negative or directly from a TV camera mounted on a microscope, is digitized and stored on magnetic tape or disk.

Area measurement may be carried out by the summing of pixels of various gray levels (reflectances) or by a more complex technique making use of "segmentation." In the former process, a one hundred step threshhold is imposed and the number of pixels with reflectances above and below that threshhold are counted. This procedure, though effective with many images, is subject to errors if the sample has been poorly polished or contains significant noise, because individual pixels can be misclassified. In the latter process the GIPSY system subdivides each image into discrete segments or areas of similar nature by using an edge operator (14) to determine the boundary surrounding each homogeneous region.

Once an image has been segmented, it can be processed in terms of phase identification. The individual segments are assigned a gray-level representing the average of all pixels included within them. Gray level discrimination is routinely based on a scale of 255 recognized levels; however, the averages of individual segments are reported to a precision of 0.001 of a gray level. The sizes of individual segments may be defined in terms of number of pixels contained, percent of total image area, or percent of area identified as that phase. The shapes of segments may be calculated on the boundaries recognized by the edge operator relative to the boundaries expected of ideal shapes.

The sulfide materials used in this study were synthesied by heating weighed amounts of 99.999+% pure iron, nickel, and sulfur in evacuated sealed silica glass tubes in the manner described in (14) and employed by many workers.

Various mss compositions (as shown in Fig. 2), after initial synthesis were annealed in sealed evacuated silica capsules for varying lengths of time and then quenched in ice water and opened to examine the compositions and textures of the products.

Representative portions of each of the products were mounted in cold setting epoxy resin, ground and polished using a modified version of techniques described in standard texts such as Craig and Vaughan (1981). This involved making an epoxy blank 1cm in thickness, drilling the blank with a series of 4 or 5 mm holes then replacing the drilled blank in its mold. The samples were then inserted into individual holes, labelled and the holes refilled with cold-setting epoxy resin. Using care in the grinding and polishing to avoid removal of material by plucking, high quality polished surfaces of up to fifteen samples can be prepared in each epoxy resin block. This allows a considerable saving in time and effort compared with mounting each sample in its own epoxy block, and has the added advantage of keeping the individual grain aggegates of each sample in close proximity.

Results and Discussion

The annealing of originally homogeneous mss compositions at various temperatures for differing lengths of time produced samples which possessed a variety of textures (Figure 3) which are very similar to those observed in natural pyrrhotite-pentlandite ores.

Figure 5 shows a series of photomicrographs of polished sections obtained in this way from a sample (no.16) which initially contained 36.9 wt % S, 52.14 wt % Fe and 10.96 wt % Ni. Fig. 5a shows the homogeneous material and Figs. 5b,c and d show the products of annealing this starting composition at 400°C for 10 hours, 100 hours and 1780 hours respectively.

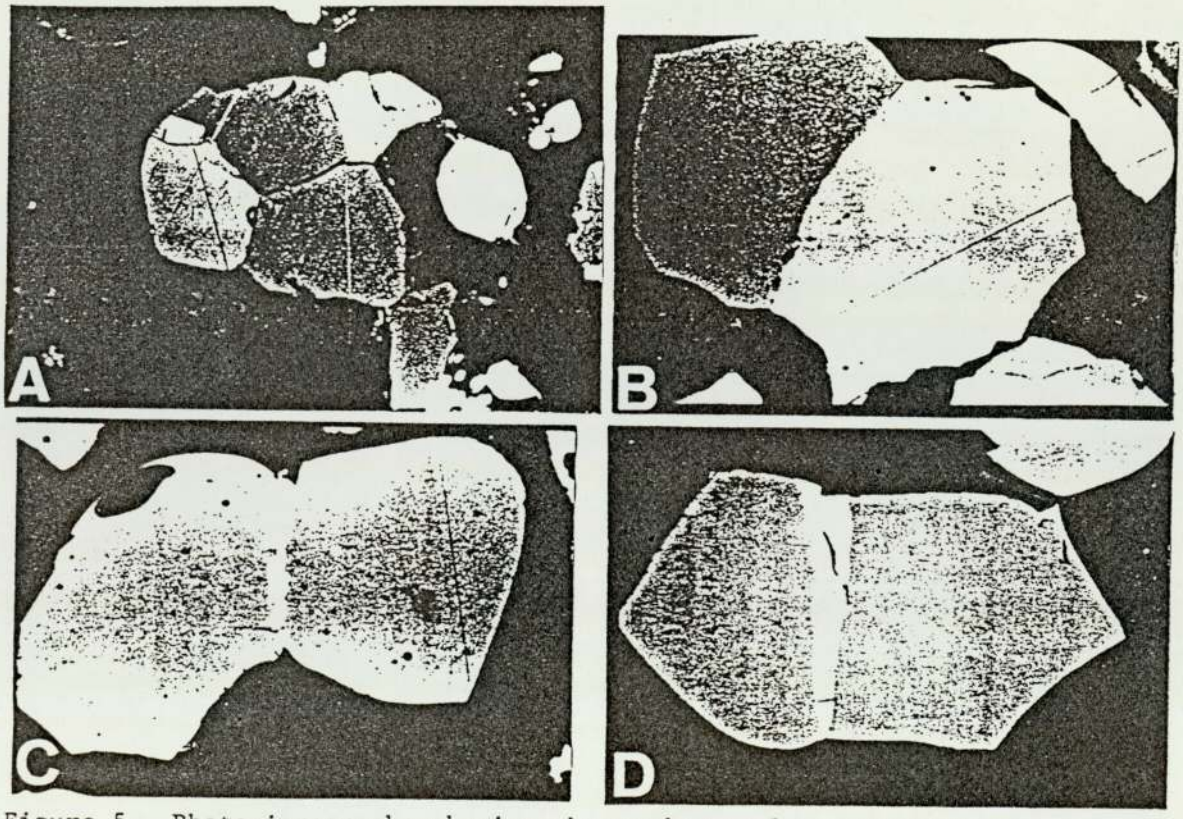

Figure 5. Photomicrographs showing the products of experimental run no. 16. (A) following initial homogenization (x-nicols);(B) after annealing at 400°C for 10 hrs; (C) after annealing at 400°C for 100 hrs; (D) after annealing at 400°C for 1780 hrs. (field of view = 0.5mm).

Table 1. Compositional and Image Analysis Data

SAMPLE	COMPOSITIONAL DATA				GIPSY DATA				
	Weight %				Total	MSS	Pentlandite	Vol %	
	S	Fe	Ni	Total	Area	Area	Area	Pentlandite	
16. (initial comp.)	36.9	52.14	10.96	100.00					
16.1 (10 hrs @ 400°C)					4028	3994	34	0.84	
					2241	2221	20	0.89	
					3256	3227	29	0.89	av.
					3168	3134	34	1.07	1.02
					3232	3193	39	1.21	
					3955	3906	49	1.24	
16.2 (100 hrs @ 400°C)	Composition of Residual MSS:				3242	3173	69	2.13	
	37.26	52.76	10.37	100.39	3842	3793	49	1.28	
					3330	3256	74	2.22	av.
					2553	2519	34	1.33	1.74
					2807	2788	19	0.68	
					3979	3867	112	2.81	
16.6 (1780 hrs @ 400°C)	Composition of Residual MSS:				3095	2973	122	3.94	
	37.39	53.17	10.00	100.56	2885	2768	117	4.06	
					3901	3793	108	2.77	av.
					2929	2861	68	2.32	3.50
					2290	2167	123	5.37	
					3056	2978	78	2.55	
17. (initial comp.)	36.7	52.3	11.0	100.00					
17.1 (10 hrs @ 400°C)					3847	3764	83	2.16	
					2783	2661	122	4.38	
					3310	3242	68	2.05	av.
					2460	2358	102	4.15	2.90
					3261	3183	78	2.39	
					3247	3173	74	2.28	
17.2 (100 hrs @ 400°C)	Composition of Residual MSS:				1972	1865	107	5.43	
	37.20	53.13	9.61	99.94	3730	3593	137	3.67	av.
					3105	2939	166	5.35	4.77
					3076	2934	142	4.62	
17.6 (1780 hrs @ 400°C)	Composition of Residual MSS:				3608	3320	288	7.98	
	37.43	53.75	9.29	100.47					

Table 1 contains information on the initial (weighed out) starting compositions of two experimental samples of different starting composition which were subjected to the same annealing treatment and the subsequent data obtained from analysis of the products by GIPSY.

The annealing for longer periods of time resulted in a progressive increase in the amount of pentlandite exsolved as noted in Figure 4 and Table 1. A major problem in the determination of the amount of pentlandite exsolved is ascertaining which, if any, sample surface observed is truly representative. This problem can be especially significant if there is any preferential orientation between the host and exsolved phases; such an orientation effect is known to exist when pentlandite initially exsolves from mss (16). In order to minimize bias caused by orientation effects, a minimum of 5-6 fields of view were selected from the hundred or so grain aggregates present within the polished sections of each sample. The results of all images for a given sample were averaged (Table 1). Although there are significant variations among the images for each sample, the results are not nearly so divergent as might be expected considering the potential problems. The data of Table 1 were obtained through the analysis of black and white photomicrographs; good results have also been obtained using negatives or by taking images directly from the polished specimen using a television camera mounted on the microscope. The reason for using photographs in this case was so that specimens prepared and photographed in Birmingham, England, could be analyzed in the Laboratory in Virginia, without having to mail specimens which might be needed for further study.

The GIPSY data presented in Table 1 show the total area of sulfide on any single photographic image (in number of pixels) and the breakdown of this into the areas of mss and pentlandite respectively, and hence the percentage of pentlandite present. There were two major problems encountered in using image analysis to determine the quantities of mss and pentlandite: (1) irregular lighting of images (2) bireflectance of mss. The former effect can alter the appearance of the pentlandite and both effects result in a non-uniform appearance of the mss. Irregular lighting, although immediately detected by GIPSY, is very easily overlooked by the human observer when viewing a sample in the microscope or when taking a photograph. The bireflectance effect is innate in the mss because of its anisotropy; it is a feature which is useful to the human observer but difficult to discount for GIPSY. In order to overcome both of these types of problems, where they impaired GIPSY's ability to distinguish between phases, clear acetate sheets were attached over the photographs. The pentlandite, present only as lamellae, small grains, or "chains" of equant grains, was colored over on the acetate sheet. It was then simple to set the detection threshhold for GIPSY below the reflectance level of all mss and pentlandite grains (however irregularly illuminated or whatever the degree of bireflectance) and count the total area of the two sulfides on the photograph. Then the acetate mask, with the pentlandite areas darkened, was laid over the photograph and the area remeasured by GIPSY; the difference was the area of the pentlandite (Figure 6). This method can be further used to easily distinguish between types of occurrence of pentlandite - lamellar versus rim or granular - even though the different varieties may have the same reflectance. The observer can, in fact, make as many types of distinctions as desired, and progessively color the acetate sheet as appropriate.

It is interesting to compare this method of monitoring the exsolution process with the two other methods which can be employed in studies of this system. Both focus on charting changes in the bulk composition of the residual mss as exsolution proceeds. The first is electron probe

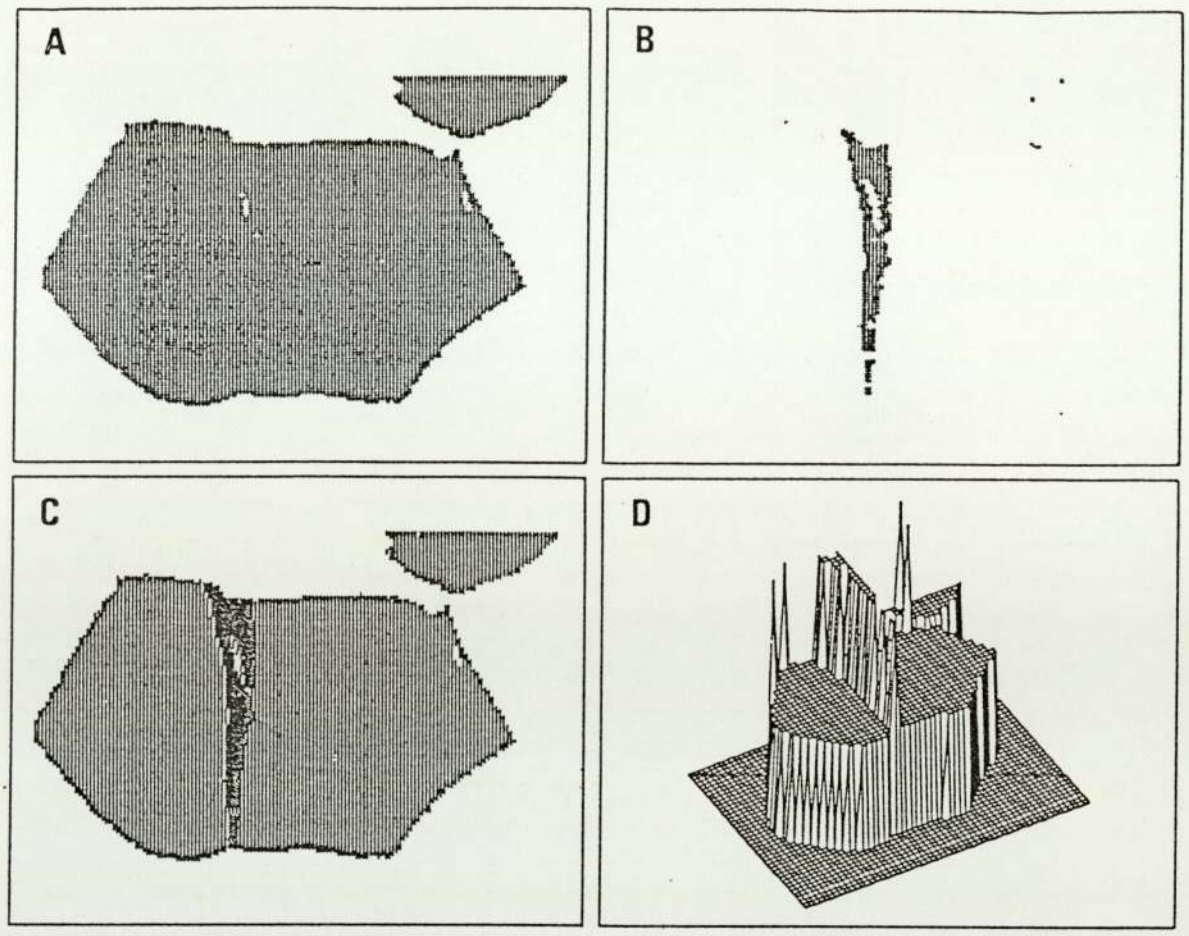

Figure 6. High speed printer figures of mss +pentlandite grain thresholded so as to detect (A) all sulfides, (B) only pentlandite, (C) both sulfides in different patterns. (D) An oblique 3-D view of the image shown in A,B,C and Fig. 4 in which the vertical axis is brightness of reflectance.

microanalysis, examples of which are also shown in Table 1. It can be seen that although the correct trends are observed in most cases through very careful analysis, the differences in composition of mss products of the various runs rarely exceed 1 wt% for any of the elements, and are commonly about 0.5 wt %. This is approximately the limit of accuracy for this method of analysis. The second technique involves determination of the d_{102} lattice spacing of the mss from measurement of X-ray powder photographs or diffraction traces. The variation of d_{102} for $Fe_{1-x}S$ and $(Fe,Ni)_{1-x}S$ compositions as a function of changing M:S or Fe:Ni ratio has been calibrated as a determinative method (Naldrett et al, 1967). However, as can be seen from figs 2a and b, the progressive decrease in nickel content of the mss compositions as exsolution proceeds follows very closely the slope of the d_{102} contours. For instance, the initial composition of sample 17 has a d_{102} value of 2.070 A while for the equilibrium composition 17.6, the d_{102} value is 2.071 A. Clearly, it would be very difficult to distinguish these two compositions using this method, and intermediate residual mss compositions would be indistinguishable.

It is worth noting that this X-ray method has been applied very successfully to measuring exsolution rates of pyrite from the pyrrhotite solid solution (the iron-end members of the mss) (17). In this case, there is a well-defined second-order polynomial expression relating d_{102} values to pyrrhotite composition (in at % Fe) (17,18) and the change in the d_{102} value with composition is very much greater (fig 2b).

An X-ray diffraction method of determining the amount of pentlandite present, relative to other phases including pyrrhotite, has been used in analysis of mill products of nickel sulfide ores from the Kambalda deposits, W. Australia (19). In this method, the relative intensities of selected peaks of each phase are measured from a diffractometer trace, the intensities of these peaks having previously been calibrated using samples where the amounts of each phase present is known. In our study, however, the amounts of pentlandite present are in most cases so small that they are not detected on a trace. In those that can be detected, the differences in the amounts of pentlandite as exsolution proceeds are even smaller and not distinguishable (see Table 1). Additionally, the small amounts of sample available from experimental runs require a smear mount preparation for use in the diffractometer (see 20 pp 146-147, for details of preparation). This leads to errors in both of the X-ray diffraction techniques described. Errors in relative peak intensities due to preferential orientation and errors in peak positions due to the surface of the sample being out of position relative to the focussing plane of the X-ray beam have both been encountered.

The data in Table 1 show, of course, that the amount of pentlandite exsolved from a given mss starting composition at a particular annealing temperature increases with time. It was assumed that the runs of 1780 hrs at 400°C had exsolved the full amount of pentlandite and hence attained equilibrium because the mss compositions all lie close to, or on, the equilibrium 400°C solvus as determined by 5 (see table 1 and figure 2a). These compositions were confirmed by electron probe microanalyses. The volume fraction of pentlandite exsolved (V) at any given time (t) is given by:

$$V = \frac{\text{volume of pentlandite at time } t}{\text{volume of pentlandite at equilibrium (1780 hrs)}}$$

By plotting V for runs of different duration on selected mss compositions, it is therefore possible to quantify the rate of the reaction for each composition and to establish the effect of varying the Fe:Ni and M:S ratios on the reaction rate. This is illustrated by Fig. 7 which shows the volume fraction of pentlandite exsolved as a function of time for a series of mss compositions with the same Fe:Ni ratio but different m:s ratios. These preliminary data are derived from estimates of pentlandite percentages using a number of methods including image analysis. They show that the exsolution rate increases as the initial M:S ratio increases. This is because the net driving force for nucleation, the volume free energy, increases while the opposing surface and strain energy terms remain essentially constant (see 9). Hence for compositions of higher initial m:s ratios such as 1.000:1 the higher nucleation rate increases the number of nuclei forming heterogeneously at defects, such as grain boundaries. Thus diffusion distances in these compositions are decreased, leading to an increase in the exsolution rate relative to compositions of lower m:s ratio, such as m:s = 0.965:1. For instance, after 10 hrs the relative proportions of pentlandite exsolved are about 5% and 8% respectively. Eventually, in the compositions of higher initial m:s ratio, the defects become effectively saturated in nuclei, impingement of adjacent nuclei increasing the diffusion distance. At this stage, homogeneous nucleation of more dispersed and fewer nuclei becomes advantageous since the diffusion distances involved are much smaller. This leads to the formation of orientated lamellae within mss grains and a decrease in the exsolution rate. At lower m:s ratios such as 0.965:1, lower nucleation rates ensure saturation does not occur and exsolution proceeds more steadily by heterogeneous nucleation. For a m:s ratio of 0.955:1, the equilibrium mss - pentlandite solvus has not been crossed at 400°C so there is no net driving force for nucleation and no pentlandite has been exsolved.

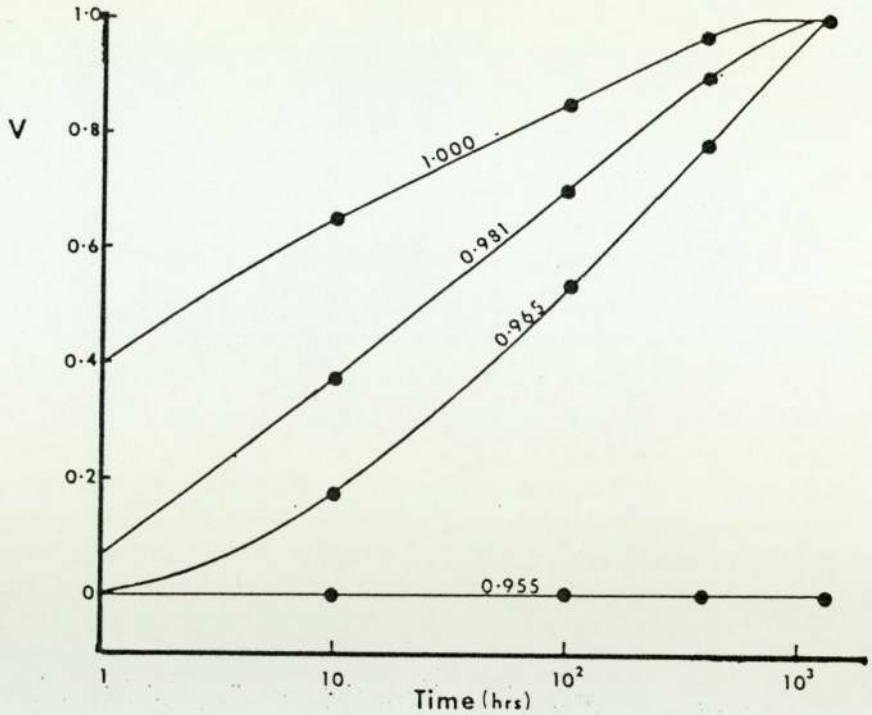

Figure 7. Diagram illustrating the dependence of the pentlandite exsolution rate on the initial M:S ratio for mss compositions of Fe:Ni = 12.3 : 3.7 (at.%) at 400°C. Volume fraction of pentlandite exsolved vs log time.

The variety of pentlandite textural types and their evolution, together with derivation of time - temperature - transformation - composition models for this reaction are discussed in (9). Reaction rates derived from image analysis will allow us not only to indicate the time taken for initiation and completion of exsolution on such diagrams but also to contour the intermediate stages, for selected compositions, showing how far the reaction has gone towards completion.

As already noted, a unique aspect of image analysis in textural studies is that it may also be used to quantitatively determine the amounts of different textural types or generations of the same phase. In the case of the Fe-Ni-S system, we are now using image analysis to determine amounts of textural types, such as 'rim' pentlandite, formed by heterogeneous nucleation relative to homogeneous nucleated lamellae. This will enable us to quantify the relative importance and rates involved in compositions where both types of nucleation occurs.

Image analysis therefore provides the best means of quantifying the progress of exsolution in a system such as Fe-Ni-S. It is rapid, relatively accurate and can be undertaken 'on line' using polished sections, which are essential to such a study, or at a distance using photographs.

Acknowledgments

The Natural Environment Research Council is thanked for provision of a research studentship to DPK. The image analysis facilities were made possible in part through a Mining and Minerals Resources and Research Institute allotment grant.

References

1. A. B. Edwards, Textures of the Ore Minerals, Aust. Inst. Min. Metall., Melbourne, 1947.
2. P. Ramdohr, The Ore Minerals and their Intergrowths, 1st and 2nd editions, Pergamon Press, Oxford, U. K. (1969, 1981).
3. J. R. Craig and D. J. Vaughan, Ore Microscopy and Ore Petrography, p.489, Wiley-Interscience, New York, N.Y. (1981).
4. G. Kullerud, "The Fe-Ni-S system," Carnegie Inst. Washington Yearbook ,62 (1963) pp.175-189.
5. A. J. Naldrett, J. R. Craig and G. Kullerud, "The central portion of the Fe-Ni-S system and its bearing on pentlandite exsolution in iron-nickel sulfide ores," Econ. Geol. 62 (1967) pp. 826-847.
6. R. W. Shewman and L. A. Clark, "Pentlandite phase relations in the Fe-Ni-S system and notes on the Monosulfide Solid Solution," Can. J. Earth Sci. 7 (1970) pp. 67-85.
7. K. C. Misra and M. E. Fleet, "The chemical composition of synthetic and natural pentlandite assemblages," Econ. Geol. 68 (1973) pp. 518-539.
8. J. R. Craig, "Pyrite-pentlandite and other low temperature relations in the Fe-Ni-S system," Amer. Jour. Sci. (1973) pp. 496-510.
9. D. P. Kelly and D. J. Vaughan, "Pyrrhotite-pentlandite ore textures: A mechanistic approach," Mineral. Mag. 47 (1983) pp.453-463.
10. J. E. Hawley, "The Sudbury Ores: Their Mineralogy and Origin," Canad. Mineral. 7 (1962), pp.1-207.
11. V. I. Smirnov, (edit.) Ore Deposits of the U.S.S.R., Vol II, Pirman, Moscow, U.S.S.R.
12. J. J. Gresham and G. D. Loftus-Hills,"The geology of the Kambalda Nickel Field, Western Australia," Econ. Geol,. 76 (1978) pp. 1373-1416.
13. A. J. Naldrett, "Nickel sulfide deposits: classification, composition and genesis," Econ. Geol. 75th Anniv. Vol. (1981) pp. 628-685.
14. R. M. Haralick, "Zero crossing of second directional derivative edge operator," IEEE Trans. on Pattern Analysis and Machine Intelligence (in press).
15. D. J. Vaughan and J. R. Craig, Mineral Chemistry of Metal Sulfides, p.493, Cambridge University Press, Cambridge, U.K., 1978.
16. C. A. Francis, M. B. Fleet, K. C. Misra, and J. R. Craig, "Orientation of exsolved pentlandite in natural and synthetic nickeliferous pyrrhotite," Amer. Min. 61 (1976) pp.913-920.
17. R. A. Yund, and H. T. Hall, "Hexagonal and Monoclinic pyrrhotite," Econ. Geol. 64 (1969) pp. 420-423.
18. R. A. Yund and H. T. Hall,"Kinetics and mechanisms of pyrite exsolution from pyrrhotite," Jour. Petrol. 11 (1970) pp. 381-404.
19. D. H. Hooton and N. E. Giorgetta, "Quantitative X-ray diffraction analysis by a direct calculation method," X-ray Spectrometry 6 (1977) pp. 2-5.
20. C. S. Hutchison, Laboratory Handbook of Petrographic Techniques, p. 527 Wiley-Interscience, New York,N. Y , 1974.